



Zachariou, Andrea (2021) *Diffusion, reactivity and structural change in microporous materials*. PhD thesis.

<https://theses.gla.ac.uk/82282/>

Copyright and moral rights for this work are retained by the author

A copy can be downloaded for personal non-commercial research or study, without prior permission or charge

This work cannot be reproduced or quoted extensively from without first obtaining permission from the author

The content must not be changed in any way or sold commercially in any format or medium without the formal permission of the author

When referring to this work, full bibliographic details including the author, title, awarding institution and date of the thesis must be given

Enlighten: Theses

<https://theses.gla.ac.uk/>  
[research-enlighten@glasgow.ac.uk](mailto:research-enlighten@glasgow.ac.uk)



University  
of Glasgow | School of  
Chemistry

# Diffusion, Reactivity and Structural Change in Microporous Materials

Andrea Zachariou  
School of Chemistry  
University of Glasgow  
March 2021

*Submitted in fulfilment of the requirements for the degree of  
Doctor of Philosophy*

I declare that, except where due reference is made, that this thesis for the degree of Doctor of Philosophy is my own work and has not been submitted for any other degree at this institution or elsewhere.

Andrea Zachariou  
University of Glasgow

## Acknowledgements

I would like to firstly thank my supervisors Prof. Stewart Parker and Prof. David Lennon, for their guidance and patience with me, my industrial sponsors Johnson Matthey and especially my industrial supervisor Dr. Paul Collier, the EPSRC and the University of Glasgow for funding my work. I would also like to thank Prof. Russel Howe, for his invaluable help throughout my project with his knowledge on zeolites and the MTH reaction. I would also like to express my sincere gratitude to the UK Catalysis Hub for hosting me for the duration of my project and making me feel part of the team. I would like to offer my special thanks to Dr June Callison for helping me throughout my project through her support and help especially when equipment was broken and needed fixing as well as Dr Josie Goodall for her help settling in the Hub. I would also like to extend my thanks to Dr Ian Silverwood, for his help with QENS beam times and his patience with helping me through the QENS data analysis. Dr Nathan Barrow for his help with NMR experiments, the support staff in ISIS and the Research Complex for making my experiments possible.

Alex, Rachel and Emma, we started this journey together, and I am most thankful that I am able to complete it with all of you by my side. Thank you for all the support, the laughs and the tears, I could not do it without you. The rest of the UK Catalysis Hub students, Monik, Evan, Jay, George, Daniela, Ellie, Dan, Lisa, James, Toni, thank you for keeping me sane and making me laugh when I needed you. A special thank you to the post-docs for supporting me when I needed it, Ines and Donnie.

Thank you to my mum and dad for their unwavering support in me and their encouragement to go after my dreams, all my family, my aunts and uncles, my cousins, and my brother for standing by me and helping me through this, especially when it was coming close to the end. I would like to especially thank George and Emily for taking me in when I needed a roof over my head to finish writing. My best friends Thalia, Andri and George, as well as all my girls back home (Leda, Christiana, Roulla, Harita, Christina, Maria, Pavlina) for keeping me motivated and helping me push through. To the friends that are actually family, (Solomonides and Vrachimides), my niece (Zoe) my nephews (Michalis, Louis, Michael) I love you all. And to the most important people in my life, my yiayides Myrofora and Theonitsa, my pappoudes Minas and Kostas and my godson Christos, this is dedicated to you.

Σας αγαπώ!

## Abstract

The Methanol-to-Hydrocarbons reaction is a group of industrially relevant reactions which focus on the use of methanol as a feedstock to turn it into light olefins (Methanol-to-Olefins) and/or gasoline-range aromatics (Methanol-to-Gasoline) over an acidic zeolite catalyst. Understanding the shift between two product regimes is important in order to be able to shift between the two. There is a lack of understanding when it comes to the mechanism of the Methanol-to-Hydrocarbons reaction, with the most widely accepted mechanism being the 'Hydrocarbon Pool' mechanism. An autocatalytic cycle in which the product distribution depends on the composition of the formed hydrocarbons within the zeolite pores.

In literature, a combination of IR, Raman, ssNMR and other spectroscopies have been used in order to try and identify the identity of the hydrocarbons at different parts of the reaction coordinate. Inelastic Neutron Scattering has only been recently used in order to study this, with this thesis focusing on expanding on those studies and identifying the hydrocarbons retained within the ZSM-5 catalyst during MTH conditions at different temperatures and time-on-stream. INS spectra showed that at a mature steady state, the retained hydrocarbons gave the same spectra irrespective of temperature. This, as well as comparing the INS spectra given from using both dimethyl ether and methyl acetate as reactants, has suggested that the spectra are the 'vibrational fingerprint of the hydrocarbon pool'. At high temperatures of 400°C, and at more than 20 wt% coke, the INS spectra were dominated by coke, with the coke being assigned to 'glassy-like' carbon suggesting that the coke is formed from growing polycyclic aromatics. Studying the diffusion of methane through the coked samples has highlighted the challenges of using coked species to complete such experiments.

The interaction between methanol and ZSM-5 at room temperature has been investigated as well. INS studies have shown that the OH functionality of the methanol has disappeared when the methanol was dosed in the zeolite at room temperature. This contradicted results obtained with other spectroscopic techniques. A variety of scenarios were explored in trying to rationalise the contradictory results. A comparison study using ssNMR, DRIFTS and INS has been completed, with it showing that methanol is present within the zeolite intact with the possibility of methoxy being present at an occupancy of less than 1% chance.

## Preface

This thesis is part of an iCase studentship award between the University of Glasgow and Johnson Matthey Plc. The project has been a collaboration between the UoG, JM and ISIS Neutron and Muon Source. INS is an underutilised technique when it comes to heterogeneous catalysis. Industrial samples are well suited to the technique due to the lack of selection rules that govern optical spectroscopies. This project highlights the advantages of using neutron spectroscopic techniques to understand industrial reactions better. The project was based in the UK Catalysis Hub, at the Research Complex at Harwell. The location of being within easy access to the ISIS Neutron and Muon Source as well as the Johnson Matthey Sonning Common research centre, was ideal in taking advantage of both facilities when needed with minimum issues or disruptions.

This project was unique in nature as two iCase studentships were awarded at the same time on using the same ZSM-5 catalyst. This project, identified as iCase-1 (student: Andrea Zachariou) which used neutron techniques to study the aspects of the Methanol-to-Hydrocarbons reaction over the ZSM-5 catalyst. In parallel the iCase-2 project (student: Alexander P. Hawkins), used neutron techniques to examine the hydrocarbon interactions over the ZSM-5 catalyst, including the matters of diffusion within the pore structure. The work has connectivity to the gasoline-to-olefin process. Understanding the multifaceted nature of the ZSM-5 zeolite has been of interest to the industrial partners and therefore the two projects were working in conjunction. The first year of the PhD projects, both Alex and myself, were working together as a training period. With the characterisation of the catalyst being overlapping for both projects. After the initial training period the projects took their separate avenues with cross collaboration between the two used to advance both projects simultaneously.

The beam time allocations for both projects were completed with the beam time team of Mr Alexander Hawkins, Prof Russell F. Howe, Dr Stewart F. Parker, Prof David Lennon and myself. A total of 21 beam time allocations were completed in the duration of both projects. The collaborative nature of both projects had collaborators from a variety of academic institutions including Prof. Russel F. Howe (University of Aberdeen), Dr Suwardiyanto (University of Jember) and resulted in 11 publications, 1 paper draft submitted and in peer review at the time of writing this (March 2021) and 3 more papers in mature drafts. The data and metadata will be available from the University of Glasgow data repository.

## Publications

A. Zachariou, A. Hawkins, D. Lennon, S.F. Parker, Suwardiyanto, S.K. Matam, C.R.A. Catlow, P. Collier, A. Hameed, J. McGregor and R.F. Howe, *Investigation of ZSM-5 Catalysts for Dimethylether Conversion Using Inelastic Neutron Scattering*, *Appl. Catal. A Gen.*, **2019**, 569, 1–7

A. Zachariou, A.P. Hawkins, P. Collier, R.F. Howe, S.F. Parker and D. Lennon, *The Effect of Co-Feeding Methyl Acetate on the H-ZSM5 Catalysed Methanol-to-Hydrocarbons Reaction*, *Top. Catal.*, **2020**, 63, 370–377.

A. Zachariou, A.P. Hawkins, P. Collier, R.F. Howe, D. Lennon and S.F. Parker, *The Methyl Torsion in Unsaturated Compounds*, *ACS Omega*, **2020**, 5, 2755–2765.

A. Zachariou, A.P. Hawkins, S.F. Parker, D. Lennon and R.F. Howe, *Neutron spectroscopy studies of methanol to hydrocarbons catalysis over ZSM-5*, *Catal. Today*, **2020**, in press, DOI:10.1016/j.cattod.2020.05.030.

A. Zachariou, A.P. Hawkins, Suwardiyanto, P. Collier, N. Barrow, R.F. Howe, S.F. Parker, and D. Lennon, *New Spectroscopic Insight into the Deactivation of a ZSM-5 Methanol-to-Hydrocarbons Catalyst*, *ChemCatChem*, **2021**, in press, DOI: 10.1002/cctc.202100286

A.P. Hawkins, A.J. O'Malley, A. Zachariou, P. Collier, R.A. Ewings, I.P. Silverwood, R.F. Howe, S.F. Parker and D. Lennon, *Investigation of the Dynamics of 1-Octene Adsorption at 293 K in a ZSM-5 Catalyst by Inelastic and Quasielastic Neutron Scattering*, *J. Phys. Chem. C*, **2019**, 123, 417–425.

A.P. Hawkins, A. Zachariou, P. Collier, R.A. Ewings, R.F. Howe, S.F. Parker and D. Lennon, *Low-Temperature Studies of Propene Oligomerization in ZSM-5 by Inelastic Neutron Scattering Spectroscopy*, *RSC Adv.*, **2019**, 9, 23136–23147

A.P. Hawkins, A. Zachariou, P. Collier, R.A. Ewings, R.F. Howe, S.F. Parker and D. Lennon, *Effect of Steam De-Alumination on the Interactions of Propene with H-ZSM-5 Zeolites*, *RSC Adv.*, **2020**, 10, 18785–18790

A.P. Hawkins, A. Zachariou, P. Collier, R.A. Ewings, I.P. Silverwood, R.F. Howe, S.F. Parker and D. Lennon, *Onset of Propene Oligomerization Reactivity in ZSM-5 Studied by Inelastic Neutron Scattering Spectroscopy*, *ACS Omega*, **2020**, 5, 7762–7770

S.K. Matam, A.J. O'Malley, C.R.A. Catlow, Suwardiyanto, P. Collier, A.P. Hawkins, A. Zachariou, D. Lennon, I. Silverwood, S.F. Parker and R.F. Howe, *The Effects of MTG Catalysis on Methanol Mobility in ZSM-5*, *Catal. Sci. Technol.*, **2018**, 8, 3304–3312

A.P. Hawkins, A. Zachariou, S.F. Parker, P. Collier, R. F. Howe, and D. Lennon, *Studies of propene conversion over H-ZSM-5 demonstrate the importance of propene as an intermediate in methanol-to-hydrocarbons chemistry*, *Cat. Sci. Tech.*, **2021**, in press, DOI: 10.1039/D1CY00048A

A. Zachariou, A.P. Hawkins, R.F. Howe, N. Barrow, J. Bradley, P. Collier, D. Lennon, and S.F. Parker, *A Spectroscopic Paradox: The Interaction of Methanol with ZSM-5 at Room Temperature*, **2021**, *in peer-review*

# Table of Contents

<b>Acknowledgements</b> .....	iii
<b>Preface</b> .....	v
<b>Publications</b> .....	vi
<b>Table of Contents</b> .....	viii
<b>Table of Figures</b> .....	xiii
<b>Table of Tables</b> .....	xviii
<b>Nomenclature</b> .....	xx
<b>Chapter 1 Introduction</b> .....	1
1.1 Introduction to Neutron Scattering .....	1
1.1.1 Neutron Sources .....	1
1.1.2 Neutron Detectors .....	3
1.1.3 Neutron Interactions.....	4
1.1.4 Why Use Neutrons .....	5
1.1.5 Neutron Scattering in Catalysis .....	8
1.2 Methanol-to-Hydrocarbons .....	9
1.2.1 The Catalyst.....	9
1.2.2 Reaction Mechanism.....	11
1.2.2.1 Initiation Stage: The First C-C Bond .....	12
1.2.2.1 Steady State: ‘Hydrocarbon Pool’ .....	14
1.2.2.2 Catalyst Deactivation Stage .....	15
1.2.3 Methods Used to Study Retained Hydrocarbons.....	17
1.3 Project Aims and Thesis Outline .....	20
References .....	21
<b>Chapter 2 Methodology</b> .....	29
2.1 Neutron Techniques.....	29
2.1.1 Neutron Scattering Basics .....	29
2.1.2 Inelastic Neutron Scattering (INS) Spectroscopy .....	31
2.1.2.1 Indirect Geometry Instruments – TOSCA.....	33
2.1.2.2 Direct Geometry Instruments – MAPS and MERLIN .....	34
2.1.2.3 INS Experimental Procedure .....	35
2.1.3 Quasi-elastic Neutron Scattering (QENS).....	37
2.1.3.1 Backscattering Spectrometers – IRIS .....	38
2.1.3.2 QENS Experimental Procedure .....	40
2.2 Infrared Spectroscopy.....	41

2.2.1 Diffuse Reflectance Infrared Fourier Transform Spectroscopy (DRIFTS) ...	43
2.2.1.1 DRIFTS Experimental Conditions.....	45
2.3 Reaction Testing.....	45
2.3.1 ISIS/Glasgow Catalysis Rig.....	46
2.3.2 Microreactor Set Up.....	49
2.4 Catalyst Characterisation Techniques.....	53
2.4.1 Nitrogen Sorption Measurements .....	53
2.4.1.1 Surface Area Analysis .....	54
2.4.1.2 Micropore Analysis .....	54
2.4.1.3 Nitrogen Sorption Experimental Conditions.....	55
2.4.2 Temperature Programmed Desorption .....	55
2.4.2.1 Ammonia TPD Experimental .....	56
2.4.3 Temperature Programmed Oxidation.....	56
2.4.3.1 TPO Experimental Conditions .....	57
2.4.4 Thermogravimetric analysis.....	57
2.4.4.1 TGA Experimental Conditions .....	57
2.4.5 Diffraction .....	58
2.4.5.1 Neutron Diffraction.....	58
2.4.5.2 Powder X-ray Diffraction.....	59
2.4.6 Solid State Nuclear Magnetic Resonance .....	59
2.4.6.1 NMR experimental conditions .....	61
References .....	61
<b>Chapter 3 Zeolite Characterisation and Reference Compounds .....</b>	<b>66</b>
3.1 Introduction .....	66
3.2 Experimental .....	67
3.2.1 Characterisation of ZSM-5 .....	67
3.2.1.1 Quantification of Acid Sites.....	68
3.2.2 Model Compounds.....	71
3.2.4.1 Computational Methods.....	71
3.3 Characterisation of ZSM-5 .....	73
3.3.1 Surface Area Analysis .....	73
3.3.2 DRIFTS .....	73
3.3.3 X-Ray Diffraction .....	74
3.3.4 XRF .....	75
3.3.5 ssNMR .....	76
3.3.5 Studying the ZSM-5 acid sites .....	78

3.3.5.1 Ammonia TPD .....	78
3.3.5.2 Quantification of Acid Sites with INS .....	79
3.3.5.3 Pyridine Desorption using INS.....	82
3.3.5.4 Neutron Diffraction.....	86
3.3.6 Summary of Characterisation .....	87
3.4 Reference Compounds.....	89
3.4.1 Methyl Rock and C-H Bending Modes .....	92
3.4.2 Computational Studies.....	94
3.4.1.1 Intra- Vs Intermolecular Effects .....	96
3.4.3 Summary .....	99
3.5 Conclusions .....	99
3.6 References .....	100
<b>Chapter 4 Interactions of Methanol in ZSM-5.....</b>	<b>106</b>
4.1 Introduction .....	106
4.2 Experimental .....	108
4.2.1 Microreactor Catalyst Testing.....	108
4.2.2 Flow Dosed Methanol Experiments.....	109
4.2.3 Static Dosed Methanol Experiments.....	109
4.2.4 Exchanged Methanol Experiments .....	110
4.2.5 In-situ experiments .....	110
4.3 Evidence For and Against Methoxylation .....	110
4.3.1 Microreactor Catalyst Testing.....	110
4.3.2 INS .....	112
4.3.3 DRIFTS .....	113
4.3.4 Solid State NMR .....	115
4.4 Rationalising the Observed Differences.....	117
4.4.1 Scenario 1: Hidden OH Modes in INS.....	118
4.4.2 Scenario 2: Both Species are Present.....	119
4.4.3 Scenario 3: Dosing Differences .....	122
4.4.4 Scenario 4: OH Peaks too Broad to Detect .....	125
4.5 Conclusions .....	126
4.6 References .....	127
<b>Chapter 5 Spectroscopic Insight into the Methanol-to-Hydrocarbons Reaction ...</b>	<b>130</b>
5.1 Introduction .....	130
5.2 Experimental .....	131
5.2.1 INS Samples.....	131

5.2.1.1 Post Reaction Catalyst Analysis.....	132
5.2.2 Reaction Testing - Microreactor .....	133
5.3 Reaction Testing.....	134
5.3.1 INS Reactor Measurements .....	134
5.3.2 Microreactor .....	139
5.4 Post Reaction Analysis .....	141
5.4.1 NMR Spectroscopy.....	145
5.4.1.1 <sup>13</sup> C-NMR .....	145
5.4.1.2 <sup>27</sup> Al NMR spectroscopy .....	148
5.4.1.3 <sup>29</sup> Si-NMR spectroscopy.....	149
5.4.2 DRIFTS .....	150
5.4.3 INS .....	152
5.4.4 INS Assignments.....	156
5.5 Changing the Contact Time.....	159
5.5.1 Reaction Monitoring .....	159
5.5.2 Post Reaction Analysis .....	160
5.6 Conclusions .....	164
5.7 References .....	166
<b>Chapter 6 Methane Diffusion Through Coked Samples.....</b>	<b>171</b>
6.1 Introduction .....	171
6.2 Experimental .....	172
6.3 Elastic Window Scans.....	173
6.4 Quasi-elastic Analysis.....	175
6.4.1 ZSM-5 Blank/ZSM-5 with Methane.....	176
6.4.2 Coked Samples .....	180
6.4.2.1 Fitting of the MTH-2h.....	182
6.4.2.2 Fitting of the MTH-110h.....	184
6.4.3 Methane Loaded Coked Samples.....	187
6.4.3.1 Fitting of the Methane Loaded MTH-2h .....	187
6.4.3.2 Fitting of the Methane Loaded MTH-110h .....	191
6.5 Conclusions .....	194
6.6 References .....	195
<b>Chapter 7 Studying the Effect of Different Feedstock on the MTH Reaction.....</b>	<b>198</b>
7.1 Introduction .....	198
7.1.1 Dimethyl Ether .....	198
7.2.1 Methyl Acetate.....	199

7.2	Experimental .....	199
7.2.1	Dimethyl Ether as Feedstock.....	200
7.2.1	Methyl Acetate/Methanol as Feedstock.....	201
7.2	Dimethyl Ether as Feedstock.....	201
7.3.1	Reaction Monitoring .....	201
7.2.2	Post Reaction Analysis .....	203
7.2.2.1	<sup>13</sup> C-NMR Spectroscopy .....	205
7.3.2.2	<sup>27</sup> Al and <sup>29</sup> Si NMR Spectroscopies .....	207
7.3.2.3	DRIFTS .....	209
7.2.3.4	INS .....	210
7.2.3	Summary .....	215
7.3	Methyl Acetate/Methanol as Feedstock.....	216
7.3.1	Reaction Monitoring .....	216
7.3.2	Post-Reaction Catalyst Characterisation.....	219
7.3.2.1	DRIFTS .....	220
7.4.2.2	INS .....	222
7.3.3	Summary .....	225
7.5	Concluding Remarks.....	225
7.6	References .....	226
<b>Chapter 8 Conclusions and Future Work .....</b>		<b>230</b>
8.1	Conclusions .....	230
8.2	Future Work .....	233
<b>Appendix: Chapter 3.....</b>		<b>A-1</b>
<b>Appendix: Chapter 4.....</b>		<b>A-11</b>
<b>Appendix: Chapter 6.....</b>		<b>A-20</b>
<b>Appendix: Chapter 7.....</b>		<b>A-22</b>

## Table of Figures

<b>Figure 1.1:</b>	Scattering length of neutrons and x-rays with varying atomic number.....	6
<b>Figure 1.2:</b>	Schematic representation of ZSM-5 structure.....	11
<b>Figure 1.3:</b>	Dual cycle scheme.....	14
<b>Figure 2.1:</b>	Scattering triangles for elastic and inelastic scattering events.....	31
<b>Figure 2.2:</b>	Schematic of the TOSCA instrument located at the ISIS Facility..	34
<b>Figure 2.3:</b>	Schematic of the MAPS instrument located at the ISIS .....	35
<b>Figure 2.4:</b>	The primary spectrometer for both OSIRIS and IRIS.....	38
<b>Figure 2.5:</b>	The schematic of the IRIS second spectrometer .....	39
<b>Figure 2.6:</b>	Schematic representation of the ISIS gas handling manifold.....	41
<b>Figure 2.7:</b>	Michelson interferometer schematic.....	43
<b>Figure 2.8:</b>	Interior of Praying Mantis accessory .....	44
<b>Figure 2.9:</b>	Schematic representation of the ISIS/Glasgow .....	47
<b>Figure 2.10:</b>	Schematic representation of the reactor set up connected to the gas manifold. ....	48
<b>Figure 2.11:</b>	Microreactor schematic. ....	51
<b>Figure 2.12:</b>	Calibration graph of GC-FID intensity vs standards of known concentrations using a calibration mixture of hydrocarbons. ....	52
<b>Figure 2.13:</b>	Calibration graph of GC-FID intensity vs standards of known concentrations. (a) Methanol (b) Propene .....	52
<b>Figure 2.14:</b>	(a) Types of isotherms with their type labelled at the left top corner (b) Types of hysteresis loops.....	53
<b>Figure 3.1:</b>	Nitrogen adsorption (square) / desorption (circles) isotherm for fresh ZSM-5 .....	73
<b>Figure 3.2:</b>	DRIFTS spectra of ZSM-5 as received and ZSM-5 after it has been calcined and dried. ....	74
<b>Figure 3.3:</b>	XRD pattern of (a) ZSM-5 as received (b) ZSM-5 after it has been calcined.....	75
<b>Figure 3.4:</b>	Peak fitting of <sup>29</sup> Si-NMR spectrum of ZSM-5.....	77
<b>Figure 3.5:</b>	Peak fitting of <sup>27</sup> Al-NMR Spectrum of ZSM-5 .....	78
<b>Figure 3.6:</b>	Ammonia TPD of calcined fresh ZSM-5, as well as peak fitting of the experimental data. ....	79
<b>Figure 3.7:</b>	INS Spectrum of Fresh ZSM-5 collected using the MAPS spectrometer.....	80
<b>Figure 3.8:</b>	(a) INS OH calibration by using the integrated areas of the brucite peaks at different concentrations. (b) The INS spectrum of ZSM-5 focused on the OH stretch region.....	81
<b>Figure 3.9:</b>	TOSCA spectra of pyridine (orange) and pyridinium chloride .....	82
<b>Figure 3.10:</b>	TOSCA Spectra of pyridine adsorption and desorption on zeolite samples .....	83
<b>Figure 3.11:</b>	MAPS Spectra after pyridine adsorption and desorption. ....	84
<b>Figure 3.12:</b>	Peak fitting of the MAPS spectra of Fresh ZSM-5 (a) after pyridine adsorption and (b) after pyridine desorption.....	85
<b>Figure 3.13:</b>	Neutron diffraction pattern of Fresh H-ZSM-5 .....	87
<b>Figure 3.14:</b>	Neutron diffraction pattern of Fresh D-ZSM-5 .....	87
<b>Figure 3.15:</b>	INS spectra collected via TOSCA of benzenes.....	90
<b>Figure 3.16:</b>	INS spectra collected via TOSCA of tri- and tetra-methylated benzenes. ....	91

<b>Figure 3.17:</b>	INS spectra collected via TOSCA of (a) pentamethylbenzene and (b) hexamethylbenzene .....	91
<b>Figure 3.18:</b>	INS Spectra collected via TOSCA of naphthalenes .....	92
<b>Figure 3.19:</b>	INS spectra collected via TOSCA of polycyclic aromatics. ....	92
<b>Figure 3. 20:</b>	INS spectra of methylated benzenes in the region of the methyl rock and the C-H bending modes.....	93
<b>Figure 3.21:</b>	Comparison of observed and DFT calculated INS spectra of hexamethylbenzene.(i) 0 – 1800 cm <sup>-1</sup> and (ii) expanded view of the region containing the methyl torsions. ....	94
<b>Figure 3.22:</b>	Comparison of the average methyl torsion transition energy of hexamethylbenzene and mesitylene as a function of the shortest intermolecular contact. ....	98
<b>Figure 3.23:</b>	The average methyl torsion energy of methylbenzenes as a function of the number of methyl groups. ....	98
<b>Figure 4.1:</b>	Product composition of MTH reaction completed at 350°C.....	111
<b>Figure 4.2:</b>	Methanol percentage conversions using GC-FID. ....	111
<b>Figure 4.3:</b>	Mass spectrometer profile of the outlet gas from the reactor for methanol over ZSM-5 at room temperature. ....	112
<b>Figure 4.4:</b>	Solid methanol and flow dosed methanol on ZSM-5 at room temperature collected with (a) TOSCA (b) MAPS .....	113
<b>Figure 4.5:</b>	DRIFTS spectra of blank ZSM-5 (black), ZSM-5 with methanol injected under flow (blue), Sample was then flushed under 100 ml/min of N <sub>2</sub> .....	114
<b>Figure 4.6:</b>	Difference Spectra of Figure 4.5 using the blank ZSM-5 as background.. ....	115
<b>Figure 4.7:</b>	ss- <sup>13</sup> C-NMR spectra (a) Methanol dosing comparable to INS, waited for 1.5h and then heated at 150 °C (b) Methanol dosing comparable to Ref 9, and then evacuated at 0.3 mbar. ....	116
<b>Figure 4.8:</b>	ss- <sup>1</sup> H-NMR spectra. (a) Methanol dosing comparable to INS, waited for 1.5 hrs then heated to 150 °C, (b) Methanol dosing comparable to Ref 9, and then evacuated to 0.3 mbar .....	117
<b>Figure 4.9:</b>	INS spectra of solid CD <sub>3</sub> OH and CD <sub>3</sub> OH flow dosed on ZSM-5 at room temperature.. ....	119
<b>Figure 4.10:</b>	DRIFTS difference spectra, 6 injections of 2 µl methanol at room temperature at 20ml/min nitrogen flow, heated to 200 °C at 5 °C/min, cooled to room temperature and 6 further injections, 2 µl methanol. ....	120
<b>Figure 4.11:</b>	Difference spectrum of Injection 6, RT, Before Heat on Figure 4.9 with the integrated areas used in determining the extinction coefficients shaded in. ....	122
<b>Figure 4.12:</b>	INS Spectrum of static dosed methanol on ZSM-5. Spectrum intensity was normalised by sample weight. ....	123
<b>Figure 4.13:</b>	<sup>13</sup> C-Methanol dosed ZSM-5 sample spectra. (a) <sup>13</sup> C-NMR spectrum (b) DRIFTS spectrum (c) INS spectrum collected with the TOSCA spectrometer (d) INS spectrum collected with the MAPS spectrometer.....	124
<b>Figure 4. 14:</b>	MAPS spectra of CH <sub>3</sub> OD dosed ZSM-5 vs exchanged CH <sub>3</sub> OH dosed ZSM-5.. ....	126
<b>Figure 5.1:</b>	Mass spectrometer reaction profiles for INS reactor as a function of reaction temperature: (a) 300 -60h (b) 350 -110h (c) 400 -44h ..	135
<b>Figure 5.2:</b>	Methanol conversion for MTH reactions in the INS reactor at three different temperatures: (a) 300, (b) 350 and (c) 400 °C .....	136

<b>Figure 5.3:</b>	GC-MS analysis of liquid products collected in the organic layer of the catch-pot: (a) 300°C-60h (b) 350°C-110h (c) 400°C-44h.....	138
<b>Figure 5.4:</b>	Percentage peak areas of the GC-MS liquid product analysis plotted against time-on-stream for the reactions of (a) 300-60h (b) 350-110h and (c) 400-44h.....	139
<b>Figure 5.5:</b>	Microreactor reaction in-line GC-FID data. The product distributions for the three reaction temperatures (300, 350 and 400°C) are presented as a function of increasing time-on-stream: (a) 55, (b) 222, (c) 395 and (d) 500 min. M signifies moles of product per litre of gas.....	140
<b>Figure 5.6:</b>	Microreactor reaction in-line GC-FID data. The product distributions for the three reaction temperatures (300, 350 and 400°C) are presented as a function of increasing time-on-stream: (a) 615, (b) 870 min. M signifies moles of product per litre of gas.....	141
<b>Figure 5.7:</b>	Microreactor reaction in-line GC-FID data. The product distributions for the three reaction temperatures (350 and 400°C) are presented as a function of increasing time-on-stream: (a) 1320 and (b) 1430 min. M signifies moles of product per litre of gas...	141
<b>Figure 5.8:</b>	Nitrogen adsorption (square) / desorption (circles) isotherms for (a) Unreacted ZSM-5 (b) 300-2h (c) 350-2h and (d) 400-2h .....	142
<b>Figure 5.9:</b>	Nitrogen adsorption (square) / desorption (circles) isotherms for (a) 300-60h (b) 350-110h (c) 400-44h .....	143
<b>Figure 5.10:</b>	TPO profiles of the reacted catalyst samples at temperatures of 300, 350 and 400 °C. ....	144
<b>Figure 5.11:</b>	Mass normalised TPO Profiles (deconvoluted) of the reacted catalysts.....	145
<b>Figure 5.12:</b>	<sup>13</sup> C cross-polarisation magic angle spinning NMR spectra of the short reaction samples: (a) 300-2h; (b) 350-h (c) 400 -2h. ....	146
<b>Figure 5.13:</b>	<sup>13</sup> C cross-polarisation magic angle spinning NMR spectra of the long reaction samples: (a) 300-60h; (b) 350-110h. ....	146
<b>Figure 5.14:</b>	<sup>13</sup> C-ssNMR spectra of the reacted ZSM-5 samples of (a) 350°C-110h (red) and (b) 400°C-44h (blue) .....	147
<b>Figure 5.15:</b>	<sup>27</sup> Al-NMR Spectra (B <sub>0</sub> = 9.4 T) of the MTH reacted samples contrasted against unreacted ZSM-5: short reaction times; and extended reaction times. (a) unreacted ZSM-5; (b) 300-2h; (c) 300-60h; (d) 350-2h; (e) 350-110h; (f) 400-2h. ....	148
<b>Figure 5.16:</b>	<sup>29</sup> Si-NMR spectra (B <sub>0</sub> = 9.4 T) of the MTH reacted samples contrasted against unreacted ZSM-5. (a) unreacted ZSM-5; (b) 300-2h; (c) 300-60h; (d) 350-2h; (e) 350-110h; (f) 400-2h.....	149
<b>Figure 5.17:</b>	Solid state <sup>29</sup> Si MAS NMR Spectra (B <sub>0</sub> = 14.1 T) of (a) 350-110h sample and (b) 400-44h sample.....	150
<b>Figure 5.18:</b>	DRIFTS spectra (4000-2500 cm <sup>-1</sup> ) of the ZSM-5 catalyst post-reaction after 2 h T-o-S at the following reaction temperatures: (b) 300, (c) 350 and (d) 400°C. ....	151
<b>Figure 5.19:</b>	DRIFTS spectra (4000-500 cm <sup>-1</sup> ) of the ZSM-5 catalyst post-reaction after extended T-o-S at the following reaction temperatures: (b) 300-60h (c) 350-110h and (d) 400-44h.. ....	152
<b>Figure 5.20:</b>	INS spectra collected with the TOSCA spectrometer for the short reaction times (2 h) as a function of reaction temperature: (i) 300, (ii) 350 and (iii) 400 °C.....	153
<b>Figure 5. 21:</b>	INS spectra of the MTH reacted ZSM-5: (i) 300°C for 60 h; (ii) 350°C for 110 h; (iii) 400°C for 44 h. ....	154
<b>Figure 5.22:</b>	Peak fitting of (a) 300-60h (b) 350-110h (c) 400-44h samples ...	155

<b>Figure 5.23:</b>	Experimental 350-110h spectrum (i) compared with the generated addition spectra (equimolar additions of model compound spectra).....	157
<b>Figure 5. 24:</b>	Experimental 400-44h spectrum (i) compared with model compounds: (ii) glassy carbon; (iii) graphite.....	158
<b>Figure 5.25:</b>	Percentage peak areas of the GC-MS liquid product analysis plotted against time-on-stream for the reactions of sample 400-44h-Frt.....	160
<b>Figure 5.26:</b>	TPO profile of sample 400-44-Frt.....	161
<b>Figure 5. 27:</b>	ssNMR of the 400-44h-Frt sample completed with the 400 MHz Spectrometer. (a) <sup>13</sup> C-NMR (b) <sup>27</sup> Al-NMR and (c) <sup>29</sup> Si-NMR.....	162
<b>Figure 5.28:</b>	DRIFTS spectra of the 400-44h sample (blue), the 350-110h sample (red) and 400-44h-Frt sample (cyan).....	163
<b>Figure 5.29:</b>	The INS spectra of the 400-44h-Frt sample collected via (a) TOSCA (b) MAPS.....	164
<b>Figure 5.30:</b>	Peak fitting of 400-44h-Frt sample. ....	164
<b>Figure 6.1:</b>	Elastic Fixed Window Scan of the empty samples compared with the methane loaded samples (a) ZSM-5 blank (b) MTH-2h and (c) MTH-110h.....	175
<b>Figure 6.2:</b>	QENS spectra at base temperature for the blank samples and their loaded counterparts (all detector groups grouped together). (a) ZSM-5 (b) MTH-2h and (c) MTH-110h.. ....	176
<b>Figure 6.3:</b>	HWHM ( $\Gamma$ ) vs. $Q^2$ for the Lorentzian fit on each temperature for the fresh ZSM-5 with methane (a) 225 K, (b) 275 K, (c) 325 K and (d) 373 K. ....	178
<b>Figure 6.4:</b>	Arrhenius plot of the natural log of the diffusion coefficient over the inverse of temperature, for the ZSM-5 with methane.....	180
<b>Figure 6.7:</b>	EISF experimental data of the MTH-2h sample fit with rotational models. The QENS EISF data fit were recorded at (a) 225 K, (b) 275 K, (c) 325 K and (d) 373 K.....	183
<b>Figure 6.8:</b>	EISF experimental data of the MTH-110h sample fitted with rotational models. QENS EISF data fitted were recorded at (a) 225 K, (b) 275 K, (c) 325 K and (d) 373 K. ....	186
<b>Figure 6.7:</b>	HWHM over $Q$ for the Lorentzian fit on each temperature for MTH-2h with methane (a) 225K (b) 275K (c) 325K and (d) 373K. Four different jump diffusion models were used to fit the data. CE: Chudley Elliot (green), HR: Hall Ross (red), SS: Singwi Sjolander (pink) and the Jobic (orange) model.....	189
<b>Figure 6.8:</b>	Arrhenius plot of the natural log of the diffusion coefficient over $1/T$ for the sample of MTH-2h loaded with methane.....	191
<b>Figure 6.9:</b>	Methane molecule rotational models labelled with bond lengths and angles. (a) Isotropic rotation (b) 2-site jump and (c) 3-site jump.....	192
<b>Figure 6.10:</b>	EISF Experimental data fitted with rotational models for the MTH-110h with methane (a) 225K (b) 275K (c) 325K and (d) 373K....	193
<b>Figure 7.1:</b>	Normalised mass spectrometer reaction profiles of gaseous products evolved during DME conversion at 350 °C for (a) DME-2D and (b) DME-3D samples.....	202
<b>Figure 7.2:</b>	Mass spectrometer reaction profiles of gaseous products evolved during DME conversion at 350 °C for the DME-1D sample. ....	203
<b>Figure 7.3:</b>	TPO profiles of DME-1D, DME-2D and DME-3D.....	205
<b>Figure 7.4:</b>	<sup>13</sup> C CPMAS spectra of : (a) , DME 1D, 2.6 kHz; (b), DME 2D, 3.5 kHz; (c), DME 3D, 3.5 kHz; (d) Zeolite reacted with methanol at 523 K for 3 days, 3.0 kHz, (e) hexamethylbenzene, 4.0 kHz. ....	206

<b>Figure 7.5:</b>	<sup>27</sup> Al NMR Spectra of (a) Fresh ZSM-5, (b) DME-1D, (c) DME-2D and (d) DME-3D.....	208
<b>Figure 7.6:</b>	<sup>29</sup> Si NMR spectra of (a) fresh catalyst; (b) DME-1D; (c) DME-2D; (d) DME 3D.....	209
<b>Figure 7.7:</b>	DRIFTS spectra of (a) Fresh ZSM-5 (b) DME-1D (c) DME-2D and (c) DME-3D.....	210
<b>Figure 7.8:</b>	Stack plot of INS spectra obtained by the TOSCA instrument of the DME reacted samples .....	211
<b>Figure 7.9:</b>	INS spectra of the DME reacted samples collected with the MERLIN spectrometer using the A-chopper package at an incident energy of 4809 cm <sup>-1</sup> . Spectra are normalised by sample weight. DME-1D, DME-2D and DME-3D .....	212
<b>Figure 7.10:</b>	Peak fitting of (a) DME-1D , (b) DME-2D and (c) DME-3D. ....	213
<b>Figure 7.11:</b>	INS spectra of the $\nu(\text{CH})$ region measured with the MERLIN instrument. Durene , o-xylene and DME-3D .....	214
<b>Figure 7.12:</b>	Mass spectral analysis of reactor exit gases during MeOH/MeOAc conversion at 350 °C. ....	217
<b>Figure 7.13:</b>	Methanol (a) and methyl acetate (b) percentage conversion versus time on stream at 350 °C.....	218
<b>Figure 7.14:</b>	Catch-pot analysis via GC-MS of liquid products accumulated during 6 hours on stream at 350 °C.....	219
<b>Figure 7.15:</b>	TPO profiles of the reacted ZSM-5 zeolites with MeOAc. ....	220
<b>Figure 7.16:</b>	DRIFTS Spectra of the reacted samples.....	221
<b>Figure 7.17:</b>	INS Spectra of the blank zeolite, methyl acetate and methyl acetate exposed to ZSM-5 at ambient temperature.....	222
<b>Figure 7.18:</b>	INS spectra of ZSM-5 samples reacted at 350 °C with a feed of 0% MeOAc, 10% MeOAc, 30% MeOAc, 60% MeOAc and 100% MeOAc.....	224

## Table of Tables

<b>Table 2.1:</b>	Specifications of the detector banks in the Polaris diffractometer <sup>48</sup> .	59
<b>Table 3. 1:</b>	MAPS experimental details for pyridine loading/desorption and cell transfer recovery for ZSM-5 fresh and steamed samples.....	69
<b>Table 3. 2:</b>	Table for TOSCA experimental details of pyridine loading/desorption for fresh ZSM-5 and steamed samples.....	70
<b>Table 3.3:</b>	The source of the compounds, their purity, the Cambridge Structural Database (CSD) refcode, space group and Monkhorst-Pack k-point grid for the molecules studied with CASTEP. ....	72
<b>Table 3.4:</b>	XRF analysis of ZSM-5 at the ISIS Neutron and Muon Facility and at JM.....	76
<b>Table 3.5:</b>	Brucite calibration data for OH quantification.....	81
<b>Table 3.6:</b>	Quantification of the OH sites of the fresh ZSM-5 .....	81
<b>Table 3.7:</b>	Summary of acid site quantification and Si:Al determination of the ZSM-5 sample using the different techniques.....	88
<b>Table 3.8:</b>	The experimentally observed, the as-calculated at the Brillouin zone $\Gamma$ -point (CASTEP) and for the isolated molecule (Gaussian), transition energies of the methyl torsion in unsaturated molecules. If known, the space group and number of the molecules in the primitive cell (Z) is also given. ....	95
<b>Table 4.1:</b>	<sup>1</sup> H-NMR Peak shifts table for Figure 4.8.a .....	117
<b>Table 4. 2:</b>	<sup>1</sup> H-NMR Peak shifts table for Figure 4.8.b .....	117
<b>Table 5.1:</b>	Experimental details of samples examined.....	132
<b>Table 5.2:</b>	Nitrogen adsorption data and coke content for the fresh unreacted catalyst and six post-reaction samples prepared using the ISIS/Glasgow reactor. ....	142
<b>Table 5.3:</b>	Nitrogen adsorption data and coke content for the 400-44h-Frt sample prepared using the ISIS/Glasgow reactor. ....	161
<b>Table 6.1:</b>	Sample experimental and characterisation details. ....	173
<b>Table 6.2:</b>	Diffusion coefficients (D), residence times ( $\tau$ ) and mean square jump lengths ( $\langle r^2 \rangle$ ), calculated using the four different jump models.....	179
<b>Table 6.3:</b>	Table of activation energies calculated from Figure 6.5 .....	179
<b>Table 6.4:</b>	Fitting parameters for rotational fitting models for MTH-2h.....	184
<b>Table 6.5:</b>	Fitting parameters for rotational fitting models for MTH-110h .....	185
<b>Table 6.6:</b>	Diffusion coefficients (D), Residence times ( $\tau$ ) and mean square jump lengths ( $\langle r^2 \rangle$ ) for the MTH-2h with methane calculated using four different jump models ,D, $\tau$ and $\langle r^2 \rangle$ are calculated for each model at all temperatures.....	189
<b>Table 6.7:</b>	Table of activation energies calculated from Figure 6.8 using all temperatures .....	190
<b>Table 6.8:</b>	Table of activation energies calculated from using only the 225K and 275K data points .....	191
<b>Table 6.9:</b>	Fitting parameters for the rotational models for MTH-110 with methane .....	192

<b>Table 7.1:</b>	Experimental details of the DME samples prepared.....	200
<b>Table 7.2:</b>	Experimental details of the MeOAc/Methanol samples .....	201
<b>Table 7.3:</b>	Nitrogen sorption data and coke content for the fresh zeolite and DME samples .....	203
<b>Table 7.4:</b>	Coke content and nitrogen sorption data for the used catalysts .....	219

## Nomenclature

<b>MTH</b>	Methanol-to-Hydrocarbons
<b>MTO</b>	Methanol-to-Olefins
<b>MTG</b>	Methanol-to-Gasoline
<b>ZSM-5</b>	Zeolite Socony Mobil-5
<b>MeOH</b>	Methanol
<b>DME</b>	Dimethyl ether
<b>MeOAc</b>	Methyl Acetate
<b>HMB</b>	Hexamethylbenzene
<b>PMB</b>	Pentamethylbenzene
<b>Mesitylene</b>	1,2,5-Trimethylbenzene
<b>Durene</b>	1,2,4,5-Tetramethylbenzene
<b>Xylene</b>	Dimethylbenzene
<b>TPO</b>	Temperature Programmed Oxidation
<b>TGA</b>	Thermogravimetric Analysis
<b>INS</b>	Inelastic Neutron Scattering
<b>QENS</b>	Quasi-Elastic Neutron Scattering
<b>DRIFTS</b>	Diffuse Reflectance Infrared Fourier Transform Spectroscopy
<b>ssNMR</b>	Solid State Nuclear Magnetic Resonance
<b>BET</b>	Brunauer-Emmet-Teller
<b>TPD</b>	Temperature Programmed Desorption
<b>XRF</b>	X-ray Fluorescence
<b>XRD</b>	X-ray Diffraction
<b>T-o-S</b>	Time on Stream
<b>CCR</b>	Closed Cycle Refrigerator
<b>S<sub>BET</sub></b>	Brunauer-Emmet-Teller Surface Area
<b>V<sub>micropore</sub></b>	Micropore volume
<b>S<sub>external</sub></b>	External Surface Area

# Chapter 1

## Introduction

---

The main focus of the iCASE-1 project has been to utilise neutron spectroscopic techniques, in combination with other analytical and characterisation techniques, in order to observe the changing nature of a heterogeneous catalyst during a catalytic reaction. The reaction of choice is the Methanol-to-Hydrocarbons (MTH) reaction over a ZSM-5 zeolite catalyst. This chapter will focus on describing why neutron techniques were chosen to study this reaction, with a brief introduction to neutron scattering, as well as giving some background on the MTH reaction itself. The research aims of this project as well as the outline of the thesis will be presented at the end of this chapter.

### 1.1 Introduction to Neutron Scattering

The neutron was first discovered by James Chadwick in 1932 with the first neutron diffraction experiment completed at 1944 at the nuclear reactor in Oak Ridge, USA.<sup>1,2</sup> Since their discovery, neutrons have proven to be very useful in studying varying aspects of science, over the last 20 years this has also included catalytic systems.<sup>3,4</sup>

#### 1.1.1 Neutron Sources

In order to use neutron techniques, a neutron source is required. This means that neutron experiments cannot be completed with standard laboratory equipment, but rather require access to a facility which houses a high flux neutron source. There are two main ways in which neutrons are produced in sufficient quantities for studies of materials: reactor and spallation sources. How the neutrons are produced affects the design of both instruments and experiments, as well as how the data are analysed in order to be of scientific importance.<sup>5,6</sup>

Reactor sources, such as the High Flux Reactor at the Institut Laue-Langevin (ILL) at Grenoble, France, rely on nuclear reactions and have a continuously

produced stream of neutrons. In a nuclear reactor, a slow neutron collides with a fissile material ( $^{235}\text{U}$ ), which then leads to fission, fission fragments and approximately two and a half neutrons.<sup>4,7</sup> One of the neutrons is used to maintain the chain reaction and the other is available for experimental use.<sup>5</sup> The reaction also produces a large amount of heat which cannot be utilised, hence the core needs to be externally cooled, which is one of the limitations of the reactor source.<sup>4</sup> That is because the ILL, and similar reactor sources, are very close to the thermal limit of being able to handle the heat produced in the core due to the fission reaction.<sup>8</sup> The neutrons produced in the core are highly energetic and need moderators to slow them down.<sup>5,9</sup> The first moderator they pass through is usually made from heavy water ( $\text{D}_2\text{O}$ ).<sup>4,10</sup> The fast neutrons collide with the moderator material and lose energy by scattering inelastically.<sup>9</sup> The neutrons are then passed through a monochromator in order to focus them into a singular energy before they reach the instruments.

Spallation sources like the ISIS Facility located at the Rutherford Appleton Laboratory, use a solid target and an accelerator in order to provide pulses of neutrons instead of a continuous stream like reactor sources.<sup>4,5,11</sup> High energy protons collide with a solid target, usually comprised of a heavy element (lead, tungsten, etc.) which in turn produces a lot of neutrons. In the ISIS Facility, the target consists of thin tungsten plates surrounded by cooling heavy water and beryllium reflectors.<sup>4</sup> There are two moderators located above and two below the target.<sup>4</sup> The accelerated protons hit the tungsten plates and generate neutrons, some of which are moderated, whereas the others are reflected back into the moderators by the beryllium reflectors, which helps increase the neutron flux.<sup>4</sup> At ISIS, the protons incident on the target are accelerated using a LINAC to feed a proton synchrotron ring in order to have enough energy (800 MeV) to create a neutron beam of high flux.<sup>5</sup> The proton beam itself is generated in pulses, which means that instrument design must take that into consideration in order to avoid frame overlap.<sup>5,12</sup> Frame overlap is when the slow neutrons of a pulse overlap with the fast neutrons of the next pulse, which can lead to data corruption.<sup>5</sup>

For the ISIS target station 1, there are a total of four moderators. A methane moderator kept at 100 K, a liquid hydrogen moderator kept at 20 K and two water moderators kept at room temperature.<sup>12</sup> The moderators allow the neutrons to reach their thermal equilibrium before reaching the instrument.<sup>5,12</sup>

The neutron energies coming out of the moderator depend on the moderator temperature, as well as the moderator material.<sup>5,9</sup> Due to the fact that neutrons come in pulses, the principles of detection in a pulsed source are different than in a reactor source, where the neutron beam is constant. In a pulsed source, the time of flight technique must be used.<sup>10</sup>

In general, reactor sources are more common around the world, with a lot more facilities than spallation sources. The different sources have different advantages in how they can be used. In the duration of this project, only the ISIS neutron source has been used, which is a spallation source. One of the main reasons has been ease of access, as well as the fact that spallation sources have, in general, neutrons with higher energies which are needed for vibrational spectroscopy, which is the technique of choice for this project.

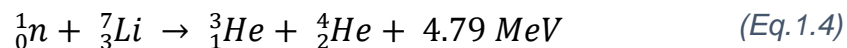
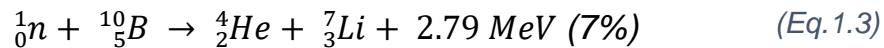
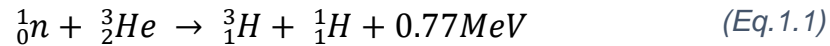
### **1.1.2 Neutron Detectors**

Neutron sources in general have a low flux, therefore a lot more sample is needed than most other analytical techniques. Better design of neutron sources as well as focusing neutrons using neutron guides has helped improve the flux dramatically.<sup>1</sup> Neutron scattering is inherently weak which makes it difficult to detect the scattered neutrons directly.<sup>4,6</sup> This means that neutron scattering needs to be detected indirectly. The scattered neutrons are used to create a nuclear reaction, and the detectors are tuned in order to detect the products of that reaction caused by the scattering event.<sup>6</sup>

Gas counters using  $^3\text{He}$  or  $\text{BF}_3$  (enriched with  $^{10}\text{B}$ ) are often used. The incoming neutron is absorbed by the helium (equation 1.1) or boron (equation 1.2, 1.3) and the ion pairs created from the reaction are converted into an electrical pulse which is then detected.<sup>4,6</sup> Gas counters can also be used as position sensitive detectors, that can happen when an array of tubes are available at specific angles to the sample so as to get the different neutrons scattered in specific directions.<sup>4</sup>

In cases where space is a limitation scintillator detectors can be used.<sup>6</sup> They are solid state detectors using  $^6\text{Li}$  as either  $^6\text{LiF}$  (ceramic/plastic) or  $^6\text{LiO-SiO}_2$  (glass).<sup>4,6</sup> A nuclear reaction still takes place (1.4), however they detect light as a flash is created when ions pass through them. They use a photomultiplier tube in order to detect it. They are also denser, so the detectors can be made

a lot thinner, and have a lot better spatial resolution than the gas counters. However, they are sensitive to both light and  $\gamma$ -rays. Due to the fact that they also use a photomultiplier tube, they also require shielding against magnetic fields.



### 1.1.3 Neutron Interactions

Neutrons interact with matter in different ways, they are highly penetrative and non-destructive, as they do not have the ability to ionise the sample.<sup>1,3</sup> They can either interact with the nucleus of the atom or they can have a magnetic dipole interaction with any unpaired electrons that are present.<sup>9,13</sup> A magnetic interaction with the electrons is able to happen because neutrons have a non-zero spin (1/2). The neutron is scattered from the magnetic moment of the material in question and this can be used to study magnetism.<sup>14</sup>

When using neutrons to study materials, or more specifically catalysts, the interaction of interest is the interaction of the neutron with the nucleus.<sup>1,3,14</sup> The neutron can either be absorbed or scattered by the nucleus. The absorption is nucleus dependent, with some elements being good neutron absorbers whereas other nuclei are not.<sup>1,15</sup> The scattering of neutrons depends on the scattering cross section ( $\sigma$ ) of the nucleus.<sup>1,2</sup> The scattering cross section is the area of the nucleus which is presented to the neutron, and each isotope of every element has a unique scattering cross section which causes the neutron to be scattered with different scattering intensities.<sup>1,9,14</sup> As neutrons are scattered by the nucleus, elements that are next to each other on the periodic table can have a vast difference in scattering cross section. The scattering cross section is also isotope dependent and isotopes of the same element can have very different cross sections.<sup>1,16,17</sup> There is no clear trend in the scattering cross section of the different elements therefore, a list of scattering lengths can

be found in the NIST website adapted from a journal article by V.F. Sears in 1992.<sup>17,18</sup>

Neutron scattering can be separated into coherent and incoherent scattering, and the interaction itself can either be elastic or inelastic.<sup>9</sup> When an interaction is elastic there is no loss or gain in the neutron energy from its interaction with the nucleus.<sup>4,9</sup> An inelastic interaction is when the energy of the neutron changes when interacting with the nucleus by either gaining or losing energy.<sup>4,9</sup>

Coherent scattering is when there is a constructive interference between the scattering of the different nuclei present in the sample.<sup>19</sup> Coherent scattering leads to neutrons scattering strongly in a particular direction. It depends both on magnitude and the direction of the scattering vector as well as the distance between the different nuclei.<sup>9</sup> When the coherent scattering is elastic, it gives information on the structure of the material by giving the relative position of atoms.<sup>4</sup> Therefore, coherent scattering is utilised by diffraction instruments.<sup>4</sup> When the coherent scattering is inelastic, it can provide information about the collective motion of atoms.<sup>9</sup>

Incoherent scattering is when the scattering is uniform in all directions.<sup>9</sup> Elastic incoherent scattering is the same in all directions and usually appears as background.<sup>9</sup> Inelastic incoherent scattering happens when the neutron interacts with the same nucleus at different positions and times.<sup>9</sup> Incoherent scattering is also the type of interaction that provides spectroscopic information.<sup>4</sup> The spectroscopic information could be in the form of vibrational spectroscopy or information of atomic diffusion of said nuclei.<sup>4,9</sup>

Due to the different types of interactions that exist, it is difficult to design instruments that can detect all the different types of neutron interaction. It is therefore important to understand the sample under investigation, and what information one is looking to get out of the sample when a neutron experiment is being planned.

### **1.1.4 Why Use Neutrons**

Although neutrons are now widely used and are becoming more popular, X-ray, optical and electron scattering techniques are still considered the more conventional characterisation techniques. However, neutrons have proven to be complementary to X-ray's since they have different advantages than X-

rays.<sup>15</sup> Neutrons are neutral, which makes them highly penetrative and give information on the bulk of the sample.<sup>1,3,14</sup> They are also non-destructive since they do not ionise the sample, which is highly advantageous as the same sample could then be used for a variety of characterisation techniques afterwards.<sup>1</sup>

An advantage of neutrons over X-rays, is that they can be used to distinguish between elements with similar atomic numbers. X-rays are scattered by the electron cloud surrounding the nucleus.<sup>1,4</sup> Elements with similar atomic numbers have very small differences in the scattering intensity of the X-ray's which makes it difficult to directly differentiate such elements using X-ray sources.<sup>1,14</sup> Neutrons are scattered by the nucleus and therefore elements which are next to each other on the periodic table can have different cross sections and hence scatter the neutrons with different scattering intensities.<sup>1,14,16</sup> Neutrons are also isotope sensitive for the same reason, as isotopes can have different cross sections and scattering lengths.<sup>1,5,16,17</sup> This is clearly illustrated in Figure 1.1, which plots the scattering length of both neutrons and x-rays with the increasing atomic number.<sup>14</sup> As can be seen, isotopes and elements with similar atomic numbers would be indistinguishable when using an X-ray source but not when using a neutron source. X-ray's also have difficulty observing and distinguishing between light elements (carbon, hydrogen, oxygen) due to the small number of electrons present as the scattering is not intense enough, this is particularly the case in the presence of heavy elements.<sup>3</sup> Neutrons do not have that problem and light elements, especially hydrogen, are easily identified.<sup>5</sup>

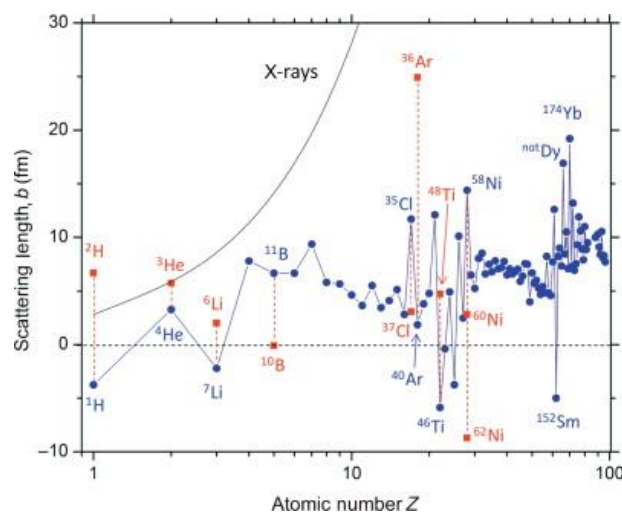


Figure 1.1: Scattering length of neutrons and x-rays with varying atomic number (taken from Ref<sup>14</sup>)

Quasi-elastic neutron scattering (QENS) can be used in order to study the rotational and translational motions of a molecule, usually within a confined volume.<sup>20,21</sup> With the QENS timescales being comparable with timescales obtainable by molecular dynamic simulations.<sup>20,21</sup> This offers a strong advantage in the study of diffusion of molecules within a sample. Vibrational neutron spectroscopy (inelastic neutron scattering, INS) also has various advantages in its use for studying materials and is often comparable to IR or Raman. INS however, has no selection rules which makes all modes available.<sup>3,4</sup> The intensity of the band will depend on the incoherent scattering cross section of the element studied and then how many of those scatterers are present within the sample.<sup>3,4,20</sup> This makes INS very sensitive to the presence of hydrogen as it has the largest incoherent cross section in comparison with all other elements.<sup>17</sup> This is ideal when studying hydrogen containing systems. It also means that INS intensity is directly proportional to the amount of scatterers present and therefore quantitative.

Density functional theory (DFT) calculations can also be readily used in order to model the INS spectra with reasonable accuracy. The DFT calculations can be made from first principles without having additional assumptions, with AbINS being a new software developed by ISIS, which can calculate the INS spectra from ab initio phonon calculations derived from DFT.<sup>22</sup>

Although neutrons offer a lot of advantages, they also have limitations. Neutron sources have a lot less flux than X-ray sources, hence a lot more sample needs to be used in order to get the sensitivity and resolution required.<sup>1</sup> Better design of neutron sources and focusing neutrons using neutron guides have dramatically improved the flux problem.<sup>1</sup> How big the sample needs to be is dependent on the amount of scatterer's present, with a usual normal size for INS being about 10 – 15 g.<sup>4,23</sup> This is not usually a problem for industrial samples, but could cause issues for academic studies.

Another limitation is that the intensity of the INS bands is affected by the Debye-Waller factor, part of which is determined by the thermal motion of all the molecules present within the sample.<sup>3</sup> For INS measurements the samples need to be recorded at low temperatures (below 20 K), this is to avoid any broadening due to the Debye-Waller factor.<sup>3</sup> This means that *in-situ* or *operando* measurements of samples is not really an option. There has been an attempt to record INS spectra at room temperature by using the MAPS

spectrometer, which has access to low momentum transfers.<sup>24</sup> The attempt as a first try has been markedly successful, and has shown that there is a possibility of expanding the temperature constraint of the INS technique, however, it is difficult, and the broadness of the spectra would mean it could only be completed on chemically simple systems. Another complex issue is the fact that INS has no selection rules and all vibrational modes are allowed. This, as was described earlier, is an advantage, however, for complex systems it may cause complications when it comes to spectral assignment. DFT calculations can help with this issue.

### 1.1.5 Neutron Scattering in Catalysis

Neutrons, and more specifically neutron scattering, can be used in order to study heterogeneous catalysts, and although the techniques and instruments have been around for more than 60 years, the methods are under-utilised by the catalysis community. The advantages of using such techniques in general have been discussed above and their advantages for use in catalysis have been highlighted in reviews, as their use is becoming more widely used by the community.<sup>3,4,20,21,23</sup>

INS has been successfully used in order to study a variety of systems including Fischer-Tropsch synthesis over iron based catalysts, where industrial samples have been assessed by INS in order to identify the retained hydrocarbonaceous species on the catalyst.<sup>25</sup> The quantitative feature of INS was used in order to study and quantify the hydrogen partitioning within iron based catalysts used for the Fisher-Tropsch reaction.<sup>26</sup> The quantification of the INS spectra was also used in the study of nickel/alumina catalysts used for methane reforming.<sup>27</sup> Accurate quantification of hydrogen is not easily obtained with other techniques. Hydride species on heterogeneous catalysts have also been extensively investigated and the topic has been recently reviewed.<sup>28</sup>

Just before the beginning of this project, INS was used in order to study ZSM-5 samples used in the MTH reaction.<sup>29,30</sup> The two investigations were used as a basis for this project. ZSM-5 samples reacted under MTH conditions were used, obtaining the INS spectral pattern of retained hydrocarbons for the first time. The investigations were preliminary in nature, and no molecular assignment was made, however, the presence of both  $sp^2$  and  $sp^3$  hybridised

C-H species was identified with their ratio changing with increased temperature and time-on-stream.<sup>30</sup>

QENS techniques have been used to explore diffusion of substrates within catalytic systems, mostly within zeolites. The diffusion of hydrocarbons within zeolite cavities has become important in understanding the zeolite-hydrocarbon interactions.<sup>21</sup> The complementarity of the QENS experiments with MD calculations allow for detailed information about the motion within a constrained volume to be obtained.<sup>31</sup> The close match between theory and observable motions, allow for accurate predictions for the motion of molecules in such systems.<sup>31</sup>

## 1.2 Methanol-to-Hydrocarbons

The Methanol-to-Hydrocarbons (MTH) reaction is a term used to describe a group of industrial reactions which differ in their product distributions. The reaction uses an acidic zeolite catalyst in order to convert methanol into a mixture of light olefins (Methanol-to-Olefins, MTO) or a mixture of olefins and mostly aromatic hydrocarbons (Methanol-to-Gasoline, MTG).<sup>32,33</sup> There is an increased interest in the MTH reaction, both industrially and academically, as it uses methanol which is a relatively cheap and readily available feedstock, and converts it into more industrially relevant products. Methanol can be easily obtained from natural gas, coal and biomass and therefore is a viable alternative to oil.<sup>30,34</sup>

### 1.2.1 The Catalyst

The catalyst used for the MTH reactions is an acidic zeolite catalyst. There have been other types of catalyst used in the past, such as molten zinc chloride ( $\text{ZnCl}_2$ ) and a combination of alumina ( $\text{Al}_2\text{O}_3$ ) and silica ( $\text{SiO}_2$ ), but none came close to the acidic zeolites in terms of methanol conversion and selectivity.<sup>35</sup> Zeolites are highly porous, crystalline materials that can be found in nature or synthesised.<sup>34,36</sup> They are popular as catalysts due to their shape selectivity, thermal and mechanical stability, as well as the fact that they can be easily modified.<sup>37</sup>

Zeolites in general are comprised of  $\text{SiO}_4$  and  $\text{AlO}_4$  tetrahedral building blocks linked through oxygen atoms.<sup>38,39</sup> This forms their three dimensional structure,

with the presence of the trivalent Al giving a negative charge to the zeolite framework.<sup>38,40</sup> Al-O-Al linkages within the zeolite framework are forbidden according to Löwensteins rule,<sup>41</sup> which therefore limits the number of Al that can be present within the zeolite. The negative charge needs to be compensated by a positive one, usually in the form of a cation within the zeolite framework. These cations readily exchange, which is what gives the zeolites such good ion exchange properties.<sup>38</sup> When that negative charge is compensated by the addition of a proton, it creates a Brønsted acid site.<sup>40,42</sup> Lewis acidity can also be generated by mild steaming which can induce the formation of extra framework aluminium (where the Al is no longer tetrahedral but octahedral).<sup>40</sup> The morphology of the zeolite might affect the strength of the acid sites, their location, density and overall composition of the framework may affect their acid strength as well.<sup>43</sup>

The zeolite's catalytic activity is induced by both their Brønsted acidity and their pore size, which are key properties for being used successfully as an MTH catalyst.<sup>32,44</sup> Different zeolite topologies are better for different product distributions. ZSM-5 is an aluminosilicate zeolite of medium pore size which is preferably used for MTG reactions, whereas a smaller pore, less acidic silicoaluminophosphate zeolite or zeolite-like material, SAPO-34, is used for MTO type reactions.<sup>45</sup> SAPO-34 has a different pore structure to ZSM-5, with SAPO-34 being a chabazite, with a large cage but a small 8-ring pore opening.<sup>46</sup> Although this makes SAPO-34 selective to light olefins such as propene and ethene, it also induces deactivation.<sup>46,47</sup> ZSM-5 on the other hand, has a different topology. ZSM-5 is an MFI type zeolite, which means that it has a three dimensional structure, with straight channels parallel to the [010] face and sinusoidal channels parallel to the [100] face.<sup>35,48</sup> The channels are ellipsoidal, with a 10 ring opening, and dimensions of 5.4 Å x 5.6 Å for straight channels, and 5.1 Å x 5.4 Å for the sinusoidal channels.<sup>37,48</sup> Figure 1.2 shows the schematic representation of ZSM-5 and the channel structure of the zeolite.<sup>48</sup> The range of hydrocarbons usually favoured by the ZSM-5 is a mixture of light olefins and methylated aromatics.<sup>33</sup>

The catalyst chosen for this project is a ZSM-5 zeolite provided to us by Johnson Matthey plc, in powder form without binder present. Therefore, this thesis and this introduction will mostly focus on MTH reactions with ZSM-5 as a catalyst.

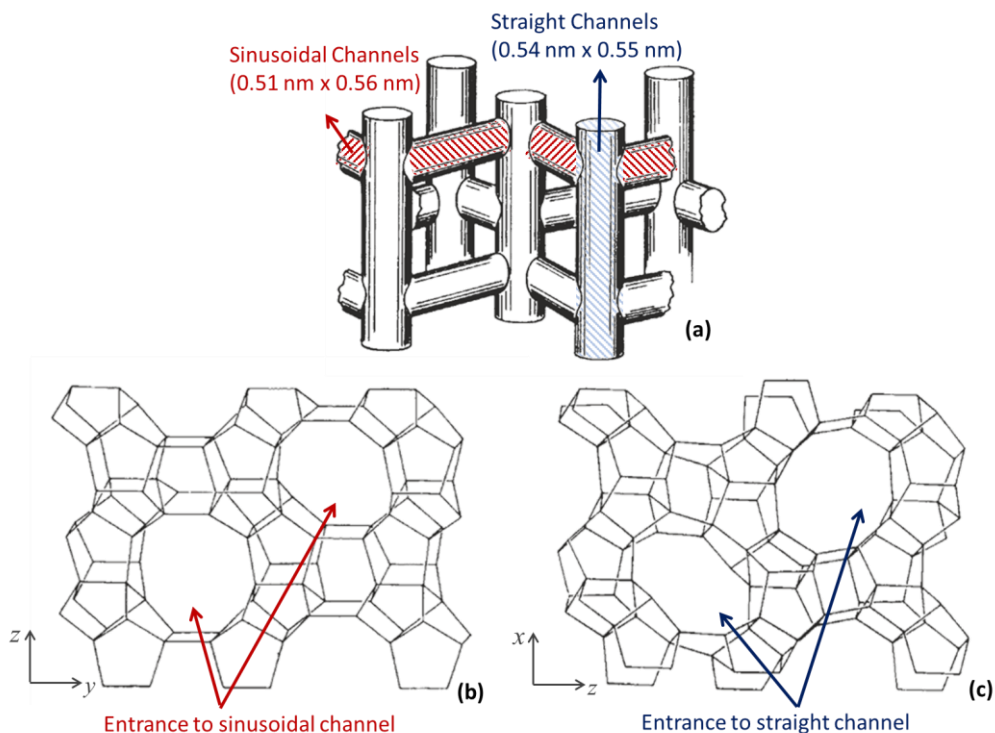


Figure 1.2: Schematic representation of ZSM-5 structure adapted from Kokotailo *et al.*<sup>49</sup> (a) Channel structure of ZSM-5 with the sinusoidal and straight channels highlighted on the schematic. (b) and (c) Skeletal diagram representation with the oxygen atoms not shown with (b) showing the [100] face of the zeolite unit cell and (c) showing the [010] face.

### 1.2.2 Reaction Mechanism

MTH is a complex reaction which has gained a renewed academic and commercial interest over the past decade. Understanding the reaction mechanism will lead to important information about catalyst lifetime and product distribution. The reaction mechanism however, has been a matter of debate since the reaction's discovery in the 1980's.<sup>35</sup>

The MTH reaction proceeds in three main stages in its catalyst lifetime:

1. Initiation/Induction stage: Methanol is introduced in the catalyst and the first hydrocarbons are formed.
2. Steady state stage: A period where the catalyst has a steady stream of product formation.

3. Deactivation stage: Coke formation causes blockage of pores, product formation and methanol conversion decreases.

The exact mechanism for each of the main stages of the catalytic lifetime still remain under debate, with the origin of the first C-C bond poorly understood.<sup>33,50,51</sup> The mechanism under steady state has been accepted to be autocatalytic in nature, with the 'hydrocarbon pool' mechanism<sup>33,50</sup> being the most popular one. It is important to understand all the different catalytic lifecycle steps in order to be able to identify the exact conditions that can affect product distribution, catalytic activity and catalyst lifetime.

### ***1.2.2.1 Initiation Stage: The First C-C Bond***

The first steps of the MTH reaction are often referred to as the formation of surface methoxy groups and the dehydration of methanol to form dimethyl ether.<sup>33,35,52-54</sup> However, the origins of the first C-C bond are still under investigation, with little consensus about how it forms. One of the most common theories was that impurities within the methanol feed, or within the zeolite itself, could promote the first C-C bond. It has been shown, however, that impurities within the methanol feed do not play any significant role in the reaction rate nor do they govern hydrocarbon pool (HCP) product formation.<sup>55</sup> It is becoming apparent from the literature that a direct mechanism of some sort may need to take place in order for the first C-C bond to be formed and before the autocatalytic nature of the MTH reaction starts to take over. Over the years a number of direct mechanisms have been proposed, with many of them being rejected because of either a high activation energy, as derived from computational studies, or have unstable intermediates which are unlikely to occur in the zeolite.<sup>51,56</sup> One of the most common proposals was the oxonium ylide mechanism, which relied on DME reacting with methoxy species. Theoretical calculations on the proposed intermediates showed that oxonium ylides are highly unstable and the zeolite framework is not able to stabilise them as was previously suggested.<sup>57</sup>

The methane-formaldehyde mechanism was introduced after formaldehyde and methane production at low methanol coverages was observed.<sup>58,59</sup> The mechanism relies on the formation of methane and formaldehyde in the initial steps of the MTH reaction, which would then interact in order to form ethanol

which will be dehydrated to ethene.<sup>60</sup> Although the first theoretical calculations on this have been promising,<sup>60</sup> it has not been experimentally verified. A more recent study by Liu et al., has shown that formaldehyde, CO and methane are present at MTH reaction conditions in ZSM-5, and have reached their maximum production at 290 °C.<sup>61</sup> The three products are also seen in the mass spectrometer traces before any olefin traces.<sup>61</sup> They went further as to connect the formaldehyde-methane mechanism with a newly proposed methyl acetate mechanism.

It has been recently suggested that methyl acetate could play an important part in the creation of the first C-C bond. This was proposed by two different groups independently, both suggesting that methyl acetate is the first intermediate which contains a C-C bond. Liu et al. in 2016 reported that methyl acetate could be responsible for the first C-C bond, which would require the carbonylation of methanol or DME.<sup>62</sup> This was proposed after the observation of methanol conversion into formaldehyde, methane, CO and hydrogen with silicalite, meaning the conversion happens without the presence of Brønsted acid sites.<sup>62</sup> This led to the suggestion, that when methanol is first introduced into ZSM-5, those four products would be present and so could be intermediates in the first C-C bond.<sup>62</sup> They suggested that the CO carbonylates the surface methoxy to form surface acetate species which in turn form methyl acetate and acetic acid. They detected methyl acetate and acetic acid in their product stream at very low concentrations, however, this is the only study where this is seen.<sup>62</sup> Choudhary et al., showed that some of the intermediates needed for this mechanism to occur could be experimentally observed by a combination of UV-Vis diffuse reflectance and solid state nuclear magnetic resonance (ssNMR).<sup>63,64</sup> Surface bound formate and acetate species, as well as dimethoxymethane, were observed in SAPO-34 by 2D <sup>1</sup>H-<sup>13</sup>C-ssNMR, which indicates that the suggested mechanism may be feasible.<sup>64</sup>

Understanding the initial steps of the reaction is difficult, as the initiation steps are fast, with the concentration of the intermediate species being low, making any detection of intermediates difficult to isolate and observe. There have been many alternative direct mechanisms for the creation of the first C-C bond, and several reviews of the different proposed mechanisms.<sup>33,51,65</sup> No clear consensus has yet been reached.

### 1.2.2.1 Steady State: 'Hydrocarbon Pool'

The mechanism most commonly accepted for the MTH reaction under steady state conditions is the 'Hydrocarbon Pool' (HCP) mechanism.<sup>33,35,50,66</sup> This is an autocatalytic mechanism in which the hydrocarbons formed within the zeolite undergo a series of reactions which cause them to act as both the activating and deactivating species.<sup>33</sup> This depends on the 'dual cycle' theory, where an aromatic cycle and an olefinic cycle are working in tandem in order to create the hydrocarbon products.<sup>33,66</sup> A simplified version of the 'dual cycle' can be seen in Figure 1.2.<sup>67</sup> The two cycles are dependent on a series of methylation, hydrogen transfer, cyclisation/aromatisation, cracking and dealkylation reactions which lead to the formation of the active hydrocarbons.<sup>44,66</sup> The distribution of the products focuses on the catalyst and its operating conditions and occurs via dominance of one cycle over the other.<sup>44,66</sup> The two cycles are interconnected, therefore, although sometimes one cycle may take precedence over the other, both are happening at the same time within the zeolite catalyst.

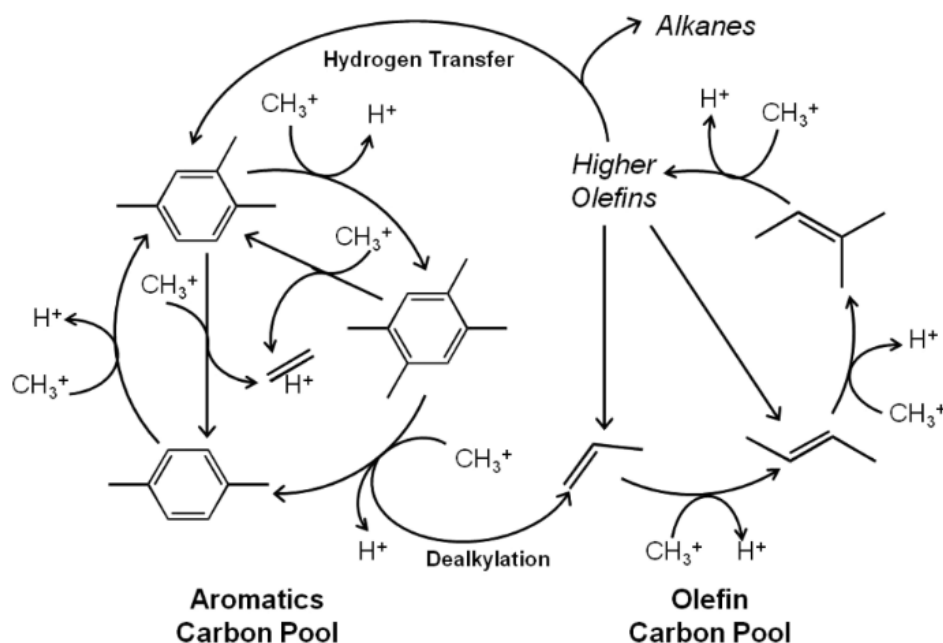


Figure 1.3: Dual cycle scheme taken from Ilias and Bhan<sup>66</sup>

A range of mechanistic studies have been carried out over the years in order to understand how one cycle takes precedence over the other. Identifying the hydrocarbon species present within the zeolite during the steady state stage could give a mechanistic insight into how to tune the product distribution from MTG to MTO and vice versa. Unfortunately, observing said hydrocarbons

directly has been challenging. Indirect methods of observation, by isotopic experiments, has proven that methyl aromatics are important intermediates within the HCP mechanism.<sup>33,50,67,68</sup> Olefinic species, polymethylated benzenes, polymethylated naphthalenes and cyclopentyl species have been identified as active species within the HCP.<sup>33,69,70</sup>

The first products seen out of a zeolite catalyst during MTH conditions are ethene and propene.<sup>35</sup> It has been recently proven by using synchrotron IR microspectroscopy, that the first alkenes are formed directly from surface methoxy species.<sup>71</sup> They then either diffuse out of the zeolite, oligomerise or cyclise to form dimethylcyclopentadienyl cations, which are precursors to aromatic formation. Ethene later on in the reaction, has been proven to come through the aromatic cycle rather than the olefinic cycle. Isotopic and co-feeding experiments, show that the formation of ethene is actually a termination step in the aromatic cycle, with methyl benzenes being the intermediates for ethene production, rather than cracking of oligomeric species present within the ZSM-5 zeolite.<sup>67,69,72</sup> Ethene could then be used, once steady state conditions have been reached in order to identify which cycle is dominant within the ZSM-5 zeolite. Ilias and Bhan used the ratio of ethene production and isobutene as an indication of cycle propagation with ethene being the indicator for the aromatic cycle and isobutene as an indicator for the olefin cycle.<sup>66</sup>

Product selectivity is also heavily dependent on the zeolite morphology and pore size. It is widely known that when comparing the SAPO-34 and ZSM-5 zeolites, SAPO-34 favours olefin production (MTO) and ZSM-5 favours high octane gasoline-like products (MTG).<sup>50,73</sup> The Si:Al ratio of the zeolite also plays an important role in its activity, however, it has also been proven that the presence of defects could affect product distribution.<sup>74</sup> Sazama et al., have shown the importance of sample preparation and showed how changes in framework Al and the number of defects found within the ZSM-5 zeolite could affect both the product distribution and the catalyst life time.<sup>74</sup>

### **1.2.2.2 Catalyst Deactivation Stage**

With the uncertainty in the mechanism, also comes the uncertainty of the mechanism of catalyst deactivation. In MTH, the deactivation is thought to occur in two forms. One, is 'true' deactivation, where the active sites of the zeolite are completely dead and cannot be regenerated. This is the result of dealumination, which is usually caused by steam produced during the reaction

or when the catalyst is regenerated.<sup>52</sup> The other type of deactivation is by some form of pore blocking, either internally which blocks access to the acid sites and blocks the pores from the inside, or externally which blocks the zeolite pores from the outside. This deactivation form is temporary deactivation or 'quasi'-deactivation, as the coke present can be burned off at high temperatures under oxygen, and most of the acid sites can be regenerated.<sup>75</sup> This section will focus only on the second type of deactivation.

'Coke' is a generic term which will be used throughout the thesis, and with respect to the MTH reaction, it is defined as any hydrocarbons remaining within the zeolite pores at the end of the reaction that can no longer diffuse out of the pores during the reaction. Deactivation is heavily influenced by the type of zeolite and its pore dimensions, as well as the density and location of its acid sites.<sup>33,65,76</sup> When comparing five different topologies, Rojo-Gama and co-workers, showed that topology plays an important role in both the catalytic activity and the deactivation.<sup>77</sup> All five topologies compared showed a different percentage of soluble coke for comparable periods of reaction, with different compositions.<sup>77</sup> Earlier research has also established that different topologies (ZSM-5 and SAPO-34) when reacted under the same conditions have shown that the coke composition is different. This suggests that the deactivating species between the two topologies is different, which means that a deactivating species in one zeolite may not necessarily also be deactivating in a different zeolite.<sup>78</sup>

The Si/Al ratio of the zeolites also plays an important role, with many studies showing that an increased Si/Al ratio has a slower deactivation rate and thus a longer catalytic lifespan.<sup>79-81</sup> Reaction conditions are also important when it comes to catalyst deactivation, with temperature seeming to influence the method of coke deposition happening on the zeolite. It was shown by Mores et al., that acid site density influences the coke deposition. However, above a Si/Al ratio of 17, the change in acid density does not play as great a role, but rather temperature becomes the dominating parameter.<sup>79</sup> They showed that increasing reaction temperature showed a faster rate of formation for aromatic species, which in turn caused the formation of graphitic-like coke on the external surface of the zeolite.<sup>79</sup> This phenomena has been explained by Schulz et al., in which he discussed the role of reaction temperature in coke deposition.<sup>82</sup> He suggested that at higher temperatures (above 350 °C), the

deactivation of the zeolite happened by external coking, which blocks the pores from the outside preventing diffusion in or out of the zeolite.<sup>82</sup> However, at lower reaction temperatures (270-300 °C), the deactivation of the ZSM-5 catalyst proceeds via blockage of the internal pores by alkylated benzene molecules.<sup>82</sup> These block the pores and restrict access to acid sites within the zeolite, thus effectively deactivating it.

It must be noted that the different reactors used for the MTH reaction could also have an influence in the way the catalyst bed is deactivated. The 'cigar effect' is a commonly observed effect where the catalyst bed deactivates progressively from the inlet of the reaction to the outlet.<sup>33</sup> It has been noted that using a continually stirred reactor could enhance catalytic lifetime when compared with a plug flow reactor, as it mixes the methanol which causes an even distribution of methanol over the whole reactor volume.<sup>83</sup> In the plug flow reactor, coke formation depends heavily on the position of the catalyst bed.<sup>83</sup>

### 1.2.3 Methods Used to Study Retained Hydrocarbons

As was mentioned above, any retained hydrocarbon present at the end of the MTH reaction is considered to be 'coke'. The direct observation of the retained hydrocarbons without destruction of the zeolite is challenging. The Guisnet method is when hydrofluoric acid (HF) is used to dissolve the zeolite and an organic medium (usually dichloromethane) is used to extract the 'coke' which is then analysed by GC-MS.<sup>84</sup> This technique allows for the characterisation of the retained hydrocarbons, as the HF would dissolve only the zeolite framework. The graphitic coke is insoluble, therefore an accurate description of it would be difficult to obtain.

Another way of studying the coked samples is by use of thermogravimetric analysis (TGA) or temperature programmed oxidation (TPO). These techniques burn the coke off and measure the changing weight and/or the eluting gasses respectively. The profile derived from these two techniques often gives information about the type of coke present within the zeolite, and may give an estimate of the H/C ratio of the coke as well.<sup>85</sup> The coke can be described by the temperature peak maxima and has been named by Muller and Bauer separately as Type I and Type II.<sup>83,85</sup> Type I coke is defined as hydrogen rich, possibly with oxygenates present and has a temperature maximum of about 400 °C.<sup>83,85</sup> This is usually present at the initial stages of the MTH reaction

or as a combination with Type II coke. Type II coke needs higher temperatures in order to combust, and is usually due to polyaromatic compounds with a low H/C.<sup>83,85</sup> The temperature of the peak maximum is usually between (550 – 600 °C). Graphitic-like coke burns at temperatures greater than 600 °C.<sup>86</sup> The higher the temperature, the lower the H/C ratio.<sup>86</sup>

The methods described so far require destroying the zeolite structure. Surface analysis techniques such as nitrogen sorption are also used in order to give an idea of pore blockage. Different methodologies have been attempted in order to study the retained hydrocarbons, either during reaction or after reaction within the zeolite. Spectroscopic techniques such as IR, UV and Raman spectroscopies, have been used in order to characterise the hydrocarbons within the zeolite. Usually a combination of multiple techniques is needed in order to get a complete picture of the retained hydrocarbons.

Raman spectroscopy is an important tool in characterising heterogeneously catalysed reactions. However, it often suffers from fluorescence from the zeolite samples, which can cause important information to be lost. Different excitation wavelengths can help, however, they can also be too weak or cause photo degradation of the sample. A recent study by Lezcano-Gonzalez, focused on using Kerr-Gated Raman spectroscopy in conjunction with DFT calculations in order to study the hydrocarbon species within SSZ-13 and ZSM-5 catalysts used under MTO conditions.<sup>87</sup> Kerr-Gated Raman is able to temporally separate fluorescence from the Raman signal, which helped them study the differences between the hydrocarbons created within the two different topologies.<sup>87</sup> This technique allowed the identification of hydrocarbons which would be otherwise unobservable with a normal Raman spectrometer due to the fluorescence caused by the polycyclic aromatics present in the coked samples. *Operando* Raman spectroscopy has been successfully used in the past as well, to account for the fluorescence a shorter wavelength (UV-Raman) was needed and a fluidised bed in order to minimise the effect of photodegradation.<sup>88</sup> The fluidised bed seemed to increase the signal to noise ratio and help correlate reaction products with intermediates present on the catalyst identified from the spectra.<sup>88</sup>

IR spectroscopy has been used more frequently than Raman spectroscopy. It has its own limitations which make its use for studying the MTH reaction challenging at times. The zeolite framework adsorbs in the region of 0-2000

$\text{cm}^{-1}$ , which makes the identification of any hydrocarbonaceous species below  $2000 \text{ cm}^{-1}$  difficult. This is partly overcome by using the blank zeolite in order to create a difference spectrum. Another issue is that when coke starts building-up within the zeolite, the catalyst becomes dark which makes it IR inaccessible. Either because the sample has lost all its reflectivity, therefore the DRIFTS signal is either minimal (or not there at all), or due to the IR beam not able to transmit through the sample. Most IR spectroscopic studies therefore are usually focused on the early steps of the reaction. IR techniques have been used in order to try and capture the first C-C intermediates or tried to identify the nature of the hydrocarbons retained within the zeolite during reaction.<sup>51,89,90</sup>

Synchrotron IR micro-spectroscopy has also been used in order to help identify the hydrocarbons within single crystals of zeolites. The first study using this technique by Stavitski et al., has shown that IR micro-spectroscopy coupled with UV-Vis micro-spectroscopy, was able to follow reagents through the single crystal. A shift to IR spectroscopy by Howe and co-workers showed the direct formation of ethene from the surface methoxy species, as well as comment on the effect of crystal size to the induction period.<sup>71,91</sup> They found that the induction period seemed to decrease in small crystals and with increasing temperature.<sup>91</sup>

IR spectroscopy was also the first technique to explore the concept of surface methoxy species and their importance to the Methanol-to-Hydrocarbons reaction. With studies showing how methanol forms strong hydrogen bonded species within the zeolite framework at room temperature, and methoxylates at elevated temperatures.<sup>54,92,93</sup> This observation was also confirmed by ss-NMR experiments.<sup>94</sup> However, recent studies using INS and QENS have shown that this may not be the case.<sup>95</sup> Studies of O'Malley et al., have shown that the methanol seems to be static within ZSM-5, with no OH functionality being observed in comparison with zeolite HY which shows methanol hydrogen bonded.<sup>95</sup> This was followed by complementary DRIFTS studies and theoretical calculations which showed that it could be possible for methanol to methoxylate at room temperature depending on the methanol loading.<sup>96-98</sup> This new avenue would not be explored had it not been for neutron spectroscopy, however, if methoxylation is possible or not is still under debate due to the techniques inconsistencies and is something that will be explored within this thesis.

There are various methods that can be used to study zeolite catalysts used for the MTH reaction. This thesis will focus on using INS in order to understand this reaction better, with many of the techniques discussed used in order to confirm the applicability of the INS data.

### 1.3 Project Aims and Thesis Outline

The general aim of the project has been to identify the suitability of using neutron spectroscopic techniques in order to study the changing nature of heterogeneous catalysts. The reaction of choice has been the Methanol-to-Hydrocarbons reaction over a ZSM-5 catalyst.

The main project aims are:

- The same ZSM-5 catalyst will be used for all experiments in order to limit any changes in the retained species from differences in the zeolite structure. Therefore, catalyst characterisation is imperative and one of the main objectives of the project.
- Understanding the interactions of methanol within the ZSM-5 catalyst is important in establishing the first stages of the reaction. Recent conflict between neutron techniques and NMR/IR techniques concerning room temperature methoxylation need to be addressed and understood.
- It has been shown in preliminary studies before the start of the project that INS can be used in order to obtain the vibrational spectra of MTH reacted ZSM-5 catalysts.<sup>29,30</sup> This project aims to study the MTH reaction at different stages in the catalyst lifetime and use INS in order to attempt to assign the spectra and give information on the retained hydrocarbons at each stage. This will in turn answer the questions of (i) how does the composition of the hydrocarbon pool change at the different reaction stages, and (ii) investigate whether INS is able to provide information on catalyst deactivation and the first steps of the MTH reaction
- Once a good understanding of the retained hydrocarbons has been obtained, the neutrons ability to follow diffusion will be used in order to study how the diffusion is affected by the coke present within the pores.

This thesis will show how those aims have been tackled and achieved with the thesis comprised of eight chapters. Each chapter is a separate piece of work and will have its own introduction and experimental section. Chapter 2 will focus on describing the different techniques used within the thesis and will provide an overview of any experimental techniques used recurrently. In Chapter 3, the ZSM-5 catalyst which has been used for the duration of the project will be characterised using a variety of techniques, including INS, which has been used for a detailed analysis of the acid sites present within the zeolite. In Chapter 3, a series of hydrocarbon pool reference INS spectra have been collected and analysed in order to create an INS database which will help in the assignment of the vibrational spectra obtained from reacted ZSM-5 samples.

Chapter 4 will focus on the methanol interaction at room temperature and in trying to resolve the conflict between techniques mentioned above. This chapter shows how a number of different techniques (INS, IR, NMR) have been used in order to answer the question: is room temperature methoxylation in ZSM-5 possible? Chapter 5 will focus on studying the MTH reacted catalysts at different reaction temperatures and time-on-stream. The used samples will be characterised by different techniques including INS. Vibrational spectra of the early stages, matured steady state stage and a deactivation stage of the catalyst have been obtained. The assignment of the steady state and deactivation spectra have been successful with the help from the spectra shown in Chapter 3 as well as from the online INS database of ISIS.

Chapter 6 will explore the effect of coking on methane diffusion using QENS, using selected samples from Chapter 5. Chapter 7 will focus on trying to understand the effect of dimethyl ether and methyl acetate on the MTH reactions. Reactions with dimethyl ether and methyl acetate/methanol as feedstock have been carried out under MTH reaction conditions and their INS spectra obtained. Finally, the concluding remarks and suggestions for future work for this project can be found in Chapter 8.

## References

- 1 H. Fritzsche, J. Huot and D. Fruchart, *Neutron Scattering and Other Nuclear Techniques for Hydrogen in Materials*, Springer, Switzerland :, 2016.

- 2 J. Chadwick, *Nature*, 1932, **129**, 312.
- 3 S. F. Parker, D. Lennon and P. W. Albers, *Appl. Spectrosc.*, 2011, **65**, 1325–1341.
- 4 P. C. H. Mitchell, S. F. Parker, A. J. Ramirez-Cuesta and J. Tomkinson, *Vibrational spectroscopy with neutrons with applications in chemistry*, World Scientific, Singapore, 2005.
- 5 K. Andersen, M. Arai and K. Crawford, in *Neutron Imaging and Applications*, 2009, pp. 13–30.
- 6 R. Hempelmann, *Quasielastic Neutron Scattering and Solid State Diffusion*, Oxford University Press, 2000.
- 7 F. J. Bermejo and F. Sordo, in *Experimental Methods in the Physical Sciences*, 2013, vol. 44, pp. 137–243.
- 8 S.F. Parker, in *Encyclopedia of Spectroscopy and Spectrometry (Third Edition)*, eds. J. C. Lindon, G. E. Tranter and D. W. Koppenaal, Academic Press Inc., 3rd edn., 2017, pp. 246–256.
- 9 R. Pynn, *Los Alamos Sci.*, 1990, **19**, 1–31.
- 10 T. A. Harroun, G. D. Wignall and J. Katsaras, in *Neutron Scattering in Biology*, Springer-Verlag, Berlin/Heidelberg, 2006, pp. 1–18.
- 11 M. Bernauer, E. Tabor, V. Pashkova, D. Kauck, Z. Sobalík, B. Wichterlová, J. Dedecek and J. Heyrovsk, *J. Catal.*, 2016, **344**, 157–172.
- 12 ISIS - How ISIS works - in depth, <http://www.isis.stfc.ac.uk/about/how-isis-works---in-depth4371.html>, (accessed 15 April 2017).
- 13 R. Pynn, An Introduction to Neutron and X-ray Scattering, [http://neutrons.ornl.gov/sites/default/files/IntroductoryLectures\\_2016.pdf](http://neutrons.ornl.gov/sites/default/files/IntroductoryLectures_2016.pdf), (accessed 17 April 2017).
- 14 D. L. Price, F. Fernando-Alonso, F. P. Price and F. Fernando-Alonso, in *Experimental Methods in the Physical Sciences*, 2013, vol. 44, pp. 1–136.
- 15 R. Pynn, in *Neutron Applications in Earth, Energy and Environmental Sciences, Neutron Scattering Applications and Techniques*, Springer US, 2009, pp. 1–29.

- 16 J. Dawidowski, J. R. Granada, J. R. Santisteban, F. Cantargi and L. A. R. Palomino, *Exp. Methods Phys. Sci.*, 2013, **44**, 471–528.
- 17 V. F. Sears, *Neutron News*, 1992, **3**, 26–37.
- 18 A. Munter, Neutron Scattering Lengths and cross sections, <https://www.ncnr.nist.gov/resources/n-lengths/list.html>, (accessed 17 April 2017).
- 19 P. M. Gehring, Basic Elements of Neutron Inelastic Scattering, [https://www.ncnr.nist.gov/summerschool/ss12/pdf/SS2012\\_Gehring\\_InelasticScattering.pdf](https://www.ncnr.nist.gov/summerschool/ss12/pdf/SS2012_Gehring_InelasticScattering.pdf), (accessed 17 April 2017).
- 20 S. F. Parker and P. Collier, *Johnson Matthey Technol. Rev*, 2016, **60**, 132–144.
- 21 A. J. O'Malley, S. F. Parker and C. Richard. A Catlow, *Chem. Commun.*, 2017, **53**, 12164–12176.
- 22 K. Dymkowski, S. F. Parker, F. Fernandez-Alonso and S. Mukhopadhyay, *Phys. B Condens. Matter*, 2018, **551**, 443–448.
- 23 B. S. Hudson, in *Frontiers of Molecular Spectroscopy*, Elsevier B.V., First edit., 2009, pp. 597–622.
- 24 S. F. Parker, *Chem. Commun.*, 2011, **47**, 1988–1990.
- 25 N. G. Hamilton, I. P. Silverwood, R. Warringham, J. Kapitán, L. Hecht, P. B. Webb, R. P. Tooze, S. F. Parker and D. Lennon, *Angew. Chemie Int. Ed.*, 2013, **52**, 5608–5611.
- 26 A. L. Davidson, P. B. Webb, S. F. Parker and D. Lennon, *Ind. Eng. Chem. Res.*, 2020, **59**, 52–60.
- 27 I. P. Silverwood, N. G. Hamilton, C. J. Laycock, J. Z. Staniforth, R. M. Ormerod, C. D. Frost, S. F. Parker and D. Lennon, *Phys. Chem. Chem. Phys.*, 2010, **12**, 3102–3107.
- 28 F. Polo-Garzon, S. Luo, Y. Cheng, K. L. Page, A. J. Ramirez-Cuesta, P. F. Britt and Z. Wu, *ChemSusChem*, 2019, **12**, 93–103.
- 29 R. F. Howe, J. McGregor, S. F. Parker, P. Collier and D. Lennon, *Catal. Letters*, 2016, **146**, 1242–1248.

- 30 Suwardiyanto, R. F. Howe, R. C. A. Catlow, E. K. Gibson, A. Hameed, J. McGregor, P. Collier, S. F. Parker and D. Lennon, *Faraday Discuss.*, 2017, **197**, 447–472.
- 31 H. Jobic and D. N. Theodorou, *Microporous Mesoporous Mater.*, 2007, **102**, 21–50.
- 32 S. Teketel, L. F. Lundegaard, W. Skistad, S. M. Chavan, U. Olsbye, K. P. Lillerud, P. Beato and S. Svelle, *J. Catal.*, 2015, **327**, 22–32.
- 33 U. Olsbye, S. Svelle, K. P. Lillerud, Z. H. Wei, Y. Y. Chen, J. F. Li, J. G. Wang and W. B. Fan, *Chem. Soc. Rev.*, 2015, **44**, 7155–7176.
- 34 B. M. Weckhuysen and J. Yu, *Chem. Soc. Rev.*, 2015, **44**, 7022–7024.
- 35 C. D. Chang, *Catal. Rev.*, 1983, **25**, 1–118.
- 36 A. Martin, *Catalysts*, 2016, **6**, 118.
- 37 M. Niwa, N. Katada and K. Okumura, in *Springer Series in Materials Science*, Springer, 2010, vol. 141, pp. 1–8.
- 38 P. A. Wright, in *Microporous Framework Solids*, ed. J. A. Connor, Royal Society Chemistry, 2008, vol. 8–78.
- 39 J. Weitkamp, *Solid State Ionics*, 2000, **131**, 175–188.
- 40 E. G. Derouane, J. C. Védrine, R. Ramos Pinto, P. M. Borges, L. Costa, M. A. N. D. A. Lemos, F. Lemos and F. Ramôa Ribeiro, *Catal. Rev. - Sci. Eng.*, 2013, **55**, 454–515.
- 41 W. Loewenstein, *Am. Mineral.*, 1954, **39**, 92–96.
- 42 A. Corma, in *Journal of Catalysis*, Academic Press Inc., 2003, vol. 216, pp. 298–312.
- 43 E. Rebrov and G. Hu, in *Advanced Nanomaterials for Catalysis and Energy: Synthesis, Characterization and Applications*, Elsevier, 2018, pp. 321–356.
- 44 M. Westgård Erichsen, S. Svelle, U. Olsbye, M. W. Erichsen, S. Svelle and U. Olsbye, *Catal. Today*, 2013, **215**, 216–223.
- 45 S. Xu, Y. Zhi, J. Han, W. Zhang, X. Wu, T. Sun, Y. Wei and Z. Liu, *Advances in Catalysis for Methanol-to-Olefins Conversion*, Elsevier Inc.,

- 1st edn., 2017, vol. 61.
- 46 S. Wilson and P. Barger, *Microporous Mesoporous Mater.*, 1999, **29**, 117–126.
- 47 D. Chen, K. Moljord and A. Holmen, *Microporous Mesoporous Mater.*, 2012, **164**, 239–250.
- 48 G. T. Kokotailo, S. L. Lawton, D. H. Olson and W. M. Meier, *Nature*, 1978, **272**, 437–438.
- 49 G. T. Kokotailo, S. L. Lawton, D. H. Olson and W. M. Meier, *Nature*, 1978, **272(5652)**, 437–438.
- 50 K. Hemelsoet, J. Van Der Mynsbrugge, K. De Wispelaere, M. Waroquier and V. Van Speybroeck, *ChemPhysChem*, 2013, **14**, 1526–1545.
- 51 I. Yarulina, A. D. Chowdhury, F. Meirer, B. M. Weckhuysen and J. Gascon, *Recent trends and fundamental insights in the methanol-to-hydrocarbons process*, Nature Publishing Group, 2018, vol. 1.
- 52 F. J. Keil, *Microporous Mesoporous Mater.*, 1999, **29**, 49–66.
- 53 Y. Ono and T. Mori, *J. Chem. Soc. Faraday Trans. 1 Phys. Chem. Condens. Phases*, 1981, **77**, 2209–2221.
- 54 T. R. Forester and R. F. Howe, *J. Am. Chem. Soc.*, 1987, **109**, 5076–5082.
- 55 Y. Jiang, W. Wang, V. R. Reddy Marthala, J. Huang, B. Sulikowski and M. Hunger, *J. Catal.*, 2006, **238**, 21–27.
- 56 D. Lesthaeghe, V. Van Speybroeck, G. B. Marin and M. Waroquier, *Angew. Chemie - Int. Ed.*, 2006, **45**, 1714–1719.
- 57 D. Lesthaeghe, V. Van Speybroeck, G. B. Marin and M. Waroquier, *Chem. Phys. Lett.*, 2006, **417**, 309–315.
- 58 L. Kubelková, J. Nováková and P. Jirů, *Stud. Surf. Sci. Catal.*, 1984, **18**, 217–224.
- 59 G. J. Hutchings, F. Gottschalk and R. Hunter, *Ind. Eng. Chem. Res.*, 1987, **26**, 637–638.
- 60 N. Tajima, T. Tsuneda, F. Toyama and K. Hirao, *J. Am. Chem. Soc.*,

- 1998, **120**, 8222–8229.
- 61 Y. Liu, F. M. Kirchberger, S. Müller, M. Eder, M. Tonigold, M. Sanchez-Sanchez and J. A. Lercher, *Nat. Commun.*, 2019, **10**, 1–9.
- 62 Y. Liu, S. Müller, D. Berger, J. Jelic, K. Reuter, M. Tonigold, M. Sanchez-sanchez and J. A. Lercher, *Angew. Chem., Int. Ed.*, 2016, **55**, 5723–5726.
- 63 A. D. Chowdhury, A. L. Paioni, K. Houben, G. T. Whiting, M. Baldus and B. M. Weckhuysen, *Angew. Chemie - Int. Ed.*, 2018, **57**, 8095–8099.
- 64 A. D. Chowdhury, K. Houben, G. T. Whiting, M. Mokhtar, A. M. Asiri, S. A. Al-Thabaiti, S. N. Basahel, M. Baldus and B. M. Weckhuysen, *Angew. Chemie - Int. Ed.*, 2016, **55**, 15840–15845.
- 65 M. Stöcker, *Microporous Mesoporous Mater.*, 1999, **29**, 3–48.
- 66 S. Ilias and A. Bhan, *ACS Catal.*, 2013, **3**, 18–31.
- 67 S. Ilias and A. Bhan, *J. Catal.*, 2012, **290**, 186–192.
- 68 Ø. Mikkelsen, P. O. Rønning and S. Kolboe, *Microporous Mesoporous Mater.*, 2000, **40**, 95–113.
- 69 S. Svelle, F. Joensen, J. Nerlov, U. Olsbye, K. P. Lillerud, S. Kolboe and M. Bjørgen, *J. Am. Chem. Soc.*, 2006, **128**, 14770–14771.
- 70 J. F. Haw, J. B. Nicholas, W. Song, F. Deng, Z. Wang, T. Xu and C. S. Heneghan, *J. Am. Chem. Soc.*, 2000, **122**, 4763–4775.
- 71 I. B. Minova, S. K. Matam, A. Greenaway, C. R. A. Catlow, M. D. Frogley, G. Cinque, P. A. Wright and R. F. Howe, *ACS Catal.*, 2019, **9**, 6564–6570.
- 72 M. Bjørgen, F. Joensen, K.-P. Lillerud, U. Olsbye, S. Svelle, M. Bjørgen, F. Joensen, K.-P. Lillerud, U. Olsbye and S. Svelle, *Catal. Today*, 2009, **142**, 90–97.
- 73 S. Teketel, W. Skistad, S. Benard, U. Olsbye, K. P. Lillerud, P. Beato and S. Svelle, *ACS Catal.*, 2012, **2**, 26–37.
- 74 P. Sazama, B. Wichterlova, J. Dedecek, Z. Tvaruzkova, Z. Musilova, L. Palumbo, S. Sklenak and O. Gonsiorova, *Microporous Mesoporous*

- Mater.*, 2011, **143**, 87–96.
- 75 G. D. McLellan, R. F. Howe and D. M. Bibby, in *Studies in Surface Science and Catalysis*, Elsevier Inc., 1988, vol. 36, pp. 633–637.
- 76 U. Olsbye, S. Svelle, M. Bjørgen, P. Beato, T. V. W. Janssens, F. Joensen, S. Bordiga, K. P. Lillerud, M. Bjørgen, P. Beato, T. V. W. Janssens, F. Joensen, S. Bordiga and K. P. Lillerud, *Angew. Chemie Int. Ed.*, 2012, **51**, 5810–5831.
- 77 D. Rojo-Gama, M. Signorile, F. Bonino, S. Bordiga, U. Olsbye, K. P. Lillerud, P. Beato and S. Svelle, *J. Catal.*, 2017, **351**, 33–48.
- 78 M. Bjørgen, S. Svelle, F. Joensen, J. Nerlov, S. Kolboe, F. Bonino, L. Palumbo, S. Bordiga and U. Olsbye, *J. Catal.*, 2007, **249**, 195–207.
- 79 D. Mores, J. Kornatowski, U. Olsbye, B. M. Weckhuysen, J. Kornatowski, U. Olsbye and B. M. Weckhuysen, *Chem. - A Eur. J.*, 2011, **17**, 2874–2884.
- 80 D. M. Bibby, N. B. Milestone, J. E. Patterson and L. P. Aldridge, *J. Catal.*, 1986, **97**, 493–502.
- 81 K. G. Ione, G. V. Echevskii and G. N. Nosyreva, *J. Catal.*, 1984, **85**, 287–294.
- 82 H. Schulz, *Catal. Today*, 2010, **154**, 183–194.
- 83 S. Müller, Y. Liu, M. Vishnuvarthan, X. Sun, A. C. Van Veen, G. L. Haller, M. Sanchez-Sanchez and J. A. Lercher, *J. Catal.*, 2015, **325**, 48–59.
- 84 P. Magnoux, P. Roger, C. Canaff, V. Fouche, N. S. Gnep and M. Guisnet, *Stud. Surf. Sci. Catal.*, 1987, **34**, 317–330.
- 85 F. Bauer and H. G. Karge, *Mol. Sieves - Sci. Technol.*, 2006, **5**, 249–364.
- 86 V. R. Choudhary, P. Devadas, S. D. Sansare and M. Guisnet, *J. Catal.*, 1997, **166**, 236–243.
- 87 I. Lezcano-Gonzalez, E. Campbell, A. E. J. Hoffman, M. Bocus, I. V. Sazanovich, M. Towrie, M. Agote-Aran, E. K. Gibson, A. Greenaway, K. De Wispelaere, V. Van Speybroeck and A. M. Beale, *Nat. Mater.*, 2020, **19**, 1081–1087.

- 88 P. Beato, E. Schachtl, K. Barbera, F. Bonino and S. Bordiga, *Catal. Today*, 2013, **205**, 128–133.
- 89 Q. Qian, C. Vogt, M. Mokhtar, A. M. Asiri, S. A. Al-Thabaiti, S. N. Basahel, J. Ruiz-Martínez and B. M. Weckhuysen, *ChemCatChem*, 2014, **6**, 3396–3408.
- 90 L. Palumbo, F. Bonino, P. Beato, M. Bjørgen, A. Zecchina and S. Bordiga, *J. Phys. Chem. C.*, 2008, **112**, 9710–9716.
- 91 I. B. Minova, S. K. Matam, A. Greenaway, C. R. A. Catlow, M. D. Frogley, G. Cinque, P. A. Wright and R. F. Howe, *Phys. Chem. Chem. Phys.*, 2020, **22**, 18849–18859.
- 92 T. R. Forester, S.-T. Wong and R. F. Howe, *J. Chem. Soc. Chem. Commun.*, 1986, 1611.
- 93 A. Zecchina, S. Bordiga, G. Spoto, D. Scarano, G. Spanò and F. Geobaldo, *J. Chem. Soc., Faraday Trans.*, 1996, **92**, 4863–4875.
- 94 S. M. Campbell, X.-Z. Z. Jiang and R. F. Howe, *Microporous Mesoporous Mater.*, 1999, **29**, 91–108.
- 95 A. J. O'Malley, S. F. Parker, A. Chutia, M. R. Farrow, I. P. Silverwood, V. García-Sakai and C. R. A. Catlow, *Chem. Commun.*, 2016, **52**, 2897–2900.
- 96 S. K. Matam, R. F. Howe, A. Thetford and C. Richard. A Catlow, *Chem. Commun.*, 2018, **54**, 12875–12878.
- 97 S. K. Matam, S. A. F. Nastase, A. J. Logsdail and C. R. A. Catlow, *Chem. Sci.*, 2020, **11**, 6805–6814.
- 98 S. A. F. Nastase, A. J. O'Malley, C. R. A. Catlow and A. J. Logsdail, *Phys. Chem. Chem. Phys.*, 2019, **21**, 2639–2650.

# Chapter 2

## Methodology

This chapter will focus on describing the instruments and techniques used throughout this project and describe some of the experimental procedures used for the characterisation measurements. However, each chapter will have its own experimental section which will explain the exact experimental parameters used.

### 2.1 Neutron Techniques

Neutron spectroscopy is one of the main techniques used throughout this project. The use of these techniques requires access to a central facility: all of the experiments conducted in this study were completed at the ISIS Neutron and Muon Source, located in Oxfordshire, UK.

#### 2.1.1 Neutron Scattering Basics

In a neutron scattering event, there is both momentum transfer and energy transfer between the neutron and the sample. Therefore, both need to be taken into account when thinking of instrumentation and how it works.

A change in momentum transfer can be calculated by Equation 2.2, where  $k$  is the wavevector in  $\text{\AA}^{-1}$  and its value is given by Equation 2.1.  $Q$  is the momentum transfer and  $\lambda$  is the neutron wavelength in  $\text{\AA}$ .<sup>1</sup>

$$k = 2\pi/\lambda \quad \text{Equation 2.1}^1$$

$$Q = k_i - k_f \quad \text{Equation 2.2}^1$$

When  $k_i$  and  $k_f$  are equal, the scattering is elastic, however, when  $k_i$  and  $k_f$  are different, the scattering is inelastic. The neutron energy transfer ( $E_T$ ) can be calculated by the Equation 2.3, where  $E_i$  is the incident energy and  $E_f$  is the final energy.

$$E_T = E_I - E_F \quad \text{Equation 2.3}^{1,2}$$

Energy is given by Equation 2.4, where the  $\hbar$  is the reduced Planck's constant ( $2\pi/h$ ) and  $\omega$  in this case is the angular frequency.<sup>2-4</sup> However, the energy of a neutron is equal to its kinetic energy, where  $m$  is the mass of the neutron and  $v$  is the average velocity of the neutron.

$$E = \hbar\omega = \frac{1}{2}mv^2 \quad \text{Equation 2.4}^{2-4}$$

Therefore, the energy and momentum are related through the neutron velocity which can be used to calculate the neutron wavelength as seen in Equation 2.5 by the de Broglie relationship since a neutron exhibits wave-particle duality.<sup>2-4</sup> The neutron velocity is known once the neutrons passes through the moderator.

$$\lambda = h/mv \quad \text{Equation 2.5}^{2-4}$$

The momentum of the neutron ( $p$ ) can therefore be explained by Equation 2.6.

$$p = mv = \hbar k \quad \text{Equation 2.6}^{2-4}$$

Which means that the neutron kinetic energy can be given as either form of Equation 2.7.<sup>2-4</sup>

$$E = \hbar^2 k^2 / 2m = h^2 / 2m\lambda^2 \quad \text{Equation 2.7}^{2-4}$$

Therefore, for the scattering event both momentum and energy transfer need to be accounted for. The scattering triangles for both elastic and inelastic scattering can be found in Figure 2.1. The incoming neutron with vector  $k_i$  and energy  $E_i$  is being scattered by the particle at an angle of  $2\theta$ , and the deflected neutron having a vector  $k_f$  and energy  $E_f$ . When  $k_i$  is equal to  $k_f$  then the scattering triangle is an isosceles triangle and  $Q$  can be calculated by Equation 2.8.<sup>3</sup>

$$Q = 2|k| \sin \theta = \frac{4\pi \sin \theta}{\lambda} \quad \text{Equation 2.8}^3$$

When  $k_i \neq k_f$ , then the scattering triangle has unequal sides which can be solved using the cosine rule for triangles as seen in Equation 2.9.<sup>3</sup>

$$Q^2 = k_i^2 + k_f^2 - 2k_i k_f \cos 2\theta \quad \text{Equation 2.9}^3$$

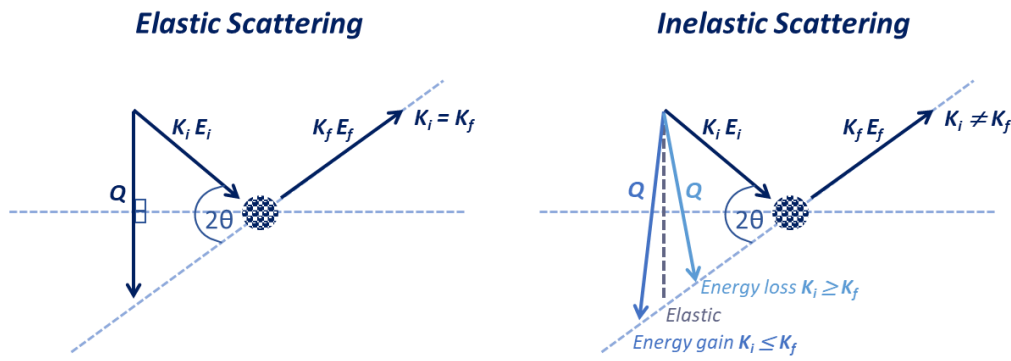


Figure 2.1: Scattering triangles for elastic and inelastic scattering events. Schematics adapted from D.S. Sivia<sup>3</sup>

ISIS is a pulsed spallation source, therefore, the instruments are time-of-flight instruments. This means that all neutrons have a common starting point with a known time. Time can be correlated with distance over velocity therefore by application of Equation 2.4, the time taken for the neutron to reach the detector ( $t$ ) can be described in Equation 2.10 in terms of wavelength and Equation 2.11 in terms of energy. To convert Equation 2.10 to 2.11 the wavelength term is substituted with a rearranged version of Equation 2.7. Where  $m$  is the mass of the neutron,  $h$  is Planck's constant,  $d_I$  is the flight path distance from the moderator to the sample and  $\lambda_I$  is the wavelength associated with that.  $d_F$  is the distance between the sample and the detector,  $E_I$  and  $E_F$  is the incident and final energy.

$$t = \frac{m}{h} (d_I \lambda_I + d_F \lambda_F) \quad \text{Equation 2.10}^3$$

$$t = \left( \sqrt{\frac{m d_I^2}{2E_I}} \right) + \left( \sqrt{\frac{m d_F^2}{2E_F}} \right) \quad \text{Equation 2.11}^4$$

The time it takes the neutron to reach the detector is known, and so is the path-length of the neutron. The distances are known and for elastic scattering,  $\lambda_I = \lambda_F$  ( $E_I = E_F$ ), so the arrival time at the detector enables the wavelengths and energy to be determined. For inelastic scattering, either the incident energy or the final energy must be fixed in order to be able to calculate the other.

### 2.1.2 Inelastic Neutron Scattering (INS) Spectroscopy

Incoherent Inelastic Neutron Scattering Spectroscopy or INS is a spectroscopic technique that allows the study of molecular vibrations within the sample of

interest.<sup>1,5,6</sup> INS is a complementary technique to IR and Raman optical spectroscopies.<sup>1,5,6</sup>

There are some inherent advantages to using INS over Raman and IR as already mentioned in Chapter 1. In INS there are no selection rules as the scattering of the neutron occurs from the atomic nucleus and not due to optical excitations.<sup>4,5</sup> This means that all vibrations are allowed and hence can, in theory, be observed.<sup>4,5</sup> Due to the neutron scattering resulting from the interaction between the nucleus and the neutron, INS is also isotope sensitive.<sup>5</sup> Neutrons can also penetrate matter, therefore making sample environment easier, as samples can be encased in aluminium cans. Aluminium has a very small to non-existent incoherent scattering cross section of 0.0082 Barn in comparison with hydrogen which has the largest cross section of 82.26 Barn.<sup>7</sup> This means that using Al as the sample holder would not cause any problems as neutrons will pass right through and only interact with the sample.<sup>4</sup> INS is a bulk technique due to the neutrons penetrative nature.<sup>4</sup> This means that the spectroscopy is an accurate representation of the bulk of the sample and not just the surface. This could cause problems when it comes to differentiating between the surface and what is in the bulk.

Another important advantage is that the low energy region below 400  $\text{cm}^{-1}$  is accessible with INS.<sup>1,4,8</sup> This is particularly important when studying catalysts, especially supported catalysts where in conventional optical spectroscopies the support absorbs the incident energy and blacks out parts of the spectra.<sup>9</sup> This is not a problem with INS as most of the vibrations from conventional supports, such as silica, are not visible to neutrons.<sup>9</sup> INS is also very sensitive to hydrogen due to it being a large incoherent scatterer. Optical spectroscopies are generally more sensitive to heavier elements, than lighter ones.<sup>4,5</sup> Another difference between optical spectroscopies and neutrons, is that neutrons have mass, hence both the energy transfer and the momentum transfer need to be considered in the interaction between sample and the neutron, as both are important. Photons used in optical spectroscopies have negligible momentum exchange with the sample.

The intensity of the bands in INS are described by Equation 2.12, the INS band intensity equation. Where  $S$  is the intensity,  $\omega_i$  is the  $i$ th mode at the transition energy  $\omega$ ,  $n$  is dependent on the type of mode (1 is for fundamental, 2 first

overtone or binary combination and so on),  $Q$  is the momentum transfer,  $U_i$  is the displacement of the atoms in the  $i$ th mode and  $\sigma$  is the inelastic cross section. The exponential term is the Debye-Waller factor, where the  $U_{Tot}$  is the sum of the displacements for all atoms in all the modes. This factor is also responsible for the need to measure the samples at low temperatures (below 20 K) in order to minimise its effect.<sup>1,10</sup>

$$S(Q, n\omega_i) \propto \frac{-(QU_i)^{2n}}{n!} \exp[-(QU_{Tot})^2] \sigma \quad \text{Equation 2.12}^{1,10}$$

The measured INS intensity of the peaks is dependent on the transition energy and the momentum transfer due to the neutron having a mass. IR, Raman and INS are complementary techniques. Some vibrations are more visible in one of these techniques and maybe non-existent in the others.<sup>1</sup> Hence, it is desirable to use a combination of all three in order to present accurate scientific results. There are different types of instruments that can be used to measure INS spectra and these fall into two main categories: indirect and direct geometry spectrometers. Indirect geometry instruments have a fixed final energy, whereas direct geometry instruments have a fixed incident energy.

### 2.1.2.1 Indirect Geometry Instruments – TOSCA

An indirect geometry spectrometer is when the final energy of the scattered neutrons is fixed with a continuous spectrum of incident energy. Indirect geometry spectrometers have been traditionally used for vibrational spectroscopy experiments. The advantage of having a fixed final energy is that the detector design is very simple, as there is no variation in energy and therefore no variation in detection.<sup>4</sup> An example of an indirect spectrometer is TOSCA located at the ISIS Facility (Rutherford Appleton Laboratory), with a schematic representation of the instrument seen in Figure 2.2.<sup>2,11</sup>

The pulse of neutrons hits the target which produces high energy neutrons that enter the moderator.<sup>2</sup> The moderator used for the TOSCA instrument is room temperature water. A disk chopper is present in between the moderator and the sample which is placed in the cryostat seen in blue in Figure 2.2.a. The chopper is present to remove any high energy neutrons that may escape the moderator as well as prevent frame overlap. The flight path of the neutrons is known (17 m) so as to be able to back calculate the initial energy of the incident neutrons.<sup>2</sup> The neutrons are scattered from the sample and then sent to the

two analysers which are located at  $45^\circ$  for forward scattering and  $135^\circ$  for backward scattering.<sup>11–13</sup> The neutrons are then Bragg reflected from the pyrolytic graphite analyser (002), as seen in Figure 2.2.b, at an energy of  $32 \text{ cm}^{-1}$  (4 meV). The cooled Be filter only allows neutrons with the correct energy to pass through to the detectors.<sup>11–13</sup> The detectors are comprised of 10 banks in total, 5 for each analyser. One detector bank comprises of 13  $^3\text{He}$  tubes.<sup>11</sup> TOSCA offers high resolution spectra that are comparable to optical spectroscopies at low energies.<sup>4</sup>

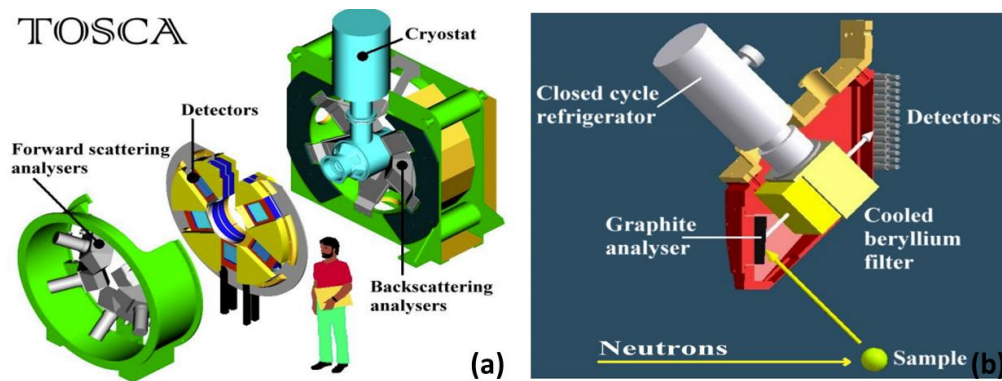


Figure 2.2: (a) Schematic of the TOSCA instrument located at the ISIS Facility (Rutherford Appleton Laboratory, UK) showing the detector/analyser modules. (b) A section through one of the analyser modules of TOSCA. Schematic was taken from publication of S.F. Parker et al.<sup>11</sup>

### 2.1.2.2 Direct Geometry Instruments – MAPS and MERLIN

Direct geometry instruments are instruments where the incident energy is set and the final energy of the scattered neutrons is variable.<sup>4,6,9</sup> The incident energy is fixed either by using choppers or by using a monochromator.<sup>4</sup> The disadvantage of ‘fixing’ the incident energy of the neutrons is that there is a decrease in the neutron flux, therefore large area detectors are used in order to compensate for that loss.<sup>4</sup> It is only recently that direct geometry instruments have been used for vibrational spectroscopy as their initial purpose has been to study magnetism.<sup>6</sup> The advantage of the direct geometry instrument is the ability to measure both  $Q$  and  $\omega$  independently. Their disadvantage of having a ‘fixed’ energy is that the scattered neutrons have a wide range of energies.<sup>4</sup> Slow neutrons will be captured by the detectors more easily than fast neutrons. The detector signal must therefore, be normalised in order to account for this.<sup>4</sup> Normalisation is done by recording the spectra of vanadium, which has a low absorption cross section and is a purely incoherent scatterer.<sup>4</sup>

Two examples of direct instruments that have been used in this project are the MAPS and MERLIN instruments located at the ISIS Facility (Rutherford Appleton Laboratory, UK). Both instruments follow the same principles and have similar designs, with MAPS being a high resolution spectrometer and MERLIN being a high intensity but medium energy resolution spectrometer.<sup>14</sup> Figure 2.3 presents the schematic of the MAPS spectrometer.<sup>1</sup> As described in Section 1.1, the protons hit the target in order to produce neutrons which enter the moderator, in the case of both MAPS and MERLIN the moderator is water at 300 K.<sup>15,16</sup> The Nimonic chopper made from a strong scattering metal scatters  $\gamma$ -rays and high energy neutrons escaping the moderator when the proton hits the target.<sup>4</sup> The Fermi chopper is made from alternating layers of aluminium (transparent to the incoming neutrons) and thin sheets of a strong neutron absorber such as boron carbide.<sup>4</sup> The chopper rotates and the incident energy is chosen by the speed of the rotation and by phasing the chopper rotation with the neutron pulses.<sup>4,16</sup> The neutrons that reach the sample all have the same energy and are scattered to an array of  $^3\text{He}$  detectors.<sup>1</sup>

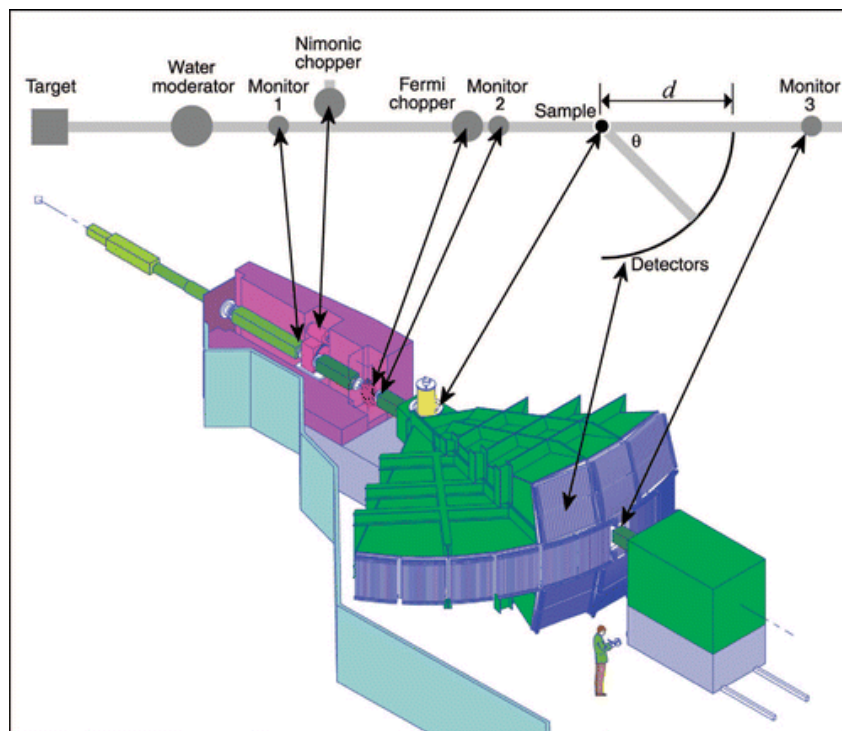


Figure 2.3: Schematic of the MAPS instrument located at the ISIS Facility (Rutherford Appleton Laboratory, UK). Figure adapted from Parker et al.<sup>1</sup>

### 2.1.2.3 INS Experimental Procedure

All three spectrometers use a closed circle refrigerator (CCR) system in order to keep the temperature of the sample below 20 K. For the direct

spectrometers, the high resolution A-chopper package was used with incident energies dependent on the type of experiment needed. Usually, an incident energy around  $2000\text{ cm}^{-1}$  was used for low energy spectra collection and around  $5000\text{ cm}^{-1}$  for high energy spectra.

In all three spectrometers the sample preparation was similar. The zeolite sample was loaded in Al sachets (usually  $50\text{ mm} \times 50\text{ mm}$ ) which were then loaded in Al flat cans ( $50\text{ mm} \times 50\text{ mm}$ ) sealed with indium wire. Most of the samples were loaded within a glove box filled with argon atmosphere in order to avoid atmospheric contamination. The cans were mounted on a centre-stick, where the length of the centre-stick is adapted for each instrument so that the sample is located in the middle of the neutron beam. The sample was cooled to liquid nitrogen temperature before being dropped into the instrument CCR. After the centrestick is placed in the CCR, it is evacuated and refilled with He in order to remove any vapour or air which may cause issues with the spectra or cause ice formation to occur. This is repeated three times, and then about 30-40 mBar of He is left within the chamber to act as an exchange gas in order to cool the sample to below 20 K. The temperature of the sample is recorded by a thermocouple placed in the middle of the centrestick and spectral acquisition does not commence until after the temperature drops below 20 K.

For the model compounds, smaller Al cans were used with a path length of 1 mm, although 2 mm path length was also used when needed. The cells are sealed with an indium wire and loaded through sealable holes in the front panel of the cell. For recording the INS spectra of the model compounds in Chapter 3, the TOSCA sample changer was used, which is able to have up to 24 samples loaded at one time. The samples were not cooled in liquid nitrogen before being loaded on the sample changer. The sample changer moves the liquid cells in the direction of the beam one at a time, which avoids a lot of sample changes. The same procedure with filling the sample chamber with He and evacuating is completed, however, this time this is completed by a trained beam line scientist.

When the samples are removed from the spectrometers, they need to be moved carefully and without touching them with bare hands to a lead-lined cupboard as they are radioactive. A Geiger counter is used in order to measure their activity and ISIS personnel need to sign them off before the samples can be unloaded. Time-of-flight data from both instruments was reduced to INS

spectra using Mantid<sup>17</sup> and the MAPS spectra were integrated over the momentum transfer range of  $0 \leq Q \leq 12 \text{ \AA}^{-1}$  using the MSlice software package.<sup>18</sup>

### 2.1.3 Quasi-elastic Neutron Scattering (QENS)

Quasi-elastic neutron scattering (QENS) is a technique that allows the observation and measurement of the diffusion of a species.<sup>19,20</sup> QENS uses neutrons with energies and wavelengths within the range of the diffusion processes and interatomic distances of interest.<sup>20</sup> The energy exchange between the nucleus and the neutron is very small and it is therefore required that it is measured at high resolution.<sup>19,20</sup> The small energy exchange also causes a broadening of the elastic peak as the energy is not quantised.<sup>19</sup> There are both incoherent and coherent contributions to the quasi elastic broadening of the elastic peak.<sup>19</sup> Incoherent scattering is the diffusion of individual particles, whereas coherent scattering is the collective dynamics of all particles present.<sup>19,20</sup> The scattering functions for a quasi-elastic experiment have the space-time (van Hove) correlation functions incorporated as seen in Equation 2.13 and Equation 2.14 for the incoherent and coherent scattering function for a QENS experiment respectively.  $G_s(r,t)$  is the self-correlation function which describes the probability of the nucleus which at time zero was at the origin, to be found at position  $r$  at time  $t$ .  $G(r,t)$  is the pair correlation function which describes the probability of finding any atom at time  $t$  in position  $r$  when one atom is found at the origin at time zero.

$$S_{inc}(Q, \omega) = \left(\frac{1}{2\pi}\right) \iint G_s(r, t) \exp[iQ \cdot r + \omega t] dr dt \quad \text{Equation 2.13}$$

$$S_{coh}(Q, \omega) = \left(\frac{1}{2\pi}\right) \iint G(r, t) \exp[iQ \cdot r + \omega t] dr dt \quad \text{Equation 2.14}$$

From the incoherent scattering function one can obtain  $D_s$ , which is the self-diffusivity constant and from the coherent scattering function,  $D_t$  (transport diffusivity) can be derived.<sup>21</sup> Each detector is fixed at a certain scattering angle, which corresponds to a particular value of  $Q$  (scattering vector).<sup>21</sup> The broadening of the elastic peak in the QENS spectra can be described by Lorentzian functions and  $D_s$  can be found by relating the  $Q^2$  with the half-width, half-max (HWHM) of the Lorentzian. The simplest form of diffusion is Fickian diffusion shown in Equation 2.15.<sup>19,21</sup> Where  $\Gamma$  is HWHM,  $D_s$  is the diffusion coefficient,  $Q$  is the scattering vector.

$$\Gamma = D_s Q^2 \quad \text{Equation 2.15}$$

For diffusion in zeolites, the Fickian diffusion model is often not enough and cannot describe fully the type of diffusion that is taking place.<sup>21</sup> Fickian diffusion is only representative of motion at large distances (low  $Q$  values), therefore other models needed to be developed in order to better describe the motions within a system.<sup>21</sup> The different models used for fitting the QENS data will be discussed in Chapter 6.

### 2.1.3.1 Backscattering Spectrometers – IRIS

There are different types of spectrometers that can be used to measure diffusion. As only the IRIS spectrometer has been used for this project, this section will focus on that instrument. Backscattering spectrometers have the advantage of having a wide dynamic range and a high  $Q$  resolution which is paramount when recording QENS spectra.<sup>22</sup> The spectrometer is able to complete an elastic window scan, which is observing the broadening of the elastic peak as a function of temperature. It can also record spectra at specific temperatures, from which both the diffusion coefficient and the activation energy of that motion can be deduced.

IRIS has two different spectrometers. The primary spectrometer (see Figure 2.4) is used for neutron beam transport from the moderator to the sample located in the secondary spectrometer. It uses two disk choppers in order to select a neutron beam containing wavelengths in the 6 - 7.5 Å range.<sup>22,23</sup> The neutrons are transported to the sample through a curved neutron guide which does not allow any neutrons with a wavelength less than 1.5 Å to pass through.<sup>23,24</sup> At the end of the neutron guide, a nickel-titanium supermirror helps to focus the neutron beam to the sample position and also increases the incident neutron flux. The moderator used for the IRIS spectrometer is a liquid hydrogen moderator cooled to 22 K.

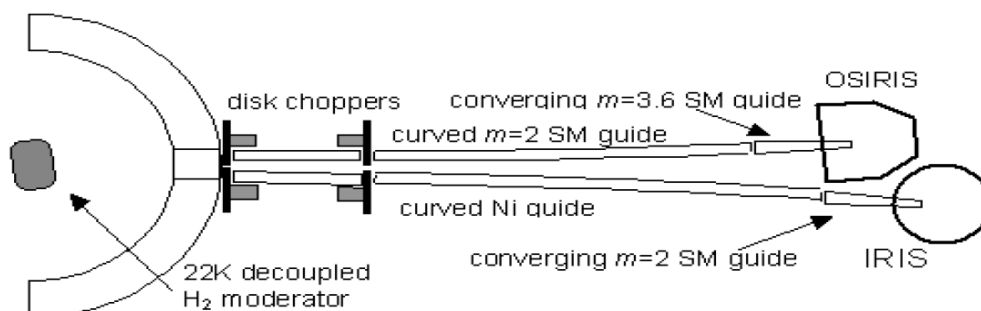


Figure 2.4: The primary spectrometer for both OSIRIS and IRIS. Figure obtained from Telling and Andersen<sup>23</sup>

The secondary spectrometer is where the sample is located (See Figure 2.5). The spectrometer has two analyser banks: a graphite bank analyser (pyrolytic graphite using either the (002) or (004) reflections) and the mica analyser bank. The pyrolytic graphite analyser bank is cooled to approximately 10 K. This is in order to reduce any background contributions from thermal diffuse scattering.<sup>25</sup> The bank used for our experiments is the (002) reflection of pyrolytic graphite array. There are 51 ZnS scintillator detector banks for each analyser at positions of  $\theta = 27.07^\circ$  ( $0.442 \text{ \AA}^{-1}$ ) to  $158.4^\circ$  ( $1.854 \text{ \AA}^{-1}$ ).<sup>25</sup> The spectrometer is also fitted with a diffraction detector bank at  $2\theta = 170^\circ$ .<sup>25,26</sup> Diffraction detectors are  $^3\text{He}$  gas tubes.

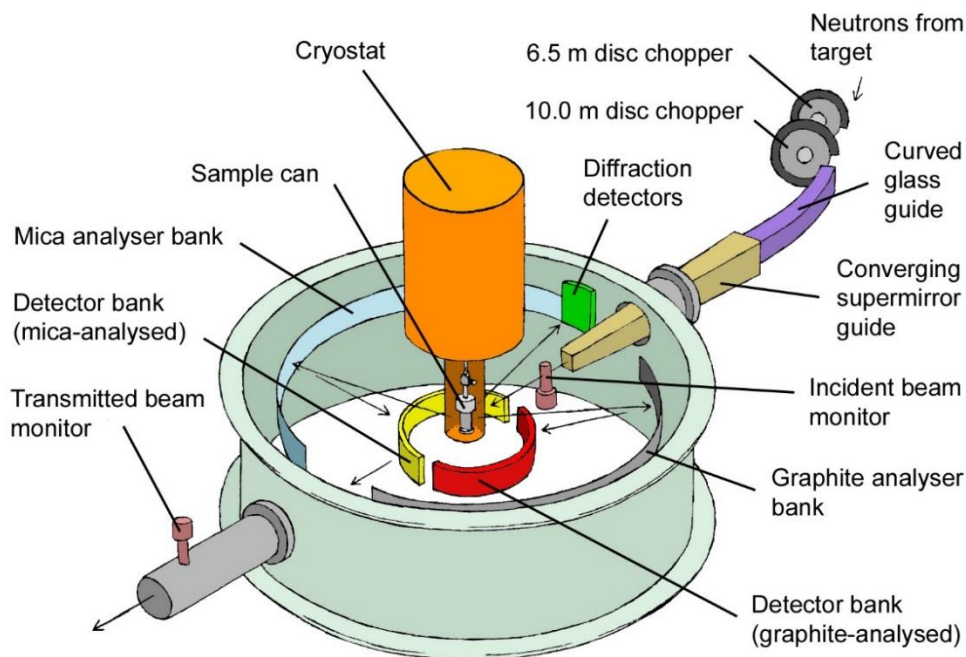


Figure 2. 5: The schematic of the IRIS second spectrometer. Figure taken from the IRIS website<sup>26,27</sup>

For the neutrons to be scattered towards the detector bank, the Bragg scattering condition of  $\lambda = 2d\sin\theta$  must be satisfied, hence only neutrons with a specific energy can pass through. Therefore, equation 2.4 can be re-written as Equation 2.16, where the  $d_a$  is the d-spacing of the analysing crystal.

$$E = \frac{h^2}{2m(2d_a\sin\theta)^2} \quad \text{Equation 2.16}$$

Equation 2.8, in section 2.1 describes how the time taken for a neutron with mass 'm', to travel from the moderator to the detector over a known length. There are two known distances here  $L_i$  would be the distance from the

moderator to the sample, and although the distance is known, the time for each neutron to reach the sample is different.  $L_f$  is the distance between the sample and the detector, which is again known, therefore the time taken can be calculated by equation 2.17, which is the first part of Equation 2.10.

$$t_f = \frac{m}{h} (L_f \lambda_f) = \frac{m}{h} (L_f) (2d \sin \theta) \quad \text{Equation 2.17}$$

Therefore, by measuring the total time-of-flight and knowing accurately the  $L_i$ ,  $L_f$ , and  $t_f$ , the  $t_i$  can be calculated and hence the energy exchange between sample and neutron. The neutron energy transfer (Equation 2.3) can then be written as Equation 2.18

$$\Delta E = \frac{1}{2} m \left[ \left( \frac{L_i}{t-t_f} \right)^2 - \left( \frac{L_f}{t_f} \right)^2 \right] \quad \text{Equation 2.18}$$

### 2.1.3.2 QENS Experimental Procedure

The QENS samples were prepared in a glovebox under argon atmosphere. The sample cans used were niobium annular cans with gas handling capabilities and an annulus of 2 mm. The cans were loaded on a centrestick by the ISIS Pressure and Furnace team, with the sample can connected through the centrestick on a gas manifold provided by the team as well. The centrestick is lowered within the CCR, and the CCR is evacuated and re-filled with He three times before 40 mbar was left in the sample chamber as an exchange gas for cooling. Data reduction was completed using the Mantid software<sup>17</sup> and data analysis was completed using the DAVE software package.<sup>28</sup>

Dosing was carried out using the gas manifold at room temperature, whilst the sample was in the IRIS spectrometer. A schematic representation of the manifold used can be found in Figure 2.6. The manifold has a container of a known volume (buffer volume) which was filled with methane and then isolated from the rest of the manifold. The manifold was then evacuated using a vacuum line. Once the manifold was evacuated and isolated from the vacuum, the buffer volume was opened up to both the manifold and the cell containing the sample. Once equilibration was reached, the cell was once again isolated and the manifold was evacuated. The loading procedure (filling buffer volume and then evacuating manifold) was completed again before the new buffer volume was introduced into the cell. Methane was allowed to equilibrate before isolating the cell and evacuating out the residual methane. The cell was then opened up to

the evacuated manifold, and it was left open for the duration of the experiment. This was done as a safety measure as methane could desorb through heating and in order to adhere to ISIS gas handling procedures.

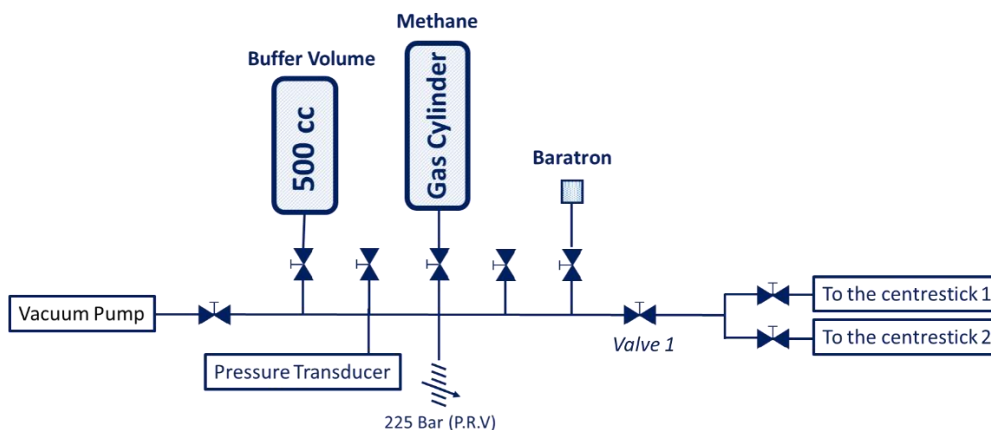


Figure 2.6: Schematic representation of the ISIS gas handling manifold

The manifold volume was calibrated using He in order to calculate the dead volume and be able to know how much methane was loaded in the sample. The buffer volume was filled with a known volume; the rest was evacuated. The buffer volume was opened to the manifold with the pressure recorded. This gave the volume of the manifold and buffer until valve 1. All valves, including valve 1 are Swagelok high pressure ball valves which can be used to isolate each section when needed. The volume between valve 1 and each of the valves before the centre sticks was measured separately. The volume of the lines connecting the manifold to the centresticks was then measured until the top of the cell, there is a valve on top of the cell in order to isolate the sample.

## 2.2 Infrared Spectroscopy

IR spectroscopy is commonly used to characterise heterogeneous catalysts. IR is widely known, with fast sample preparation and spectral collection as well as a vast library of IR data which have been studied extensively in the past. It is a non-destructive technique. The technique can be used both qualitatively and under the right conditions, quantitatively. The infrared spectral range is divided into three main regions, far-IR: 400 – 10  $\text{cm}^{-1}$  region, mid-IR: 4000 – 400  $\text{cm}^{-1}$  region and near IR which is the 14000 – 4000  $\text{cm}^{-1}$  region.<sup>29</sup> The far-IR and near-IR regions, although interesting, require advanced instrumentation to be observed. The mid-IR region is easily accessible and can be observed at high resolution by most laboratory spectrometers.

IR spectroscopy is based on the ability of molecules to absorb electromagnetic radiation within the IR region. The energy absorbed is characteristic of the molecular vibrational frequencies of specific bonds or functional groups.<sup>30,31</sup> A simplistic view is to think of the atoms bonded together as two masses at the end of a spring. This allows the vibrational frequency of that bond to be described by Hooke's law (Equation 2.19). Where the vibrational frequency ( $\tilde{\nu}$ ) is in wavenumbers,  $c$  is the speed of light,  $k$  is the force constant is a function of the bond energy of a two atom bond (description of the strength of the bond, Å) and  $\mu$  the reduced mass of the two atoms, described by equation 2.20.  $m_1$  is the mass of atom 1 and  $m_2$  is the mass of atom 2 when thinking of the connection between the two atoms as a spring.<sup>30,32</sup>

$$\tilde{\nu} = \frac{1}{2\pi c} \sqrt{\frac{k}{\mu}} \quad \text{Equation 2.19}$$

$$\mu = \frac{m_1 m_2}{m_1 + m_2} \quad \text{Equation 2.20}$$

This means that both the strength of the bond and the mass of atoms are important in determining the vibrational frequency of the bond, thus it is characteristic of the bond-type. The vibrational frequency is proportional to the strength of the bond and inversely proportional to the reduced mass. The stronger the bond, and the lighter the atoms at the end of the bond, the higher the vibrational frequency of that specific bond.

For a vibration to be IR active, the transition must give rise to a dipole moment (an allowed transition).<sup>30</sup> The molecule absorbs IR radiation only when its frequency is the same as one of the modes of vibration. A fundamental mode is when the molecule is excited from one level of quantised vibrational level to one level above or the molecule drops one energy level down.<sup>30,33</sup> Therefore, the change in energy level is  $\pm 1$ . Multiples of that frequency can also be absorbed giving rise to overtone bands. The number of fundamental vibrations for linear molecules is  $3N-5$  (where  $N$  is the number of atoms), and for non-linear molecules it is  $3N-6$ .<sup>30</sup> Bond vibrations can be symmetric or asymmetric stretching or bending modes. Rock, wag, twist and deformation modes are all classified as bending modes. Each vibrational mode will have its own unique frequency.

IR spectroscopy has been used for this project for both *ex-situ* characterisation analysis of the samples used for MTH chemistry, but also for understanding the

interactions of methanol with zeolite samples. There are many different IR techniques, however, for this project only diffuse reflectance infrared Fourier transform spectroscopy (DRIFTS) has been used.

### 2.2.1 Diffuse Reflectance Infrared Fourier Transform Spectroscopy (DRIFTS)

Fourier transform spectroscopy uses an interferometer in order to separate light into individual components. The schematic of the Michelson interferometer can be seen in Figure 2.7.<sup>30</sup> The IR source shines a polychromatic light onto a beam splitter which splits it into two beams. One is directed to the stationary mirror whilst the other is directed to the moving mirror. The light is then reflected back from both mirrors and is recombined before being directed to the sample. The sample then absorbs, scatters, reflects and transmits light which is then collected by the detector. The moving mirror moves back and forth with a known distance changing the distance the beam of light is reflected back. This causes the recombination beam to be of varying intensity due to constructive and destructive interference. This results in the interferogram, a sinusoidal signal with the optical path difference in mm which can then be Fourier transformed to give the IR spectrum, which most people are familiar in wavenumbers. For DRIFTS, the reflected light from the sample is what is being directed into the detector, which then gives the interferogram.

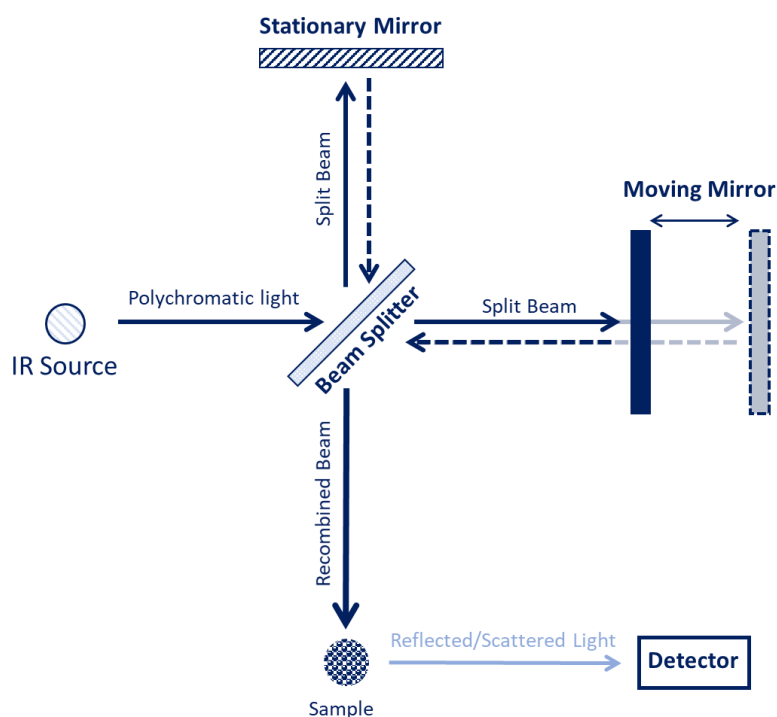


Figure 2. 7: Michelson interferometer schematic adapted from B. H. Stuart<sup>30</sup>

DRIFTS is often used for strongly absorbing powder samples. Diffuse reflectance is when the IR beam directed on the sample penetrates the particles and is scattered in multiple directions. The IR beam can also be reflected off the surface of the particles without penetration, with multiple reflections from multiple particles also being possible. The diffusely scattered IR beam is focused by mirror arrays in an accessory added to the spectrometer, and directed into the detector.

The instrument used for the DRIFTS experiments is an Agilent Carey 680 FT-IR spectrometer, with a KBr beam splitter and a mercury-cadmium-telluride (MCT) semiconducting material as the detector. In order to carry out DRIFTS experiments in this spectrometer, the Harrick 'praying mantis' accessory was used with the praying mantis optics being installed inside the spectrometer (see Figure 2.8.) The incident light enters the accessory with it hitting the first slanted mirror (1) which reflects the light into an adjustable mirror (2) which is calibrated for maximum light reflectance with respect to the height of the sample holder. Mirror 2 then reflects the light to the ellipsoidal mirror at the back (3), which is tilted  $90^\circ$  off its axis. The mirror then directs the light to the sample which diffusely scatters it. The ellipsoidal mirror (4) collects the diffusely scattered radiation at an azimuthal angle of  $120^\circ$ . This is to minimise background interference from the diffusely reflected light. The scattered radiation is then reflected back to mirror 5 and then 6 which finally directs it to the detector.

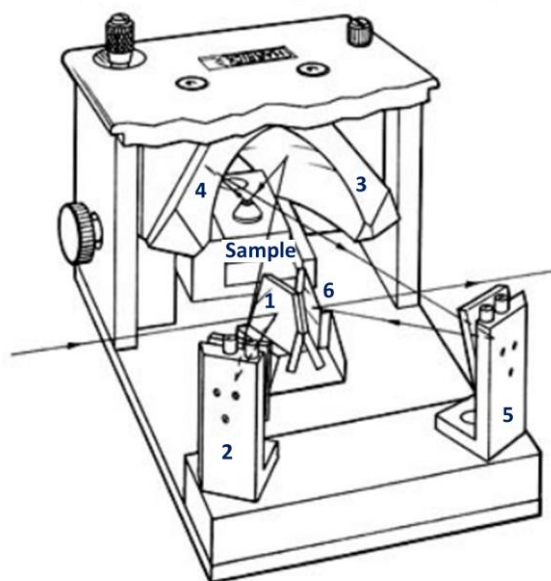


Figure 2. 8: Interior of Praying Mantis accessory, schematic taken from Harrick<sup>34</sup>

### 2.2.1.1 DRIFTS Experimental Conditions

The Harrick high temperature reaction cell was used for all samples measured. This allowed the samples to be dried *in-situ* before either an experiment took place or the MTH reacted samples were measured. The Harrick cell is a domed shaped reactor with the sample holder placed in the middle, the dome is sealed with a Viton O-ring and the lid is screwed in place. The dome is equipped with two ZnSe windows in order to allow for the IR beam to enter and the scattered radiation to exit. There is a heat cartridge beneath the sample holder, which can raise the temperature of the sample. The cell has an inlet and outlet for water cooling the exterior frame and the windows. There are stainless tube fittings that allow gases to be introduced within the sample chamber, with an inlet and an outlet. A mixture of gases can be used simultaneously, if needed, by the use of mass flow controllers and a Valco VICI 6-port valve which allows for efficient mixing of the gases. The option of connecting a mass spectrometer or another type of detector in the outlet stream in order to monitor reactions is also possible. There is a Hiden HPR-20 mass spectrometer connected to the DRIFTS at all times, but it can be bypassed or disconnected if needed.

The MCT detector is liquid nitrogen cooled. The spectra for both sample acquisitions and the background were collected at 64 scans at a resolution of  $4\text{ cm}^{-1}$ . A KBr background was collected before an experiment was conducted, with the KBr being dried before the background was collected. KBr is chosen because it is poorly absorbing, but highly scattering. DRIFTS are measured in pseudo absorbance, which means that the intensity of the sample over the intensity of the KBr background is used in order to calculate the pseudo absorbance (Equation 2.21). Where  $I_s$  is the intensity of the measured sample and  $I_{bckg}$  is the intensity of the background (which needs to be highly scattering).<sup>35</sup>

$$A_{DRIFTS} = -\log_{10} \left( \frac{I_s}{I_{bckg}} \right) \quad \text{Equation 2.21}$$

## 2.3 Reaction Testing

The sample preparation for the MTH reactions carried out with the microreactor and for INS measurements using the ISIS/Glasgow Rig will be discussed in this section. INS needs large sample sizes ( $\sim 10\text{ g}$ ) which needs a specialised reactor in order to prepare them. A detailed experimental section of the samples created will be provided for each chapter separately. This section will discuss

the reactor design for both the ISIS and microreactor set ups, as well as show the calibrations for the GC-FID of the microreactor.

### 2.3.1 ISIS/Glasgow Catalysis Rig

The ISIS/Glasgow Catalysis Rig is a gas handling experimental rig located in the ISIS Neutron and Muon Source. The design of the apparatus has been described in a publication by Warringham et al., and the schematic of the gas handling panel system is seen in Figure 2.9.<sup>36</sup> The system was designed for methane reforming and Fischer-Tropsch catalysis, however, it was able to be used successfully for the MTH reactions. The reactor set up schematic can be found on Figure 2.10.

The catalyst is loaded in the barrel reactor with an internal diameter of 35 mm and 60 mm length. The reactor sits in a furnace, the furnace is placed on a jack so the height can be adjusted in order to be able to load the samples in and out. The reactor is connected to the gas manifold, where only the He line was used for flowing He carrier gas. When the dimethyl ether experiments were completed, a cylinder of DME (Sigma Aldrich,  $\geq 99.9\%$ ) was connected to the empty line next to the CO line on Figure 2.9. The saturator was not used in the MTH experiments. Methanol was introduced to the catalyst via an HPLC Pump (Teledyne SSI, model M1010SNN1C). The HPLC pump is connected on the inlet, when the tap is opened, the He carrier gas is used to carry the methanol droplets into the reactor. The He stream is heated to 60 °C by the use of heated tapes. That and the inlet tube, which is already at reaction temperature within the furnace, are hot enough to vaporise the methanol. The He carrier gas enters the reactor through the inlet at the bottom of the barrel reactor. The reactor temperature was monitored by a thermocouple placed directly on the barrel reactor itself, and the furnace temperature was controlled by a thermocouple placed at the middle of the furnace. There was a 20 °C difference between the furnace temperature and the reactor temperature, which is to be expected. The reactant feed enters the reactor from the bottom, pushes through the catalyst bed and products are pushed out from the top of the reactor.

The product stream is then passed through a catch-pot, which is at room temperature. Liquid products condense within the catch-pot and gaseous products are taken back into the gas manifold through heated lines in order to be analysed by MS. The system also has a micro-GC attached to it, however,

it could not be used during the reactions for this project due to installation problems. Any cold spots between the catch-pot and the manifold, or between the manifold and the MS could cause issues with product condensation and eventually the outlet could be blocked. Cleaning out the outlet by passing ethanol through the outlet pipe was sometimes needed to dissolve any polyaromatic molecules not being caught by the catch-pot. The catch-pot has a drainage system which is used to collect the liquid products whilst the reaction is ongoing.

This set up has been used for both drying the ZSM-5 sample and for the MTH reactions. In all cases the ZSM-5 was calcined under static air in a furnace for 12 hours at 500 °C, in order to remove any residual template (tetrapropyl ammonium bromide) left within the sample. It was then dried at 350 °C for at least three hours (or until no more water was produced), right before the reaction was started. The exact experimental conditions will be found in their respective chapters. The formulas used to calculate the weight hourly gas velocity (WHSV) and the contact time ( $\tau$ ) of all reactions completed have been given in Equations 2.22 and 2.23.

$$WHSV (h^{-1}) = \frac{\text{feedstock flow } (g h^{-1})}{\text{Catalyst Mass } (g)} \quad \text{Equation 2.22}$$

$$\tau (h) = \frac{\text{volume of reactor } (cm^3)}{\text{Total gas flow } (cm^3 h^{-1})} \quad \text{Equation 2.23}$$

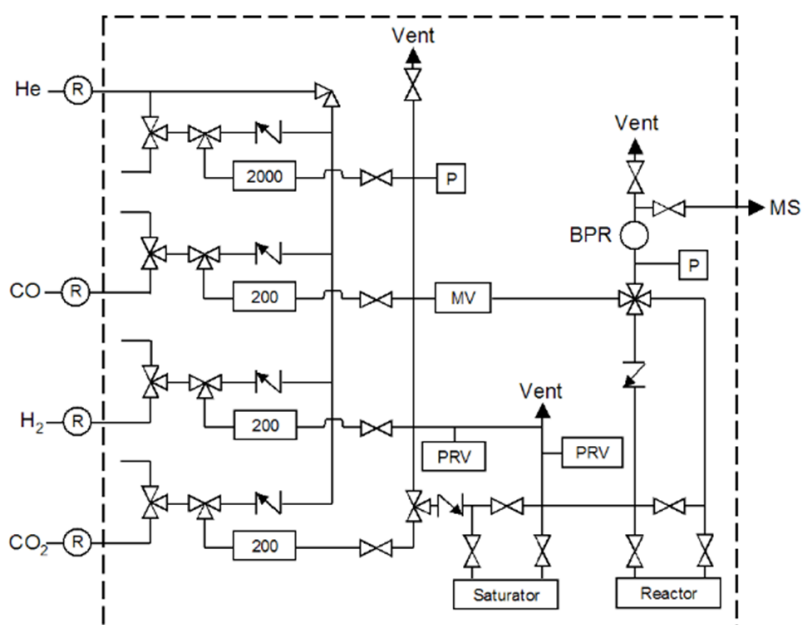


Figure 2.9: Schematic representation of the ISIS/Glasgow Rig taken from Warringham et al.<sup>36</sup>

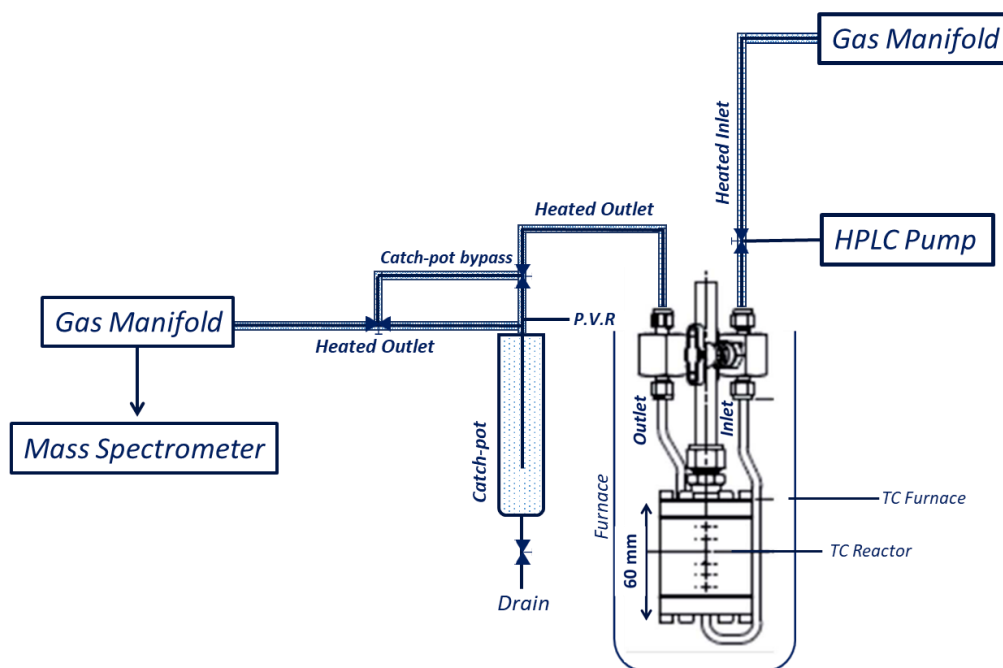


Figure 2.10: Schematic representation of the reactor set up connected to the gas manifold. The reactor cell schematic was taken from Suwardiyanto et al.<sup>37</sup>

A mass spectrometer (Hiden Analytical, HPR-20) was used in order to analyse the effluent gases while the reaction is ongoing. Mass spectrometry is often used in catalysis for reaction monitoring. The gas enters the spectrometer where it is fragmented and ionised by electron bombardment. The electrons are generated from a hot wire filament. The ions produced by the electron bombardment are accelerated in order to have the same kinetic energy. They are then entered into a magnetic field which deflects them by their mass/charge ratio ( $m/z$ ). The smaller the  $m/z$  ratio, the higher the deflection by the magnetic field. The deflected ions hit the detector which produces an ion current which can then be recorded with the current intensity being proportional to the number of ions arriving to the detector. This means that for complex reactions like the MTH, the ion fragments being chosen to monitor are important, as they are directly related to the concentration of products. Smaller mass fragments however, may have more than one molecular origin.

The liquid products were analysed off-line by a GC-MS/FID (Agilent 7890A/5975C GC/MSD/FID, DB-1MS Capillary I: 60 m, d: 0.25 mm, t: 0.25  $\mu\text{m}$ ) at an initial oven temperature of 40  $^{\circ}\text{C}$  for 2 min, increased at 10  $^{\circ}\text{C min}^{-1}$  until 150  $^{\circ}\text{C}$  then held for 3 min. Gas chromatography is a popular technique used for the separation and quantification of liquid sample mixtures. A column is used to separate the different sample components, based on their affinity to the

column's stationary phase. The temperature of the column and the flow could also influence the separation of the sample components. The separated components reach the detector at different times, with their retention time being characteristic of their identity. Depending on the type of detection, the identity can either be confirmed by the retention time with comparison to reference standards or by their mass spectrometry profile. The GC-MS has a mass spectrometer detector, therefore injected liquid samples are vaporised, and the different products are separated within the DB-1MS column. Each hydrocarbon product will reach the mass spectrometer at a different time, giving rise to a chromatograph in which each peak corresponds to a different product.

### 2.3.2 Microreactor Set Up

The reactions carried out with the ISIS/Glasgow rig were the ones where the catalyst was heavily characterised. The microreactor set up was used in order to carry out MTH reactions on a smaller scale with a more in-depth characterisation of the product stream.

The microreactor set up can be found in Figure 2.12. The infrastructure for the reactors was already present at the UK Catalysis Hub laboratory, however, some adjustments needed to be made in order for the MTH reaction to be possible. The design to the modifications was completed by Mr Alex Hawkins and the implementation of the changes was completed by both myself and Alex. The microreactor is set up to run three gases at the same time, with a maximum pressure of 50 Bar. The MTH reaction only needs an inert carrier gas, (He) usually placed in position of Gas 1, and methanol. The methanol was introduced into the expansion volume by an HPLC pump, check valves were placed on either side of the expansion volume in order to prevent back flow. The heat from the heated tapes, kept at 90 °C, in the inlet, is enough to vaporise the methanol in the He flow. Above and below the reaction cell there is a three-way valve in order to switch the reactant flow from the bypass to the reactor and vice-versa. The bypass was needed in order to know when the methanol flow has been stabilised, the methanol concentration at time 0 was measured before the methanol stream was switched over to the reactor.

The reactor tube is a stainless steel tube of inner diameter 10.2 mm. The catalyst bed length was constrained with quartz wool at either end to be 1 cm in length. The inlet is at the top of the reactor, with the reactant feed going

through the catalyst bed, and the product stream coming out from the bottom of the reactor. A needle valve was used to constrain the flow to the GC-FID to 10 ml/min, with the rest of the flow being directed through a condenser to the catch-pot. The total volume of He used was 20 ml/min. The heated lines for the bypass system and the outlet were kept at 130 °C. Even with the heated tapes in place, some blockage from build-up of organics was noticed. The blockage was cleaned by pumping ethanol through the outlet line.

The gaseous products are analysed by GC-FID (Shimadzu GC-2014 fitted with a BP20 column of dimensions 30 m x 0.25 mm x 0.5 µm). The GC method used was at an initial temperature of 40 °C for 4 mins, temperature ramp of 5 °C/min to 100 °C and hold for an additional 2 mins, another temperature ramp of 5 °C/min to 120 °C holding at that temperature for 4 mins and a final temperature ramp of 5 °C/min to 150 °C and holding for a final 15 minutes.

A flame ionisation detector (FID) was used. The effluent gas is separated with the BP20 column into the individual hydrocarbon products. The hydrocarbon is burned with a hydrogen flame producing ions. The ions cause a current between two electrodes, which is then recorded by the instrument. The intensity of the current is directly proportional to the number of ions being generated by the flame and, therefore, a direct measure of how much of each hydrocarbon was present at that particular retention time. The only way of identifying the peaks when using an FID is by comparing their retention time with the retention time of known standards. The GC-FID can also be calibrated in order for quantification to be possible. Different concentrations of methanol, benzene, toluene, o-xylene, p-xylene, mesitylene, 1,2,4 trimethylbenzene, durene and 1 methyl-naphthalene were created and passed through the GC-FID for calibrating the instrument. The different calibration concentrations were created in solution. Propene calibration was also completed but using He carrier gas in order to create the different dilutions. The molarity is therefore moles per 1000 cm<sup>3</sup> of gas rather than in solution. For the hydrocarbon mix, dichloromethane was used as the solvent. Durene was first diluted into ethanol. The calibration plots can be found in Figures 2.12 and 13.

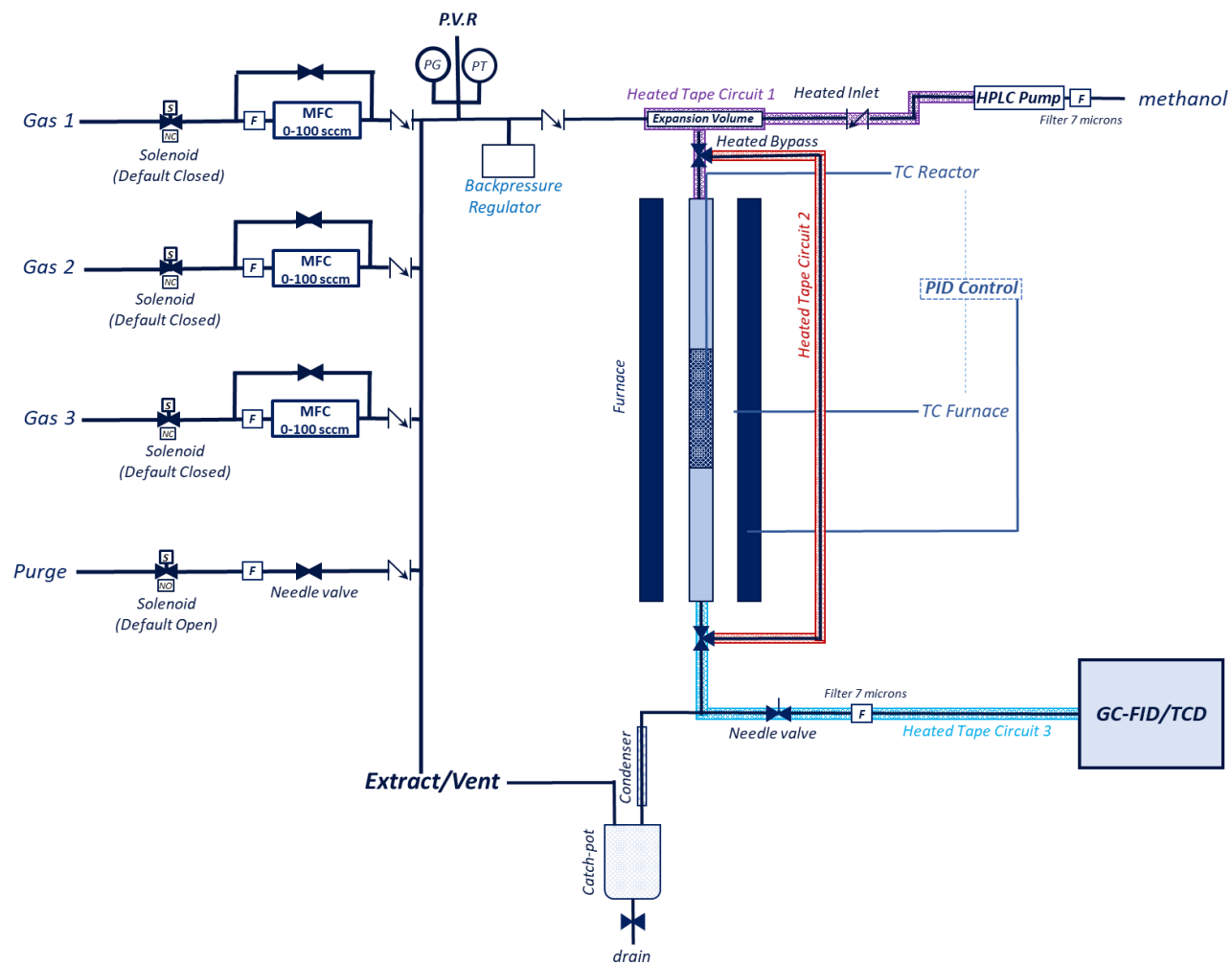


Figure 2.11: Microreactor schematic. PG is the pressure gauge and PT is the pressure transducer. F is a flashback arrestor with a 7 microns filter

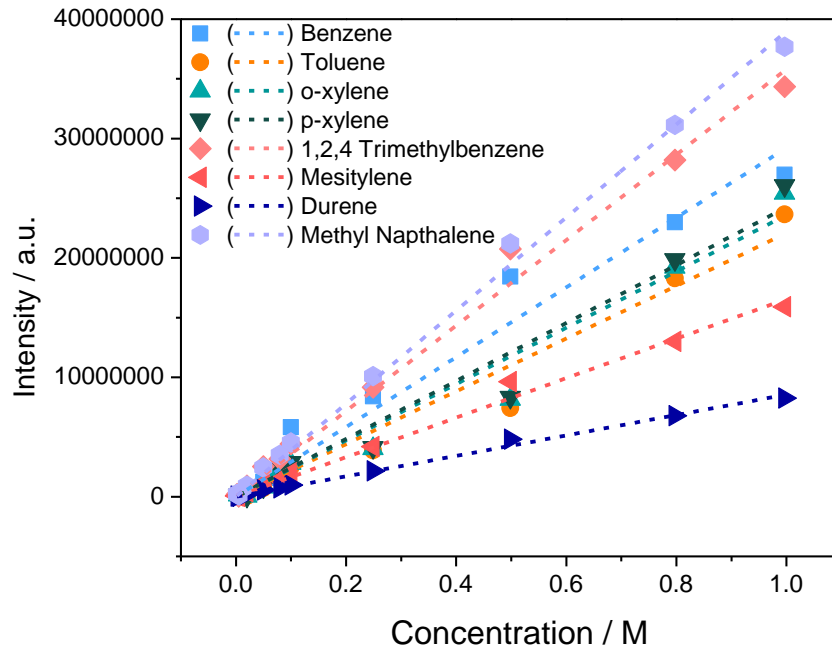


Figure 2.12: Calibration graph of GC-FID intensity vs standards of known concentrations using a calibration mixture of hydrocarbons.

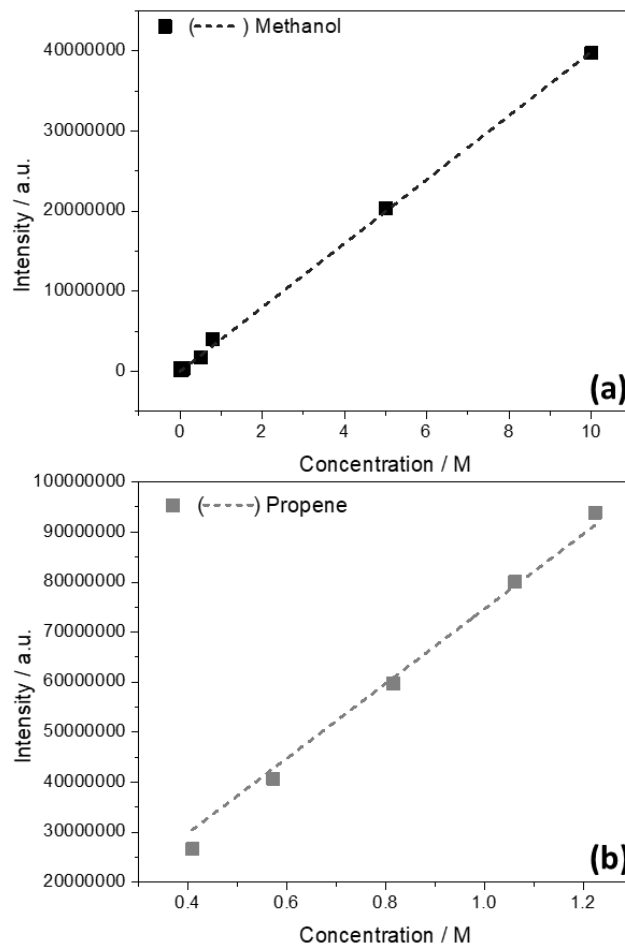


Figure 2.13: Calibration graph of GC-FID intensity vs standards of known concentrations. (a) Methanol (b) Propene

## 2.4 Catalyst Characterisation Techniques

A variety of characterisation techniques have been used in order to characterise both the fresh catalyst and the coked samples after being used for the MTH reaction. The techniques used will be briefly discussed in this section.

### 2.4.1 Nitrogen Sorption Measurements

Zeolite catalysts are porous materials, with their catalytic activity being heavily influenced by their pore size and surface area, as discussed in Chapter 1. The most common way of characterising the porosity and surface area of catalysts is by sorption experiments. The isothermal adsorption or desorption of a probe gas molecule, small enough to enter the pores of the zeolite as a function of its partial pressure will give an isotherm plot. The isotherm plot is a plot of volume of the gas absorbed, which is nitrogen in our case, against the partial pressure. The adsorption and desorption measurements of nitrogen are carried out at liquid nitrogen temperature (77 K). The isotherm obtained will give information about surface area, pore volume and size of a material. There are different types of isotherms seen in Figure 2.14.<sup>38</sup>

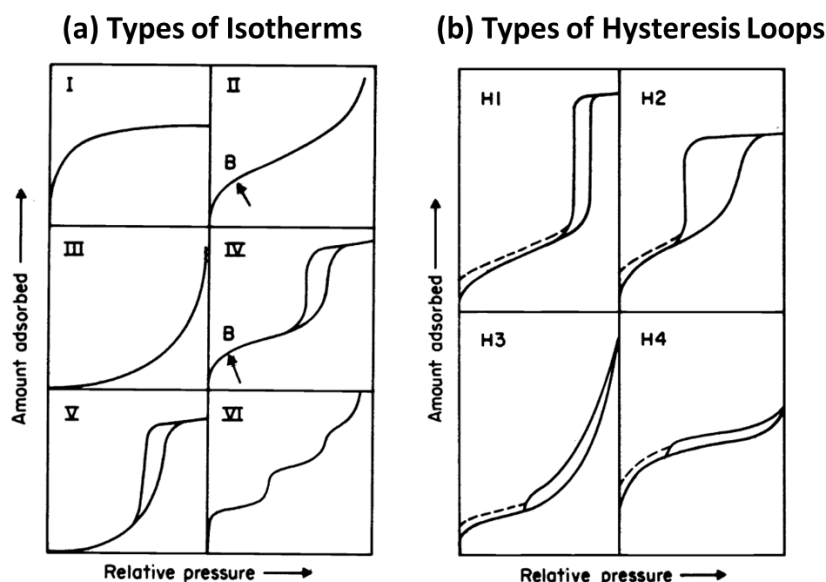


Figure 2.14: (a) Types of isotherms with their type labelled at the left top corner (b) Types of hysteresis loops. The figures were taken from K. Sing et al.<sup>38</sup>

Type I is usually given by microporous solids such as zeolites. There is high uptake at low pressures and then progressively slower as the micropores are filled and access to them becomes more difficult.<sup>38</sup> Type II is typical of non-

porous materials with point B being the point where monolayer adsorption is complete. Type IV is indicative of mesoporosity within the sample. When the isotherm presents a hysteresis loop, this is indicative of capillary condensation taking place within mesopores or agglomerates of particles. Point B again shows when monolayer adsorption is complete and multilayer adsorption begins. The type of hysteresis loop can be indicative of the type of mesoporosity. H4 is the hysteresis that can be indicative of mesopores present within microporous materials. The rest of the isotherms (Type III, Type V and Type VII) are not associated with microporous materials, but rather usually describe multilayer adsorption of non-porous surfaces, or are cases where the adsorbate-adsorbate interactions are more important than the porous structure.

#### 2.4.1.1 Surface Area Analysis

The surface area of the samples were characterised by using the Brunauer-Emmet-Teller (BET) method.<sup>39</sup> Equation 2.24 describes how the surface area from a limited region within the adsorption isotherm is calculated. The limited  $P/P_0$  range needs to be linear in order for Equation 2.24 to work.

$$\frac{1}{W((P_0/P)-1)} = \frac{1}{W_m C} + \frac{C-1}{W_m C} \left(\frac{P}{P_0}\right) \quad \text{Equation 2.24}$$

$W$  is the weight of the adsorbed gas at a relative pressure of  $P_0/P$  and  $W_m$  is the weight of the adsorbate constituting a monolayer of surface coverage.  $C$  is the BET constant related to the energy of adsorption in the first adsorbed layer. (indicative of the adsorbate/adsorbate interactions).

The slope and intercept of the plot of  $1/W((P_0/P) - 1)$  as a function of  $P_0/P$  can be used to derive the weight of the adsorbate from equation 2.22. Once that is obtained, the total surface area of the sample can be calculated from Equation 2.25.  $A_{cs}$  is the molecular cross sectional area of the adsorbate molecule which for  $N_2$  is  $16.2 \text{ \AA}^2$ .<sup>40</sup>  $N_A$  is Avogadro's number ( $6.022 \times 10^{23}$  molecules/mole) and  $M$  is the molecular weight of the adsorbate.

$$S_{BET} = \frac{W_m N_A A_{cs}}{M} \quad \text{Equation 2.25}$$

#### 2.4.1.2 Micropore Analysis

Micropore analysis of the sample uses the V-t method, where the adsorption isotherm of the sample is compared against a reference non-porous solid. The t-plot is a graph of the volume of the adsorbate gas as a function of  $t$ . The  $t$ -

values are calculated as a function of the relative pressure, see Equation 2.26. Where  $\alpha$  and  $b$  are pre exponential terms and for nitrogen adsorption at 77 K are 6.0533 and 3 respectively.<sup>40</sup>

$$t = \alpha \left[ \frac{1}{\ln P_0/P} \right]^{\frac{1}{b}} \quad \text{Equation 2.26}$$

For non-porous solids the t-plot shows a straight line passing through the origin.<sup>41</sup> When the volume of gas adsorbed is corrected from a gas volume to a liquid volume, the slope of the line can give the surface area of all the pores present within the sample, and the positive intercept of the line is the micropore volume.<sup>41</sup>

### **2.4.1.3 Nitrogen Sorption Experimental Conditions**

Surface area analysis was performed using a Quantachrome Quadrasorb EVO/Si gas adsorption instrument. Approximately 0.15 g of a pre-weighed sample was placed in a 9 mm quartz sample tube and degassed at <20 mTorr at 200°C using a degassing accessory (FloVac Degasser, Quantachrome instruments) for 20 h. Liquid nitrogen was used as a coolant and N<sub>2</sub> (BOC, 99.9%) was used as the adsorbent gas. The BET method was used to calculate the surface area in the pressure range  $P/P_0$  of 0.02 - 0.04. The micropore volume was calculated from the t-plot curve using the thickness range between 5 and 6.9 Å. Adsorption isotherm analysis was carried out with the QuadraWin software.

### **2.4.2 Temperature Programmed Desorption**

Temperature programmed desorption (TPD) usually consists of adsorbing a probe molecule on the sample and then using a temperature ramp to observe the probe's desorption. For zeolites, ammonia TPD is usually used to characterise its active sites. Ammonia is a basic molecule that is able to interact with the zeolite acid sites. TPD of ammonia can give information about the strength of the acid sites by the temperature the ammonia is desorbed. The detector used for this experiments was a thermal conductivity detector (TCD), which offers no molecular assignment, but rather a signal difference between the reference gas (He) and the gas being desorbed from the sample. When the TCD signal is calibrated, this technique can be quantitative.

The temperature of ammonia adsorption, the amount of purging before the TPD is started, temperature ramp and the flow of the carrier gas, can all play an

important role into when the ammonia is desorbed from the sample.<sup>42</sup> Because of that, quantitative use of the technique can be challenging and, although a relative number of acid sites is found, the result should ideally to be confirmed by another technique. The low temperature desorption peak of ammonia from zeolites, which is usually found between 100 – 400 °C depending on the conditions mentioned above, is usually due to physisorbed ammonia or interaction of ammonia with weak acid sites.<sup>42,43</sup> A high temperature peak which is usually above 400 °C and below 700 °C, is associated with Brønsted acid sites.<sup>42,43</sup> There is always the danger of ammonia re-adsorbing on the acid sites, although it is more unlikely to happen at higher temperatures.

#### **2.4.2.1 Ammonia TPD Experimental**

For the ammonia TPD, the Quantachrome ChemBET Pulsar instrument was used. The zeolite was placed in a quartz tube and dried under He flow in-situ. A cold trap was placed before the TCD in order to trap any water produced by the drying process. The cold trap was removed when the TPD started. The cell was cooled to 100 °C, and ammonia gas flowed over the zeolite sample for a period of 1 hour. The system was then purged with He until the TCD detector stabilised. The cell was then heated at 10 °C/min until 700 °C, with the TCD signal recording the desorbed species.

The ChemBET was calibrated with ammonia gas as a standard procedure beforehand in order to be able to quantify the sample. Acid site quantification was accomplished by peak fitting with split Gaussian functions with the TPRWin software.

#### **2.4.3 Temperature Programmed Oxidation**

Temperature Programmed Oxidation (TPO) is used for analysis of coke retained within zeolites. The coked sample is exposed to an oxygen rich atmosphere and the coke is oxidised as a function of temperature. The combustion products (water, carbon monoxide and carbon dioxide) are monitored by a detector, usually a mass spectrometer. The temperature at which the combustion products are produced is indicative of the type of coke present within the zeolite. With the coke of interest for this project being defined from the literature as Type I for oxygenates and light olefins and Type II for polyaromatic compounds.<sup>44,45</sup> Type I usually peaks at about 350 °C and Type II usually peaks at about 550 °C. Graphitic coke usually burns at temperatures

higher than 600 °C. The higher the temperature needed for the coke to burn, the lower the H/C ratio present.<sup>46</sup>

#### **2.4.3.1 TPO Experimental Conditions**

TPO was carried out using a Hiden CatLab Microreactor with an integrated mass spectrometer. Approximately 0.05g of reacted catalyst was placed in a quartz reactor and dried under He at 300 °C until no more water was detected in the mass spectrometer, then cooled down to room temperature. The TPO measurement used 10% O<sub>2</sub>/He whilst being heated at 10 °C min<sup>-1</sup> to a final temperature of 800 °C. The final temperature was held for 20 minutes in order to ensure complete combustion of any carbonaceous species. The weight percentage of coke was calculated by recording the weight before and after the TPO experiment.

#### **2.4.4 Thermogravimetric analysis**

Thermogravimetric analysis (TGA) has been used in this project as a way of confirming the percentage of coke present within the reacted samples. It measures the changing weight of the sample with controlled heating. The TGA method can be improved by the addition of a detector capable of both qualitative and quantitative analysis of the effluent gas stream. Detectors often used are FTIR, MS and TCD detectors depending on the needs of the experiment. Even if no detectors were used, the weight changes of a sample could provide important information, especially when wanting an overall coke content of a sample.

##### **2.4.4.1 TGA Experimental Conditions**

TGA experiments were carried out using the same procedure as the TPO experimental conditions described in Section 2.3.3.1. The instrument used was a TGA Q50, TA instrument, with no detector for the gas outlet. The sample weight of the TGA was about 15-20 mg. Instead of oxygen in helium, the gas used was compressed air and nitrogen at similar flow rates as the TPO experiments. This is a more accurate way of measuring the weight percentage of coke than using the CatLab microreactor, as to measure the changing weight the sample needed to be removed from the inert environment.

## 2.4.5 Diffraction

Two types of diffraction were used in this project, both to analyse the fresh ZSM-5: Powder X-ray diffraction and neutron diffraction. Diffraction is a technique often used in catalysis in order to study crystalline materials. Both X-ray and neutron diffraction use the Bragg scattered radiation from the interaction of the incoming (X-ray or neutron) and the atomic plane of the sample to provide structural information. Bragg scattering is when there is constructive interference between the scattered rays. This happens when the path length of the two diffracted X-rays or neutrons differ by an integral number of wavelengths, Equation 2.27.<sup>47</sup>  $n$  is a positive integer,  $\lambda$  is the wavelength of the incident ray,  $d$  is the distance between the scattered planes and  $\theta$  is the Bragg scattering angle (angle of incident beam with the Bragg plane) therefore,  $2\theta$  is the angle between the incident beam and the scattered beam.

$$n\lambda = 2d\sin\theta \quad \text{Equation 2.27}$$

### 2.4.5.1 Neutron Diffraction

Neutron diffraction was carried out with the POLARIS instrument at the ISIS Neutron and Muon source. Neutron diffraction involves elastic scattering which means neutrons are scattered without exchange of energy with the sample. The wavelength of the neutron is related to the neutron mass and velocity as mentioned in Equation 2.4. The velocity is defined as the time it takes for a neutron to travel a specific distance, therefore the Bragg law for neutrons on a spallation source can be described with Equation 2.28. Where  $m$  is the mass of the neutron,  $L$  is the total flight path from the moderator to the detector,  $d$  is the inter-planar spacing,  $h$  is Planck's constant and  $2\theta$  is the Bragg scattering angle

$$n \frac{ht}{mL} = 2d\sin\theta \quad \text{Equation 2.28}$$

The detectors in Polaris are present in distinct banks which cannot move, therefore since the angle of scattering is determined by the neutron energy, the  $d$ -spacings available are determined by the location of those detector banks. The detector banks with the available  $d$ -spacings and  $2\theta$  ranges can be found in Table 2.1.

Table 2.1: Specifications of the detector banks in the Polaris diffractometer<sup>48</sup>

Detector Bank	Bank Description	2 $\theta$ range (°)	$\Delta d/d$ resolution (%)	$d_{\max}$ (Å)
1	Very Low Angle	6.7 - 14.0	2.7	>40
2	Low Angle 1	19.5 – 34.1	1.5	13.5
3	Low Angle 2	40.4 – 66.4	1.85	7.0
4	90°	75.2 – 112.9	0.51	4.1
5	Back Scattering	134.6 – 167.4	0.30	2.65

Both a fresh ZSM-5 and deuterated ZSM-5 were measured by the POLARIS diffractometer. The samples were dried and packed in a cylindrical vanadium sample holder, sealed with indium wire. The sample collection was performed by the POLARIS team since this was an Xpress route measurement, where samples are mailed in for quick experiments with minimal user interaction.

#### 2.4.5.2 Powder X-ray Diffraction

Powder X-ray diffraction (XRD) was undertaken at the ISIS Materials and Characterisation laboratory using a Rigaku Smartlab with a 9 kW source, Cu K $\alpha$  anode with Ge (220) monochromation. Scans performed at 3° min<sup>-1</sup> with the high resolution spectra being performed at a 1° min<sup>-1</sup>, with a 6 rpm sample rotation.

The sample is placed in the middle of the diffractometer. A filament in the X-ray source ejects electrons which are used to bombard the anode (metal target), which causes the metal to lose electrons within the inner shell of the atom. A cascade effect of electrons filling the inner electron hole produce photons with a characteristic energy and wavelength of that specific metal. The metal chosen must emit photons within the X-ray region. The X-ray beam is collimated and then directed onto the sample which scatters the beam in multiple directions. The sample and detector are moved at known angles so as to record the scattered beam at known  $\theta$  angles.

#### 2.4.6 Solid State Nuclear Magnetic Resonance

Solid state nuclear magnetic resonance (ss-NMR) is a widely used technique in characterising zeolite catalysts. NMR relies on the spin interaction of the nuclei with a static magnetic field, which are usually dependent on the orientation of the molecule within that field. For the molecule to be NMR active, it needs to have a non-zero spin quantum number.<sup>49</sup> The quantum spin number

is dependent on the number of protons and neutrons within the nucleus, if the protons and neutrons are even then the quantum spin number is 0, which means that the atom is not NMR active. When a NMR active nucleus is entered within the magnetic field, it causes the energy spin state levels to become non-degenerate in energy and separate.<sup>49,50</sup> This is called the Zeeman effect. The extent of separation depends on the strength of the magnetic field, as well as on the interactions between the nuclei themselves.

There are four interactions which can affect the NMR spectra. The chemical shift anisotropy, dipole-dipole interactions (direct and indirect – J coupling), and quadrupolar interactions. Indirect dipolar interactions are often referred to as J coupling. This is the coupling of two nuclei of the same molecule but connected via a series of bonds.<sup>50</sup> This interaction is usually weak within solid samples. The chemical shift is proportional to the strength of the magnetic field, but is also affected by the density of the electron cloud surrounding the nuclei, which have a shielding effect on the nucleus.<sup>50</sup> In a liquid, the anisotropic effect of the spin interactions are averaged due to the nuclei being able to freely move (Brownian motion) within the matrix, in solids the nuclei are fixed in space and therefore the anisotropy causes line broadening in the NMR spectra.<sup>49</sup> The nuclear spin is also affected by dipole-dipole interactions with a nuclei spin interacting with a neighbouring one. The interaction could be both inter and intra molecular.<sup>50</sup> Due to the fixed positions of the atoms in solids, the dipole-dipole interactions are usually strong which cause poor resolution in the spectra. Quadrupolar interactions are interactions with nuclei with a larger spin than  $\frac{1}{2}$ . The nuclei with such spins have their own electric quadrupole moment, which interacts with the electric field gradient.<sup>51</sup> This broadens the NMR spectral peaks.

Various techniques have been employed to deal with this implication of ssNMR. Magic angle spinning is routinely used as it helps minimise the chemical shift anisotropy and the dipole-dipole coupling. This is achieved by spinning the sample at an angle of  $54.7^\circ$  with respect to the direction of the magnetic field, which makes the anisotropy average to zero, as in a liquid.<sup>51</sup> This makes the NMR spectral peaks narrower, which helps with characterisation of solid samples. Decoupling experiments removes the interaction between different atomic nuclei by using a frequency which cancels the resonance frequency of the unwanted nuclei, whilst cross polarisation (CP) enhances the signal of low abundance nuclei by coupling them with a more abundant nucleus. It must be

noted however, that when CP and MAS are used together, the efficiency of the polarisation transfer between the abundant nuclei and the enhanced one decreases.<sup>50</sup>

#### 2.4.6.1 NMR experimental conditions

The ssNMR experiments conducted in this project were completed by Prof. Russell F. Howe at the University of Aberdeen and Dr. Nathan Barrow at Johnson Matthey Sonning Common. Two different spectrometers were used to obtain spectra of the reacted samples, operating at magnet field strengths of 9.4 and 14.1 T, with the majority of the measurements performed on the lower field instrument. Subsequently, a small number of samples were selected for analysis using the higher field spectrometer. The exact experimental conditions are discussed at the experimental sections of the relevant chapters.

## References

- 1 S. F. Parker, D. Lennon and P. W. Albers, *Appl. Spectrosc.*, 2011, **65**, 1325–1341.
- 2 B. S. Hudson, *Vib. Spectrosc.*, 2006, **42**, 25–32.
- 3 D. S. Sivia, *Elementary Scattering Theory*, Oxford University Press, New York, 2011.
- 4 P. C. H. Mitchell, S. F. Parker, A. J. Ramirez-Cuesta and J. Tomkinson, *Vibrational spectroscopy with neutrons with applications in chemistry*, World Scientific, Singapore, 2005.
- 5 G. J. Kearley and M. R. Johnson, *Vib. Spectrosc.*, 2010, **53**, 54–59.
- 6 S. F. Parker, A. J. Ramirez-Cuesta, P. W. Albers and D. Lennon, in *Journal of Physics: Conference Series*, 2014, vol. 554, p. 012004.
- 7 V. F. Sears, *Neutron News*, 1992, **3**, 26–37.
- 8 D. L. Price, F. Fernando-Alonso, F. P. Price and F. Fernando-Alonso, in *Experimental Methods in the Physical Sciences*, 2013, vol. 44, pp. 1–136.
- 9 S. F. Parker and D. Lennon, *J. Phys. Conf. Ser.*, 2016, **746**, 012066.
- 10 A. J. O'Malley, S. F. Parker and C. Richard. A Catlow, *Chem. Commun.*, 2017, **53**, 12164–12176.

- 11 S. F. Parker, F. Fernandez-Alonso, A. J. Ramirez-Cuesta, J. Tomkinson, S. Rudic, R. S. Pinna, G. Gorini and J. Fernández Castañón, in *Journal of Physics: Conference Series*, IOP Publishing, 2014, vol. 554, p. 012003.
- 12 S. F. Parker, C. J. Carlile, T. Pike, J. Tomkinson, R. J. Newport, C. Andreani, F. P. Ricci, F. Sacchetti and M. Zoppi, *Phys. B Condens. Matter*, 1997, **241–243**, 154–156.
- 13 D. Colognesi, M. Celli, F. Cilloco, R. J. Newport, S. F. Parker, V. Rossi-Albertini, F. Sacchetti, J. Tomkinson and M. Zoppi, *Appl. Phys. A Mater. Sci. Process.*, 2002, **74**, 64–66.
- 14 R. I. I. Bewley, R. S. S. Eccleston, K. A. A. McEwen, S. M. M. Hayden, M. T. T. Dove, S. M. M. Bennington, J. R. R. Treadgold and R. L. S. L. S. S. Coleman, *Phys. B Condens. Matter*, 2006, **385**, 1029–1031.
- 15 ISIS - Merlin technical information, <http://www.isis.stfc.ac.uk/instruments/merlin/technical/merlin-technical-information4807.html>, (accessed 18 April 2017).
- 16 ISIS - MAPS technical information, <http://www.isis.stfc.ac.uk/instruments/maps/technical/maps-technical-information7026.html>, (accessed 18 April 2017).
- 17 O. Arnold, J. C. Bilheux, J. M. Borreguero, A. Buts, S. I. Campbell, L. Chapon, M. Doucet, N. Draper, R. Ferraz Leal, M. A. Gigg, V. E. Lynch, A. Markvardsen, D. J. Mikkelson, R. L. Mikkelson, R. Miller, K. Palmen, P. Parker, G. Passos, T. G. Perring, P. F. Peterson, S. Ren, M. A. Reuter, A. T. Savici, J. W. Taylor, R. J. Taylor, R. Tolchenov, W. Zhou and J. Zikovsky, *Nucl. Instruments Methods Phys. Res. Sect. A Accel. Spectrometers, Detect. Assoc. Equip.*, 2014, **764**, 156–166.
- 18 R. Coldea, MSlicea, [http://mslice.isis.rl.ac.uk/Main\\_Page](http://mslice.isis.rl.ac.uk/Main_Page), (accessed 30 March 2020).
- 19 H. Fritzsche, J. Huot and D. Fruchart, *Neutron Scattering and Other Nuclear Techniques for Hydrogen in Materials*, Springer, Switzerland :, 2016.
- 20 M. Karlsson, *Phys. Chem. Chem. Phys.*, 2015, **17**, 26–38.

- 21 H. Jobic and D. N. Theodorou, *Microporous Mesoporous Mater.*, 2007, **102**, 21–50.
- 22 J. Fitter, T. Gutberlet and J. Katsaras, *Neutron Scattering in Biology*, Springer Berlin Heidelberg New York, 2006.
- 23 M. T. F. Telling and K. H. Andersen, *The OSIRIS user-guide*, Science and Technology Facilities Council, 2003.
- 24 K. H. Andersen, D. Martin y Mareno and M. J. Barlow, *Appl. Phys. A*, , DOI:10.1007/s003390201804.
- 25 ISIS Neutron and Muon Source and Molecular Spectroscopy Group, *The IRIS User Guide 4 th Edition*, 2017.
- 26 ISIS Neutron and Muon Source, ISIS IRIS Spectrometer, <https://www.isis.stfc.ac.uk/Pages/iris.aspx>, (accessed 29 January 2021).
- 27 F. Demmel, T. F. Council, S. Mukhopadhyay, T. F. Council, F. Fernandez-alonso, J. Armstrong and T. F. Council, *IRIS & OSIRIS International Beamline Review - Report Presented to the Panel*, 2014.
- 28 R. T. Azuah, L. R. Kneller, Y. Qiu, P. L. W. Tregenna-Piggott, C. M. Brown, J. R. D. Copley and R. M. Dimeo, *J. Res. Natl. Inst. Stand. Technol.*, 2009, **114**, 341–358.
- 29 P. Larkin and P. Larkin, in *Infrared and Raman Spectroscopy*, 2011, pp. 1–5.
- 30 B. H. Stuart, *Infrared Spectroscopy: Fundamentals and Applications*, John Wiley & Sons, Ltd, Kent, UK, 2004.
- 31 N. B. Colthup, L. H. Daly and S. E. Wiberley, *Introduction to Infrared and Raman Spectroscopy*, Academic Press Inc London, Third., 1990.
- 32 P. Larkin, in *Principles and Spectral Interpretation*, Optris GmbH, Berlin, 2011, pp. 7–25.
- 33 P. Larkin and P. Larkin, in *Infrared and Raman Spectroscopy*, Elsevier Inc., 2011, pp. 7–25.
- 34 Harrick, The Praying Mantis , [www.harricksci.com](http://www.harricksci.com), (accessed 30 January 2021).

- 35 F. Zaera, *Chem. Soc. Rev.*, 2014, 43, 7624–7663.
- 36 R. Warringham, D. Bellaire, S. F. Parker, J. Taylor, R. A. Ewings, C. M. Goodway, M. Kibble, S. R. Wakefield, M. Jura, M. P. Dudman, R. P. Tooze, P. B. Webb and D. Lennon, in *Journal of Physics: Conference Series*, 2014, vol. 554.
- 37 Suwardiyanto, R. F. Howe, R. C. A. Catlow, E. K. Gibson, A. Hameed, J. McGregor, P. Collier, S. F. Parker and D. Lennon, *Faraday Discuss.*, 2017, **197**, 447–472.
- 38 K. S. W. Sing, D. H. Everett, R. A. W. Haul, L. Moscou, R. A. Pierotti, J. Rouguerol and T. Siemieniewska, *Pure Appl. Chem.*, 1985, **57**, 603–619.
- 39 S. Brunauer, P. H. Emmett and E. Teller, *J. Am. Chem. Soc.*, 1938, **60**, 309–319.
- 40 Q. Instruments, *QUADRASORB EVO/SI and QuadraWin User Manual*, 2013.
- 41 S. Storck, H. Bretinger and W. F. Maier, *Characterization of micro-and mesoporous solids by physisorption methods and pore-size analysis*, .
- 42 L. Damjanović and A. Auroux, in *Zeolite Characterization and Catalysis: A Tutorial*, 2010, pp. 107–167.
- 43 W. E. Farneth and R. J. Gorte, *Chem. Rev.*, 1995, **95**, 615–635.
- 44 S. Müller, Y. Liu, M. Vishnuvarthan, X. Sun, A. C. Van Veen, G. L. Haller, M. Sanchez-Sanchez and J. A. Lercher, *J. Catal.*, 2015, **325**, 48–59.
- 45 F. Bauer and H. G. Karge, *Mol. Sieves - Sci. Technol.*, 2006, **5**, 249–364.
- 46 D. M. Bibby, R. F. Howe and G. D. McLellan, *Appl. Catal. A, Gen.*, 1992, **93**, 1–34.
- 47 G. Will, in *Powder Diffraction*, Springer-Verlag, Berlin/Heidelberg, 1964, vol. 58, pp. 1–39.
- 48 R. I. Smith, S. Hull, M. G. Tucker, H. Y. Playford, D. J. McPhail, S. P. Waller and S. T. Norberg, *Rev. Sci. Instrum.*, 2019, **90**, 115101.

- 49 J. Xu, Q. Wang, S. Li and F. Deng, Springer, Singapore, 2019, pp. 1–55.
- 50 A. Zheng, S. J. Huang, Q. Wang, H. Zhang, F. Deng and S. Bin Liu, *Cuihua Xuebao/Chinese J. Catal.*, 2013, 34, 436–491.
- 51 S. E. Ashbrook and S. Sneddon, *J. Am. Chem. Soc.*, 2014, **136**, 15440–15456.

# Chapter 3

## Zeolite Characterisation and Reference Compounds

---

This chapter will focus on two main sections. The characterisation of the ZSM-5 zeolite catalyst used for the experiments conducted in the following chapters, and the reference compound analysis which was needed in order to help assign the spectra obtained with INS. The zeolite characterisation was done as a part of a combined investigation with Mr Alexander P. Hawkins. The same zeolite was used in both iCASE projects, therefore, the characterisation of the zeolite was carried out in tandem with him. The DFT calculations reported in this chapter were undertaken in partnership with Professor Stewart Parker (ISIS).

### 3.1 Introduction

The ZSM-5 zeolite is the catalyst chosen for this project in order to study the MTH reaction using neutron techniques. The ZSM-5 used throughout this project has been provided in a powdered form by Johnson Matthey Plc. The zeolite is without binder although small amounts of residual template may be present (tetrapropyl ammonium bromide). Good characterisation of the zeolite sample is needed in order to have a strong baseline which the following chapters rely on.

Zeolites have been characterised using a variety of techniques including optical spectroscopies, diffraction and nuclear magnetic resonance spectroscopies. The synthesis method of the ZSM-5 can have an effect on the ZSM-5 by inducing different structural defects, number and strength of the acid sites, morphology and crystallinity of the ZSM-5.<sup>1,2</sup> Since its discovery in the 1980's, ZSM-5 has had many applications, with one of its uses being as a catalyst for the MTH reaction. Having a good understanding of the catalyst, would help in tuning its selectivity in the MTH reaction. One of the main aims has been trying to study the zeolites acid sites. The more information about the acid sites, the better the understanding for how they work. However, studying the acid sites has been challenging, especially the ones located in the zeolite itself.

This chapter will also focus on studying the compounds that could be found in the hydrocarbon pool within the ZSM-5 catalyst. The hydrocarbons were chosen as they have been previously identified as part of the hydrocarbon pool products. Using INS to study these model compounds also shows modes previously not accessible with IR. Particularly, the methyl torsion mode, as the vibration is both too low for standard IR spectrometers and it is also often forbidden by symmetry based selection rules or has a very low intensity.<sup>3</sup>

It has been noted in the previous studies of MTH using INS that there is no distinct methyl torsion mode below  $400\text{ cm}^{-1}$ .<sup>4,5</sup> This was curious, as it was expected that the methyl groups would have a strong torsional mode that would be easily visible in the INS. Of the methyl modes, the torsion has been the least studied. In the INS spectrum, the methyl torsion is a strong peak usually found around  $250\text{ cm}^{-1}$ . In this chapter, a special focus will be on studying the methyl torsion mode of poly-methylated aromatics and polycyclic aromatic molecules in order to understand why the methyl torsion mode has not been observed in the previous MTH studies.

## 3.2 Experimental

### 3.2.1 Characterisation of ZSM-5

The ZSM-5 catalyst has been characterised using a combination of a variety of techniques. Nitrogen sorption was used for surface area analysis, with the experimental arrangements described in Chapter 2, Section 2.4.1.3. DRIFTS spectra of the zeolite were collected with the method described in Section 2.2.1.1, with the drying of the zeolite being monitored *in-situ*. Both an as-received ZSM-5 catalyst sample and a calcined ZSM-5 sample were measured. Both samples were dried under a dry  $\text{N}_2$  flow from liquid nitrogen boil off. Spectra were collected every  $20\text{ }^\circ\text{C}$  with the final spectrum collected after 30 mins at  $350\text{ }^\circ\text{C}$ .

X-ray diffraction was undertaken at the ISIS Materials and Characterisation Laboratory (MCL) with the experimental being described at Section 2.4.4.2. The XRF analysis of the zeolite was provided by JM when the zeolite sample was received. The sample was also analysed by XRF elemental analysis at the ISIS-MCL, with the PANalytical Epsilon3 XL instrument. The instrument

software is able to provide both a qualitative and quantitative analysis of the zeolite.

For the ss-NMR analysis, the ZSM-5 fresh/calcined sample was loaded in air into 7.5 mm MAS rotors and spectra recorded on a Varian Infinity Plus 400 MHz spectrometer. Sample rotor was spun in dry air at typically 3–4 kHz.  $^{27}\text{Al}$  spectra were recorded at 104.2 MHz using a one pulse Bloch decay with a 0.5  $\mu\text{s}$  pulse width ( $\pi/20$ ) and a 5 s pulse delay. All samples were measured with the same number of 500 acquisitions to allow comparison of signal to noise. The chemical shifts were externally referenced to a kaolin standard (-2.5 ppm relative to  $\text{Al}(\text{H}_2\text{O})_6^{3+}$ ).  $^{29}\text{Si}$  spectra were recorded at 79.4 MHz using a one pulse Bloch decay with proton decoupling, a  $\pi/2$  pulse width of 6  $\mu\text{s}$  and a 5 s pulse delay, typically 1000 acquisitions.  $^{29}\text{Si}$  spectra were externally referenced to TMS via a kaolin standard (-91.2 ppm). This analysis was completed by Prof Russell Howe in Aberdeen.

### **3.2.1.1 Quantification of Acid Sites**

Both the study and quantification of the acid sites present within ZSM-5 was attempted using a combination of techniques. Ammonia TPD was one of the techniques used, with the experimental details described in Section 2.4.2.1 in Chapter 2. INS was also used to quantify the acid sites.

- **Direct Acid Site Quantification**

The MAPS spectrometer was used in order to quantify the acid sites present in the ZSM-5 sample. The ZSM-5 sample was dried at 350 °C under a helium flow and then transferred to an Al sample can in an argon glovebox. The MAPS spectrometer was calibrated using a series of brucite ( $\text{Mg}(\text{OH})_2$ ) samples of different weights (53 mg, 154 mg, 320 mg, 620 mg). The MAPS spectra were collected at below 20 K, with the A-chopper package at an incident energy of 5243  $\text{cm}^{-1}$ .

- **Pyridine INS Experiments – MAPS**

The fresh ZSM-5 was calcined and then dried at 350 °C, under a He flow. An Inconel flow through cell was used for the dosing. Pyridine loading used a bubbler which was kept at 21 °C. Helium was used as a carrier gas at a flow of 100 ml/min. Pyridine dosing was done at 100 °C for 1 hour, it was then flushed with helium for 10 minutes. The samples were then transferred into an aluminium can for the MAPS spectra to be recorded with the loaded ZSM-5.

The sample was then transferred back into the gas flow cells in order to desorb the pyridine. Pyridine desorption was done at 250 °C under helium flow. The sample was transferred back into the aluminium cans for the MAPS measurements to take place. Reference spectra of pyridine and pyridinium chloride were taken with the MAPS spectrometer to help with distinguishing between chemisorbed and physisorbed pyridine. The same procedure was repeated with the steamed samples which were created for Alex P. Hawkins's project studies (iCASE-2). The steamed samples were used only for comparison purposes in this experiment and will not be discussed further in this thesis.

Table 3. 1: MAPS experimental details for pyridine loading/desorption and cell transfer recovery for ZSM-5 fresh and steamed samples.

	ZSM-5 Fresh	ZSM-5 Stm873K	ZSM-5 Stm1073K
<b>Pyridine Adsorption</b>			
ZSM-5 weight (g)	10.01	10.43	9.59
Pyridine weight (g)	1.15	0.97	0.1
ZSM-5 (moles)	0.0018	0.0018	0.0017
Pyridine (moles)	0.0145	0.0095	0.0013
Transfer 1 mass (g)	11.10	10.93	8.23
% Recovery 1	99.5	97.8	85.0
Loading ( $\text{mol}_{\text{py}}/\text{mol}_{\text{ZSM5}}$ )	8.30	5.24	0.76
<b>Pyridine Desorption</b>			
Transfer 2 mass (g)	11.02	10.71	7.64
% Recovery 2	99.3	98.0	92.8
Mass change (g)	-0.64	-0.80	-0.27
ZSM-5 (moles)	0.0018	0.0018	0.0017
Pyridine (moles)	0.0065	0.0053	assume no py left
Loading ( $\text{mol}_{\text{py}}/\text{mol}_{\text{ZSM5}}$ )	3.54	2.93	N/A
Transfer 3 mass (g)	10.41	9.28	6.65
% Recovery 3	100.30	93.60	90.20

- **Pyridine INS Experiments – TOSCA**

Due to the induced activity of the samples when they come out of the TOSCA spectrometer, the MAPS experimental plan was not able to be followed. (The samples were not safe to handle in order to carry out sample transfers.)

Therefore, the samples were kept in the Inconel cans for both the measurement and the adsorption/desorption stages.

A background of an empty Inconel-can was taken at the start of the experiment, and that was used for background subtraction. The pyridine loadings and desorptions were done in the same way as the MAPS Experimental described above. A complication of keeping the sample in the can was that pyridine that was stuck on the inlet line could have possibly diffused down through the inlet when the desorption was happening, but there was no way to our knowledge that we could prevent that from happening. Reference spectra of pyridine and pyridinium chloride were also recorded with the TOSCA spectrometer. Again, the steamed samples will only be used as a comparison point, rather than fully investigated in this thesis.

Table 3. 2: Table for TOSCA experimental details of pyridine loading/desorption for fresh ZSM-5 and steamed samples.

	ZSM-5 Fresh	ZSM-5 Stm873K	ZSM-5 Stm1073K
<b>Inconel Can Weight (g)</b>	2339.11	2306.19	2314.20
<b>ZSM-5 weight – dry (g)</b>	8.89	4.17	9.74
<b>Pyridine Adsorption</b>			
<b>Pyridine weight (g)</b>	1.89	0.09	0.29
<b>ZSM-5 (moles)</b>	0.0015	0.0007	0.0017
<b>Pyridine (moles)</b>	0.0239	0.0011	0.0037
<b>Loading (mol<sub>py</sub>/mol<sub>ZSM5</sub>)</b>	15.50	1.57	2.17
<b>Pyridine Desorption</b>			
<b>Mass change (g)</b>	-0.46	-0.09	-0.14
<b>Pyridine (moles)</b>	0.01934	0	0.0019
<b>Loading (mol<sub>py</sub>/mol<sub>ZSM5</sub>)</b>	12.50	N/A	1.12

- **Neutron Diffraction**

Neutron diffraction was used in order to attempt to locate the protons and hence the acid sites within the zeolite catalyst. A proposal was submitted and approved through the ISIS 'Xpress' access route, which gives access to researchers to test ideas or for one-off experiments that do not require full beam time allocation. The measurements are performed by ISIS staff. Hydrogen has a large incoherent scattering cross section, that results in an unwanted

background to the diffraction data.<sup>6</sup> Because of that, both a freshly calcined and dried ZSM-5 was used as well as a deuterated sample (D-ZSM-5).

The ZSM-5 sample was deuterated by passing D<sub>2</sub>O over the sample at 300 °C in a sealed flow through cell using a bubbler arrangement under a He flow for five hours. The temperature is high enough to promote the exchange of the hydrogen in Brønsted acid sites without being high enough to cause steam de-alumination of the zeolite.<sup>7,8</sup> The sample was cooled and then dried at 250 °C under vacuum in order to remove any excess D<sub>2</sub>O still present in the sample.

About 1.1g of each sample was packed under inert atmosphere in a cylindrical vanadium sample cell with indium wire gaskets. Vanadium is used due to its negligible coherent scattering cross section. The samples were measured using the Polaris diffractometer located at the ISIS Neutron and Muon source. The data were collected using all five different detector banks of the Polaris instrument (Table 2.1).

### 3.2.2 Model Compounds

The compounds were obtained from commercial sources (see Table 3.3) and used as received. Liquid samples were loaded into 1 mm path length indium wire-sealed Al sample holders, solid samples were wrapped in aluminium foil before being placed in the holder. Sample masses ranged from 0.5–3.4 g. The INS spectra were recorded at  $\leq 20$  K using the TOSCA spectrometer.<sup>9</sup>

#### 3.2.4.1 Computational Methods

Isolated molecule DFT calculations were performed with Gaussian 09.<sup>10</sup> The B3LYP functional with the 6-311G(d) basis set was used in all cases. Periodic DFT calculations were carried out with the plane wave pseudopotential program CASTEP.<sup>11</sup> The geometry optimization used the generalized gradient PBE<sup>12</sup> functional together with the TS dispersion correction.<sup>13</sup> The plane wave cut-off was 750 eV, and the forces were converged to better than  $|0.01| \text{ eV \AA}^{-1}$ , the k-point grid used depended on the initial structure and is given in Table 3.3. The vibrational spectra at the  $\Gamma$ -point in the Brillouin zone were calculated using density functional perturbation theory.<sup>14</sup> Phonon dispersion was calculated along high-symmetry directions throughout the Brillouin zone. Dynamical matrices were computed on a regular grid of wave-vectors throughout the Brillouin zone and Fourier interpolation was used to extend the computed grid to the desired fine set of points along the high-symmetry paths.

The initial structures were taken from the Cambridge Structural Database,<sup>15</sup> the reffcodes are included in Table 3.3. Calculated INS spectra were generated from the Gaussian or CASTEP output using ACLIMAX<sup>16</sup> or AbINS.<sup>17</sup>

Table 3.3: The source of the compounds, their purity, the Cambridge Structural Database<sup>15</sup> (CSD) reffcode, space group and Monkhorst-Pack *k*-point grid for the molecules studied with CASTEP.

Compound	Source (purity)	CSD reffcode	Space group	Monkhorst-Pack <i>k</i> -point grid (no. of <i>k</i> -points)	Ref.
<b>Benzenes</b>					
<b>Benzene</b>	Sigma Aldrich (99.8%)				
<b>1-Methylbenzene (toluene)</b>	Sigma Aldrich (99.8%)	TOLUEN02	<i>P</i> 2 <sub>1</sub> / <i>c</i>	6 × 8 × 2 (24)	<sup>18</sup>
<b>1,2-Dimethylbenzene (ortho-xylene)</b>	Fisher Scientific (99%)	ZZZRTI01	<i>Pmmm</i>	4 × 8 × 6 (48)	<sup>19</sup>
<b>1,3-Dimethylbenzene (meta-xylene)</b>	Fisher Scientific (99%)	ZZZSPY02	<i>Pbca</i> *	5 × 7 × 4 (24)	<sup>20</sup>
<b>1,4-Dimethylbenzene (para-xylene)</b>	Sigma Aldrich (99%)	ZZZITY02	<i>P</i> 2 <sub>1</sub> / <i>n</i>	9 × 8 × 4 (72)	<sup>20</sup>
<b>1,2,3-Trimethylbenzene</b>	Sigma Aldrich (98%)				
<b>1,2,4-Trimethylbenzene</b>	Sigma Aldrich (98%)				
<b>1,3,5-Trimethylbenzene (mesitylene)</b>	Fisher Scientific (99% extra pure)	SOPLAL SOPLAL02	<i>P</i> 2 <sub>1</sub> 3* <i>P</i> $\bar{1}$	6 × 3 × 6 (36) 6 × 4 × 6 (72)	<sup>21</sup> <sup>21</sup>
<b>1,2,3,4-Tetramethylbenzene</b>	Fisher Scientific (95%)				
<b>1,2,3,5-Tetramethylbenzene</b>	Sigma Aldrich (98%)				
<b>1,2,4,5-Tetramethylbenzene (durene)</b>	Sigma Aldrich (98%)	†	<i>P</i> 2 <sub>1</sub> / <i>a</i>	6 × 10 × 8 (120)	<sup>22</sup>
<b>Pentamethylbenzene</b>	Fisher Scientific (99%)	COPMUR	<i>P</i> $\bar{1}$	8 × 8 × 3 (96)	<sup>23</sup>
<b>Hexamethylbenzene</b>	Sigma Aldrich (99%)	HMBENZ06	<i>P</i> $\bar{1}$	6 × 6 × 6 (108)	<sup>24</sup>
<b>Polycyclic aromatics</b>					
<b>Naphthalene</b>	Fisher Scientific (99%)				
<b>1-Methylnaphthalene</b>	Sigma Aldrich (95%)				
<b>2,3-Dimethylnaphthalene</b>	Sigma Aldrich (96%)				
<b>Anthracene</b>	Fisher Scientific (99%)				
<b>9-Methylantracene</b>	Fisher Scientific (99%)	MANTHR15	<i>P</i> 2 <sub>1</sub> / <i>c</i>	6 × 4 × 6 (36)	<sup>25</sup>
<b>9,10-Dimethylantracene</b>	Sigma Aldrich (99%)	DMANTR01	<i>P</i> 2 <sub>1</sub> / <i>c</i> *	6 × 8 × 4 (48)	<sup>26</sup>

## 3.3 Characterisation of ZSM-5

### 3.3.1 Surface Area Analysis

Surface area analysis was undertaken by nitrogen sorption analysis with the nitrogen sorption isotherm of the fresh ZSM-5 shown in Figure 3.1. The plot shows the isotherm to be a Type IV isotherm with a H4 hysteresis loop. This suggests that the ZSM-5 is a microporous system with some mesopores present. The mesopores could be a by-product of the calcination process. The BET surface area of the ZSM-5 is calculated to be  $404 \pm 22 \text{ m}^2\text{g}^{-1}$ , the micropore volume and the external surface area are calculated using the t-plot method and are found to be  $0.156 \pm 0.01 \text{ cm}^3\text{g}^{-1}$  and  $36.9 \pm 1.7 \text{ m}^2\text{g}^{-1}$  respectively.

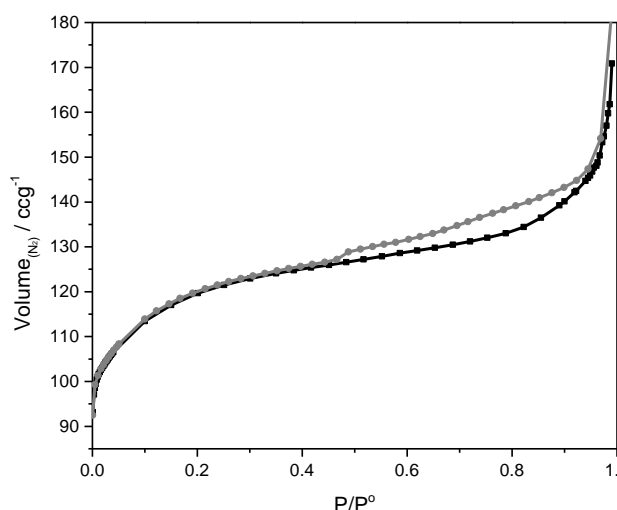


Figure 3.1: Nitrogen adsorption (square) / desorption (circles) isotherm for fresh ZSM-5

### 3.3.2 DRIFTS

The ZSM-5 as-received from Johnson Matthey Plc., still has some residual template present. The template is tetrapropyl ammonium bromide and needs to be removed before the ZSM-5 can be used for the MTH reaction as a catalyst. The calcination procedure needs to be done reproducibly, as it has been shown in the past that calcination could potentially affect the number of defects present in zeolites, as well as their structure.<sup>27-29</sup> The calcination method chosen was used throughout the duration of the project.

DRIFTS spectra of the as received ZSM-5 needed to be dried in order to remove excess water. The water and template are clearly visible as broad peaks in the  $3200 - 2500 \text{ cm}^{-1}$  region (Figure 3.2.a).<sup>30</sup> Upon calcination, the

template is seen to have disappeared and the spectrum of ZSM-5 resembles that seen in the literature.<sup>31,32</sup> The region below  $2000\text{ cm}^{-1}$  is dominated by the zeolite framework modes, a combination of strong adsorbing bands allocated to the zeolites  $\text{SiO}_4$  and  $\text{AlO}_4$  units as well as due to the pentasyl units present.<sup>30,33,34</sup> With drying, the ZSM-5 acid sites become visible in the IR spectrum. The detailed view of the acid site region can be found in Figure 3.2.b. There are three OH environments detected in the ZSM-5; the  $3592\text{ cm}^{-1}$  peak is assigned to Brønsted acid sites,<sup>35</sup> the  $3648\text{ cm}^{-1}$  peak is associated with extra framework Al,<sup>36,37</sup> and the  $3735\text{ cm}^{-1}$  peak is assigned to silanol groups.<sup>38</sup>

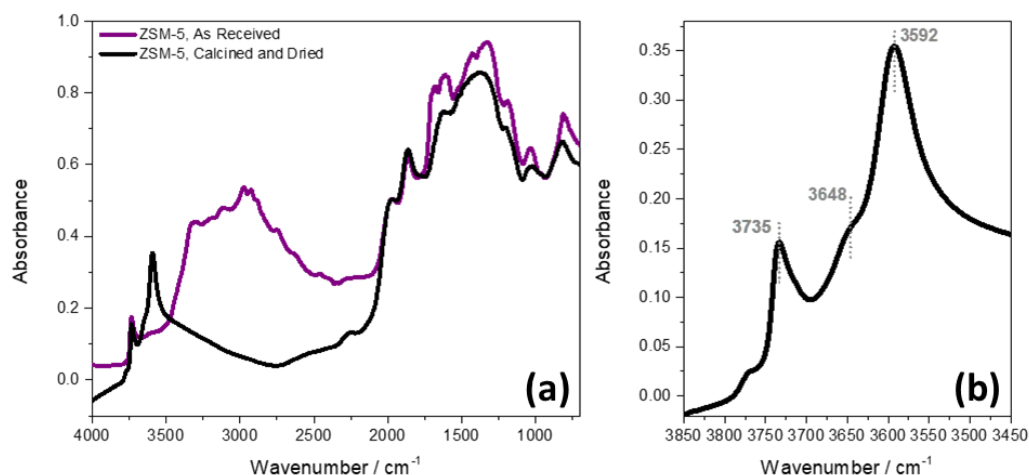


Figure 3.2: DRIFTS spectra of ZSM-5 as received and ZSM-5 after it has been calcined and dried. (a)  $4000\text{ cm}^{-1}$ – $700\text{ cm}^{-1}$  region (b) Detailed view of the acid sites of calcined and dried ZSM-5 spectrum ( $3850\text{ cm}^{-1}$ – $3450\text{ cm}^{-1}$  region)

### 3.3.3 X-Ray Diffraction

The XRD patterns of the as-received ZSM-5 and the calcined ZSM-5 are shown in Figure 3.3. Both XRD patterns are very similar and matching the ZSM-5 XRD pattern reported in the literature.<sup>39</sup> The distinctive XRD peaks of the orthorhombic ZSM-5 structure are clearly visible at  $2\theta = 7.9, 8.7, 23, 23.2^\circ$ .<sup>39–41</sup> The orthorhombic framework has subtle differences from the monoclinic one, with single diffraction peaks observed at  $2\theta$   $24.4, 29.3$  and  $48.7^\circ$  rather than doublets.<sup>42</sup> The only difference between the calcined and the as received zeolite is that the peak at  $2\theta = 7.9$ , becomes broader and more intense with calcination. There are several factors that could affect both the line broadening and the intensity of the XRD peaks varying from sample packing to stacking faults and structural disorder within the zeolite. Calcination of tetrapropyl

ammonium bromide ZSM-5, has shown that there could be some intensity increases at high d-spacing (small 2theta degrees).<sup>43</sup>

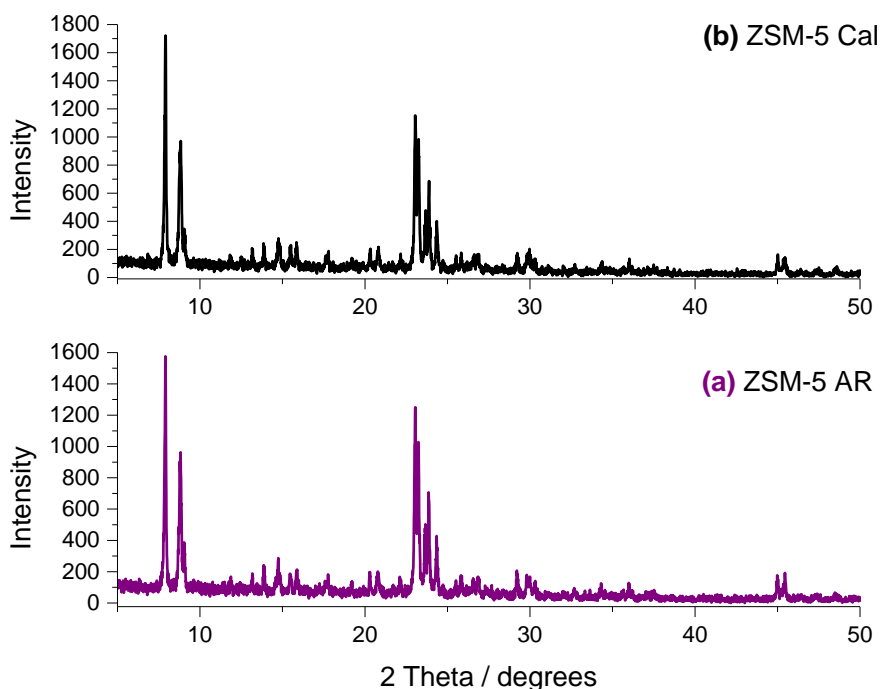


Figure 3.3: XRD pattern of (a) ZSM-5 as received (b) ZSM-5 after it has been calcined

### 3.3.4 XRF

The actual Si:Al ratio of the ZSM-5 needed to be confirmed experimentally. The JM synthesis ratio implied that the Si:Al ratio of the ZSM-5 should be 15 rather than the 30 we originally believed it to be. XRF analysis carried out by Johnson Matthey seemed to agree that the Si:Al ratio should be close to 15, with a repeat XRF measurement with the ISIS XRF spectrometer agreeing with that observation (see Table 3.4). However, the rest of the experimental results that will be further discussed in this chapter seemed to disagree with the XRF result.

The XRF technique cannot distinguish between different forms of Al, therefore, the ratio given in Table 3.4 includes extra-framework Al as well as the framework Al. The Si:Al ratio, traditionally only refers to the ratio of the framework Al compared to the framework Si. From the IR seen above, it was already established that not all of the Al used in the synthesis ended up in the framework, some of it appearing as extra-framework Al. This suggests that the ratio obtained from the XRF is showing the total Al content (both in the and out of the framework) in comparison with the total Si content. Other elemental analysis that could have been used in order to obtain the Si:Al ratio could be MP-AES. The instrument was available in the CatHub laboratory for use,

however, there were no facilities for using HF which is needed in order to completely dissolve the zeolite. HF training was completed in the middle of 2019, however, the local rules still did not allow for HF to be used on site.

Table 3.4: XRF analysis of ZSM-5 at the ISIS Neutron and Muon Facility and at JM

	SiO <sub>2</sub> wt%	Al <sub>2</sub> O <sub>3</sub>	Si:Al
<b>ISIS</b>	95.10	4.85	16.6:1
<b>JM</b>	95.00	4.96	16.3:1

### 3.3.5 ssNMR

A technique that has proven useful in quantifying the Si:Al ratio of a zeolite is ssNMR and in particular <sup>29</sup>Si-NMR. <sup>29</sup>Si-NMR as described by Fyfe, shows the different chemical shifts for silicon bonded through oxygen to its nearest neighbour aluminium, *i.e.* Si(OSi)<sub>4</sub>, Si(OSi)<sub>3</sub>(OAl), Si(OSi)<sub>2</sub>(OAl)<sub>2</sub> and so on.<sup>44</sup> For high silica zeolites like ZSM-5, it is only the first two of these that contribute to the spectrum. A signal at the same chemical shift as Si(OSi)<sub>2</sub>(OAl)<sub>2</sub> is also seen due to silanol groups, *i.e.* Si(OSi)<sub>3</sub>(OH). From the relative intensities of these signals it is possible to estimate the *framework* aluminium content of the zeolite, assuming Lowenstein's rule (no AlOAl linkages) is followed. Equation 3.1 shows how to determine the Si:Al ratio of a zeolite. It must be noted, however, that <sup>29</sup>Si-NMR does not detect Al that is not bonded through oxygen to a silicon atom. Figure 3.4 shows the <sup>29</sup>Si-NMR spectrum of fresh dried ZSM-5 with the three overlapping Si signals identified (-113.1 ppm for Si(OSi), -106.5 ppm for Si(OAl) and finally -102 ppm for silanols, SiOH). Quantification requires curve fitting of the spectrum; the *framework* Si:Al ratio is then calculated from the integrated intensities of the fitted peaks.

$$\frac{Si}{Al} = \frac{\sum_{n=0}^n I_{Si(nAl)}}{\sum_{n=0}^n 0.25n[I_{Si(nAl)}]}$$

Equation 3.1: Equation to determine the Si:Al ratio, *n* is the number of Al present in each of the peaks, *I* is the integrated area of the Gaussian used for fitting the peak (adapted from Ref<sup>44</sup>).

The curve fitting used Origin Pro and Mantid Plot. Various fitting parameters were used, from fitting the whole spectrum, to fitting only the region where the peaks in question were needed. A Gaussian curve was always used to fit the data, with different constraints used on peak centres fixed in place and FWHM tied together, to no constraints used at all. The values obtained for the Si:Al

ratio varied from 24 to 36. The graph shown in Figure 3.4, shows the peak fitting of the  $^{29}\text{Si}$ -NMR of the ZSM-5 spectrum, using Origin Pro Peak Analyser. A flat linear background was used, and the spectrum was fit only in the region of -95 ppm to -122 ppm. No other constraints were used. The Si:Al ratio found was 30.2.  $^{27}\text{Al}$  NMR of the zeolite was also completed. It was seen from the DRIFTS spectra that there is enough extra framework Al to be IR visible (Figure 3.1).  $^{27}\text{Al}$ -NMR can give us an estimate percentage of the extra framework Al present in the ZSM-5 sample. Figure 3.5 shows the  $^{27}\text{Al}$ -NMR of the fresh ZSM-5 sample (hydrated), peak fitted using Origin Pro Peak Analyser. The majority of the Al is present within the framework,  $\text{AlO}_4$  tetrahedral seen as the major peak at 52.7 ppm (70% of the NMR intensity). The shoulder present at 33 ppm, is usually found when the zeolite has undergone steaming.<sup>45,46</sup> In steamed samples, this peak is dominant, whereas here it is more of a shoulder. About 7% of the NMR intensity is given by the peak present at -3 ppm which is allocated to octahedral extra framework Al.

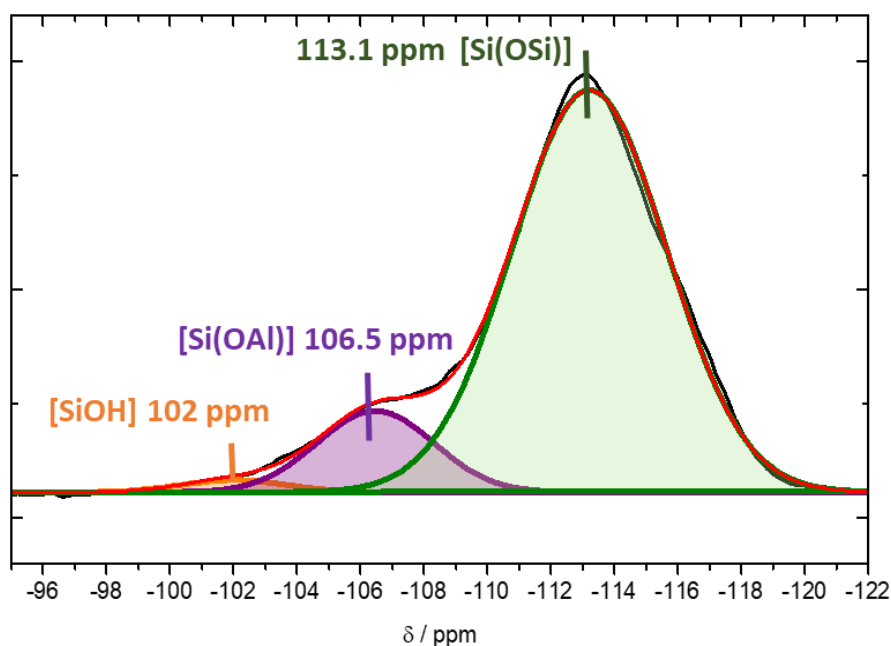


Figure 3.4: Peak fitting of  $^{29}\text{Si}$ -NMR spectrum of ZSM-5 from -95 to 122 ppm. Three peaks taken to simulate the experimental spectrum (black), total fit (red), Si atoms with only Si atom neighbours (green), silicon atoms with one aluminium atom attached to it (purple) and silanols (orange).

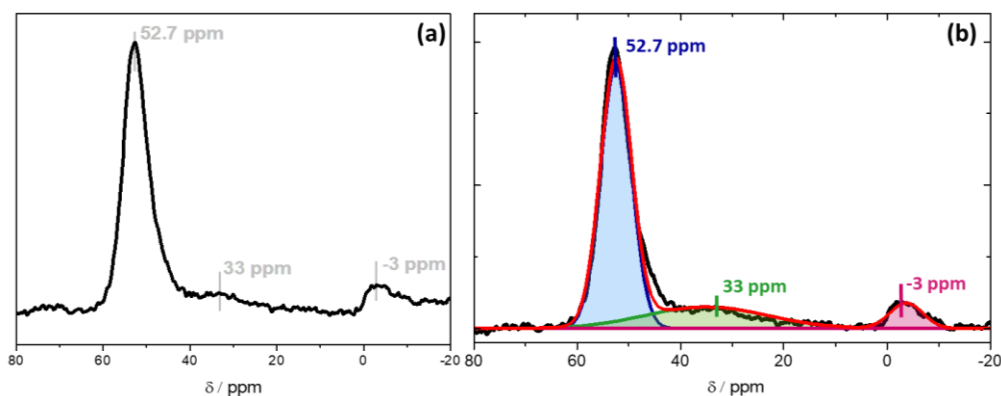


Figure 3.5: (a)  $^{27}\text{Al}$ -NMR Spectrum of ZSM-5 (b) Peak fitting of experimental spectrum (black), total fit (red), tetrahedral Al (blue), octahedral extra framework Al (pink) and unknown Al species (green).

### 3.3.5 Studying the ZSM-5 acid sites

The acid site location and strength are one of the important features of ZSM-5 that make it important as a catalyst. Quantifying the acid sites, as well as establishing where they are in the zeolite, is both important and complicated to do. There are a number of techniques that can be used in order to try and achieve that goal. The DRIFTS spectra found in Figure 3.2 show the spectra of a fresh ZSM-5. From that, the three different acid sites can be distinguished. However, without knowing the extinction co-efficient for each vibration, the number of acid sites cannot be accurately quantified. Therefore, different techniques need to be used in order to quantify the acid sites.

#### 3.3.5.1 Ammonia TPD

One of the most commonly used methods to try and quantify the number of acid sites is ammonia TPD. It is important to note that, although ammonia TPD is routinely used for zeolite characterisation, it is often used qualitatively rather than quantitatively. The peak maxima can be affected by experimental conditions and a shift of 150 °C has been noticed when measuring the same zeolite but by changing the experimental conditions.<sup>47</sup> Ammonia TPD was carried out on a dried zeolite sample (Figure 3.6). The ammonia adsorption was done at 100 °C and the sample was then purged with He until the TCD baseline returned to zero. These two steps were added in order to minimise any re-adsorption when the desorption experiment starts, although it does not completely eliminate the possibility of re-adsorption happening. For data fitting, the TPRWin software was used, this is provided with the instrument by Quantachrome. Due to the increased temperature, the TCD signal at the end of the experiment does not reach zero, therefore a baseline correction is

needed. For the fitting of the desorption peaks, three bi-Gaussian peaks were used. The low temperature peaks correspond to physisorbed ammonia, whereas the high temperature peak with a peak maximum of 530 °C is associated with Brønsted acid sites.<sup>48,49</sup> From peak fitting the desorption peaks, the high temperature peak associated with Brønsted acidity showed that in a fresh zeolite there were 2.43 Brønsted sites / ZSM-5 unit cell which corresponds to a framework Si:Al of 38.5., assuming one aluminium for every acid site in the lattice. The full calculation about how this numbers were obtained can be found in the Appendix.

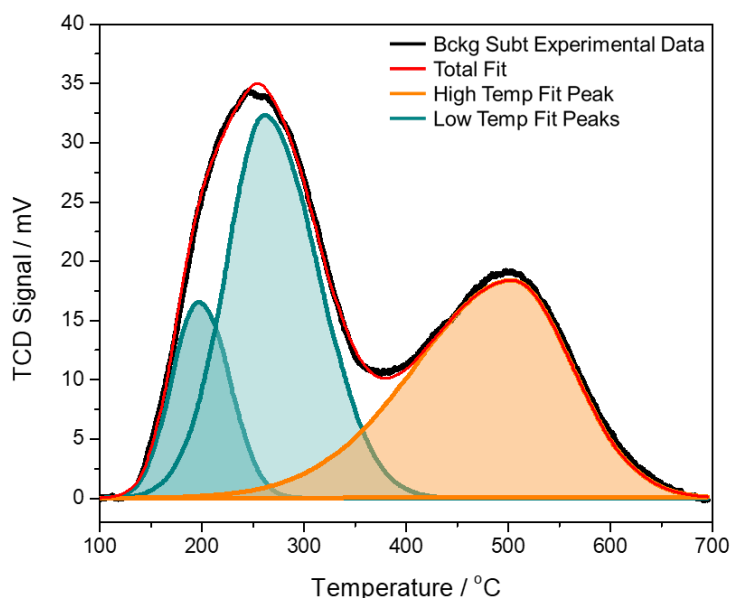


Figure 3.6: Ammonia TPD of calcined fresh ZSM-5, as well as peak fitting of the experimental data. The experimental data were background subtracted due to the TCD signal not becoming completely zero at higher temperatures (black). Total fit of the experimental data is seen by the red line, two peaks needed to fit the low temperature peak (green), and one peak needed to fit the high temperature peak (orange).

### 3.3.5.2 Quantification of Acid Sites with INS

As was discussed above, although TPD is straightforward and is frequently used to study and quantify acid sites in zeolites, the technique has been questioned as to how accurate it is, especially on an instrument that is not used only specifically for TPDs. Therefore, a better method was needed in order to correctly quantify the acid sites present within the ZSM-5 zeolite. INS is a quantitative technique, as the intensity of the peaks is directly related to the number of scatterers present in the sample.<sup>3</sup> Considering that both Si and Al have no contribution in the INS intensity, quantifying the OH environments should be relatively uncomplicated. Figure 3.7 shows the INS spectrum of the

fresh ZSM-5 (calcined and dried). The only peaks visible in the ZSM-5 spectrum are the OH deformation peaks seen at 1128 and 1178  $\text{cm}^{-1}$  as well as the OH stretch peaks seen at the 3400  $\text{cm}^{-1}$  – 4000  $\text{cm}^{-1}$  region. It must be noted that the OH stretch peaks seem to have downshifted by approximately 100  $\text{cm}^{-1}$  each from their IR equivalents. The origin of this shift is unknown at this time. All OH environments are present in the INS, as in the IR, with the issue of being shifted and the intensity ratios being the only differences. The intensity ratios were anticipated due to INS being a quantitative technique, the shift in wavenumber was not. The ZSM-5 sample has been measured multiple times in the duration of the project, and the shift in the OH stretch modes has always been the same. This suggests that it is not due to calibration errors in the spectrometer. Unfortunately, no plausible explanation has been found for this issue as of yet.

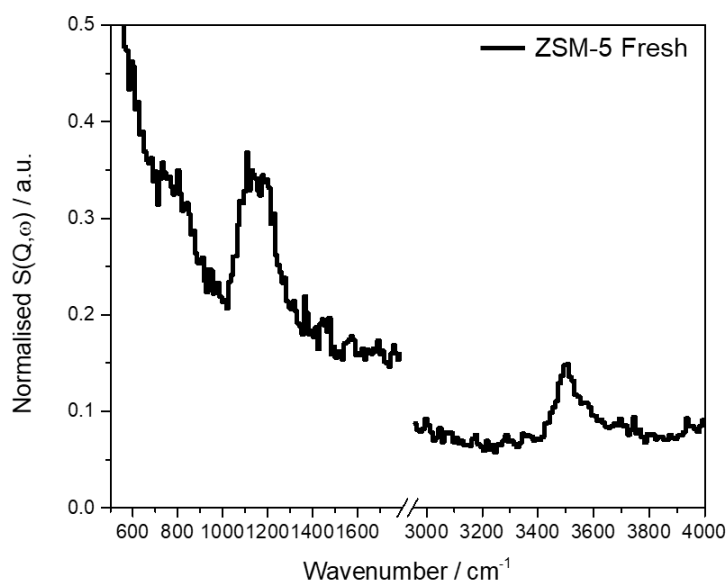


Figure 3.7: INS Spectrum of Fresh ZSM-5 collected using the MAPS spectrometer with the A-chopper package. Region of 500 – 1900  $\text{cm}^{-1}$  collected at an incident energy of 2044  $\text{cm}^{-1}$  and the region of 3000 – 4000  $\text{cm}^{-1}$  collected at an incident energy of 5244  $\text{cm}^{-1}$ .

For quantification of the ZSM-5, only the OH stretch modes were used. This is because the OH stretch region of the ZSM-5 has been characterised extensively with IR, the OH deformation modes are not IR accessible. Therefore, there is no information available in determining which OH deformation belongs to which OH environment present in the zeolite. The INS spectrometer was calibrated by measuring a series of brucite,  $(\text{Mg}(\text{OH})_2)$ , samples of different weights (Figure 3.8.a). This calibration was then applied to the ZSM-5 sample. The INS spectrum in Figure 3.8.b was resolved into the three components identified above, and the amounts of each type of hydroxyl

group determined. The INS quantification gives 3.26 OH Brønsted acid sites in a ZSM-5 unit cell (Table 3.6). Equating the Brønsted acid site concentration to aluminium in the zeolite framework suggests that the *framework* Si:Al ratio is 28. The peaks were fitted using Origin Pro Peak Analyser, with Lorentzians used to fit the peaks (both for the ZSM-5 acid sites and the brucite samples.) Table 3.5 shows the calibration peak areas used to create Figure 3.8. All calculations can be found in the Appendix of this Chapter.

Table 3.5: Brucite calibration data for OH quantification

Brucite mg	OH Concentration mg	Integrated Peak Area
54	30.9	43.95
154	89.8	73.66
320	186.6	140.64
620	361.5	325.83

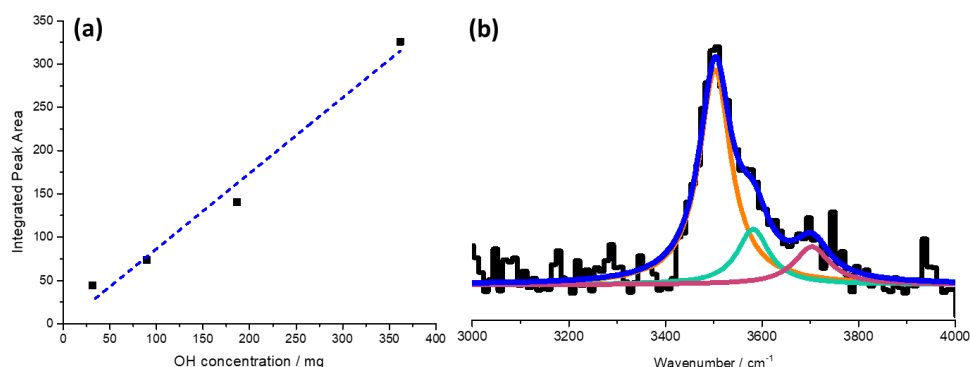


Figure 3.8: (a) INS OH calibration by using the integrated areas of the brucite peaks at different concentrations. (b) The INS spectrum of ZSM-5 focused on the OH stretch region. Black original ZSM-5 spectrum, Orange is the fitted curve for the Brønsted peak, green is for the extra framework aluminium and pink is for the silanols.

Table 3.6: Quantification of the OH sites of the fresh ZSM-5

OH Site	OH Concentration mg/g <sub>ZSM-5</sub>	OH site/Unit Cell
Brønsted	9.77	3.26
Extra Framework Al	3.32	1.11
Silanol	1.98	0.66

### 3.3.5.3 Pyridine Desorption using INS

An experiment where pyridine was used as a probe molecule in order to study the strength of the acid sites was designed using INS as it would be more easily quantified. The steamed ZSM-5 samples shown here were created and used throughout Alex P. Hawkins' project. They are shown here for comparison purposes. Figure 3.9, shows the INS spectra of the reference compounds pyridine and pyridinium chloride. Pyridinium chloride is a model compound of what a pyridinium ion would look like in the zeolite if the pyridine reacted with the zeolite's acid sites. Understanding the differences between the spectra is important in order to identify if the pyridine in the zeolites is in its molecular form or if it is chemisorbed in the form of the pyridinium ion. The first obvious difference in the spectra is that pyridine has a doublet at  $378\text{ cm}^{-1}$  and  $406\text{ cm}^{-1}$ , whereas, the pyridinium chloride only has one peak at  $404\text{ cm}^{-1}$ . Other differences are more subtle, with some of the peaks shifted in wavenumber. Another distinct difference is that pyridine has a sharp peak at  $991\text{ cm}^{-1}$ . This peak is present in the pyridinium chloride only as a shoulder to the  $1047\text{ cm}^{-1}$  peak rather than a distinct peak of its own. Pyridine also has sharp peaks at  $1351\text{ cm}^{-1}$ ,  $1427\text{ cm}^{-1}$  and  $1478\text{ cm}^{-1}$ , whereas the peaks are not as sharp or obvious in the pyridinium chloride spectra.

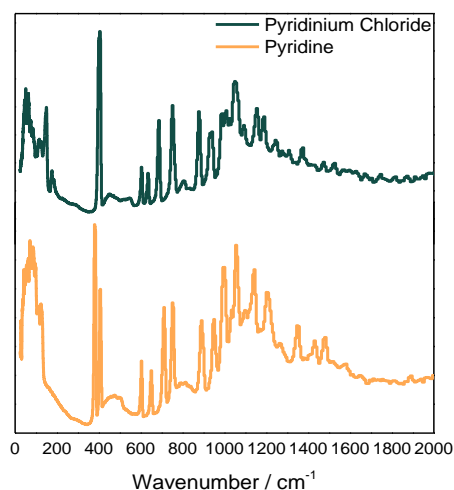


Figure 3.9: TOSCA spectra of pyridine (orange) and pyridinium chloride

Figure 3.10 shows the fresh ZSM-5, Stm873K\_48hrs, Stm1073K\_12hrs after the pyridine loading (Pyridine Adsorption) and after the pyridine desorption, as measured on TOSCA. Both fresh ZSM-5 with pyridine adsorbed (Fig 3.10.a) and after pyridine desorption (Fig 3.10.d), resemble more closely the pyridinium chloride spectrum (Fig. 3.9). The fresh ZSM-5 with pyridine shows broadened peaks which suggest an excess of pyridine is also present. The peaks become sharper after desorption, with the only pyridine present within the zeolite being

in its pyridinium ion form, chemisorbed on the zeolite hydroxyls. The main indication that the pyridine is in its pyridinium form is the single peak at  $400\text{cm}^{-1}$ .

The steamed samples are expected to have less acid sites than the fresh sample due to loss of Al during steaming. This has caused a very low level of pyridine adsorption and retention within the zeolites with Figure 3.10.b and c showing increased levels of noise. Both steamed samples spectra show that the pyridine is still in its molecular form due to the doublet peak found in  $376$  and  $404\text{cm}^{-1}$ . After pyridine desorption, no pyridine is seen to be left in the zeolite from the spectra in the steamed ZSM-5 at  $1073\text{K}_{12\text{hrs}}$  sample (Figure 3.10.e). The weight change in the sample suggests that some pyridine is present after desorption in this sample, however, it could either be too small to be observed through the noise, or it could be stuck in the inlet and outlet lines of the Inconel can. It must be noted that the steamed ZSM-5 at  $873\text{K}$  for 48 hours' sample have caused some problems with the Inconel cell subtraction, which makes it very difficult to identify what is happening in the sample especially after desorption, with both Figure 3.10.c and Figure 3.10.f looking very similar.

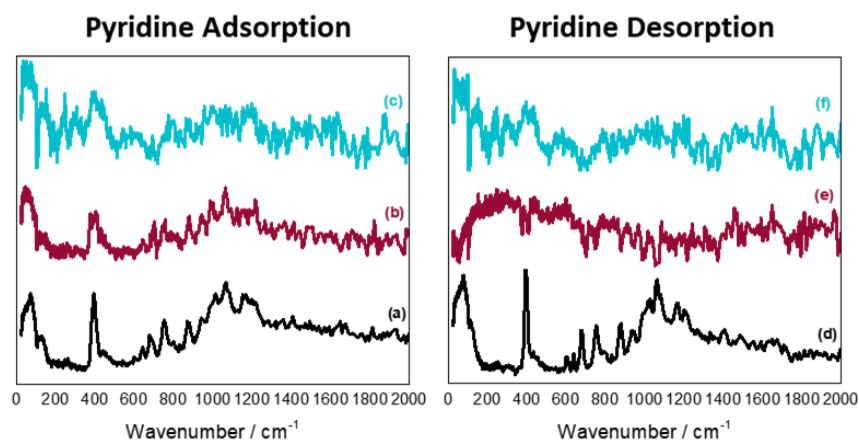


Figure 3. 10: TOSCA Spectrum of pyridine adsorption on (a) Fresh ZSM-5 (b) Steamed ZSM-5 at  $1073\text{K}$  for 12 hours (c) Steamed ZSM-5 at  $873\text{K}$  for 48 hours. After pyridine desorption (d) Fresh ZSM-5 (e) Steamed ZSM-5 at  $1073\text{K}$  (f) steamed ZSM-5 at  $873\text{K}$ . The spectra are stacked. All spectra have both the Inconel can subtracted and the empty zeolite except for (c) and (f) which the subtraction could not work. So a simple linear background was used with the Inconel can still present.

Figure 3.11 shows the corresponding MAPS spectra. The samples are not the same, but they were prepared in the same way. They were also not measured in the Inconel can, as were the TOSCA spectra, but rather Al cans were used in this case. This improved the signal to noise ratio as there is no background from the cell to remove. Figure 3.11.a, shows the reference compounds. The

pyridine peak maxima is at  $3086\text{ cm}^{-1}$ , whereas, the pyridinium chloride the peak is shifted slightly to a peak maxima of  $3106\text{ cm}^{-1}$ . This slight shift will be used in order to identify in which form pyridine is adsorbed on the zeolite. On a first look at Figure 3.11.b and c, it is seen that there is a significant drop in the intensity after the pyridine desorption step on all samples. This shows that even with flushing the sample after dosing, there is some physisorbed pyridine present. All the peak maxima are shown to be a little bit higher than the pyridinium chloride (both before and after pyridine desorption). This shift in the peak maxima could be because the pyridinium ion in the zeolite is actually chemisorbed on the zeolite hydroxyls which could shift the peak maxima slightly.

For the fresh ZSM-5, the peak maximum is at  $3120\text{ cm}^{-1}$ , which shifts to  $3135\text{ cm}^{-1}$  after pyridine desorption. This means in Figure 3.11.b, the peak is a mixture of pyridine and pyridinium. The steamed  $873\text{K}$  sample, retains a lot more pyridine than the steamed  $1073\text{K}$  sample. When the pyridine is desorbed, it is seen that most of the pyridine in both samples is gone, although the steamed  $1073\text{K}$  seems to have a little bit more pyridinium present than the steamed  $873\text{K}$  sample has. This could be due to either the strength or the density of the Brønsted acid sites present in both samples. It is also important to note, that the peak maxima before desorption on the steamed  $873\text{K}$  sample is at  $3096\text{ cm}^{-1}$  and a hump is seen at  $3125\text{ cm}^{-1}$ , whereas the steamed  $1073\text{K}$  sample, is seen to have a peak maximum of  $3110\text{ cm}^{-1}$  suggesting a mixture of pyridine and pyridinium present. The peak maxima of both samples after desorption shifts to  $3135\text{ cm}^{-1}$  as in the fresh zeolite. (Further discussion on the steamed samples is in Alex P. Hawkins thesis).

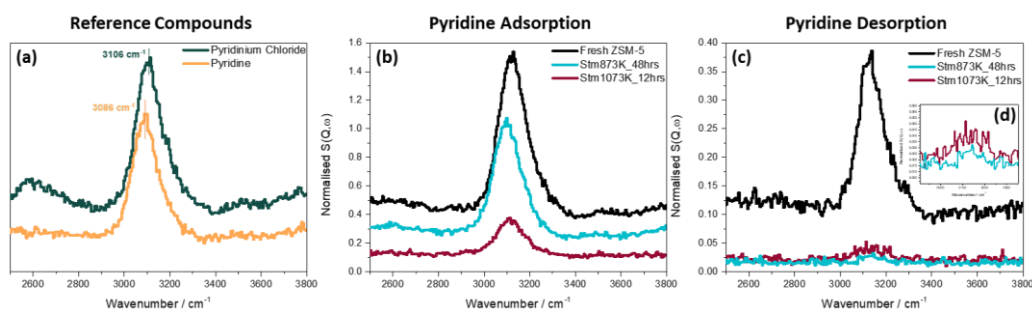


Figure 3.11: MAPS Spectra collected using the A-chopper package at an incident energy of  $5243.55\text{ cm}^{-1}$ . (a) Reference compounds of pyridine and pyridinium chloride (b) Spectra of samples (Fresh ZSM-5, Steamed ZSM-5 at  $1073\text{K}$  for 12 hours, Steamed ZSM-5 at  $873\text{K}$  for 48 hours) with pyridine adsorbed (c) Spectra of samples (Fresh ZSM-5, Steamed ZSM-5 at  $1073\text{K}$  for 12 hours, Steamed ZSM-5 at  $873\text{K}$  for 48 hours) after pyridine desorption (d) Magnified section  $\times 8$  in order to be able to view the steamed samples after desorption.

Peak fitting of the spectra of Fresh ZSM-5 with pyridine adsorption and after pyridine desorption can be seen in Figure 3.12.a and b respectively. From the peak fits, it is seen that after the pyridine adsorption there is pyridine in the ZSM-5 that has not been chemisorbed on the acid sites. In fact 56% of the peak is due to pyridine still being in its molecular form within the zeolite and 44% of the signal is due to pyridinium. When the pyridine is desorbed, no peak for molecular pyridine is observed, which means all the pyridine left is in the pyridinium form. The drop in intensity from the adsorption spectrum to the desorption spectrum, suggests that some of the pyridinium present in the adsorption spectrum has also been desorbed. This could be due to weak interactions with the acid sites, either due to their location or possibly due to pyridine interacting with weaker acid sites.

Unfortunately, there was no time for proper quantification. Using the reference compounds as a one-point calibration has shown that in the initial pyridine adsorption, the pyridinium present in the initial adsorption seems to be 0.0097 moles per sample and after adsorption it seems to have dropped to 0.0047 moles per sample. This would give a Si:Al ratio of 36.5. The pyridinium calculated from the INS peak in the desorbed sample is also lower than the loading of pyridine calculated from the weight change (0.0065 moles per sample), gave a Si:Al ratio of 26.1 which is closer to the ratio obtained from the direct quantification from INS. In order to complete this quick calibration, the zeolite contribution needed to be removed from both the adsorbed and desorbed samples. Proper quantification of the pyridine and pyridinium species could be plausible with the right reference samples for calibrating the instrument and having multiple calibration points. There was no time in the beam allocation for a proper calibration.

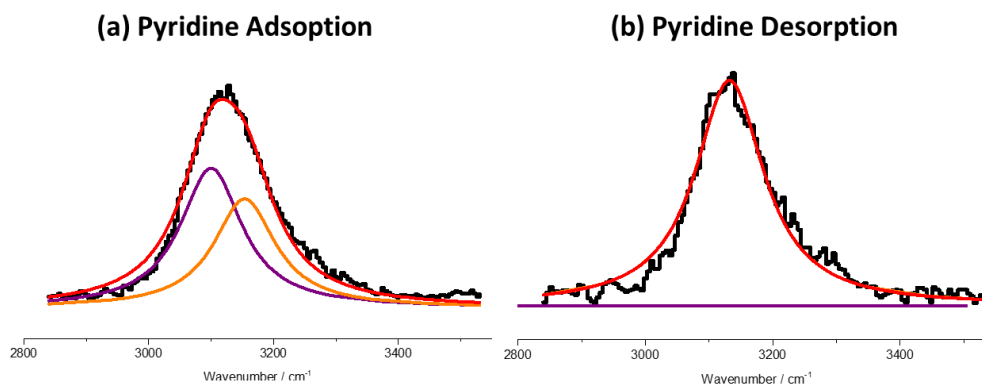


Figure 3.12: Peak fitting of the MAPS spectra of Fresh ZSM-5 (a) after pyridine adsorption and (b) after pyridine desorption.

### 3.3.5.4 Neutron Diffraction

The reason neutron diffraction was chosen was to try and directly determine the location of the acid sites within the zeolite. Identifying the location of the acid sites within zeolites is challenging, however, the location of an acid site could have great influence in the strength of the acid site, as well as its accessibility. Neutron diffraction differs from X-ray diffraction in that it can resolve contributions from the hydrogen atoms. There are a small number of reports determining the location of the protons within a zeolite.<sup>6,50</sup> With Czjzek and Jobic<sup>50</sup> using neutron diffraction in order to attempt to find the locations of protons within zeolite Y, and Mentzen et al.,<sup>6</sup> using a combination of techniques including neutron diffraction to obtain information on different monovalent cations in ZSM-5. Both studies had issues with the hydrogen samples due to increased level of background noise. With Czjzek and Jobic observing that the preferential location of the hydrogen population was near the oxygen sites with the smallest T-O-T angles. The fact that there are so few studies suggests how difficult it is to actually locate the protons within zeolites.

The experimental data have been collected and can be seen at Figures 3.13 and 3.14. The H-ZSM-5 and D-ZSM-5 diffraction spectra don't have any visible differences. The Rietveld refinement of the data has been undertaken by Professor Jan Skalke at the University of Aberdeen using the GSAS-II analysis software.<sup>51</sup> At the time of writing, the analysis is incomplete and this remains a 'work in progress' and will therefore not be considered further here. Initial Rietveld analysis showed a good initial fit of the data for both D and H samples. However, it has not been possible to define the contributions from the hydroxyl groups.

Further analysis of the data has been more complicated than anticipated. These complications have been attributed to the fact that there is a relatively low density of acid sites within the overall zeolite matrix. There is also some disorder being observed in the samples, which could arise from possible mobility or site exchange of the proton between Brønsted acid sites. The presence of extra framework Al complicates the analysis further and is thought to be contributing to the measured diffraction data. As was seen from both the IR and the INS, the presence of extra framework Al is not insignificant, with INS quantitative analysis showing approximately 1 extra framework Al in every ZSM-5 unit cell. This contribution from the extra framework Al is something that requires further investigation. The analysis of the data at the University of

Aberdeen continues. At this time, it is shown that the location of the acid sites has not been discernible and that the application of neutron diffraction is more challenging in achieving this than previously anticipated.

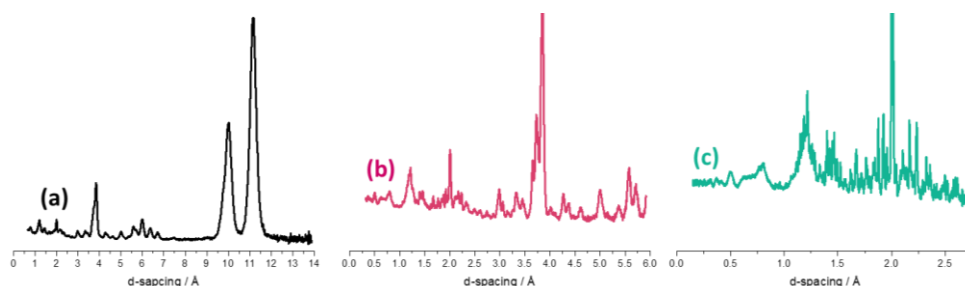


Figure 3.13: Neutron diffraction pattern of Fresh H-ZSM-5 (a) Detector bank 2 (d-spacing; 0.5-13.5 Å) (b) Detector bank 3 (d-spacing; 0.3-5.9 Å) and (c) Detector bank 5 (d-spacing; 0.2-2.7 Å)

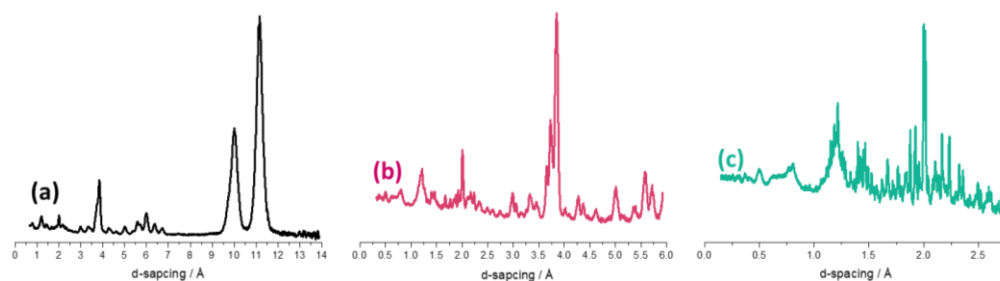


Figure 3.14: Neutron diffraction pattern of Fresh D-ZSM-5 (a) Detector bank 2 (d-spacing; 0.5-13.5 Å) (b) Detector bank 3 (d-spacing; 0.3-5.9 Å) and (c) Detector bank 5 (d-spacing; 0.2-2.7 Å)

### 3.3.6 Summary of Characterisation

The ZSM-5 sample has been characterised using a variety of techniques. Table 3.7 compares the acid site and Si:Al determination using the various techniques. As can be seen from the table, the Si:Al ratios vary with the different techniques with most techniques showing a Brønsted acid site of about 3 per unit cell and a Si:Al ratio of about 30. The XRF technique shows a Si:Al ratio almost half to what the other techniques indicated. This suggests that there is a lot more Al present than previously thought. From both the IR and the INS it has been shown that there is a high level of extra-framework Al, something that could have affected the Si:Al ratio determined by XRF. XRF would not be able to discern between the different forms of Al, therefore, the Si:Al ratio presented is not a representation of the Si to framework Al ratio as is custom. Therefore, a technique that would be able to discern the two types of Al is needed in order to have a more accurate look into the zeolites acid sites.

Using ammonia TPD experiments is a good way of identifying the acid sites and in giving a relative number for the acid sites. Although quantitative

ammonia TPD can be attempted, it comes with limitations. Slight changes in conditions could cause issues when it comes to the reproducibility of the method. And although certain steps could be taken, like purging the sample and completing it at raised temperatures it does not completely eliminate the possibility of ammonia re-adsorbing on an acid site. The fact that the Si:Al ratio is a lot higher than the XRF value however, indicates that most likely the Si:Al lies with what the other techniques have shown. The pyridine desorption experiments using INS also works on the same principles as the ammonia TPD experiment. Pyridine interacts strongly with the Brønsted acid sites due to its basic nature.<sup>52</sup> Estimating the Si:Al ratio based on the weight change occurring after the excess pyridine is desorbed from the sample, gives a Si:Al of 26. Estimating the Si:Al ratio using the one point pyridine calibration gives a rough value of Si:Al of 36. Both ratios are closer to the determined values of both NMR and INS direct quantification.

Both NMR and INS have shown a very similar result when it comes to the acid site calculation and Si:Al ratio estimation. Both techniques are quantitative, and although both have their limitations it is believed that the Si:Al ratio derived from them is closer to the true value for this sample than the other techniques. Therefore, the Si:Al ratio of 28.4, from the direct quantification of the acid sites using INS will be used throughout this thesis. This corresponds to approximately 3 Brønsted acid sites per unit cell of the ZSM-5 structure.

*Table 3.7: Summary of acid site quantification and Si:Al determination of the ZSM-5 sample using the different techniques.*

	<b>Si:Al Ratio</b>	<b>Brønsted Acid Sites /unit cell</b>
<b>XRF</b>	16.3:1 ↔ 16.6:1	5.55 ↔ 4.46
<b><sup>29</sup>Si-NMR</b>	30.2	3.08
<b>Ammonia TPD</b>	38.5:1	2.43
<b>INS (Pyridine Desorption)</b>	26.1:1 ↔ 36.5:1	3.54 ↔ 2.56
<b>INS (Direct Quantification)</b>	28.4	3.26

### 3.4 Reference Compounds

For the MTH reaction it is well accepted that a hydrocarbon pool mechanism is in effect. This means a variety of hydrocarbons could be present within the zeolite. INS is able to observe all vibrational modes without any of the selection rules which govern optical spectroscopies, which could lead to complex spectra as was seen in the preliminary MTH investigations.<sup>3-5</sup> Therefore, a database of hydrocarbons that could be present in the zeolite was collected and analysed by INS in order to be able to characterise the MTH spectra seen in the following chapters. The spectra of all possible methylated benzenes (Figure 3.15-3.17) and some polycyclic aromatic compounds (Figure 3.18 and 3.19) were measured using the TOSCA spectrometer.

The INS spectra of most of the compounds have been previously reported (benzene<sup>53</sup>, toluene<sup>54</sup>, xylene<sup>54,55</sup>, mesitylene<sup>56</sup>, durene<sup>22</sup>, pentamethylbenzene<sup>23</sup> and hexamethylbenzene<sup>57</sup>). However, most of the spectra are either of a much lower resolution or with a more restricted energy transfer than the spectra shown in Figures 3.15-3.19.

In benzene, all of the external (lattice) modes occur at  $\leq 150 \text{ cm}^{-1}$  and this appears to be the case for all the isomeric methylated benzenes.<sup>53</sup> Therefore, modes above this energy observed in the rest of the methylated benzenes must be related to the presence of the methyl group. It must be noted that in addition to the torsion, in-plane and out-of-plane (with respect to the aromatic ring) bending modes of the methyl group will also occur below  $600 \text{ cm}^{-1}$ . (These are not the C–C–H bending modes, which occur around  $1400 \text{ cm}^{-1}$ , but the C–C–Me, where the methyl (Me) group behaves approximately as a point mass).

It has been assumed that the methyl torsion is one of the most intense modes in the spectra.<sup>3</sup> Based on that assumption, some patterns can be observed when looking at the region below  $600 \text{ cm}^{-1}$  in Figures 3.15-3.17. Molecules which have methyl groups that are not adjacent to another methyl group; toluene, m-xylene, p-xylene and mesitylene, exhibit torsions at a lower energy than those with adjacent methyl groups. With the non-adjacent methyl group molecules having their methyl torsions at about  $100 \text{ cm}^{-1}$  or lower and molecules with adjacent methyl groups having the torsion at about  $150\text{-}200 \text{ cm}^{-1}$ . It is also noticed that even though it has always been assumed that the methyl torsion is one of the strongest (in intensity) peaks,<sup>3</sup> there are other modes which approach the methyl torsion intensity in the low region of the

spectra (most evident in tri- and tetra- methylbenzenes). This observation is important for the MTH reaction, as one of the things noted from the preliminary studies is that no methyl torsion peak was detected in the study of the used ZSM-5 samples.<sup>4,5</sup>

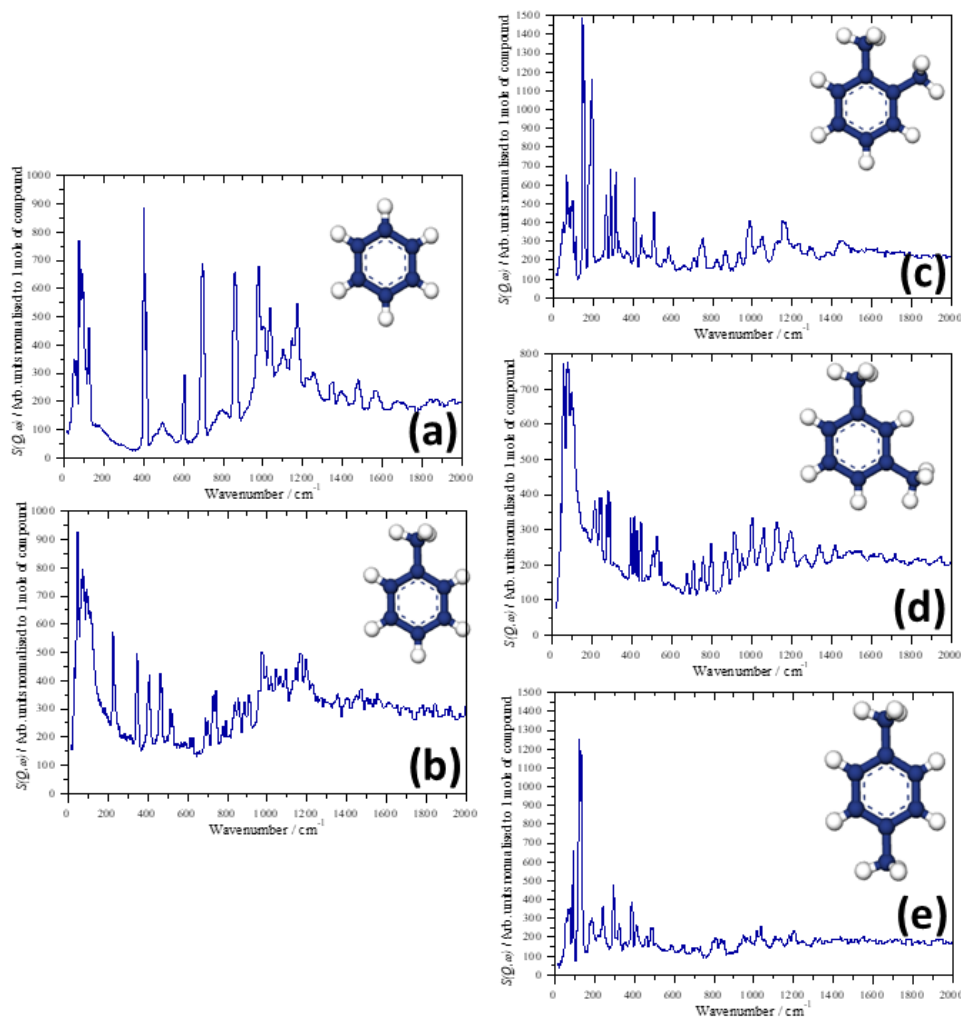


Figure 3.15: INS spectra collected via TOSCA of benzenes. (a) Benzene (b) toluene (c) *o*-xylene (d) *m*-xylene (e) *p*-xylene (f) 1,2,3-trimethylbenzene

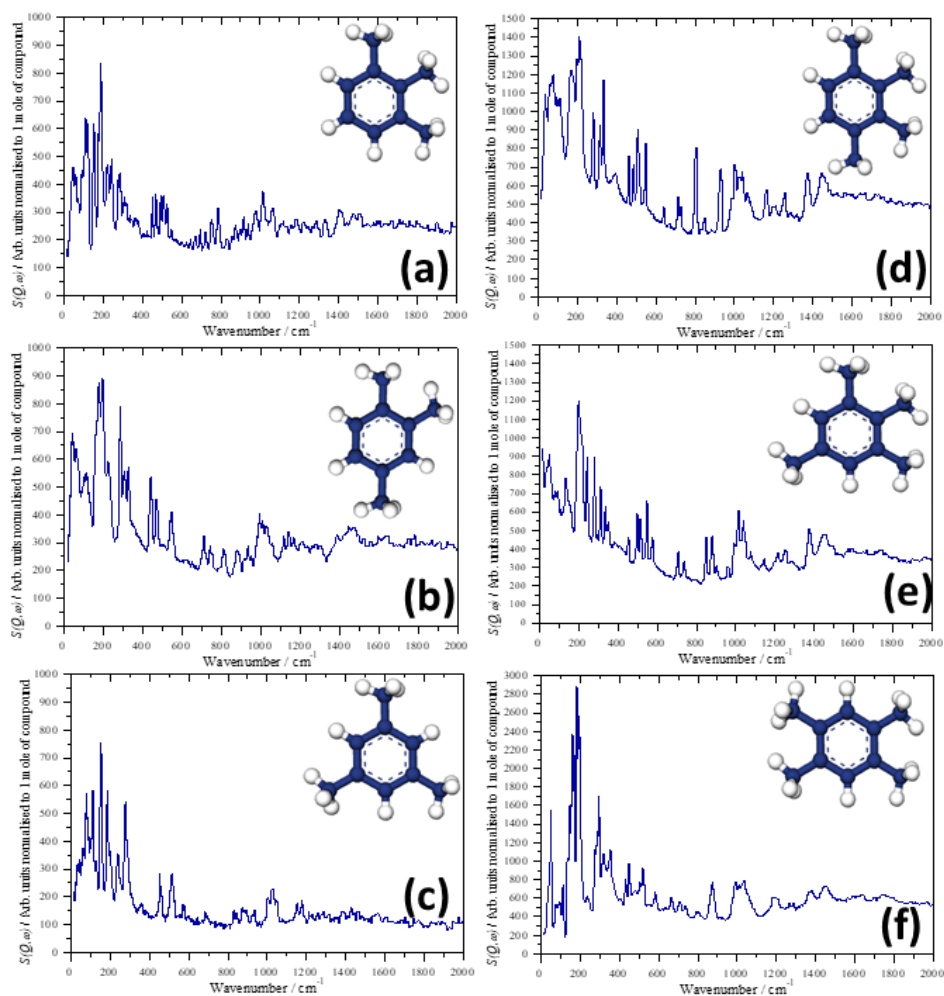


Figure 3.16: INS spectra collected via TOSCA of tri- and tetra-methylated benzenes. (a) 1,2,3-trimethylbenzene (b) 1,2,4-trimethylbenzene (c) 1,3,5-trimethylbenzene (mesitylene) (d) 1,2,3,4-tetramethylbenzene (e) 1,2,3,5-tetramethylbenzene (f) 1,2,4,5-tetramethylbenzene (durene)

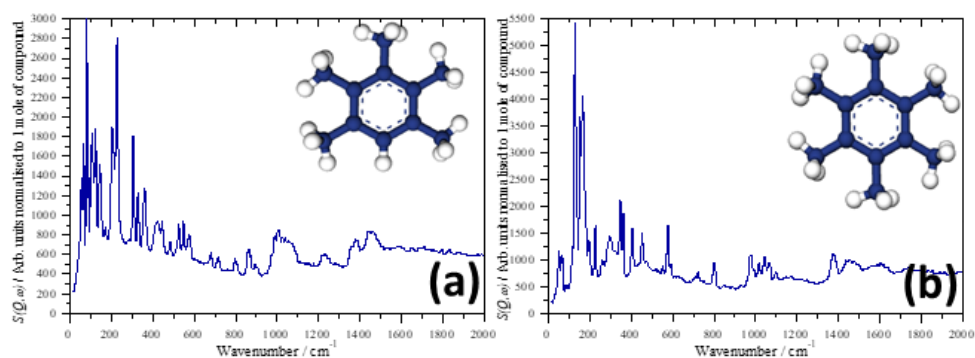


Figure 3.17: INS spectra collected via TOSCA of (a) pentamethylbenzene and (b) hexamethylbenzene

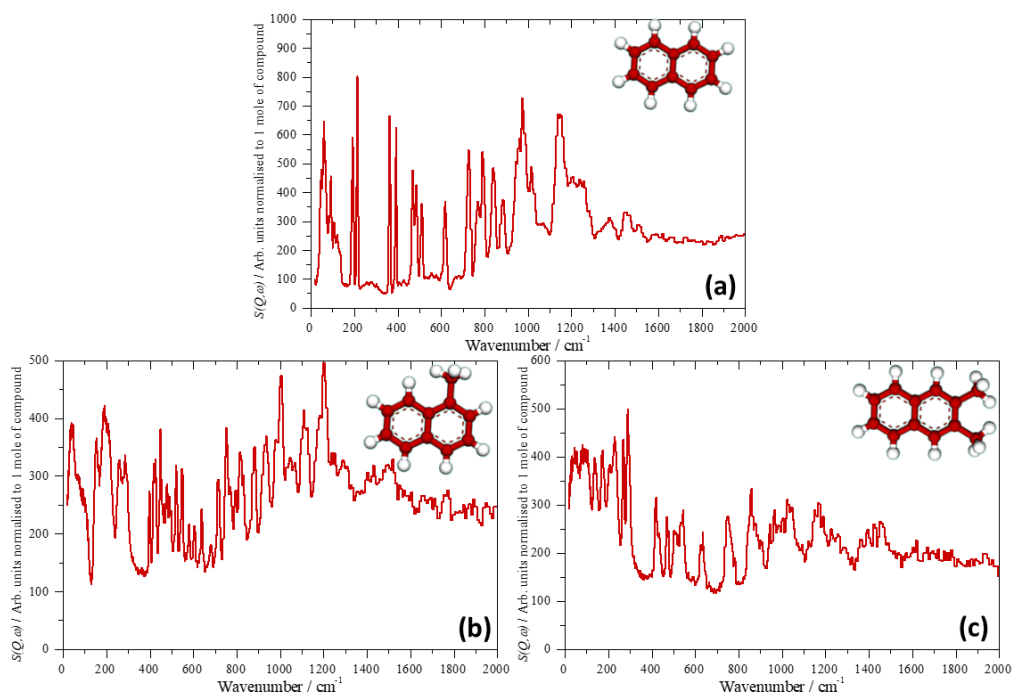


Figure 3.18: INS Spectra collected via TOSCA of naphthalenes: (a) naphthalene (b) 1-methylnaphthalene, (c) 2,3-dimethylnaphthalene

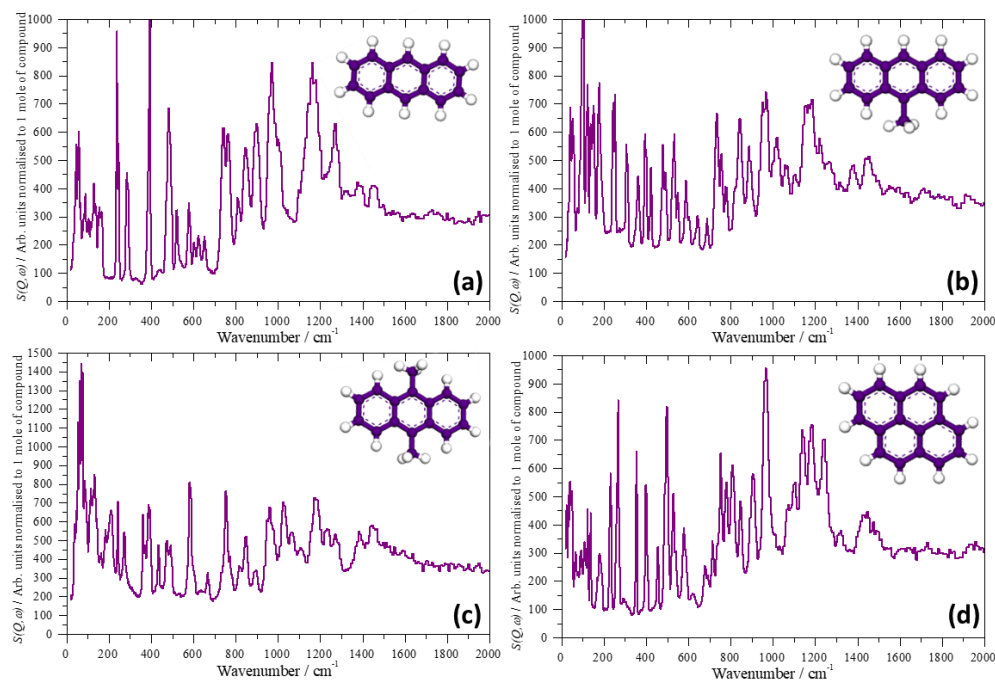


Figure 3.19: INS spectra collected via TOSCA of polycyclic aromatics: (a) anthracene (b) 9-methylanthracene, (c) 9,10-dimethylanthracene and (d) pyrene.

### 3.4.1 Methyl Rock and C-H Bending Modes

Figure 3.20 shows all the methyl benzenes in the region of 600 – 1600  $\text{cm}^{-1}$ , where the methyl rock and C-H bending modes are visible. The methyl rock, previously thought to be a distinguishable and recognisable mode usually found in the region of 800-1000  $\text{cm}^{-1}$ , is not easy to distinguish with INS for these

samples.<sup>58-60</sup> The C-H bending modes can be found at  $1375\text{ cm}^{-1}$  (symmetric C-H bend) and  $1445\text{ cm}^{-1}$  (asymmetric C-H bend). In toluene, the modes are almost invisible as is also the case in methylbenzenes with up to 3 methyl substitutions, although they are present, they are difficult to pick out. For methylbenzenes with 4 or more methyl substitutions (Figure 3.20 h-l), both C-H bending modes are clearly seen.

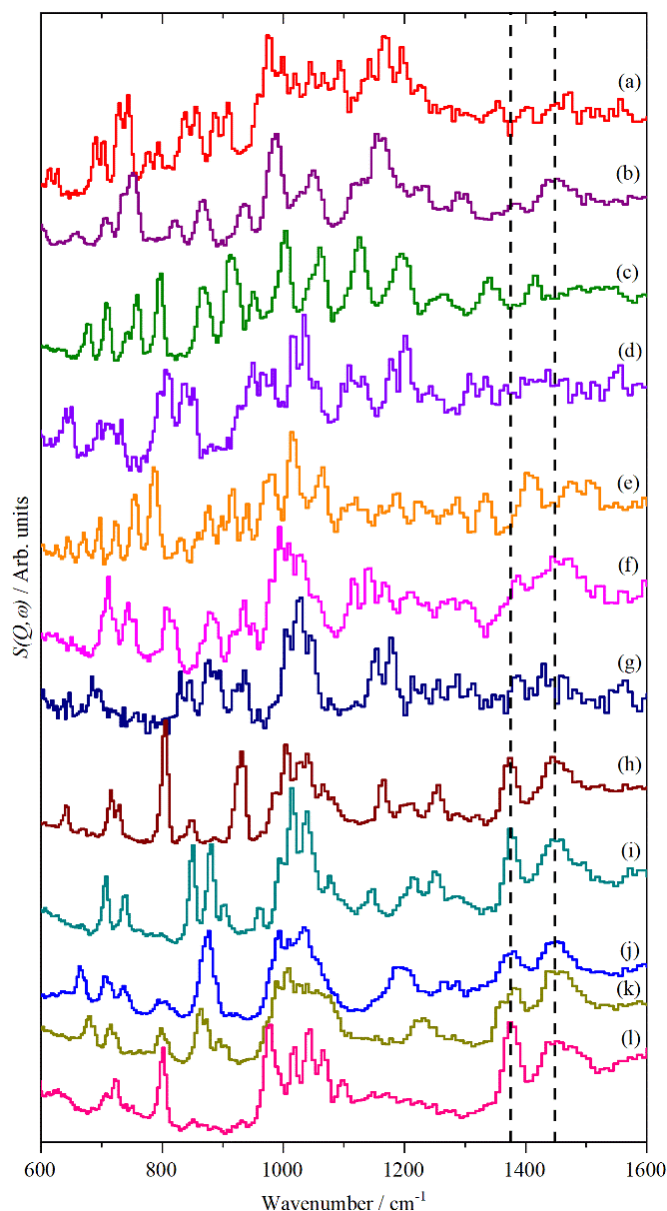


Figure 3. 20: INS spectra of methylated benzenes in the region of the methyl rock and the C-H bending modes. (a) Toluene (b) *m*-xylene (c) *o*-xylene (d) *p*-xylene (e) 1,2,3 trimethylbenzene (f) 1,2,4-trimethylbenzene (g) mesitylene (h) 1,2,3,4-tetramethylbenzene (i) 1,2,3,5-tetramethylbenzene (j) durene (k) pentamethylbenzene and (l) hexamethylbenzene. Vertical lines show position of the symmetric ( $1357\text{ cm}^{-1}$ ) and asymmetric ( $1445\text{ cm}^{-1}$ ) methyl C-H bending mode.

### 3.4.2 Computational Studies

To better understand these systems computational studies needed to be carried out. The studies focused on trying to assign the methyl torsion and were carried out and analysed by Professor Stewart F. Parker. As it was mentioned above, the methyl torsion mode is a mode that was always thought to be intense and easily recognisable. As was seen from the INS spectra in Figures 3.15-3.19, this is evidently not the case.

As all the molecules are uncharged and have either zero or near-zero dipole moment, it follows that in the solid state the dominant interactions are van der Waals forces. In these circumstances, it would be expected that isolated (*i.e.*, gas phase) molecule calculations should provide a good description of the system. To test this, hexamethylbenzene was used as a model system. Hexamethylbenzene was chosen because the solid state structure has only one molecule in the primitive cell.<sup>24</sup> Using CASTEP, different methods were used in order to simulate the INS spectra of hexamethylbenzene including both the isolated molecule and a periodic system calculation. All the simulated spectra were compared to the experimental spectrum. It was found that simulated spectra although they show good agreement with the higher wavenumbers, when it comes to the comparing the two in the region below 300  $\text{cm}^{-1}$ , the spectra differed greatly (Figure 3.21).

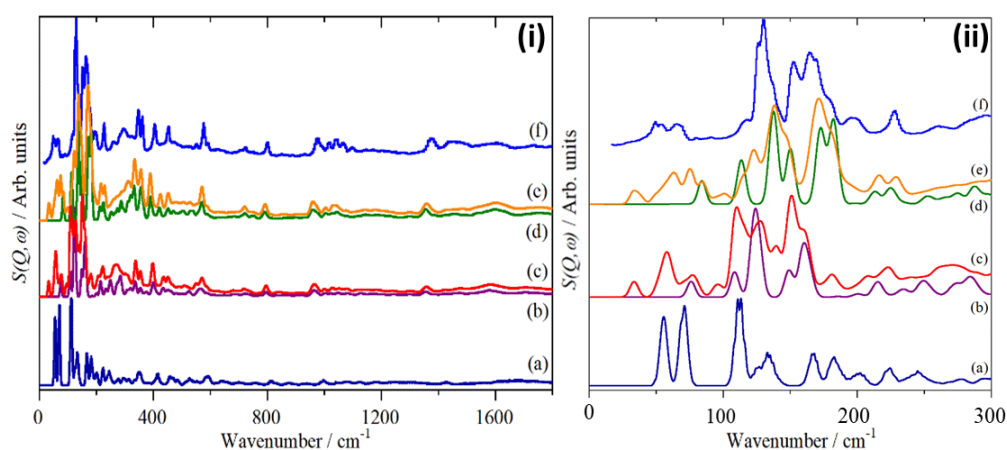


Figure 3.21: Comparison of observed and DFT calculated INS spectra of hexamethylbenzene. (i) 0 – 1800  $\text{cm}^{-1}$  and (ii) expanded view of the region containing the methyl torsions. (a) Isolated molecule (Gaussian), periodic-DFT (CASTEP) without the Tkatchenko and Scheffler correction (b) at the  $\Gamma$ -point only and (c) for the complete Brillouin zone, periodic-DFT (CASTEP) with the Tkatchenko and Scheffler correction (d) at the  $\Gamma$ -point only and (e) for the complete Brillouin zone, (f) experimental spectrum.

The absolute accuracy of density functional theory (DFT) calculations of vibrational transition energies for gas phase molecules has been extensively investigated.<sup>61–63</sup> For molecules with more than 10 or so atoms, the vibrational modes are usually accurate to around  $\pm 10 \text{ cm}^{-1}$  (typically they are underestimated). It is important to note that the errors are apparently random and are not a simple fraction of the transition energy. Therefore, assignments in the calculated modes of higher wavenumbers, although not the same as observed peaks, they are close enough that the error is negligible. However, as it has been observed above, the calculated modes present below  $300 \text{ cm}^{-1}$  where the methyl torsions are, have a relatively much larger error (around 10%), which makes the assignments ambiguous. Having that in mind, the same procedure was adopted for all calculations, with the structures being geometry optimised (with the Tkatchenko and Scheffler dispersion correction applied) at the experimental lattice parameters. The experimental and calculated methyl torsion energies can be found in Table 3.7. For some molecules the methyl torsion was unknown, therefore, the highest intensity modes in the low energy region of the spectra were assumed to be due to methyl torsions.

Table 3.8: The experimentally observed, the as-calculated at the Brillouin zone  $\Gamma$ -point (CASTEP) and for the isolated molecule (Gaussian), transition energies of the methyl torsion in unsaturated molecules. If known, the space group and number of the molecules in the primitive cell ( $Z$ ) is also given.

Compound	Methyl torsion transition energies / $\text{cm}^{-1}$			Space group	Z	Ref.
	Experimental	CASTEP	Gaussian			
<b>Methylated Benzenes</b>						
<b>Toluene</b>	47	112, 115, 116, 118, 119, 127, 127, 127	38	P2 <sub>1</sub> /c	4	<sup>17</sup>
<b>o-xylene</b>	147, 156, 178, 193	164, 168, 169, 174, 176, 184, 185, 195	130, 170	P2 <sub>1</sub> /a	4	<sup>18</sup>
<b>m-xylene</b>	56	114, 116, 119, 122, 124, 125, 130, 130, 130, 132, 136, 138, 139, 139, 140, 145	28,37	Pbca*	8	<sup>19</sup>
<b>p-xylene</b>	124, 133	102, 111, 118, 140	35,50	P2 <sub>1</sub> /n	2	<sup>19</sup>

<b>1,2,3-Trimethylbenzene</b>	186		72, 176, 186	Unknown		
<b>1,2,4-Trimethylbenzene</b>	175, 196		42, 138, 171	Unknown		
<b>1,3,5-Trimethylbenzene (mesitylene)</b>	151, 156	116, 116, 116, 120, 120, 122, 122, 122, 136, 148, 148, 148, 124, 132, 134, 137, 145, 145, 150, 152, 157, 175, 178, 180	238, 239, 239	$P\bar{1}$  P213*	4  4	<sup>20</sup>  <sup>20</sup>
<b>1,2,3,4-Tetramethylbenzene</b>	169, 200, 210, 218		61, 142, 192, 193	Unknown		
<b>1,2,3,5-Tetramethylbenzene</b>	178		19, 51, 178, 199	Unknown		
<b>1,2,4,5-Tetramethylbenzene (durene)</b>	148, 158, 167, 182, 195	148, 153, 167, 173, 173, 177, 197, 197	130, 132, 169, 197	P2 <sub>1</sub> /a	2	<sup>14</sup>
<b>Pentamethylbenzene</b>	81, 106, 124, 203, 210, 228	93, 97, 128, 132, 138, 139, 211, 225, 227, 229	23, 152, 156, 189, 208	$P\bar{1}$	2	<sup>15</sup>
<b>Hexamethylbenzene</b>	126, 130, 152, 165, 170, 179	137, 138, 150, 172, 173, 182	55, 70, 70, 111, 111, 113	$P\bar{1}$	1	<sup>21</sup>
<b>Methylated polycyclic aromatics</b>						
<b>1-Methylnaphthalene</b>	38		193	Unknown		
<b>2,3-Dimethylnaphthalene</b>	172, 228		144, 197	P2 <sub>1</sub> /c*	2	<sup>22</sup>
<b>9-Methylantracene</b>	102	88, 96, 99, 99	20	P2 <sub>1</sub> /c	4	<sup>23</sup>
<b>9,10-Dimethylantracene</b>	53, 60, 69, 73	100, 120, 122, 122	†	P2 <sub>1</sub> /c*	2	<sup>24</sup>

\*The space group probably does not correspond to the phase obtained.

†Unable to obtain all real modes.

### 3.4.1.1 Intra- Vs Intermolecular Effects

As was mentioned above, the number of methyl groups and if they are adjacent to each other, seems to affect the transition energy of the methyl torsion. It is therefore safe to assume that both intramolecular (the number of methyl groups present per benzene molecule) and intermolecular (the presence of neighbouring molecules either in the same unit cell or adjacent ones) could

have an effect in the transition energy of the methyl torsion. Using both CASTEP and Gaussian calculations, the average methyl torsion transition energy of hexamethylbenzene and mesitylene was compared against the changing of the shortest intermolecular distance (in all cases being the H...H contact) in Figure 3.19. The first point for both is the experimentally observed average methyl torsional energy, with the second point being the calculated average methyl torsion energy at 2.367 Å. The average methyl torsional energies were calculated using the plane-wave code CASTEP calculation. Both observed and experimental points match up, suggesting that the calculation is accurate enough for comparisons. The last point is calculated using Gaussian and is for an isolated molecule. For hexamethylbenzene, it follows the same trend as the CASTEP calculations suggesting that the Gaussian calculation can be treated as the limiting case. For mesitylene, however, the Gaussian calculation shows a steep increase in average methyl torsional energy. This is not expected and does not follow the trend of the hexamethylbenzene or of the mesitylene CASTEP calculations. As of yet, there is no explanation for this behaviour of mesitylene and more calculations might be needed to understand why the Gaussian calculation behaves anomalously.

The CASTEP trend observed in Figure 3.22, shows that after the first initial steep drop in the average methyl torsion energy from the intermolecular distance going from 2.367 Å to 4.256 Å, increasing the intermolecular distance further, shows negligible effects. This confirms that the intermolecular distance between molecules could have an effect in the methyl torsion energy.

Figure 3.23 shows the average methyl torsion transition energy of all methylbenzenes as a function of their methyl groups, comparing experimental values with calculation. The calculations are for an isolated molecule using Gaussian. In all cases (except mesitylene, labelled M in Figure 3.23), the presence of more methyl groups shows an overall increase, on the average methyl torsion energy. This effect seems to be dependent on the conformation of the methyl torsions as well, although it was not studied in detail here. The Gaussian calculations, as expected, are all lower than the experimental results. This is due to the calculation of an isolated molecule, whereas the experimental data are for the solid state and, as was discussed above, the closer the intermolecular distance, the higher the methyl torsion energy. The mesitylene calculation is the only one not following the trend. As was seen in Figure 3.19 and discussed above, the calculated methyl torsional energy is unusually high,

especially when compared to its experimental value and the trends observed in other methylbenzenes seen in Figure 3.22. Mesitylene will be treated as an anomaly for now until further examination of this takes place.

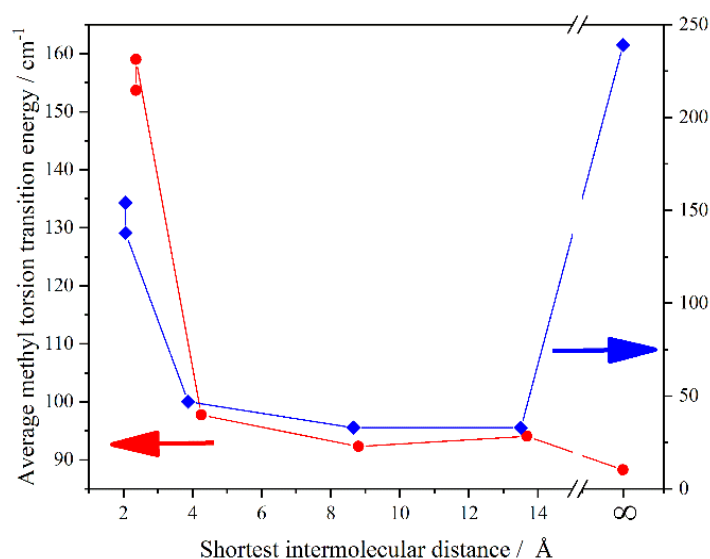


Figure 3.22: Comparison of the average methyl torsion transition energy of hexamethylbenzene (red dots, left x-axis) and mesitylene (blue diamonds, right x-axis) as a function of the shortest intermolecular contact. The first two points are the observed and calculated transition energies for the molecule at the experimental lattice parameters. The last point on the extreme right for both compounds is a Gaussian calculation for the isolated molecule. The solid lines are a guide to the eye.

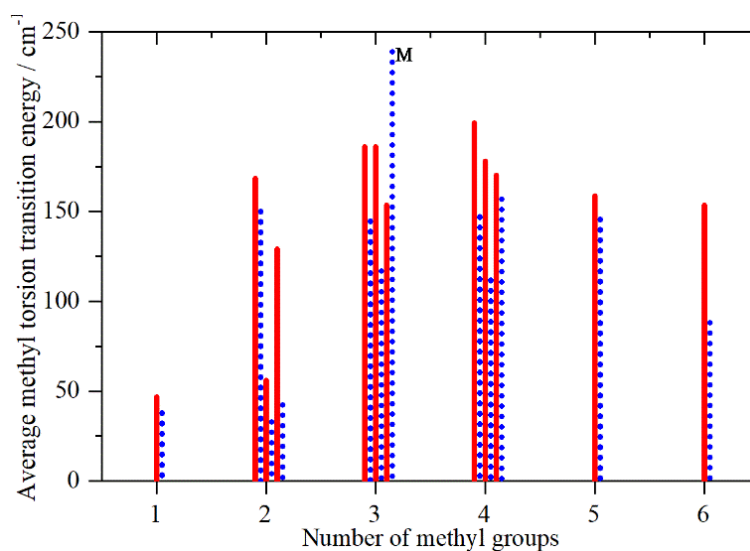


Figure 3.23: The average methyl torsion energy of methylbenzenes as a function of the number of methyl groups. The solid lines (red) are the experimental values) and the dotted lines (blue) are the Gaussian calculations of the isolated molecule. M is the calculated transition energy for mesitylene.

### 3.4.3 Summary

This section focused on studying a number of reference compounds relevant to the MTH reaction. This study was an integral part in being able to use INS and study the MTH reaction as it will be seen in the following chapters. The INS spectra of the reference compounds were key in identifying various features in the INS spectra of the retained hydrocarbons in MTH reacted zeolite samples, which is one of the main aims of the project.

From the preliminary INS studies completed on the MTH reaction,<sup>4,5</sup> a major question has been why isn't there a distinct methyl torsion peak present in the reacted samples. In this section, the methyl torsion of poly-methylated aromatics and polycyclic aromatic molecules has been studied. It was found that the methyl torsional energy is affected both by intra-molecular interactions (methyl substitutions within the same molecule) as well as inter-molecular interactions (how many molecules are close by). It was shown by a series of CASTEP calculations that increasing the methyl groups within the same molecule shows an increase in the methyl torsion energy and the same happens when the molecules are close together (at 2.367 Å). The methyl torsion energy seems to drop when the molecule distance is above 4 Å and there is negligible difference in the methyl torsion energy as the distance increases. This change in methyl torsion energy has not been observed before. It also explains why there was never an intense mode for the methyl torsions of the methylated hydrocarbons present within the zeolite matrix after an MTH reaction. This new awareness of the methyl torsion as well as having a library of INS spectra of the possible retained hydrocarbons within the zeolite has been an important milestone in understanding the INS spectra of MTH reacted zeolites.

## 3.5 Conclusions

This chapter focused on characterising the ZSM-5 catalyst which was used throughout the iCASE-1 and 2 projects. The Si:Al ratio of the ZSM-5 has been investigated with the average Si:Al ratio found to be close to 30. A quantification of the acid sites by INS has shown that there are 3.32 Brønsted acid sites per ZSM-5 unit cell. There is substantial extra framework Al present within the zeolite, with INS quantification showing it to be 1.1 per ZSM-5 unit cell and an increased presence being observed in both <sup>27</sup>Al-NMR and DRIFTS. This could

be a by-product of the calcination procedure, either before the zeolite was sent to us or during the calcination done before the zeolite was used. Neutron diffraction was attempted in order to find the location of the protons, however, problems with refinement of the data meant that the data were not analysed before this chapter was written. Analysis at the University of Aberdeen is ongoing.

The chapter also focused on the collection and analysis of the possible hydrocarbon pool products using INS. The library of INS data will be used in later chapters of the thesis. Some computer calculations using CASTEP and Gaussian were completed in order to understand what is happening to the methyl torsion peaks. It was found that the methyl torsion transition energy is affected by both the intermolecular distance between molecules, but also by the intramolecular distance between the methyl groups in the same molecule. An increased number of methyl groups also increased the average methyl torsion transition energy

### 3.6 References

- 1 W. Widayat and A. N. Annisa, in *IOP Conference Series: Materials Science and Engineering*, 2017, vol. 214, p. 012032.
- 2 J. H. C. van Hooff and J. W. Roelofsen, *Stud. Surf. Sci. Catal.*, 1991, **58**, 241–283.
- 3 P. C. H. Mitchell, S. F. Parker, A. J. Ramirez-Cuesta and J. Tomkinson, *Vibrational spectroscopy with neutrons with applications in chemistry*, World Scientific, Singapore, 2005.
- 4 Suwardiyanto, R. F. Howe, R. C. A. Catlow, E. K. Gibson, A. Hameed, J. McGregor, P. Collier, S. F. Parker and D. Lennon, *Faraday Discuss.*, 2017, **197**, 447–472.
- 5 R. F. Howe, J. McGregor, S. F. Parker, P. Collier and D. Lennon, *Catal. Letters*, 2016, **146**, 1242–1248.
- 6 B. F. Mentzen, *J. Phys. Chem. C*, 2007, **111**, 18932–18941.
- 7 M. T. Aronson, R. J. Gorte and W. E. Farneth, *J. Catal.*, 1987, **105**, 455–468.
- 8 B. Louis, S. Walspurger and J. Sommer, *Catal. Letters*, 2004, **93**, 81–

- 84.
- 9 S. F. Parker, F. Fernandez-Alonso, A. J. Ramirez-Cuesta, J. Tomkinson, S. Rudic, R. S. Pinna, G. Gorini and J. Fernández Castañón, in *Journal of Physics: Conference Series*, IOP Publishing, 2014, vol. 554, p. 012003.
- 10 M. J. Frisch, G. W. Trucks, H. B. Schlegel, G. E. Scuseria, M. A. Robb, J. R. Cheeseman, G. Scalmani, V. Barone, G. A. Petersson, H. Nakatsuji, X. Li, M. Caricato, A. Marenich, J. Bloino, B. G. Janesko, R. Gomperts, B. Mennucci, H. P. Hratchian, J. V. Ortiz, A. F. Izmaylov, J. L. Sonnenberg, D. Williams-Young, F. Ding, F. Lipparini, F. Egidi, J. Goings, B. Peng, A. Petrone, T. Henderson, D. Ranasinghe, V. G. Zakrzewski, J. Gao, N. Rega, G. Zheng, W. Liang, M. Hada, M. Ehara, K. Toyota, R. Fukuda, J. Hasegawa, M. Ishida, T. Nakajima, Y. Honda, O. Kitao, H. Nakai, T. Vreven, K. Throssell, J. Montgomery, J. A., J. E. Peralta, F. Ogliaro, M. Bearpark, J. J. Heyd, E. Brothers, K. N. Kudin, V. N. Staroverov, T. Keith, R. Kobayashi, J. Normand, K. Raghavachari, A. Rendell, J. C. Burant, S. S. Iyengar, J. Tomasi, M. Cossi, J. M. Millam, M. Klene, C. Adamo, R. Cammi, J. W. Ochterski, R. L. Martin, K. Morokuma, O. Farkas, J. B. Foresman and D. J. Fox, <http://www.gaussian.com/>, 2004.
- 11 S. J. Clark, M. D. Segall, C. J. Pickard, P. J. Hasnip, M. I. J. Probert, K. Refson and M. C. Payne, *Zeitschrift fur Krist.*, 2005, **220**, 567–570.
- 12 J. P. Perdew, K. Burke and M. Ernzerhof, *Phys. Rev. Lett.*, 1996, **77**, 3865–3868.
- 13 A. Tkatchenko and M. Scheffler, *Phys. Rev. Lett.*, 2009, **102**, 073005.
- 14 K. Refson, P. R. Tulip and S. J. Clark, *Phys. Rev. B - Condens. Matter Mater. Phys.*, 2006, **73**, 155114.
- 15 C. R. Groom, I. J. Bruno, M. P. Lightfoot and S. C. Ward, *Acta Crystallogr. Sect. B Struct. Sci. Cryst. Eng. Mater.*, 2016, **72**, 171–179.
- 16 A. J. Ramirez-Cuesta, *Comput. Phys. Commun.*, 2004, **157**, 226–238.
- 17 K. Dymkowski, S. F. Parker, F. Fernandez-Alonso and S. Mukhopadhyay, *Phys. B Condens. Matter*, 2018, **551**, 443–448.

- 18 R. M. Ibberson, W. I. F. David and M. Prager, *J. Chem. Soc. Chem. Commun.*, 1992, 1438–1439.
- 19 R. M. Ibberson, C. Morrison and M. Prager, *Chem. Commun.*, 2000, **0**, 539–540.
- 20 R. M. Ibberson, W. I. F. David, S. Parsons, M. Prager and K. Shankland, *J. Mol. Struct.*, 2000, **524**, 121–128.
- 21 R. M. Ibberson, S. Parsons, I. Natkaniec and K. Holderna-Natkaniec, in *Tenth European Powder Diffraction Conference*, Oldenbourg Wissenschaftsverlag, 2015, pp. 575–580.
- 22 M. A. Neumann, M. R. Johnson, P. G. Radaelli, H. P. Trommsdorff and S. F. Parker, *J. Chem. Phys.*, 1999, **110**, 516–527.
- 23 M. Mudge, B. K. Ng, C. J. Onie, M. Bhadbhade, R. A. Mole, K. C. Rule, A. P. J. Stampfl and J. A. Stride, *ChemPhysChem*, 2014, **15**, 3776–3781.
- 24 J. A. Stride, *Acta Crystallogr. Sect. B Struct. Sci.*, 2005, **61**, 200–206.
- 25 A. F. Mabied, M. Müller, R. E. Dinnebier, S. Nozawa, M. Hoshino, A. Tomita, T. Sato and S. I. Adachi, *Acta Crystallogr. Sect. B Struct. Sci.*, 2012, **68**, 424–430.
- 26 B. Marciniak, *Acta Crystallogr. Sect. E Struct. Reports Online*, 2007, **63**, o3183–o3183.
- 27 D. P. Serrano, R. A. García, M. Linares and B. Gil, in *Catalysis Today*, Elsevier, 2012, vol. 179, pp. 91–101.
- 28 D. P. Serrano, R. A. García, G. Vicente, M. Linares, D. Procházková and J. Čejka, *J. Catal.*, 2011, **279**, 366–380.
- 29 P. J. Kunkeler, B. J. Zuurdeeg, J. C. Van Der Waal, J. A. Van Bokhoven, D. C. Koningsberger and H. Van Bekkum, *Zeolite Beta: The Relationship between Calcination Procedure, Aluminum Configuration, and Lewis Acidity*, 1998, vol. 180.
- 30 L. Shirazi, E. Jamshidi and M. R. Ghasemi, *Cryst. Res. Technol.*, 2008, **43**, 1300–1306.
- 31 A. Zecchina, G. Spoto and S. Bordiga, *Phys. Chem. Chem. Phys.*, 2005,

- 7, 1627–1642.
- 32 U. Olsbye, S. Svelle, K. P. Lillerud, Z. H. Wei, Y. Y. Chen, J. F. Li, J. G. Wang and W. B. Fan, *Chem. Soc. Rev.*, 2015, **44**, 7155–7176.
- 33 J. C. Jansen, F. J. van der Gaag and H. van Bekkum, *Zeolites*, 1984, **4**, 369–372.
- 34 M. A. Ali, B. Bridson and W. J. Thomas, *Appl. Catal. A Gen.*, 2003, **252**, 149–162.
- 35 P. A. Jacobs and R. Von Ballmoos, *J. Phys. Chem*, 1982, **86**, 3050–3052.
- 36 L. Kubelková, J. Nováková and K. Nedomová, *J. Catal.*, 1990, **124**, 441–450.
- 37 S. M. Campbell, D. M. Bibby, J. M. Coddington, R. F. Howe and R. H. Meinhold, *J. Catal.*, 1996, **161**, 338–349.
- 38 J. C. Vedrine, A. Auroux and G. Coudurier, in *ACS Symposium Series*, 1984, pp. 254–273.
- 39 H. Robson and K. P. Lillerud, *Verified Synthesis of Zeolitic Materials*, Elsevier, 2nd Editio., 2001.
- 40 N. Mohan and L. Cindrella, *Mater. Sci. Semicond. Process.*, 2015, **40**, 361–368.
- 41 Y. Cheng, L. J. Wang, J. S. Li, Y. C. Yang and X. Y. Sun, *Mater. Lett.*, 2005, **59**, 3427–3430.
- 42 W. J. Rohrbaugh and E. L. Wu, in *Characterization and Catalyst Development. ACS Symposium Series*, ACS Symposium Series, 1989, pp. 279–302.
- 43 A. Araya and B. M. Lowe, *Zeolites*, 1986, **6**, 111–118.
- 44 C. A. Fyfe, Y. Feng, H. Grondy, G. T. Kokotailo and H. Gies, *Chem. Rev.*, 1991, **91**, 1525–1543.
- 45 A. P. Hawkins, A. Zachariou, P. Collier, R. A. Ewings, R. F. Howe, S. F. Parker and D. Lennon, *RSC Adv.*, 2019, **9**, 18785–18790.
- 46 C. S. Triantafillidis, A. G. Vlessidis, L. Nalbandian and N. P. Evmiridis,

- Microporous Mesoporous Mater.*, 2001, **47**, 369–388.
- 47 W. E. Farneth and R. J. Gorte, *Chem. Rev.*, 1995, **95**, 615–635.
- 48 D. M. Bibby, R. F. Howe and G. D. McLellan, *Appl. Catal. A, Gen.*, 1992, **93**, 1–34.
- 49 L. Damjanović and A. Auroux, in *Zeolite Characterization and Catalysis: A Tutorial*, 2010, pp. 107–167.
- 50 M. Czjzek, H. Jobic, A. N. Fitch and T. Vogt, *J. Phys. Chem*, 1992, **96**, 1535–1540.
- 51 B. H. Toby and R. B. Von Dreele, *J. Appl. Crystallogr.*, 2013, **46**, 544–549.
- 52 N. Y. Topsøe, K. Pedersen and E. G. Derouane, *J. Catal.*, 1981, **70**, 41–52.
- 53 G. J. Kearley, M. R. Johnson and J. Tomkinson, *J. Chem. Phys.*, 2006, **124**, 1442.
- 54 I. Natkaniec, K. Holderna-Natkaniec and J. Kalus, in *Physica B: Condensed Matter*, North-Holland, 2004, vol. 350, pp. E651–E653.
- 55 J. Kalus, J. Wolfrum, F. Wörlen, M. Monkenbusch, M. Prager and I. Natkaniec, *Mol. Cryst. Liq. Cryst. Sci. Technol. Sect. A. Mol. Cryst. Liq. Cryst.*, 1995, **268**, 1–20.
- 56 M. Prager, H. Grimm and I. Natkaniec, *Phys. Chem. Chem. Phys.*, 2005, **7**, 2587–2593.
- 57 J. A. Stride, J. M. Adams and M. R. Johnson, in *Chemical Physics*, North-Holland, 2005, vol. 317, pp. 143–152.
- 58 D. Lin-Vien, N. B. Colthup, W. G. Fateley and J. G. Grasselli, *The Handbook of Infrared and Raman Characteristic Frequencies of Organic Molecules*, 1991.
- 59 L. J. Bellamy, *The Infra-red Spectra of Complex Molecules*, Springer Netherlands, Dordrecht, Third., 1975, vol. 1.
- 60 N. B. Colthup, L. H. Daly and S. E. Wiberley, *Introduction to Infrared and Raman Spectroscopy*, Academic Press Inc London, Third., 1990.

- 61 A. P. Scott and L. Radom, *J. Phys. Chem.*, 1996, **100**, 16502–16513.
- 62 C. Qu and J. M. Bowman, *Phys. Chem. Chem. Phys.*, 2019, 21, 3397–3413.
- 63 C. Puzzarini, J. Bloino, N. Tasinato and V. Barone, *Accuracy and Interpretability: The Devil and the Holy Grail. New Routes across Old Boundaries in Computational Spectroscopy*, American Chemical Society, 2019, vol. 119.

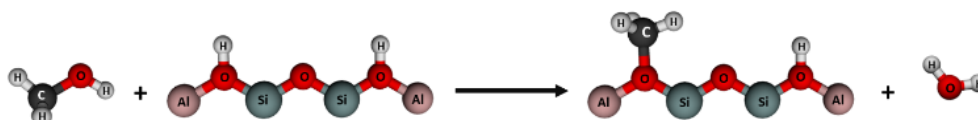
# Chapter 4

## Interactions of Methanol in ZSM-5

This chapter will focus on looking at the interactions of methanol in ZSM-5, predominantly what happens to methanol in ZSM-5 at room temperature. The ssNMR work presented in this chapter has been completed in collaboration with Dr. Nathan Barrow and Dr. Jonathan Bradley at Johnson Matthey Sonning Common.

### 4.1 Introduction

The interaction between methanol and acidic zeolite catalysts is important because of its relevance to Methanol-to-Hydrocarbons (MTH) technology. It is generally accepted that the first step of MTH, is the reaction of methanol with the zeolite's Brønsted sites to generate methoxy species, as shown in Scheme 4.1.<sup>1-3</sup> The methanol loses its OH functionality upon the interaction with the acid site, producing a surface-bound methoxy and water.



Scheme 4.1: Schematic of methoxylation reaction occurring when methanol is introduced into an acidic zeolite catalyst.

Forester and Howe<sup>3</sup> carried out an *in-situ* FTIR study of methanol in ZSM-5. At room temperature, the spectra showed only bands characteristic of hydrogen bonded species. Pulsing methanol under flowing helium at temperatures above 373 K showed methoxylation of the acid sites, revealed by loss of the zeolite  $\nu(\text{OH})$  band and appearance of new bands in the CH stretching and bending regions.<sup>3</sup> The room temperature interaction of methanol with HZSM-5 was subsequently studied in more detail by Zecchina et al.<sup>4</sup> The infrared spectra varied with the methanol loading; at low loadings (< 1 molecule per acid site) hydrogen bonding of individual methanol molecules to zeolite OH groups was observed. This assignment was based on the appearance of an ABC triplet

caused by the interaction of the broad OH stretching mode of the hydrogen bonded zeolite OH groups by Fermi resonance with overtones of the in plane and out of plane OH bending modes.<sup>4-6</sup> At higher coverages, they reported the formation of protonated clusters of methanol through complete proton transfer from the OH groups.

In contrast, a more recent study on methanol interaction on both ZSM-5 and HY using inelastic neutron scattering (INS) spectroscopy and quasielastic neutron scattering (QENS) reported complete methanol dissociation to methoxy species at room temperature on HZSM-5.<sup>7</sup> Methanol was dosed on the dehydrated zeolite at room temperature under He flow. The QENS spectra of the dosed ZSM-5 showed no broadening of the elastic peak suggesting no movement in the zeolite framework, which was contrasted with a dosed HY sample where significant broadening was observed.<sup>7</sup> The INS spectra of the dosed ZSM-5 showed no deformation or stretching modes of zeolite or methanol OH groups, whereas in HY both stretching and deformation modes of OH groups were detected, consistent with hydrogen bonding of methanol. Similar QENS evidence for lack of mobility at room temperature on the QENS time scale was later reported for methanol in both a fresh HZSM-5 catalyst and one used in an MTH reactor for three days at 623 K.<sup>8</sup> Very recently a more detailed QENS study has looked at the behaviour of methanol in HZSM-5 as a function of temperature and the aluminium content of the zeolite.<sup>9</sup> According to this study the fraction of immobile methanol depends on both temperature and the number of acid sites in the zeolite.

A DRIFTS study by S.K. Matam et al. has suggested that it is possible to see formation of methoxy groups from methanol in HZSM-5 at room temperature by infrared spectroscopy, although the methoxy bands are difficult to distinguish due to the intense ABC structure of the hydrogen bonded methanol.<sup>10</sup> The same group recently showed in a separate study using a combination of DRIFTS and computational modelling that room temperature methoxylation is methanol loading dependent, finding that methoxylation at room temperature does not occur at loadings of less than one mole of methanol per acid site.<sup>11</sup>

In this chapter, it was attempted to rationalise the apparently contradictory results obtained from the different forms of spectroscopy by applying a

combination of techniques (INS, DRIFTS and solid state NMR (ssNMR)) to look at methanol in the same ZSM-5 zeolite.

## 4.2 Experimental

The ZSM-5 zeolite was provided in powder form by Johnson Matthey and it is the same ZSM-5 catalyst that will be used throughout the thesis. Its characterisation can be found in chapter 3.

Prior to use the zeolite was calcined at 500 °C for 12 hours under static air. Prior to methanol adsorption the catalyst was dried at 350 °C under flowing He (100 ml min<sup>-1</sup>). The INS experiments used the TOSCA and MAPS spectrometers with the same procedures as outlined in Chapter 2, Section 2.1.2.3. The DRIFTS experimental set up has been described in Section 2.2.1.1. The ss-NMR experiments were carried out using two spectrometers: a Bruker Avance III (400 MHz) Fourier transform NMR spectrometer and a Bruker Avance Neo (600 MHz) NMR spectrometer. Both NMR instruments are located at the Johnson Matthey Technology Centre at Sonning Common (UK). The <sup>13</sup>C-NMR experiment used the HPDEC pulse sequence which does not rely on cross-polarisation and is therefore quantitative. The INS spectra were recorded below 20 K, the infrared and ss-NMR spectra were recorded at room temperature.

### 4.2.1 Microreactor Catalyst Testing

The microreactor set up is described in Chapter 2, Section 2.3.2 with a bed length of 1 cm and a zeolite weight of 0.5 g. Two reactions were done, one at room temperature and one at 350 °C (which is the temperature most commonly used for the Methanol-to-Hydrocarbons reaction<sup>12,13</sup>). The reaction products were monitored by a GC-FID (Shimadzu GC-2014, BP-20 column).

The room temperature reaction used the same experimental conditions for 26 hours with the products monitored by GC-FID. A shorter room temperature reaction was also carried out using a portable mass spectrometer (ESS-EcoCat-II) for monitoring the outlet gases. The mass spectrometer was attached to the reactor outlet to monitor the exhaust gases instead of the GC-FID.

### 4.2.2 Flow Dosed Methanol Experiments

The dried ZSM-5 was transferred to a flat aluminium gas handling cell in an argon filled glovebox, to prevent exposure to moisture. For flow dosed samples, the methanol dosing used a Dreschel bottle maintained at room temperature and with  $1.1 \text{ L min}^{-1}$  He flow as the carrier gas. For the flow dosed (FD) samples both  $\text{CH}_3\text{OH}$  (Sigma Aldrich, 99.8% anhydrous) and  $\text{CD}_3\text{OH}$  (Sigma Aldrich, 99.7 atom% D) were used as well as  $^{13}\text{CH}_3\text{OH}$  (Sigma Aldrich, 99 atom%  $^{13}\text{C}$ ). All of these samples were analysed by INS. The aluminium flat gas handling cans used for the flow dosed samples are compatible with use inside the INS spectrometer, therefore no transfer of sample was needed. The FD- $^{13}\text{CH}_3\text{OH}$  sample was also analysed by DRIFTS and ss-NMR using the 600 MHz spectrometer. The FD- $^{13}\text{CH}_3\text{OH}$  sample was dosed with a mixture of 14 wt%  $^{13}\text{C}$ -methanol in  $^{12}\text{C}$ -methanol. For the DRIFTS experiment, the Harrick cell dome reactor was charged with the post-reaction catalyst sample inside an argon filled glove box, before being transferred to the spectrometer. For the ss-NMR experiments, the ss-NMR rotor was packed inside the glove box and sealed in an airtight container before being transferred to the spectrometer.

### 4.2.3 Static Dosed Methanol Experiments

1 ml of methanol was injected onto ~10 g of dried ZSM-5. The zeolite was then sealed in a desiccator with a methanol saturated atmosphere at room temperature for a period of 70 hours. The sample was then transferred to an Al flat can and the INS spectrum collected with both TOSCA and MAPS spectrometers. For the ss-NMR static dosed experiments, the ZSM-5 was dried under vacuum and dosed with  $^{13}\text{C}$  enriched methanol via syringe injection. Two different loadings were chosen: (i)  $6.6 \mu\text{l}$  methanol ( $23.8 \text{ mol}_{\text{MeOH}}/\text{mol}_{\text{ZSM-5}}$ ), which is comparable to the loading concentration used for the INS experiments and (ii)  $1.2 \mu\text{l}$  ( $3 \text{ mol}_{\text{MeOH}}/\text{mol}_{\text{ZSM-5}}$ ), which is comparable to conditions used in infrared experiments by Campbell et al.<sup>23</sup>  $^{13}\text{C}$ -NMR and  $^1\text{H}$ -NMR spectra were recorded for both samples. The  $6.6 \mu\text{l}$  dosed sample was left sealed for an extra 1.5 hours before collecting another set of  $^{13}\text{C}$ -NMR and  $^1\text{H}$ -NMR spectra in order to observe any changes with time, then heated to  $150 \text{ }^\circ\text{C}$  to observe partial methoxylation.

### 4.2.4 Exchanged Methanol Experiments

The dried zeolite was loaded into an aluminium gas handling cell in an argon filled glovebox as above. The CH<sub>3</sub>OD (Sigma Aldrich, 99.5 atom% D) was loaded on the zeolite in the same way as the flow dosed samples to a level of 15.3 mol<sub>CH<sub>3</sub>OD</sub>/mol<sub>ZSM<sub>5</sub></sub>, as determined gravimetrically. The sample was analysed using the MAPS spectrometer. It was then dosed with CH<sub>3</sub>OH (Sigma Aldrich, 99.8% anhydrous) in order to exchange the OD with the OH until saturation was reached, achieving a new loading of 15.7 mol<sub>MeOH</sub>/mol<sub>ZSM<sub>5</sub></sub>, and returned to the MAPS spectrometer for collection of a post-exchange spectrum.

### 4.2.5 In-situ experiments

DRIFTS was used for the flow dosed in-situ experiments of methanol loaded ZSM-5. The ZSM-5 was dried in-situ, using liquid nitrogen boil-off as the inert gas flow in order to minimise introduced moisture and hence avoid re-hydrating the zeolite. Methanol was then introduced into the system via manual injections through a septum into the inlet gas stream at 25 °C and spectra were recorded both before and after the injections were made. The ZSM-5 was heated gradually at 5 °C min<sup>-1</sup> to 200 °C in order to induce methoxylation before being cooled down to room temperature. A second set of injections were made at room temperature on the same sample.

## 4.3 Evidence For and Against Methoxylation

### 4.3.1 Microreactor Catalyst Testing

The 350 °C reaction behaved like any other MTH reaction with the products ranging from light olefins to methylated aromatics, as is seen in Figure 4.1. Figure 4.1.a shows the product distribution over the period of 26 hours, which shows the propene production to slowly decrease, whilst trimethylbenzenes and tetramethylbenzenes increase with time-on-stream. The cumulative concentrations are found in Figure 4.1.b, this shows all products created over the course of the reaction, and shows that the ZSM-5 catalyst acts as a normal MTH catalyst.

A room temperature 'reaction' was also carried out with the same reaction conditions as the 350 °C MTH reaction with the exception of the temperature.

The methanol conversion of both reactions can be seen in Figure 4.2. The 350 °C reaction shows a high conversion of methanol, with the conversion remaining at 100% for most of the time-on-stream and ending around 80% conversion towards the end of the reaction. The room temperature reaction, shows a sudden increase in methanol conversion on the second GC sampling point around 10 mins since the start of reaction. Then it slowly drops to zero where it pretty much remains for the duration of the reaction. With the GC-FID, it is not possible to monitor water production, therefore the sudden increase in methanol conversion, could simply be the methanol uptake (adsorption) from the ZSM-5 rather than methoxylation.

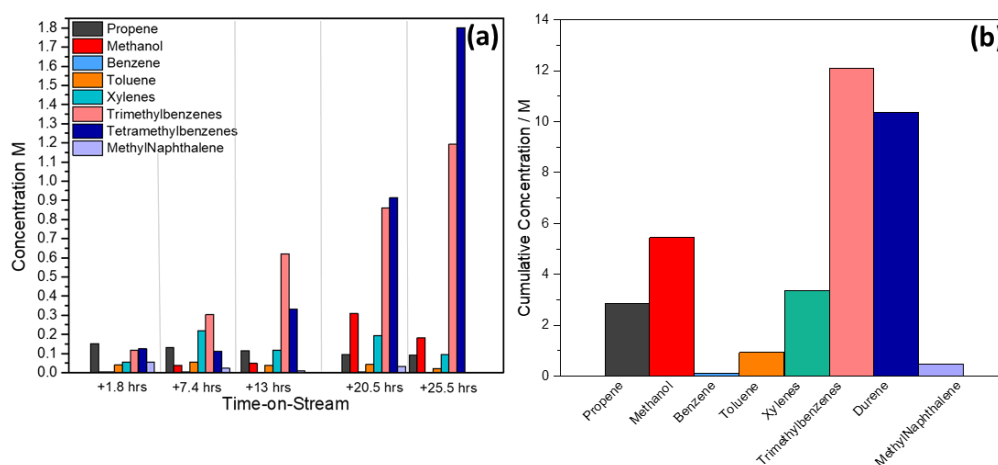


Figure 4.1: Product composition of MTH reaction completed at 350°C. (a) Product composition at 5 different times-on-stream (b) Cumulative concentration for the overall reaction

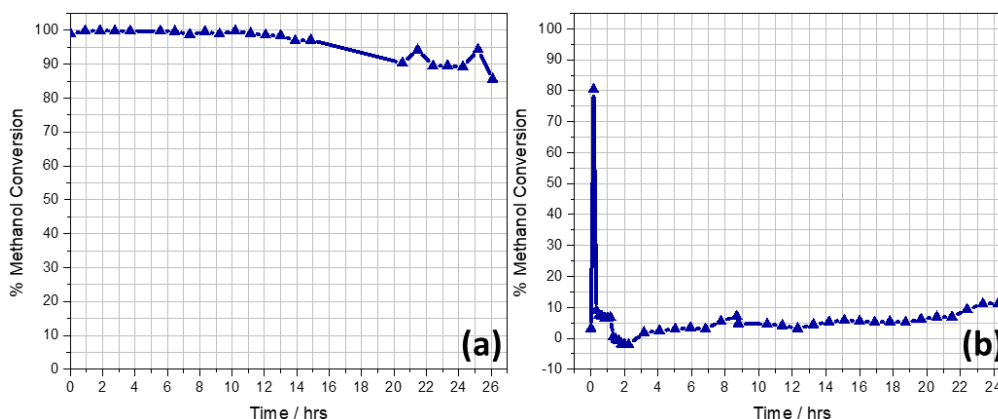


Figure 4.2: Methanol percentage conversions using GC-FID. (a) MTH over ZSM-5 at 350 °C (b) Methanol over ZSM-5 at room temperature (30 °C)

Two identical reactions were completed at room temperature, where one used GC-FID and the other used the mass spectrometer. No products were detected either by GC-FID or with the mass spectrometer. The mass spectrometer was

added in order to see if any water was produced at the beginning of the reaction when the methanol conversion at room temperature jumped to 80%. Figure 4.3 shows the mass spectrometer profile of the first five hours of reaction. When the methanol feed is switched from bypass to go through the ZSM-5 sample, both signals for methanol and water seem to drop for a period of approximately 30 minutes before increasing and stabilising again. This shows that the 80% conversion noted with the GC-FID is most probably due to methanol uptake by the zeolite, rather than methanol converting into methoxy. Methoxylation could, of course, still be taking place but at such small amounts that the mass spectrometer might not be sensitive enough to detect the water produced. No DME was observed in the product stream at all.

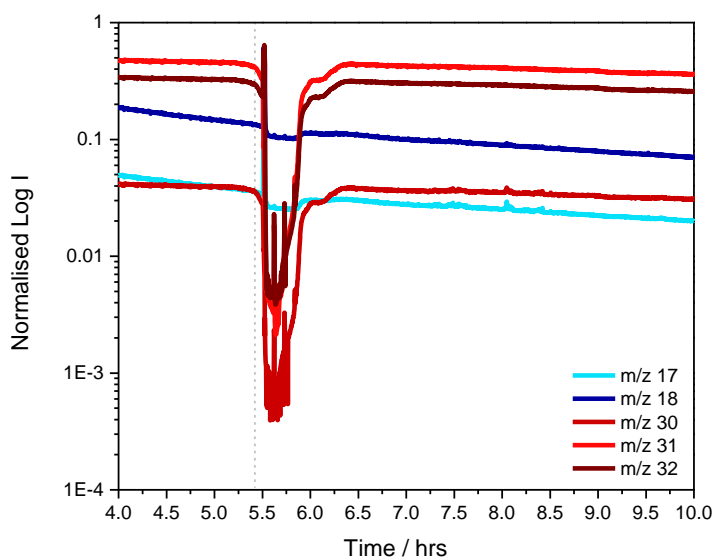


Figure 4.3: Mass spectrometer profile of the outlet gas from the reactor for methanol over ZSM-5 at room temperature. The dotted line shows when the methanol feed was switched from the bypass of the reactor to go through the ZSM-5 sample.  $m/z$  17 and  $m/z$  18 were used to monitor water and  $m/z$  30,  $m/z$  31 and  $m/z$  32 were used to monitor methanol.

### 4.3.2 INS

The quantity of sample required for INS experiments limits the ways in which room temperature dosing can be done. Flow dosing the methanol via a Dreschel bottle is the simplest way to load the methanol onto the dried zeolite in an INS-compatible flow-through cell. Figure 4.4 shows a comparison of solid methanol reference spectra obtained by both TOSCA and MAPS, as well as the spectra of the methanol dosed on ZSM-5 with the ZSM-5 contribution subtracted (FD-MeOH). The characteristic OH-related modes of methanol are the stretch above  $3200\text{ cm}^{-1}$  and the OH deformations at  $700\text{ cm}^{-1}$  and  $780\text{ cm}^{-1}$ .

<sup>1</sup> (there is more than one mode because there are four molecules in the primitive cell of methanol)<sup>14</sup>. In contrast, the FD-MeOH appears to have lost the OH functionality; neither the OH stretch or deformations are present. The spectra are in complete agreement with those previously reported by O'Malley *et al.* in an INS and QENS study of methanol in a different ZSM-5 zeolite.<sup>7</sup> The loss of the OH functionality is indeed consistent with room temperature methoxylation.

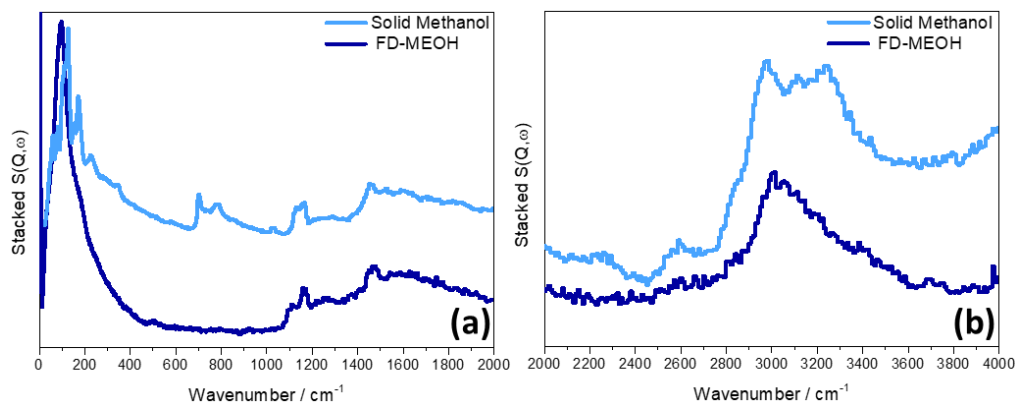


Figure 4.4: Solid methanol (light blue), flow dosed methanol on ZSM-5 at room temperature (FD-MEOH) (blue) collected with (a) TOSCA (b) MAPS (A-chopper, incident energy of 5244 cm<sup>-1</sup>)

### 4.3.3 DRIFTS

DRIFTS spectra were collected for the dried ZSM-5, after the injection of methanol (6 injections of 2 μl methanol over 20 minutes) at room temperature and during flushing with inert gas for 60 minutes. Figure 4.4.a shows the spectra of the blank ZSM-5, after methanol was injected and then flushed for 60 minutes under a fast flow rate. The spectrum recorded on initial injection of methanol closely resembles that assigned by Zecchina *et al.* to a mixture of protonated methanol clusters and single methanol molecules hydrogen bonded to zeolite OH groups.<sup>4</sup> The spectra are dominated by the ABC triplet of hydrogen bonded methanol and a broad continuum beginning around 3300 cm<sup>-1</sup>.

The difference spectra (i.e. the dried, bare zeolite used as the background spectrum) are shown in Figure 4.6 with detailed views of the acid, CH and CO regions seen in Figure 4.6.b, c and d. As seen in Figure 4.6.b, methanol interacts with all three types of zeolite OH groups (silanol groups, extra-framework AlOH, and Brønsted acid sites). On flushing at room temperature the broad OH band at ~ 3300 cm<sup>-1</sup> is removed and there is an obvious upwards

shift in the highest frequency  $\nu(\text{CH})$  band (Figure 4.6.c); the spectrum after flushing for 60 minutes closely resembles that assigned by Zecchina et al. to single methanol molecules hydrogen bonded to zeolite OH groups.<sup>4</sup> The changes on flushing are those expected for reducing the amount of adsorbed methanol.

In the initial spectrum, methanol vapour is still present in the Harrick cell, as the PQR peaks of methanol vapour are seen at  $1000\text{ cm}^{-1}$ – $1100\text{ cm}^{-1}$ . These bands disappear under nitrogen flow, as expected. Matam et al., commented on the PQR peak disappearing and a new peak at  $1004\text{ cm}^{-1}$  for the C-O stretch of methoxy appearing.<sup>10</sup> This was not observed in the spectra in Figure 4.6. However, it must be noted that the difference spectra for the  $0 - 2000\text{ cm}^{-1}$  region of zeolites are generally considered to be unreliable because of the low optical throughput due to absorption by the zeolite framework and by dispersion effects in the case of diffuse reflectance resulting in spectral distortions.<sup>15</sup> In the CH stretching region, surface methoxy groups in ZSM-5 have asymmetric and symmetric stretching modes at  $2980$  and  $2868\text{ cm}^{-1}$  respectively.<sup>3</sup> There is a band at  $2980\text{ cm}^{-1}$  but no band at  $2860\text{ cm}^{-1}$  could be distinguished in the spectra measured here from those of hydrogen bonded methanol. The band at  $2980\text{ cm}^{-1}$  disappears after flushing which suggests that it could be assigned to methanol vapour.

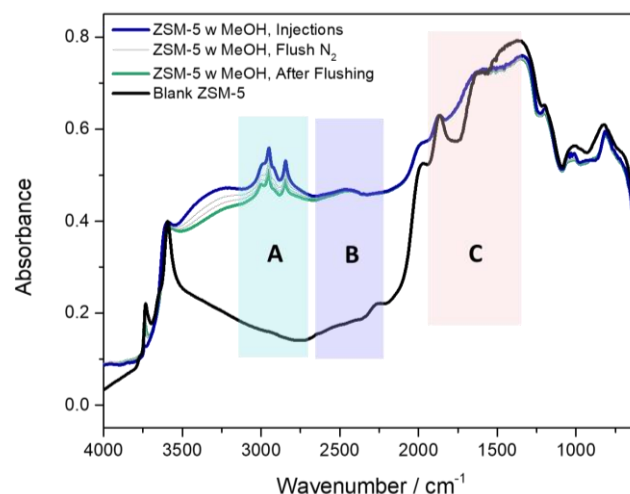


Figure 4.5: DRIFTS spectra of blank ZSM-5 (black), ZSM-5 with methanol injected under flow (blue), Sample was then flushed under 100 ml/min of N<sub>2</sub> (grey). A final spectrum was collected after 20 minutes of flushing (green). The spectra are unsubtracted, but the intensity has been normalised using the overtone band ( $1866\text{ cm}^{-1}$ ) on the blank ZSM-5. The ABC triplet is highlighted (A: green, B: purple, C: pink).

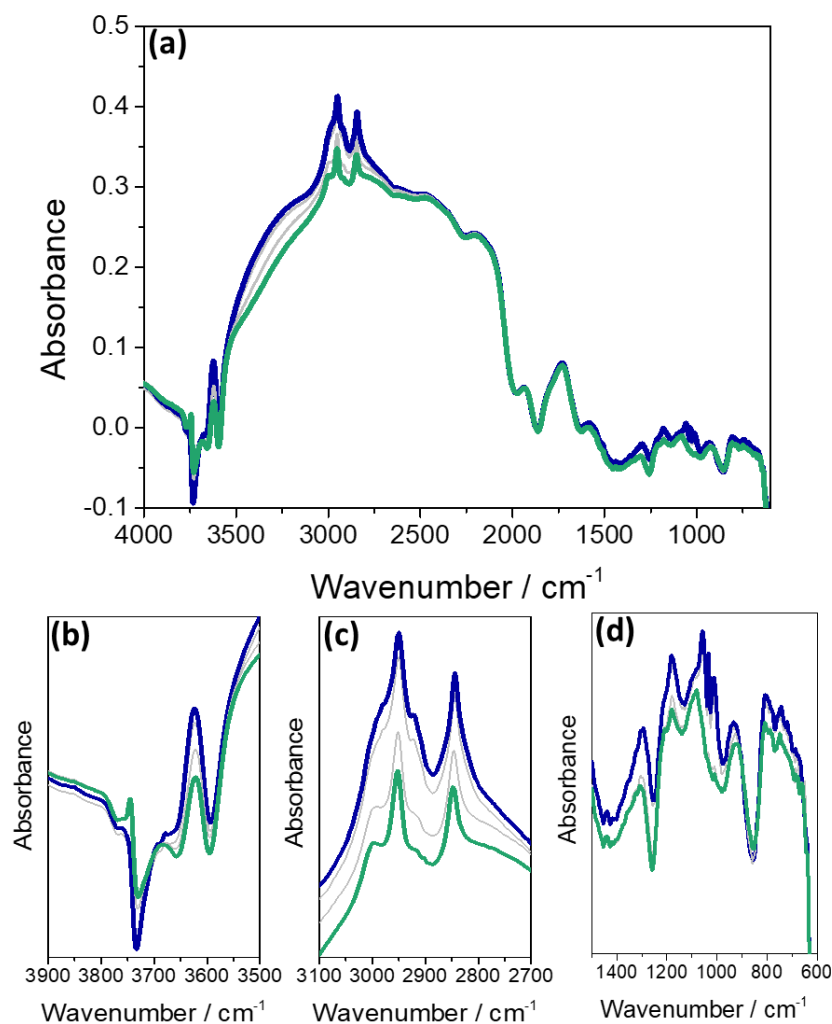


Figure 4.6: Difference Spectra of Figure 4.5 using the blank ZSM-5 as background. Detailed view of the (b) acid site region ( $4000\text{-}3400\text{ cm}^{-1}$ ) (c) CH region ( $3100\text{-}2600\text{ cm}^{-1}$ ) and (d) C-O region where the PQR bands are found in the gaseous phase.

#### 4.3.4 Solid State NMR

The ss-NMR experiments were carried out *via* static dosing of  $^{13}\text{C}$ -methanol onto dried ZSM-5. Two loadings were used: the first ( $1.2\ \mu\text{l}$  methanol) is comparable to that of previous studies in the literature<sup>16</sup> of about  $3\ \text{mol}_{\text{MEOH}}/\text{mol}_{\text{ZSM-5}}$ ; the second ( $6.6\ \mu\text{l}$  methanol) is comparable to the INS dosing experiments,  $23.8\ \text{mol}_{\text{MEOH}}/\text{mol}_{\text{ZSM-5}}$ . As seen in Figure 4.7, the spectra for the room temperature loaded samples (black lines) at both methanol loadings showed a single Lorentzian line at  $51.2\text{ppm}$ , with no contribution from any other species present. This is attributed to hydrogen-bonded methanol.<sup>16,17</sup>

Figure 4.7.a shows the NMR spectrum of the INS-comparable loaded ZSM-5 at room temperature and after waiting for 1.5 hours. The 1.5-hour wait did not

show any significant changes in the spectrum. After heating to 150 °C, the ss- $^{13}\text{C}$ -NMR spectra changes significantly. Two signals are present: the major signal at 60.2 ppm is assigned to methoxy groups and/or dimethylether<sup>16,17</sup> and the smaller signal at 51.2 ppm indicates some residual hydrogen bonded methanol in the zeolite. Figure 4.7.b shows the methanol loaded ZSM-5 at room temperature as well as the spectra of the sample after it has been evacuated to 0.3 mbar. Evacuating the sample did not cause a significant change in the spectra suggesting that the methanol is strongly adsorbed on the zeolite surface. Again, no signal was observed at 60 ppm which suggests that no methoxylation of the zeolite has occurred. By using an HPDEC pulse sequence for the  $^{13}\text{C}$  ss-NMR (which is quantitative), Figure 4.7 enables determination of an upper limit for the amount of methoxylation that could take place and be unseen by ss-NMR. This is determined by the signal-to-noise ratio, which for the signal at 51.2 ppm in Figure 4.7.a is at least 100. This means that no more than 1% of the methyl groups could be present as methoxy groups in the sample before heating. These results are in agreement with previous work.<sup>16,17</sup>

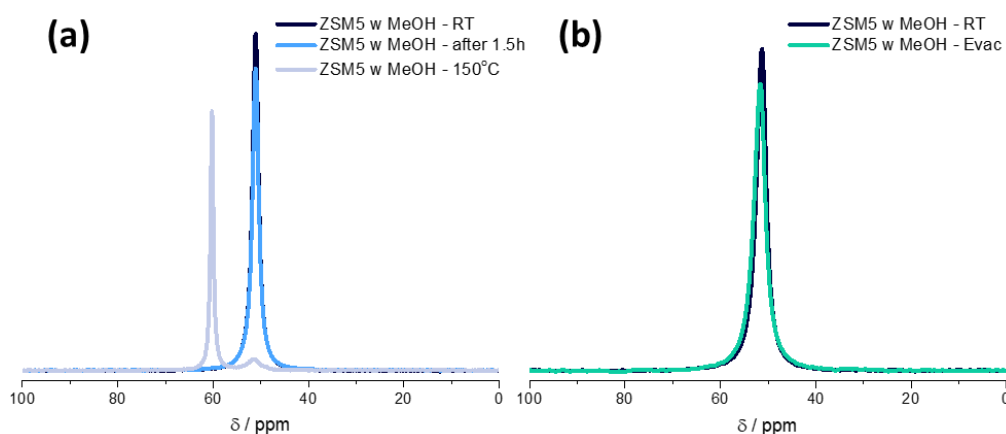


Figure 4.7: ss- $^{13}\text{C}$ -NMR spectra (a) Methanol dosing comparable to INS, waited for 1.5h and then heated at 150 °C (b) Methanol dosing comparable to Ref 9, and then evacuated at 0.3 mbar.

The  $^1\text{H}$ -NMR spectra of the samples described above were also measured and can be found in Figure 4.8. The differences between the spectra in Figure 4.8.a and 4.8.b are attributed to the different loadings of methanol in the ZSM-5. Figure 4.8.a, the methanol dose is high enough that it does not show any of the zeolite OH environments. Leaving the dosed sample for an extra 1.5 hour, showed that the proton peaks in the  $^1\text{H}$ -NMR have shifted downfield (see Table 4.1). This suggests that the hydrogen bonding is becoming stronger, or that more of the methanol is being adsorbed by the zeolite. However, as discussed above, no methoxy peak can be seen in the  $^{13}\text{C}$ -NMR.

Table 4.1:  $^1\text{H-NMR}$  Peak shifts table for Figure 4.8.a

Peaks	ZSM-5 Dosed	After 1.5 hrs	After 150 °C
1	3.77 ppm	3.96 ppm	3.59 ppm
2	6.71 ppm	7.31 ppm	3.87 ppm

The methanol loading in Figure 4.8.b is low enough that the zeolite OH hydrogens are also detected. The peak appearing at 1.9 ppm and the 2.9 ppm shoulder, are associated with hydrogens in silanol groups and extra-framework aluminium groups present in ZSM-5 respectively.<sup>18</sup> The Brønsted OH peak is merged with the methyl hydrogens in the large peak at 4 ppm.<sup>18,19</sup> Attempts to evacuate the methanol from the zeolite turned out to be unsuccessful. The hydrogen bonding is too strong to be effectively removed by vacuum. The hydrogen OH peaks of methanol moved up-field (see Table 4.2), suggesting that the hydrogen bonding became a little bit weaker, but the vacuum was unable to induce desorption.

Table 4.2:  $^1\text{H-NMR}$  Peak shifts table for Figure 4.8.b

Peak	ZSM-5 dosed	Evacuated
1	1.98 ppm	1.98 ppm
2	2.98 ppm	2.89 ppm
3	4.05 ppm	4.08 ppm
4	7.74 ppm	8.41 ppm

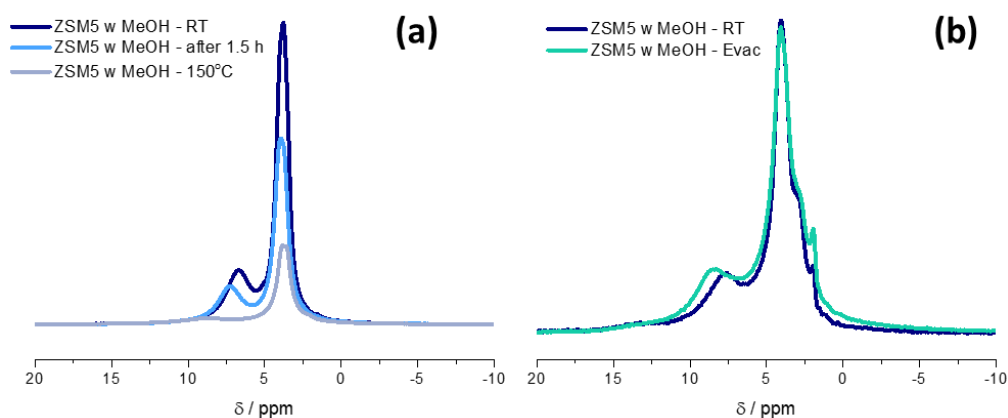


Figure 4.8:  $ss\text{-}^1\text{H-NMR}$  spectra. (a) Methanol dosing comparable to INS, waited for 1.5 hrs then heated to 150 °C, (b) Methanol dosing comparable to Ref 9, and then evacuated to 0.3 mbar

#### 4.4 Rationalising the Observed Differences

All of the spectra presented in section 4.3 (microreactor, INS,  $ss\text{-NMR}$  and DRIFTS) are compatible with previous work in the literature. However, they present different aspects. The microreactor data shows that the ZSM-5 is an

active MTH catalyst, but shows no production of water when methanol is introduced on ZSM-5 at room temperature. The INS appear to indicate complete methoxylation with no hydrogen-bonded methanol present, whereas ss-NMR shows only hydrogen-bonded methanol at room temperature, with methoxylation only occurring on heating. The DRIFTS spectra show hydrogen-bonded methanol with, at most, traces of methoxy groups. In the following section we consider four scenarios that could reconcile these apparently disparate observations.

#### 4.4.3 Scenario 1: Hidden OH Modes in INS

This scenario explores the possibility that the OH modes in the INS spectra are hidden by the C-H stretch and bending modes of methanol. The INS spectra seen in Figure 4.4 show no OH-related peaks in either the deformation or the OH stretch region. However, the CH stretch peak is quite broad suggesting that the OH peak could be contributing to the total intensity. Hydrogen bonding not only broadens peaks but also shifts them. Strong hydrogen bonding shifts the deformation modes to higher wavenumber and the stretching modes to lower wavenumber.<sup>20</sup> It is conceivable that the OH deformation modes of methanol have upshifted under the CH<sub>3</sub> rocking modes at 1100 – 1200 cm<sup>-1</sup> and that the OH stretch modes have downshifted under the CH stretching modes. To investigate this possibility, deuterated methanol (CD<sub>3</sub>OH) was used to load the zeolite under exactly the same conditions as used for the spectra in Figure 4.4. Figure 4.9 shows the solid CD<sub>3</sub>OH reference data obtained by both TOSCA and MAPS, as well as the spectra of the CD<sub>3</sub>OH dosed on ZSM-5, with the zeolite contribution subtracted (FD-CD<sub>3</sub>OH).

From the spectra, it is seen that for the adsorbed molecule the OH deformation modes at 702 and 768 cm<sup>-1</sup> are no longer present, whereas the CD<sub>3</sub> rock at 895 cm<sup>-1</sup> is still observed. There is a very broad peak (~800 cm<sup>-1</sup>) underlying the methyl deformations, which could be the broadened OH deformation peaks. The peaks at 1405 and 1455 cm<sup>-1</sup> in the reference spectrum are assigned to OH bending modes; it is unclear if the broad feature observed at 1390 cm<sup>-1</sup> for the adsorbed molecule is due to the OH bending modes broadened.

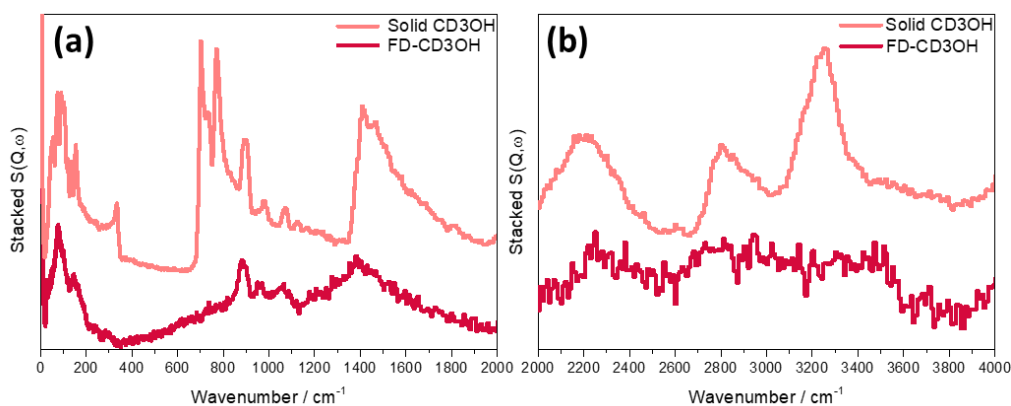


Figure 4.9: INS spectra of solid CD<sub>3</sub>OH and CD<sub>3</sub>OH flow dosed on ZSM-5 at room temperature. (a) Spectra collected via TOSCA spectrometer (b) Spectra collected with MAPS spectrometer (A-chopper) with incident energy set at 5244 cm<sup>-1</sup>.

From the MAPS reference spectrum of CD<sub>3</sub>OH (Figure 4.9), three prominent peaks are seen: one at 2220 cm<sup>-1</sup> that is assigned to the unresolved C–D stretch modes, one at 2800 cm<sup>-1</sup> assigned to the overtone of the OH in-plane bending modes found at 1405 cm<sup>-1</sup> and, finally, the 3260 cm<sup>-1</sup> feature assigned as the OH stretching mode.<sup>21</sup> From the MAPS spectrum of FD-CH<sub>3</sub>OH (Figure 4.9), the C-D stretch modes are weak but distinguishable, whereas the two OH assigned modes are either absent or broadened to >1000 cm<sup>-1</sup> width. This CD<sub>3</sub>OH experiment is therefore inconclusive, and does not give a clear answer as to the interaction of methanol with the zeolite at room temperature.

#### 4.4.2 Scenario 2: Both Species are Present

This scenario explores the possibility that both hydrogen bonded species and methoxy species are present. It is difficult to distinguish the two species via infrared spectroscopy due to the different extinction coefficients of  $\nu(\text{O-H})$  and  $\nu(\text{C-H})$ . The DRIFTS experiments of Matam et al., have suggested that at saturation levels of methanol, methoxylation is possible.<sup>10,11</sup> However, the spectra are dominated by the ABC triplet of hydrogen bonded methanol which potentially hides any methoxy peaks, as was seen in Figure 4.6. To check this possibility, methanol was injected at room temperature, the zeolite heated to 200 °C where methoxylation is expected to occur<sup>1-3</sup>, cooled back to room temperature and the same amount of methanol injected again. Both the heating and injections occurred under a nitrogen flow of 10 ml/min, with the total methanol injection each time being 12  $\mu\text{l}$ . The IR spectra recorded are shown in Figure 4.10.

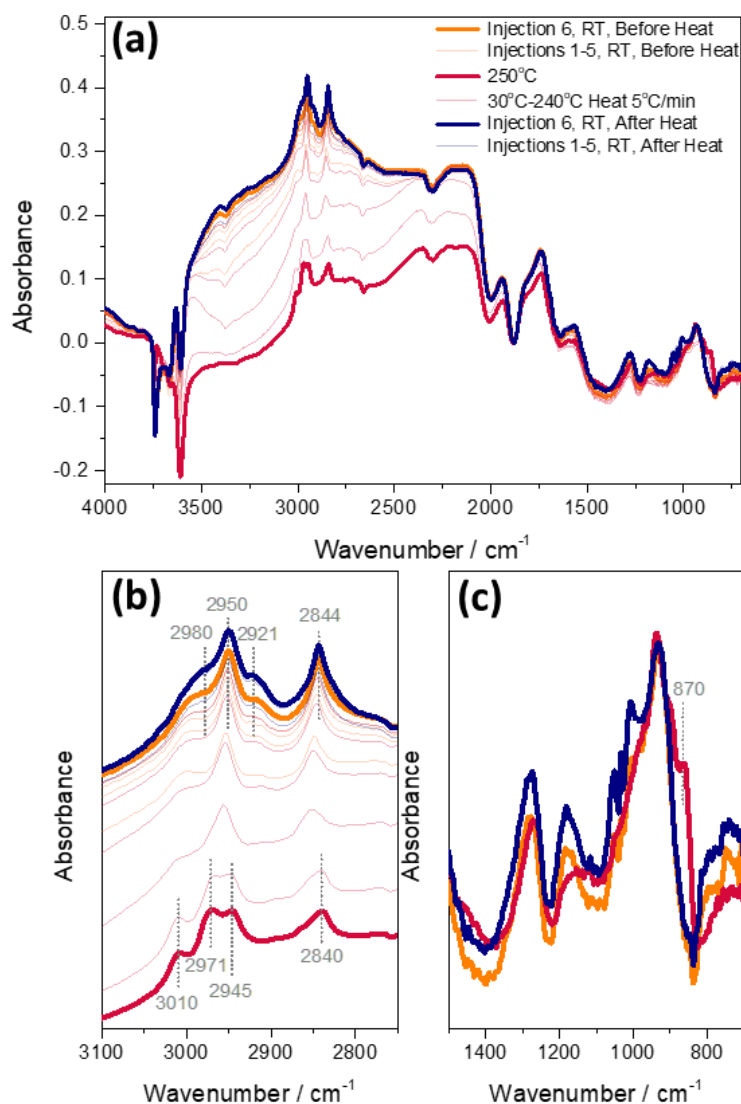


Figure 4.10: (a) DRIFTS difference spectra, 6 injections of 2  $\mu\text{l}$  methanol at room temperature at 20ml/min nitrogen flow, heated to 200  $^{\circ}\text{C}$  at 5 $^{\circ}\text{C}/\text{min}$ , cooled to room temperature and 6 further injections, 2  $\mu\text{l}$  methanol. Difference spectra obtained by subtracting the spectrum of the dehydrated zeolite. (b) Detailed view of the CH region (3100  $\text{cm}^{-1}$  – 2750  $\text{cm}^{-1}$ ) (c) Detailed view of the 700  $\text{cm}^{-1}$  - 1500  $\text{cm}^{-1}$  region. (Transition spectra were removed from this plot for simplicity)

The first room temperature spectrum is that of hydrogen bonded methanol, with the ABC triplet clearly dominating the spectra. The extinction coefficient of the OH stretching modes is clearly much larger than that of the CH stretching modes. A crude estimate of the total integrated area of the CH stretching modes compared with that of the OH stretching modes can be found in Figure 4.11. At a rough estimation it indicates a difference of at least 20-fold between the two extinction coefficients. With progressive heating, the bands due to hydrogen-bonded methanol diminish. In the CH stretching region (Figure 4.10.b) the bands observed match those reported in the literature for hydrogen bonded

dimethylether,<sup>4,16</sup> at 3010, 2971, 2945 and 2840  $\text{cm}^{-1}$ . The two bands expected for surface methoxy groups (asymmetric and symmetric stretching modes at 2980 and 2868  $\text{cm}^{-1}$  respectively) are not clearly seen, although their presence can be inferred from the formation of dimethylether. The low frequency difference spectra show the appearance of a new band at 870  $\text{cm}^{-1}$  on heating to 200 °C. This band may be the symmetric C-O-C stretch of adsorbed dimethylether, down shifted from the gas-phase value of 928  $\text{cm}^{-1}$  due to hydrogen bonding.<sup>22</sup> On cooling to room temperature and reinjection of methanol, the spectrum obtained is almost indistinguishable from that obtained initially, showing the loss of the 870  $\text{cm}^{-1}$  band of dimethylether and appearance again of hydrogen bonded methanol. Any methoxy groups which may have been formed at 200 °C are completely obscured by the hydrogen bonded methanol.

As was mentioned above, Figure 4.11 shows the crude estimation of the difference in extinction coefficients between the OH stretching modes and the CH stretching modes. To make the estimate, the ordinate scale of the spectrum needed to be changed from pseudo-absorbance to Kubelka Munk (KM) units. DRIFTS spectra are not intrinsically quantitative, as the intensity is dependent on orientation, size and number of particles in the beam, which can change from sample to sample.<sup>23</sup> For quantitative analysis, most of the literature uses the KM scale in order to minimise those effects. The estimation was done by integrating the 'difference' spectrum of Injection 6, RT before Heat seen in orange in Figure 4.10. The integration region was between 3590 – 1535  $\text{cm}^{-1}$ , which is the region of the ABC triplet intensity. The spectrum was integrated on the intensity above 0 (grey line on Figure 4.11). The integrated area highlighted in yellow is considered to be the whole integrated area of the spectrum intensity including the contributions from the OH and the CH intensities. Since it is impossible to discern between the intensities of the OH and CH peaks, for the CH region, the integrated area is the one highlighted in blue. The integrating area of the extending CH peaks without extending it down to the baseline, was in order to try and correct for the OH intensity. This is not quantitative, and it was only used as an approximation. The CH region integrated area is removed from the total area integrated, and the ratio between the two is used to estimate the difference in the extinction coefficient. This crude approximation of the difference in extinction coefficient, gives a plausible explanation on why the IR

is unable to discern between methoxy and hydrogen bonded methanol CH peaks (if room temperature methoxylation is actually occurring).

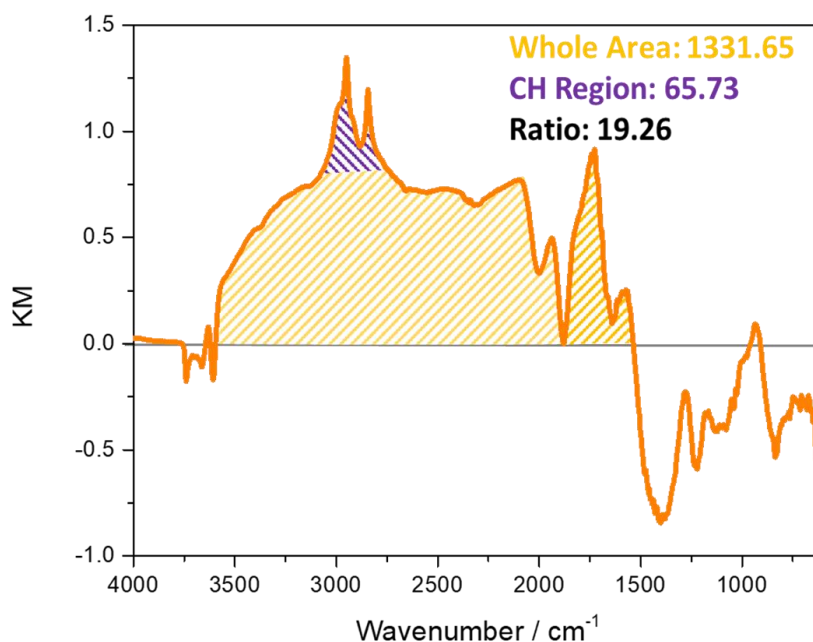


Figure 4.11: Difference spectrum of Injection 6, RT, Before Heat on Figure 4.9 with the integrated areas used in determining the extinction coefficients shaded in.

#### 4.4.3 Scenario 3: Dosing Differences

This scenario explores the possibility that the differences observed in the INS and NMR techniques could be the result of dosing differences when preparing the samples. Under the right conditions, both NMR and INS are quantitative techniques, which makes their discrepancies in this issue the more surprising. One difference between the techniques is the sample mass required: NMR having an approximate sample size of 0.5 g and INS usually needing up to 12 g of sample to obtain good S/N spectra. Due to this disparity it could be argued that a sample size effect is responsible for methoxylation occurring in the INS sample. Another possible explanation is that the INS samples have been prepared under flow conditions, whereas most NMR experiments have been performed with static dosing. Both of these possibilities are explored below.

The dosing effect was checked by preparing a static dosed ZSM-5 in large enough quantities for an INS measurement. In order to do that, the sample was dried and then kept in a desiccator containing a saturated vapour pressure of methanol for 70 hours before being transferred into the spectrometer. Figure 4.12, shows the TOSCA spectrum and MAPS spectrum recorded with an

incident energy of  $5244\text{ cm}^{-1}$ . The stretching region does not show any differences from previous INS experiments. In the deformation region, there is a broad weak feature where the OH deformation peaks should be ( $700\text{-}800\text{ cm}^{-1}$  region). The broadness suggests that the hydrogen bonding is very strong, but its intensity still does not match that expected for 15 moles of methanol per ZSM-5 unit cell. It is also noteworthy that no water is observed in the INS spectrum. Any water formed by methoxylation (scheme 4.1) should remain in the zeolite in a static experiment and be observable. Water has very characteristic librational mode which occurs at  $400\text{--}800\text{ cm}^{-1}$ , as well as characteristic HOH deformation ( $1500\text{--}1600\text{ cm}^{-1}$ ) and stretching modes ( $3200\text{--}3600\text{ cm}^{-1}$ ).<sup>24,25</sup> These water peaks do not appear in the spectrum, however, it might be difficult to distinguish these from the OH modes of the hydrogen bonded methanol.

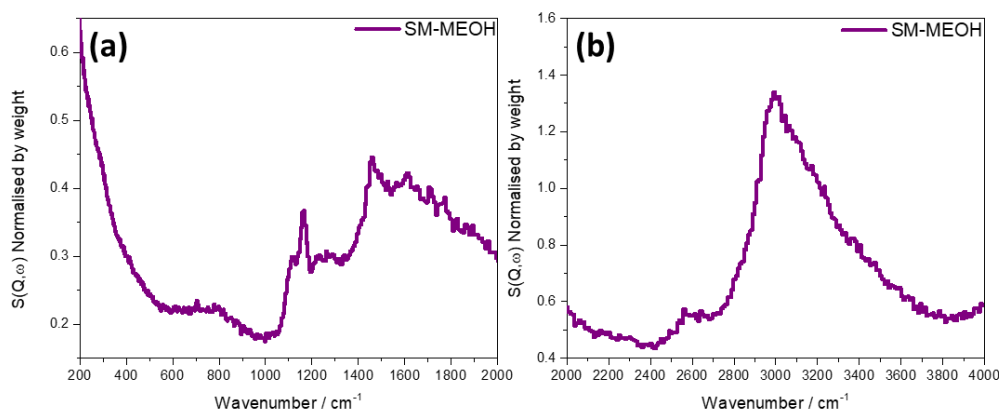


Figure 4.12: INS Spectrum of static dosed methanol on ZSM-5. Spectrum intensity was normalised by sample weight. Spectrum collected with (a) TOSCA (b) MAPS (A-chopper package, incident energy of  $5244\text{ cm}^{-1}$ )

A different experiment was designed which a flow-dosed sample was produced from a 14 wt%  $^{13}\text{C}$  methanol in  $^{12}\text{C}$ -methanol mixture in sufficient quantity to be analysed by INS,  $^{13}\text{C}$  NMR and DRIFTS. Total methanol loading is 17.8 moles<sub>MeOH</sub>/moles<sub>ZSM-5</sub>. The spectra obtained from this sample with the three different techniques are presented in Figure 4.13.

This experiment eliminates the possibility of different dosing conditions giving different results. The ss-NMR spectrum shows that there are no methoxy groups or dimethylether present in the  $^{13}\text{C}$ -methanol loaded zeolite sample, as there are no signals at 60 ppm. The DRIFTS spectrum is dominated by the bands due to hydrogen bonded methanol, as discussed above, and no bands due to methoxy groups can be distinguished. The INS spectrum shows similar

features to those described above, with the possibility at least of weak, broad bands in the OH deformation and OH stretching regions which could indicate the presence of hydroxyl groups.

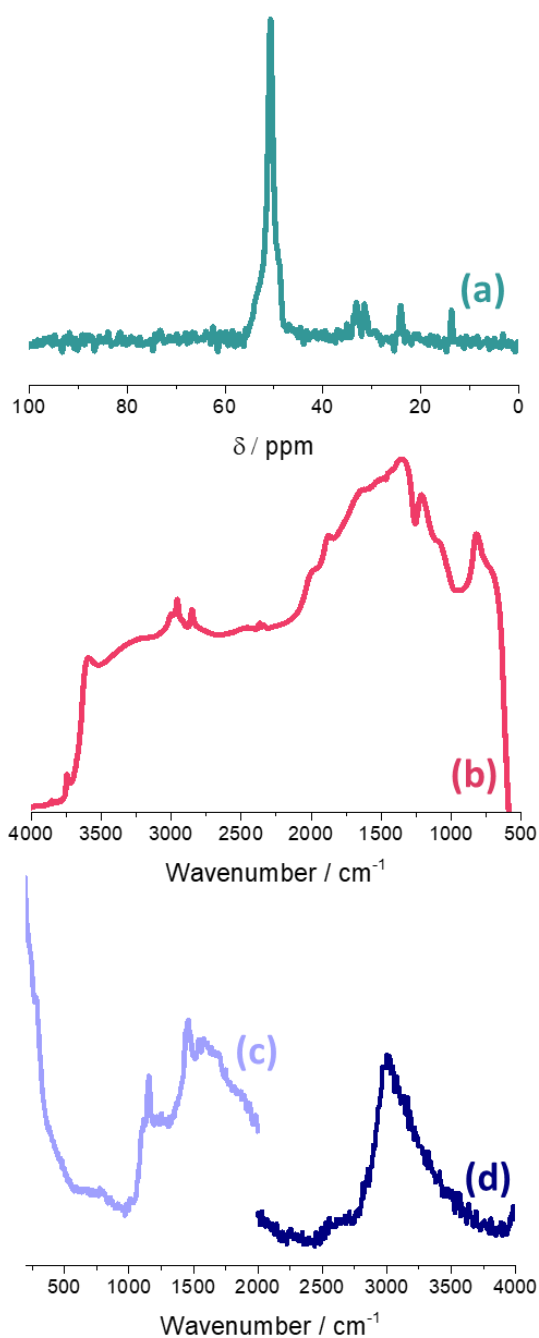


Figure 4.13:  $^{13}\text{C}$ -Methanol dosed ZSM-5 sample spectra. (a)  $^{13}\text{C}$ -NMR spectrum (b) DRIFTS spectrum (c) INS spectrum collected with the TOSCA spectrometer (d) INS spectrum collected with the MAPS spectrometer using the A-chopper package at an incident energy of  $5244 \text{ cm}^{-1}$

#### 4.4.4 Scenario 4: OH Peaks too Broad to Detect

This scenario explores the possibility that the OH peaks are present, but are broadened out to the point of no detection. It assumes that the hydrogen bonding of the methanol molecules is so strong that it causes the OH peaks to broaden out to the point where they become part of the baseline and therefore can go undetected by INS spectroscopy. Hydrogen and deuterium have very different neutron cross-sections and this allows us to test this possibility. A ZSM-5 sample was first loaded with CH<sub>3</sub>OD and the spectrum measured with the MAPS spectrometer. The same zeolite sample was then exposed to CH<sub>3</sub>OH to the same concentration and re-measured. If methoxylation had occurred, then there should be no difference between the spectra of the CH<sub>3</sub>OD and CH<sub>3</sub>OH exposed samples because the methoxy group has no deuterium incorporation. If methanol is present as a hydrogen-bonded species but with extremely broad OH-related bands, then the exchange of CH<sub>3</sub>OD for CH<sub>3</sub>OH should result in a raised baseline because of the larger total cross section of <sup>1</sup>H (82.03 barn) vs <sup>2</sup>H (7.64 barn).<sup>26</sup>

Figure 4.14 shows the results of this experiment. The sample was exposed to CH<sub>3</sub>OD first to a loading of 15.3 mol<sub>CH<sub>3</sub>OD</sub>/mol<sub>ZSM-5</sub>, and then the same sample was exposed to a flow saturated with normal methanol (CH<sub>3</sub>OH). The sample mass increased to a loading of 15.7 mol<sub>CH<sub>3</sub>OH</sub>/mol<sub>ZSM-5</sub>. It can be seen that the spectra do not overlap and that the CH<sub>3</sub>OH dosed spectra has gained intensity. This demonstrates that the methanol did not undergo methoxylation and that the methanol is present as a hydrogen-bonded species, albeit with extremely broad OH-related modes. Crucially, this interpretation is also supported by the frequencies of the CH<sub>3</sub> rocking modes.<sup>21</sup> Figure 4.14.c compares the (INS or IR) spectra of the pure CH<sub>3</sub>OD and CH<sub>3</sub>OH in the rocking mode region and it can be seen that the peaks occur at slightly different frequencies for the two isotopomers. For CH<sub>3</sub>OH they occur at 1120 and 1157 cm<sup>-1</sup>, whereas, for CH<sub>3</sub>OD they occur at 1167 and 1232 cm<sup>-1</sup>. Comparison with the spectra in Figure 4.14.a shows that this is also true of the CH<sub>3</sub>OD and CH<sub>3</sub>OH zeolite loaded spectra. This can only be the case if the CH<sub>3</sub>OD and CH<sub>3</sub>OH are intact in the zeolite.

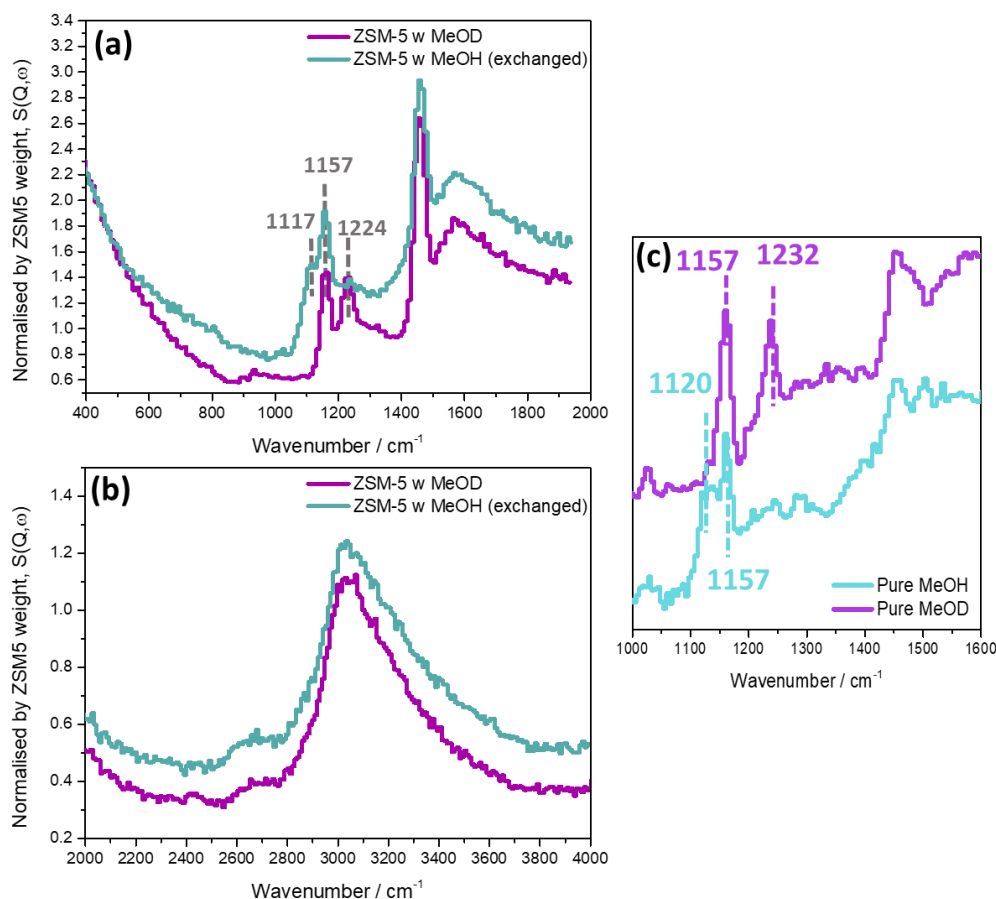


Figure 4. 14: MAPS spectra of  $\text{CH}_3\text{OD}$  dosed ZSM-5 vs exchanged  $\text{CH}_3\text{OH}$  dosed ZSM-5. Both spectra were collected using the A-chopper package at an incident energy of (a)  $2016.75 \text{ cm}^{-1}$  (b)  $5243.55 \text{ cm}^{-1}$ . (c) Detailed view at the  $1000 - 1600 \text{ cm}^{-1}$  of the pure  $\text{CH}_3\text{OD}$  and  $\text{CH}_3\text{OH}$  spectra collected via the TOSCA spectrometer for comparison purposes.

## 4.5 Conclusions

This chapter has shown that observing the OH functionality of methanol when methanol is loaded on ZSM-5 is complex with INS spectroscopy. When methanol is loaded on ZSM-5 at room temperature both infrared and ss-NMR spectroscopies show definitively that the methanol OH functionality is still present and dominates both sets of spectra. With INS spectroscopy, the OH functionality is not very evident at all, which lead to the previous conclusion that methanol is dissociated at room temperature.

A variety of scenarios have been considered that could reconcile the apparent contradictions between the techniques. The explanation that best fits the observations is that methanol is largely ( $\geq 99\%$ ) present as the hydrogen-bonded species at ambient temperature. This is consistent with the DRIFTS (Figure 4.6) and ss-NMR (Figure 4.7) data. Concerning the INS spectra (Figure

4.4), the OH-related modes have broadened to such an extent that they merge into the baseline so they are no longer clearly visible. This model also accounts for why there is no evidence of water in any of the INS spectra (Figures 4.4, 4.8, 4.12 and 4.13). It was originally assumed that if methoxylation had occurred, then the water generated would be flushed out of the zeolite. While this is conceivable for the flow dosed system, the water by-product should have still been present in the static dosed samples, which it was not (Figure 4.12). It is possible that the water stretch and bend modes could be masked by methoxy modes, however, the very strong librational modes would occur at 400 – 800  $\text{cm}^{-1}$ , which is a region that is clear of interference.

The presence of very broad OH-related modes has some precedent in a study of  $\text{KH}_2\text{AsO}_4$ , which, is strongly hydrogen-bonded in the solid state.<sup>27</sup> In this case, the O–H stretch mode extends over a range of  $\sim 2000 \text{ cm}^{-1}$ , although both the in-plane and out-of-plane As–O–H bending modes give distinct modes. For the adsorption system under consideration here, all of the methanol OH-related modes are broadened to at least  $1000 \text{ cm}^{-1}$ , which makes them very difficult to identify. After an extensive range of experiments, this study is able to rationalise the apparent paradox concerning methanol adsorption over ZSM-5 at room temperature. INS has a rich history of investigating H-bonded systems. The work presented here indicates caution needs to be exercised when assessing such systems under conditions where strong hydrogen bonding prevails. Although this scenario has been applied to a catalytic system in this instance, the scenario is equally applicable to other non-catalytic molecular systems.

## 4.6 References

- 1 Y. Ono and T. Mori, *J. Chem. Soc. Faraday Trans. 1 Phys. Chem. Condens. Phases*, 1981, **77**, 2209–2221.
- 2 W. Wang and M. Hunger, *Acc. Chem. Res.*, 2008, **41**, 895–904.
- 3 T. R. Forester and R. F. Howe, *J. Am. Chem. Soc.*, 1987, **109**, 5076–5082.
- 4 A. Zecchina, S. Bordiga, G. Spoto, D. Scarano, G. Spanò and F. Geobaldo, *J. Chem. Soc., Faraday Trans.*, 1996, **92**, 4863–4875.
- 5 M. F. Claydon and N. Sheppard, *J. Chem. Soc. D Chem. Commun.*,

- 1969, 1431–1433.
- 6 A. G. Pelmenschikov, R. A. Van Santen, J. Jänchen and E. Meijer, *J. Phys. Chem.*, 1993, **97**, 11071–11074.
  - 7 A. J. O'Malley, S. F. Parker, A. Chutia, M. R. Farrow, I. P. Silverwood, V. García-Sakai and C. R. A. Catlow, *Chem. Commun.*, 2016, **52**, 2897–2900.
  - 8 S. K. Matam, A. J. O'Malley, C. R. A. Catlow, S. Suwardiyanto, P. Collier, A. P. Hawkins, A. Zachariou, D. Lennon, I. Silverwood, S. F. Parker and R. F. Howe, *Catal. Sci. Technol.*, 2018, **8**, 3304–3312.
  - 9 T. Omojola, I. P. Silverwood and A. J. O'Malley, *Catal. Sci. Technol.*, 2020, **10**, 4305–4320.
  - 10 S. K. Matam, R. F. Howe, A. Thetford and C. Richard. A Catlow, *Chem. Commun.*, 2018, **54**, 12875–12878.
  - 11 S. K. Matam, S. A. F. Nastase, A. J. Logsdail and C. R. A. Catlowe, *Chem. Sci.*, 2020, **11**, 6805–6814.
  - 12 C. D. Chang, *Catal. Rev.*, 1983, **25**, 1–118.
  - 13 S. Ilias and A. Bhan, *ACS Catal.*, 2013, **3**, 18–31.
  - 14 B. H. Torrie, S.-X. Weng and B. M. Powell, *Mol. Phys.*, 1989, **67**, 575–581.
  - 15 S. Bordiga, L. Regli, C. Lamberti, A. Zecchina, M. Bjørgen and K. P. Lillerud, *J. Phys. Chem. B*, 2005, **109**, 7724–7732.
  - 16 S. M. Campbell, X.-Z. Z. Jiang and R. F. Howe, *Microporous Mesoporous Mater.*, 1999, **29**, 91–108.
  - 17 C. Wang, J. Xu and F. Deng, *ChemCatChem*, 2020, **12**, 965–980.
  - 18 M. Hunger and T. Horvath, *J. Am. Chem. Soc.*, 1996, **118**, 12302–12308.
  - 19 M. W. Anderson, P. J. Barrie and J. Klinowski, *Magic-Angle-Spinning NMR Studies of the Adsorption of Alcohols on Molecular Sieve Catalysts*, 1991, vol. 95.
  - 20 G. A. Jeffrey, *An Introduction to Hydrogen Bonding*, Oxford University

- Press, 1997.
- 21 M. Falk and E. Whalley, *J. Chem. Phys.*, 1961, **34**, 1554–1568.
  - 22 A. Allan, D. C. McKean, J. P. Perchard and M. L. Josien, *Spectrochim. Acta Part A Mol. Spectrosc.*, 1971, **27A**, 1409–1437.
  - 23 J. A. Lercher and A. Jentys, in *Infrared and Raman Spectroscopy for Characterizing Zeolites. Introduction to Zeolite Science and Practise*, 2007, pp. 435–476.
  - 24 C. Corsaro, V. Crupi, D. Majolino, S. F. Parker, V. Venuti and U. Wanderlingh, *J. Phys. Chem. A*, 2006, **110**, 1190–1195.
  - 25 J. Li, *J. Chem. Phys.*, 1996, **105**, 6733–6755.
  - 26 V. F. Sears, *Neutron News*, 1992, **3**, 26–37.
  - 27 J. Tomkinson, S. F. Parker and D. Lennon, *J. Chem. Phys.*, 2010, **133**, 034508.

# Chapter 5

## Spectroscopic Insight into the Methanol-to-Hydrocarbons Reaction

### *Conditioning, Steady State and Quasi-Deactivation*

---

This chapter will focus on studying the MTH reaction over ZSM-5 catalyst at different temperature ranges. A combination of different analytical techniques has been used in order to study the changing nature of the retained hydrocarbons. The beam time allocations for this work were carried out in collaboration with Antok Suwardiyanto from the University of Jember, as well as the usual experimental team (Mr Alex Hawkins, Prof Russell F. Howe, Prof. Stewart F. Parker and Prof. D. Lennon). The ssNMR presented in this chapter were performed by Prof Russell F. Howe of the University of Aberdeen and Dr. Nathan Barrow of Johnson Matthey.

### 5.1 Introduction

Deactivation in heterogeneous catalysis is a real issue,<sup>1</sup> which as discussed in the Introduction, is not so amenable to investigation by conventional molecular spectroscopy. For example, via several processes such as carbon retention, sintering, oligomer formation, *etc.*, heterogeneous catalysts tend to darken on ageing, so that for samples that have experienced extended periods of time-on-stream analysis by infrared spectroscopy is unproductive due to significant or total absorption by the substrate.<sup>2-4</sup>

This chapter concentrates on using INS to characterise different stages of the catalyst lifetime for a ZSM-5 catalyst applied to MTH chemistry. Crucially, the matter of the molecularity of the hydrocarbon pool as the catalyst approaches a deactivation regime is examined. Schulz *et al.* report on how temperature plays a role in changing the deactivation mechanism of the MTH reaction.<sup>5</sup> Reaction temperatures below 350 °C are associated with a build-up of methylated and polycyclic aromatics within the zeolite pores, causing pore blockage and deactivating the catalyst from the inside out. However, reaction in the range 350 – 500 °C showed the deactivation mechanism to have significantly altered, with graphitic coke building up rapidly on the external

surface of the zeolite.<sup>5</sup> XPS studies by Hughes *et al.* showed that external coke formed only after deactivation of the catalyst at 370 °C.<sup>6</sup> Mores *et al.* suggest that the carbonaceous build-up occurs more rapidly where the straight channels of the zeolite reached the external surface.<sup>7</sup> Building on this platform, we investigate MTH surface chemistry at three different reaction temperatures: (i) 300 °C, indicative of internal carbon build-up of the zeolite catalyst<sup>5</sup>, (ii) 350 °C for steady-state operation<sup>8-10</sup>, and (iii) 400 °C where deactivation by carbon deposition proceeds externally first before moving into the bulk.<sup>5</sup> The study is further complemented by additionally studying two temporal windows. Firstly, a time-on-stream (T-o-S) of 2 h emphasizes preliminary reactions in the catalytic cycle and, secondly, T-o-S  $\geq$  40 h samples steady-state and quasi-deactivation regimes. No constant T-o-S was used for the second class of reactions; the reaction times of 400-110h are selected as being representative of extended catalytic turnover. Vibrational assignments used the hydrocarbon study reported in Chapter 3.

The sample sizes of the INS experiments are much larger than the laboratory scale samples used for other spectroscopies. This is due to the relative insensitivity of INS. However, the sample size requirement allows for reaction testing to be completed on a larger scale as well, which is between laboratory scale samples and industrial samples. There is a gap in literature pertaining to the study of large scale samples, and how the change in sample size could affect the MTH reaction.

## 5.2 Experimental

### 5.2.1 INS Samples

The MTH reactions were completed using the ISIS/Glasgow reactor, the experimental set-up has been described fully in Section 2.3.1, Chapter 2. The experimental details are shown in Table 5.1. The ZSM-5 samples were dried before the reaction started, with the ZSM-5 sample being calcined in static air for 12 hours at 500 °C before being charged into the zeolite. Detailed catalyst characterisation has been reported in Chapter 3. For the reaction completed at 400 °C, the contact time was changed (see Table 5.1). For that reaction, issues with the in-line mass spectrometry lead to no online reaction monitoring being available. To compensate for the loss of mass spectrometry analysis, the catch-pot was emptied every 2 hours rather than every 12 with the liquid products analysed via GC-MS.

Table 5.1: Experimental details of samples examined

Sample	Catalyst mass	He	MeOH	Reaction Time		Total MeOH exposure	WHSV <sup>[1]</sup>	$\tau$ <sup>[2]</sup>	
	g	ml min <sup>-1</sup>	ml min <sup>-1</sup>	h	min	ml	$\frac{\text{mol}_{\text{MeOH}}}{\text{g}_{\text{ZSM5}} \text{h}^{-1}}$	h <sup>-1</sup>	h
300-2h	12.0	150	0.25	2	0	30	0.06	0.98	0.0064
350-2h	12.0	150	0.25	2	0	30	0.06	0.98	0.0064
400-2h	15.0	150	0.32	2	10	32	0.05	1.01	0.0064
300-60h	12.0	150	0.25	60	5	901	1.86	0.98	0.0064
350-110h	12.0	150	0.25	110	46	1662	3.42	0.98	0.0064
400-44h	12.6	150	0.27	44	2	713	1.40	1.02	0.0064
400-Frt	12.0	200	0.25	43	52	658	1.36	0.98	0.0048

$$^{[1]} \text{WHSV (Weight Hourly Space Velocity)} = \frac{\text{Methanol Flow (g h}^{-1}\text{)}}{\text{Catalyst mass (g)}}$$

$$^{[2]} \tau \text{ (contact time)} = \frac{\text{volume of reactor (cm}^3\text{)}}{\text{Total gas flow (cm}^3\text{h}^{-1}\text{)}}$$

### 5.2.1.1 Post Reaction Catalyst Analysis

The post-reaction catalyst samples were analysed using a variety of techniques. Nitrogen sorption analysis was used as described in Section 2.4.1.3, TPO and TGA analyses were carried out using the experimental techniques shown in Section 2.4.3.1 and 2.4.4.1. The DRIFTS spectra of the samples were collected using the experimental technique outlined in Section 2.2.1.1, with the samples being dried at their reaction temperature before the DRIFTS spectra were collected. The INS spectra of the samples were collected using both the TOSCA and the MAPS instruments with their experimental details being outlined in Section 2.1.2.3. The MAPS incident energies used were 5244 cm<sup>-1</sup> (600 Hz) to provide favourable resolution spectra in the CH and OH stretching region (2500 cm<sup>-1</sup> – 4000 cm<sup>-1</sup>) and for comparison purposes, spectra were also recorded at the incident energy of 2017 cm<sup>-1</sup> (400Hz), which gives a similar spectral range of the TOSCA instrument but at lower resolution.<sup>2</sup>

For NMR analysis two different spectrometers were used to obtain spectra of the reacted samples, operating at magnetic field strengths of 9.4 and 14.1 T, with the majority of the measurements performed on the lower field instrument (at the University of Aberdeen by Prof. Russell Howe). Subsequently, a small number of samples were selected for analysis using the higher field spectrometer (at the Johnson Matthey Technology Centre by Dr Nathan Barrow).

In the first instance, solid-state NMR spectra of post-reaction samples were acquired at a static magnetic field strength of 9.4 T ( $\nu_0$  (<sup>1</sup>H) = 400 MHz) on a

Varian Infinity Plus 400 MHz spectrometer. Samples were loaded into a 7.5 mm MAS rotor and spun in dry air at 2.5 – 3.5 kHz.  $^{13}\text{C}$  spectra were recorded at 100.54 MHz using a variable amplitude cross polarisation pulse sequence and a contact time of 7 ms. Chemical shifts were externally referenced to TMS (tetramethylsilane) via a hexamethylbenzene standard. 60,000 acquisitions were averaged with a 5 s pulse delay.  $^{27}\text{Al}$ -NMR spectra were recorded at 104.2 MHz using a one pulse Bloch decay with a 0.5  $\mu\text{s}$  pulse width ( $\pi/20$ ) and a 5 s pulse delay. Samples were measured at 500 acquisitions that allowed for comparison of signal to noise ratios. Chemical shifts were externally referenced to a kaolin standard (-2.5 ppm relative to  $\text{Al}(\text{H}_2\text{O})_6^{3+}$ ).  $^{29}\text{Si}$  NMR data were collected at 79.4 MHz using a one pulse Bloch decay with proton decoupling. A  $\pi/2$  pulse width of 6  $\mu\text{s}$  and a 5s pulse delay was used with an average of 1,000 acquisitions.  $^{29}\text{Si}$  spectra were externally referenced to TMS via a kaolin standard (-91.2 ppm). This was done by Russell F. Howe at the University of Aberdeen.

Two samples from the extended run series (350-110h and 400-44) were selected for further analysis on the higher field instrument. ssNMR spectra were acquired at a static magnetic field strength of 14.1 T ( $\nu_0$  ( $^1\text{H}$ ) = 600 MHz) on a Bruker Avance Neo console using TopSpin 4.0 software. For  $^{29}\text{Si}$ , the probe was tuned to 119.23 MHz and referenced to kaolin standard at -91.2 ppm. The samples were dried at 110 °C before analysis. The samples were packed into zirconia MAS rotors with Kel-F caps; before and after weighing provided the sample mass. The rotors were spun using room-temperature purified compressed air.

### 5.2.2 Reaction Testing - Microreactor

The microreactor set-up uses a plug flow reactor tube as has been described in Section 2.3.2. Approximately 0.5 g of sample were used for each reaction. Three different reaction temperatures were tested: 300, 350 and 400 °C for 24 hours. The outlet of the reaction is connected to a GC-FID. The GC-FID was calibrated with model compounds: propene, methanol, benzene, toluene, xylenes (o-xylene, p-xylene), trimethylbenzenes (mesitylene and 1,2,4-trimethylbenzene), durene, methyl-naphthalene. The full calibration can be found in Section 2.3.2.

## 5.3 Reaction Testing

Reaction testing was undertaken at 300, 350 and 400 °C using the ISIS/Glasgow Catalysis Rig located at the ISIS Neutron and Muon Facility. Due to the relatively insensitive nature of INS spectroscopy, the technique requires relatively large sample masses, which leads to distinct sample environment arrangements as considered elsewhere.<sup>11</sup> The ISIS/Glasgow Catalysis Rig is a large scale reactor which is able to accommodate a catalyst charge of up to 15 g. A conventional microreactor set up (catalyst charge of 500 mg) was also used (Section 5.2) in order to establish and confirm the reaction trends observed in the ISIS reactor.

### 5.3.1 INS Reactor Measurements

Figure 5.1 shows the in-line mass spectrometry reaction profiles for the extended-run reactions recorded at the three different temperatures: (a) 300-60h (b) 350-110h and (c) 400-44h. The intensities have been normalised with respect to the helium carrier gas signal and smoothed by taking a point approximately every 8 minutes. Some variability of signal intensity was observed over the reaction period. In part, this reflected changes in the flow as the catch-pot was sampled. There is some discontinuity in certain signal intensities over the full reaction profile. Despite that, the anticipated MTH trends have been observed with the samples and are comparable with previously published ZSM-5 catalysed MTH reactions.<sup>8,12,13</sup>

No initiation stage is observed in any of the MS traces seen in Figure 5.1. Figure 5.1.a shows the product profile of the 300 °C reaction to be composed of low molecular weight olefins and aromatic entities, typical of a MTH product profile.<sup>8,10,12,14</sup> It also shows progressive growth in methanol breakthrough, evidence of an evolving deactivation channel even at this relatively low temperature. The degree of deactivation appears to increase for reaction times longer than 45 min. Dimethyl ether (DME) is thought to be an intermediate in the MTH catalytic cycle.<sup>12</sup> Figure 5.1.a shows DME to follow a similar trajectory to methanol, albeit at an increased intensity throughout the full reaction coordinate. The ratio of propene and ethene has been shown to be indicative to the level of methylation taking place within the MTH reaction,<sup>15</sup> with higher propene signal suggesting higher methylation. Figure 5.1.a and 5.1.b show a higher ratio of propene signal to ethene, whereas Figure 5.1.c the signals are

almost overlapping. This is a small indication of different chemistries happening at different temperatures.

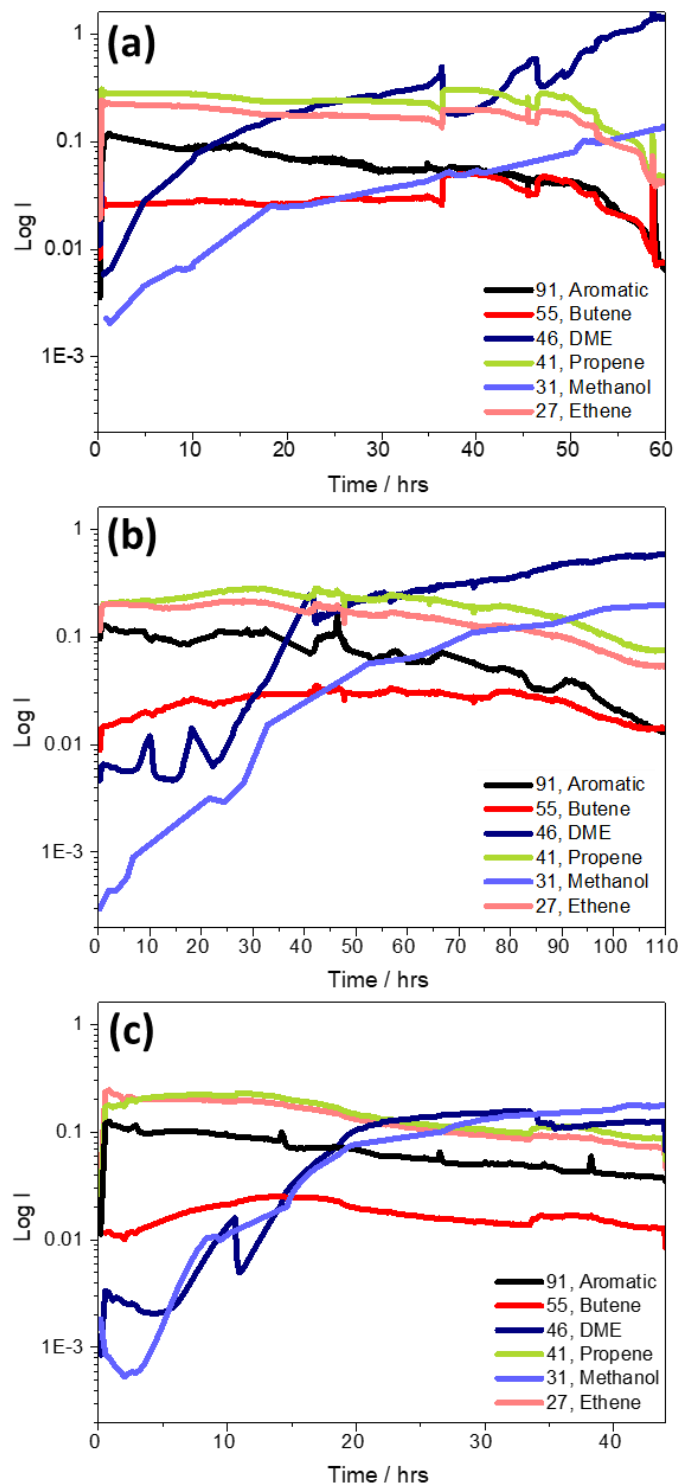


Figure 5.1: Mass spectrometer reaction profiles for INS reactor as a function of reaction temperature: (a) 300 -60h (b) 350 -110h (c) 400 -44h. Monitoring masses are as follows:  $m/z$  91 (black), the tropylium ion indicative of aromatic formation;  $m/z$  55 (red) signifies butene;  $m/z$  46 (blue) signifies dimethyl ether;  $m/z$  41 (green) signifies propene;  $m/z$  31 (light blue) signifies methanol and  $m/z$  27 (pink) signifies ethene.

Figures 5.1.b and 5.1.c display comparable trends to those observed in Figure 5.1.a. The product distributions are comparable, although the decrease in product formation rate for extended times-on-stream are not as significant as observed for the 300 °C sample. Possibly reflecting temperature-induced changes to the earlier stages of the MTH process, the higher temperature run shows the degree of methanol breakthrough to more closely resemble that of DME.

For the MTH process over ZSM-5 Bibby *et al.* suggest that the catalyst reaches deactivation when no more DME is being produced.<sup>16</sup> None of the three reaction regimes fall in to that category, indicating that extended reaction times would be required for formal deactivation but, nonetheless, if the slope of the DME profile is indicative of the deactivation rate, then Figure 5.1 shows the 400 °C run to be experiencing the greater degree of deactivation. Figure 5.2 shows the methanol conversion profiles for three different temperatures performed in the INS reactor. Initially all samples exhibit high methanol conversion, but this progressively declines on increasing T-o-S. The 300 and 350 °C runs follow similar trajectories but the steeper decline for the 400 °C sample indicates this sample to be more rapidly approaching a deactivation phase.

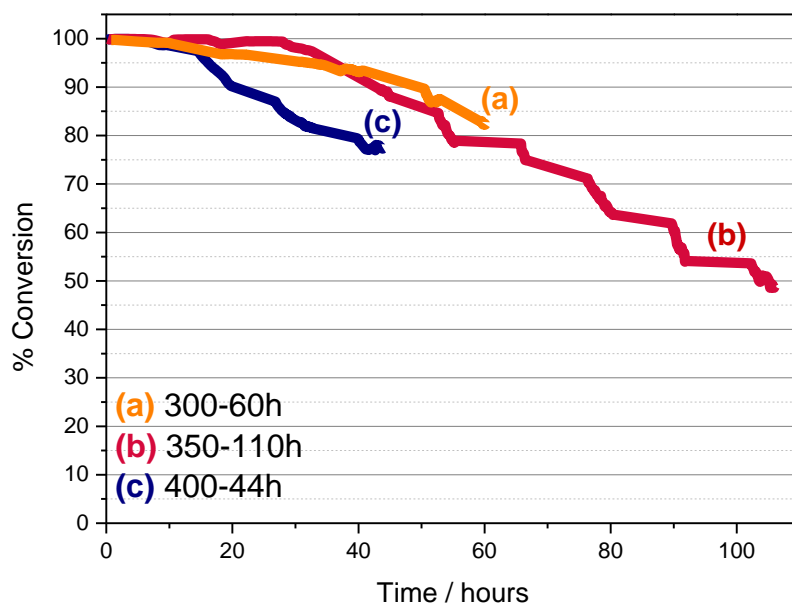


Figure 5.2: Methanol conversion for MTH reactions in the INS reactor at three different temperatures: (a) 300, (b) 350 and (c) 400 °C

Liquid products were collected in a catch-pot placed downstream of the reactor to collect the heavier hydrocarbons. Figure 5.3 shows the GC-MS/FID chromatographs of the liquid products collected via the catch-pot. Sampling

was undertaken approximately every 12 h, with the catch pot emptied completely on each occasion. Thus, the chromatographs show an average of the products collected over an ~12 h duration. Figure 5.3 shows that for all three reaction temperatures the liquid products are a mixture of methylated benzenes that is supplemented with a small contribution from methylated naphthalenes, typical for this class of reaction.<sup>8,17,18</sup> The liquid products are constrained to what can diffuse out of the zeolite pore, therefore higher molecular weight polycyclic products are not observed in the liquid product analysis, although they might be trapped within the zeolite pores.<sup>5,19</sup>

Figure 5.3 shows the catch-pot traces of the three reactions to be broadly similar; toluene and xylenes are seen to decrease with increasing T-o-S, whereas trimethylbenzenes and tetramethylbenzene (durene) are seen to increase. Some naphthalenes with up to two methyl substitutions are identified, with intensities higher at the beginning of the reactions than the end. This could be due to coke build-up within the zeolite pores and channels, so that the naphthalene molecules are no longer able to diffuse out of the zeolite pores or, alternatively, that the naphthalenes are reacted further and turned into coke. However, it must be noted that the overall intensity of the product peaks seen in Figure 5.3, the 400-44h sample shows a reduction in peak intensity by a factor of 10 when compared to the other two samples. To make the trends more observable, the peak areas corresponding to each of the major hydrocarbon groups were noted down and the average percentage areas were plotted against time-on-stream (see Figure 5.4).

Figure 5.4 shows the 350 and 400 °C runs to exhibit higher trimethylbenzene intensities than that seen for the 300 °C reaction, with the 300 °C run exhibiting the highest tetramethylbenzene concentration. A comparable trend of methylated benzene production was observed for the micro-reactor reactions seen in the following section at Figure 5.4 and 5.5. The reaction chemistry observed for the INS reactor is representative of established concepts within MTH chemistry.<sup>8,10,14</sup>

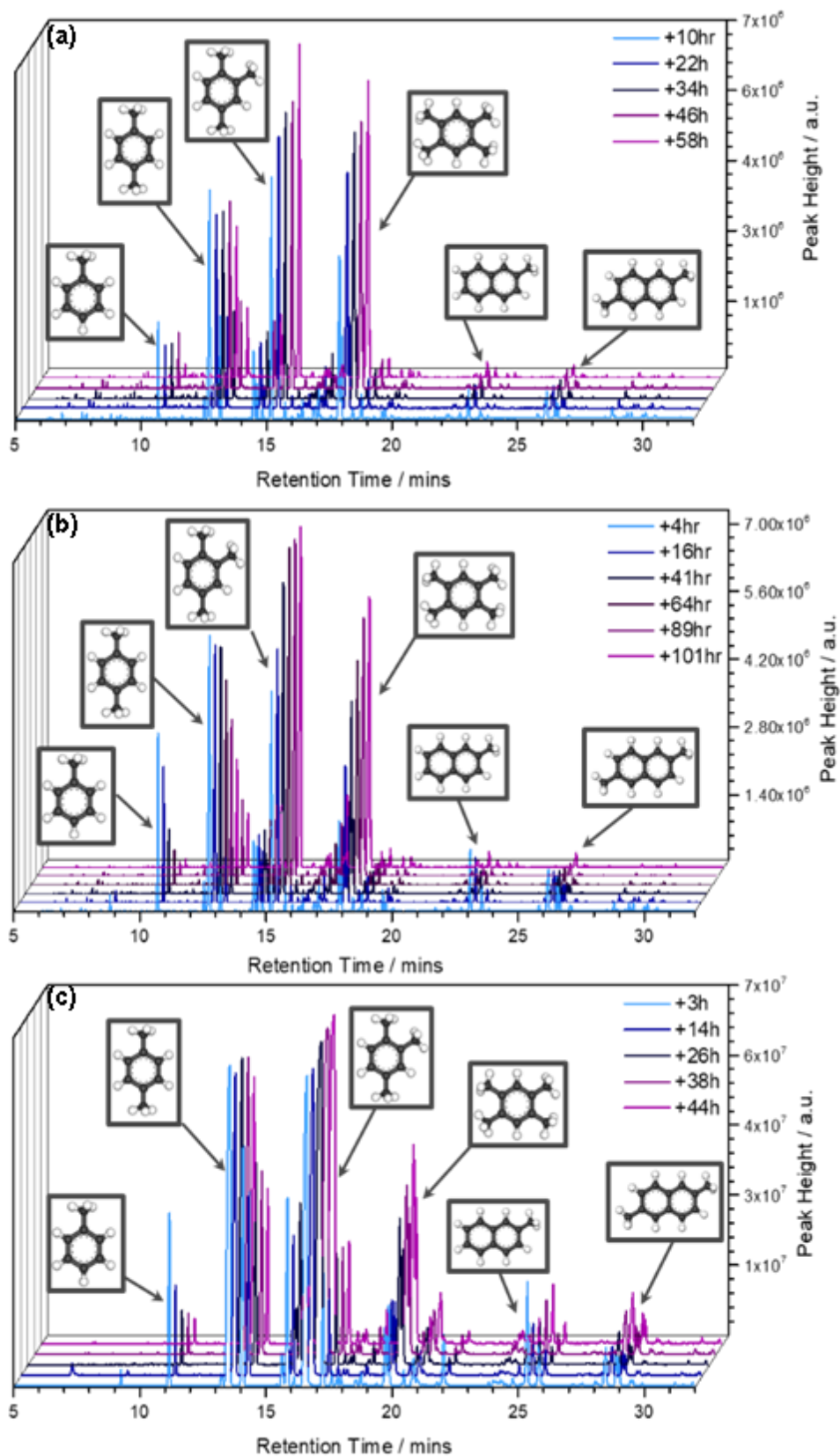


Figure 5.3: GC-MS analysis of liquid products collected in the organic layer of the catch-pot: (a) 300°C-60h (b) 350°C-110h (c) 400°C-44h.

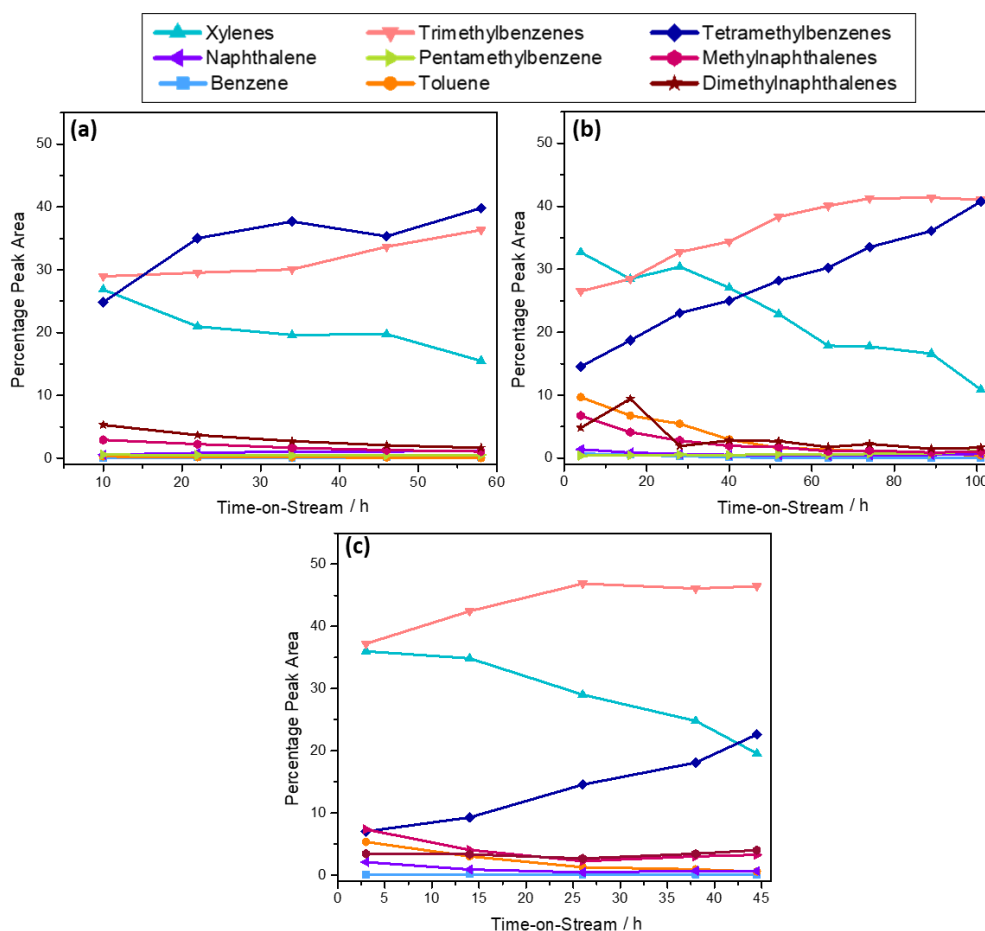


Figure 5.4: Percentage peak areas of the GC-MS liquid product analysis plotted against time-on-stream for the reactions of (a) 300-60h (b) 350-110h and (c) 400-44h

### 5.3.2 Microreactor

A series of 24 hour reactions was completed at the three different temperatures (300 °C, 350 °C, 400 °C). The product distribution was monitored by a GC-FID. The GC calibration of the main products can be found in Chapter 2. Figures 5.5, 5.6 and 5.7 shows the product distribution profiles of the MTH reactions. At T-o-S = 55 min (Fig 5.5.a) shows propene to be the dominant product at all three temperatures, with the 300 °C run exhibiting the greatest activity. At T-o-S = 222 min (Fig 5.5.b) shows enhanced activity at 350 and 400 °C; little product is observed at the lowest temperature. The 350 °C profile is dominated by toluene and xylene, whilst the 400 °C run shows a greater degree of methylation to occur, as evidenced by the presence of trimethylbenzenes (1,2,4 trimethylbenzene and mesitylene). At T-o-S = 395 and 500 min, Figures 5.5.c and 5.5.d respectively show the presence of durene at 300 °C, indicating methylation now to be prevalent at the lower temperature; the higher temperature runs are dominated by a range of methylated benzenes (*i.e.* toluene, xylene, trimethylbenzenes). At T-o-S = 615 and 815 min (Fig. 5.6.a) it

shows durene dominating at 300 °C, whilst at 400 °C trimethylbenzenes dominates. There seems to be a relative increase in methylated benzenes in all temperatures whereas toluene and methyl naphthalenes are decreased from earlier T-o-S.

The 300 °C reaction had to be stopped after 900 mins. This was due to durene building up in the GC-lines, causing a blockage. Attempting to repeat the experiment caused the blockage again. Therefore, no information about the later stage of the reaction has been observed. The reactor pressure build-up was observed from approximately the 600-minute mark, which could mean that some of the data shown for the 300 °C run may be affected as well. The basic product trends are evident. The reaction profiles at the longer run times for 350 and 400 °C (Figure 5.7.a, 5.7.b) show methylated benzenes to dominate the product slate. Thus, the well documented trend of olefin formation being observed in the first instance, which is then followed by toluene and xylene and, subsequently, higher ring methylation is reproduced.<sup>8,10,12,14</sup> Naphthalenes contribute only a minor role in the product distributions observed with a decreasing trend with increasing T-o-S. There is little evidence of benzene formation over the temperature range and timescales studied.

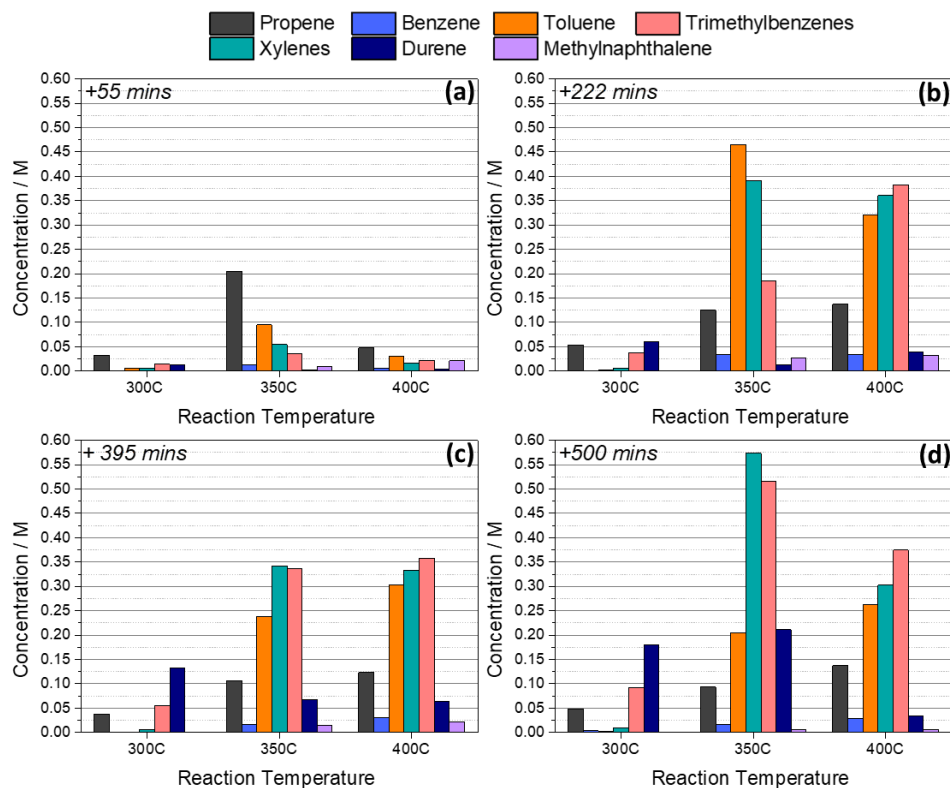


Figure 5.5: Microreactor reaction in-line GC-FID data. The product distributions for the three reaction temperatures (300, 350 and 400°C) are presented as a function of increasing time-on-stream: (a) 55, (b) 222, (c) 395 and (d) 500 min. M signifies moles of product per litre of gas.

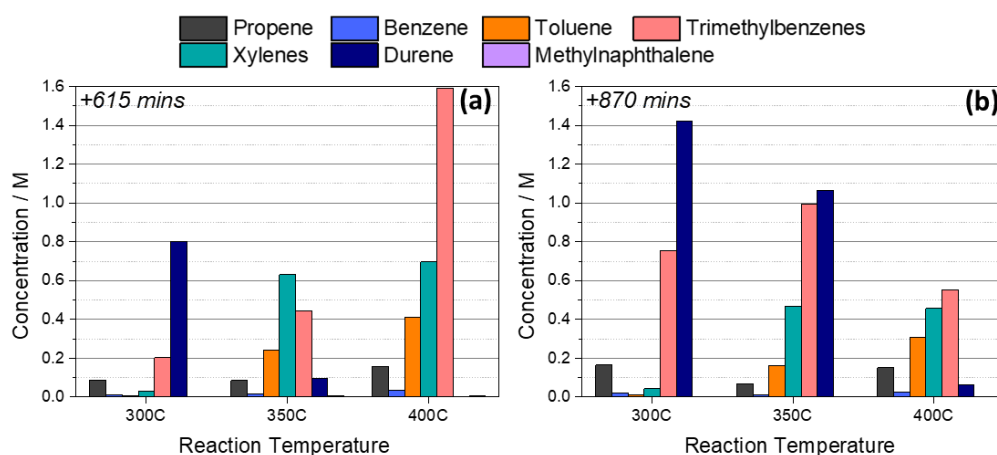


Figure 5.6: Microreactor reaction in-line GC-FID data. The product distributions for the three reaction temperatures (300, 350 and 400°C) are presented as a function of increasing time-on-stream: (a) 615, (b) 870 min. M signifies moles of product per litre of gas.

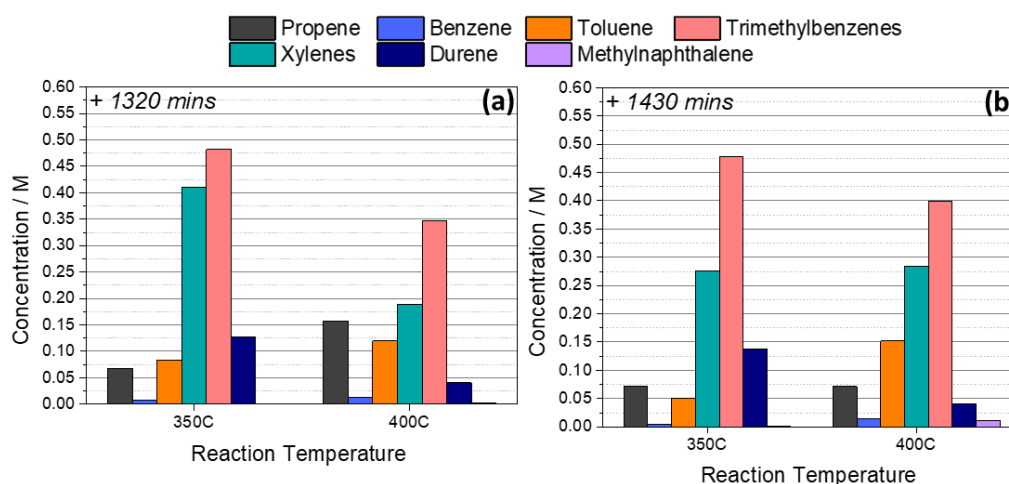


Figure 5.7: Microreactor reaction in-line GC-FID data. The product distributions for the three reaction temperatures (350 and 400°C) are presented as a function of increasing time-on-stream: (a) 1320 and (b) 1430 min. M signifies moles of product per litre of gas.

## 5.4 Post Reaction Analysis

Post-reaction samples from the ISIS/Glasgow Catalysis Rig reactor have undergone extensive characterisation. Table 5.2 presents physical characterisation of the samples post-reaction with the ISIS/Glasgow Reactor. The table shows the coke percentage values obtained from the TPO analysis (and confirmed via TGA) as well as the nitrogen adsorption data. On comparing the short runs, increasing reaction temperature does not unduly affect surface area or micropore volume, nor does it induce major differences in the coke content. However, in contrast, Table 5.2 shows the samples that have experienced extended T-o-S to exhibit decreases in internal surface area, external surface area and micropore volume. Bibby *et al.* reported that 14-18 wt% coke content is typical for deactivated catalysts used in MTH chemistry.<sup>16</sup>

Unsurprisingly, the 400-44h sample displays the highest coke content, with the extent indicative of operation within a deactivation or quasi-deactivation regime.

Table 5.2: Nitrogen adsorption data and coke content for the fresh unreacted catalyst and six post-reaction samples prepared using the ISIS/Glasgow reactor.

Sample Name	$S_{\text{BET}}$ $\text{m}^2\text{g}^{-1}$	$V_{\text{micropore}}$ $\text{cm}^3\text{g}^{-1}$	$S_{\text{external}}$ $\text{m}^2\text{g}^{-1}$	Coke Content wt%
Unreacted ZSM-5	404	0.156	37.7	N/A
300-2h	371	0.140	34.9	1.95
350-2h	396	0.150	36.0	2.58
400-2h	368	0.139	41.5	2.46
300-60h	56	0.016	18.2	8.97
350-110h	46	0.014	13.4	14.20
400-44h	38	0.011	12.2	20.20

The nitrogen sorption plots can be found in Figures 5.8 and 5.9. All samples have a degree of mesoporosity present, with the isotherms being a Type IV isotherm with what appears to be an H4 hysteresis loop.<sup>20</sup> This type of isotherm is associated with microporous systems with mesopores present.<sup>20</sup> Short reactions (Figure 5.7) show some drop in the adsorption volume, and no change in the mesoporosity of the sample, even at increased temperatures. At the longer reactions, the mesoporosity seems to drop as the pores are filled with coke. This is more evident at 350-110h and 400-44h samples.

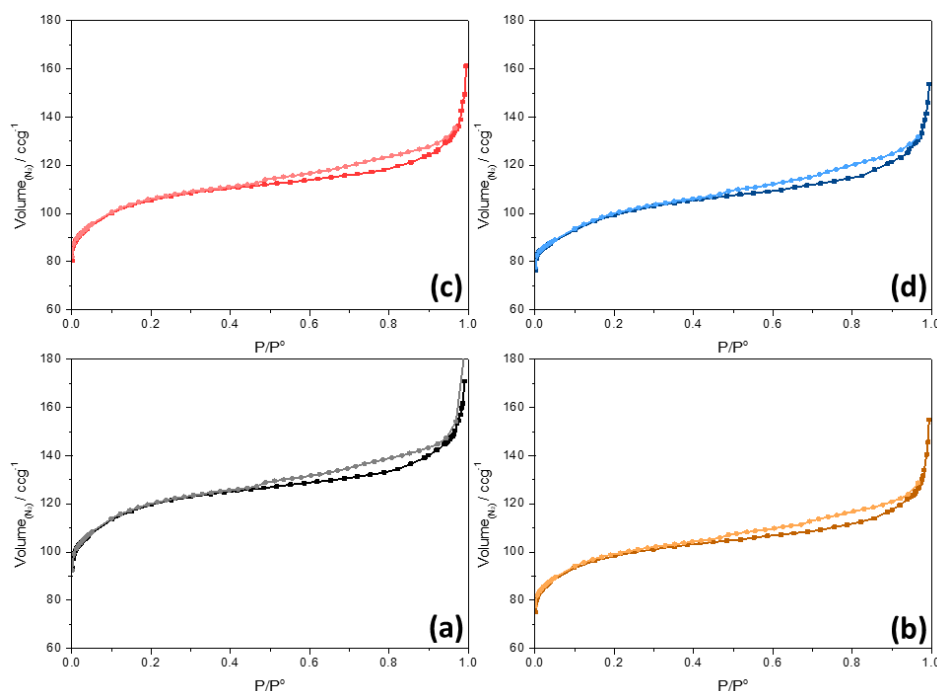


Figure 5.8: Nitrogen adsorption (square) / desorption (circles) isotherms for (a) Unreacted ZSM-5 (b) 300-2h (c) 350-2h and (d) 400-2h

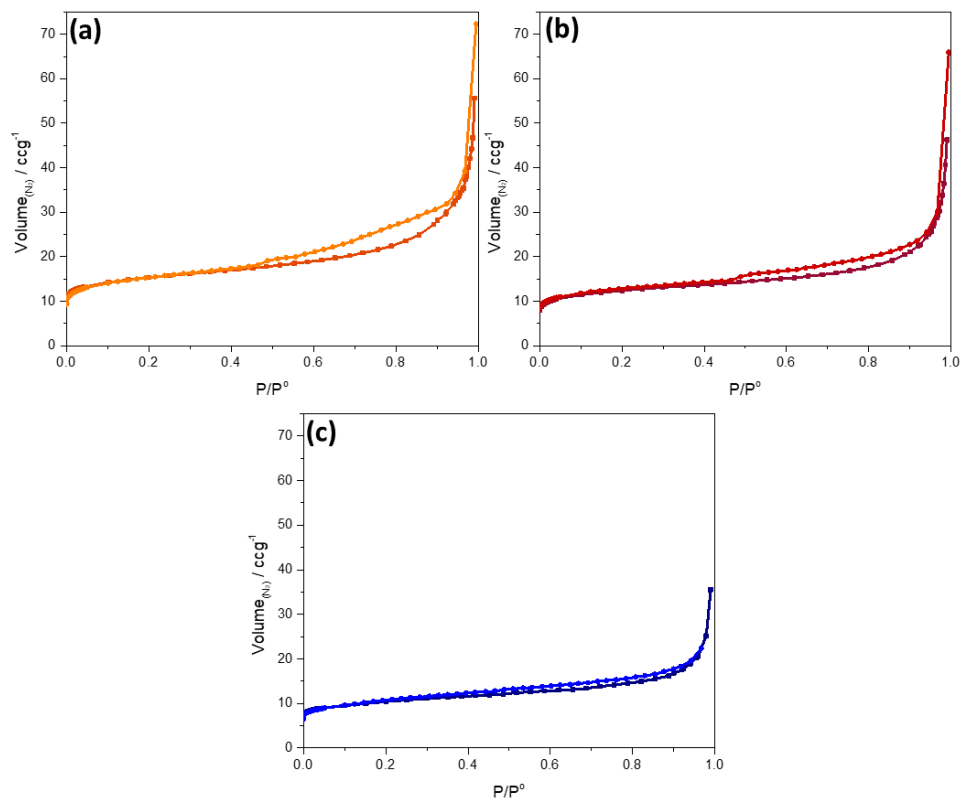


Figure 5.9: Nitrogen adsorption (square) / desorption (circles) isotherms for (a) 300-60h (b) 350-110h (c) 400-44h

The loss of mesoporosity in the longer reactions is consistent with catalyst deactivation and pore blockage. Figure 5.10 presents the temperature-programmed oxidation (TPO) profiles of the post-reaction INS reactor samples for the sets of (a) short and (b) extended runtimes, where the profiles are indicative of the type of coke present within the zeolite samples.<sup>5</sup> Type I coke exhibits a  $T_{\max} < 400$  °C and typically comprises oxygenated hydrocarbons or light olefins with a lower combustion temperature.<sup>5,17</sup> Type II coke requires higher temperatures for combustion and is typically associated with a mixture of aromatics and polycyclic hydrocarbons. The peak shapes observed in Figure 5.10 are suggestive of there being a variety of hydrocarbons present within the reacted zeolite.

For the short run reactions (Figure 5.10.a), there are contributions from Type I and Type II coke, with increasing reaction temperature leading to a greater retention of Type-II coke. From the deconvoluted peaks seen in Figure 5.11, it is shown that the sharp peak present in the short reactions is mainly water. Figure 5.10.b shows significantly different profiles for the extended reaction times. The profiles have effectively merged into a single peak that is slightly asymmetric for the 300 and 350 °C runs; the 400 °C run exhibits a symmetric profile. The absence of low temperature peaks indicate that the Type I coke

contribution is minimal. Figure 5.10.b shows peak maxima for the 300, 350 and 400 °C samples at, respectively, 540, 588 and 592 °C. The increasing peak maxima for increased reaction temperature indicates that the coke formation is further evolved at the higher temperatures. Figure 5.10.b also shows the 350 and 400 °C samples to exhibit a contribution from graphitic coke, which is typically associated with a degree of deactivation.<sup>5,17</sup>

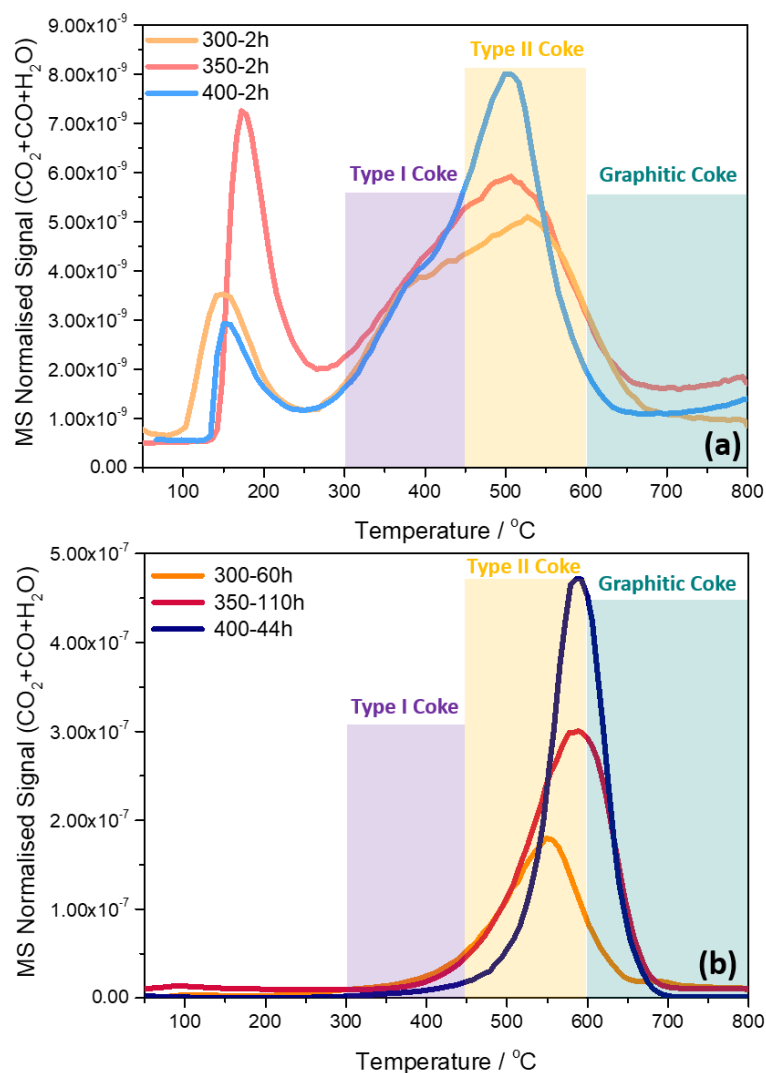


Figure 5.10: TPO profiles of the reacted catalyst samples at temperatures of 300, 350 and 400 °C. The mass spectrometer signals are normalised by catalyst mass and the CO<sub>2</sub>, CO and H<sub>2</sub>O signals have been summed together: (a) Short reaction times, (b) extended reaction times. The colour coded coke classifications (Type I coke mauve, Type II coke yellow, graphitic coke light green) indicate representative assignments as reported by Muller et al.<sup>17</sup> and Schulz.<sup>5</sup>

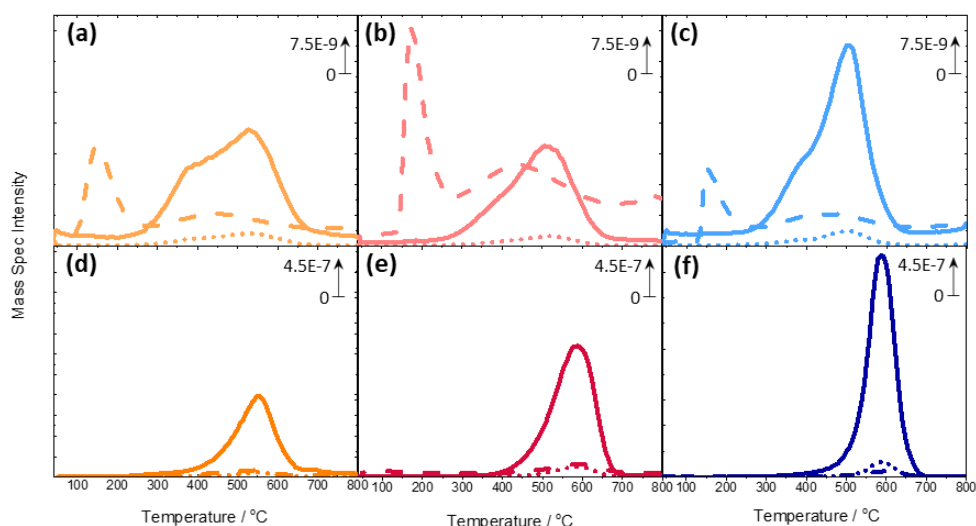


Figure 5.11: Mass normalised TPO Profiles (deconvoluted) of the reacted catalysts: the CO<sub>2</sub> profile is signified by a continuous line, the CO profile is signified by a dotted line, the H<sub>2</sub>O profile is signified by a dashed line. (a) 300-2h, (b) 350-2h, (c) 400-2h, (d) 300-60h, (e) 350-110h and (f) 400-44h

### 5.4.1 NMR Spectroscopy

NMR spectroscopy can often be used in order to understand the state of the catalyst. A combination of <sup>13</sup>C, <sup>29</sup>Si and <sup>27</sup>Al spectroscopy has been used in order to study the reacted samples.

#### 5.4.1.1 <sup>13</sup>C-NMR

Figure 5.11 presents the <sup>13</sup>C NMR spectra for the 2 h reaction runs at 300, 350 and 400 °C. The higher temperature spectra of 350 and 400 °C (Figure 5.12.b and 5.12.c) show signs of DME adsorbed on the surface (signals at 61 ppm and 61.7 ppm). The peaks at 51.7 ppm and 52.4 ppm are tentatively assigned to methanol present within the zeolite sample. It is noted that all samples were flushed with helium for about 10 minutes before being isolated; this process was expected to remove unreacted methanol. These peaks are absent in the 300 °C sample (Figure 5.12.a). Resonances with maxima at 129 and 131 ppm, indicating the presence of aromatic carbons<sup>21,22</sup>, accompanied by a manifold of spinning side bands due to the anisotropy of the aromatic carbon chemical shift, can be seen in all three samples, but are most evident in the 400 °C sample.

Figure 5.12 shows all samples to possess fine structure within the aliphatic carbon resonance peaks (10–25 ppm), indicating a range of aliphatic carbons are present during the early stages of the reaction at all temperatures. The 300 °C sample has a peak maximum at 19.6 ppm, which Meinhold and Bibby assign

to the methyl carbons of tetramethylbenzenes.<sup>23</sup> The peak maximum for the higher temperature counterparts is observed at 20.9 ppm. As increased methyl substitution is associated with up-shifting of carbon chemical shifts<sup>24</sup>, it is proposed that the aromatic species present have 2-3 methyl substitutions rather than 4. The fine structure in the resonances of both samples indicate a variety of substituted aromatics, possibly including olefins and alkanes.

Figure 5.13 shows the long reaction samples to exhibit dominant peaks at 17-20 ppm that correspond to aliphatic carbon. This is attributed to methyl groups attached to aromatic molecules.<sup>23</sup> The fine structure of the peaks seen for the short reaction samples is not so apparent, suggesting that the longer reaction times have homogenised the hydrocarbons within the HCP. The spinning side bands in Figure 5.13, identified by changing the rotation speed, are difficult to distinguish from the aromatic features (ca. 129 ppm).

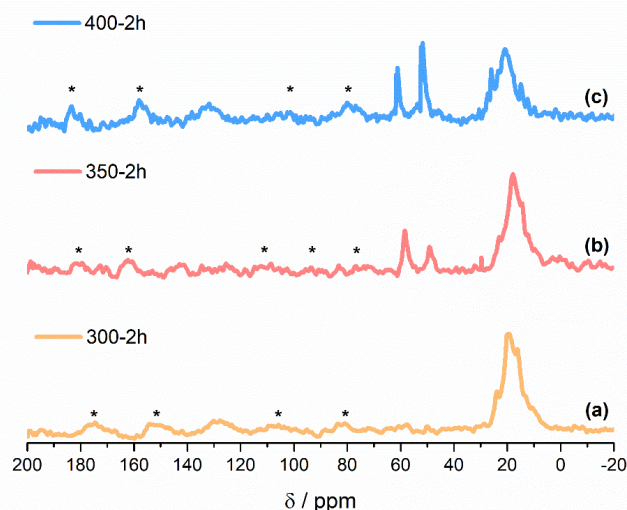


Figure 5.12: <sup>13</sup>C cross-polarisation magic angle spinning NMR spectra of the short reaction samples: (a) 300-2h; (b) 350-h (c) 400 -2h. Spinning side bands labelled with an asterisk (\*).

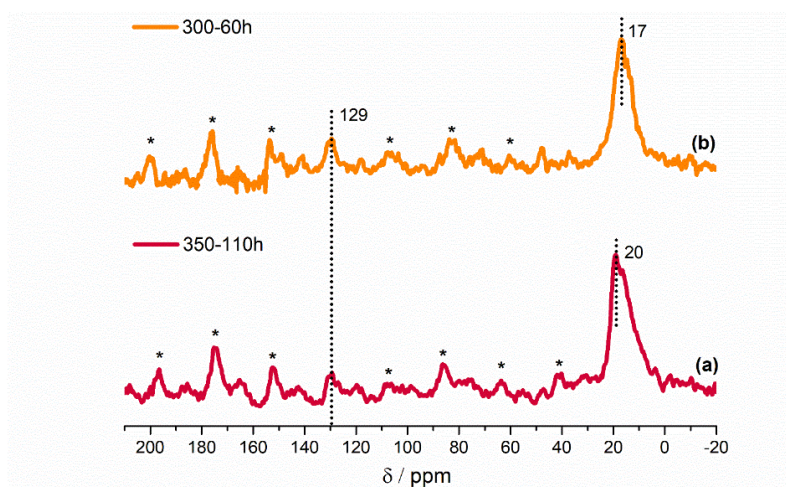


Figure 5.13: <sup>13</sup>C cross-polarisation magic angle spinning NMR spectra of the long reaction samples: (a) 300-60h; (b) 350-110h.

The 400-44h sample could not be analysed by this spectrometer because of the Aberdeen spectrometer going out of commission. Therefore, the NMR spectrometer at Johnson Matthey was used, which is a Bruker Neo 600 MHz Spectrometer. In order to compare the 400-44h with a relevant reference, the 350-110h sample was selected for examination by the same spectrometer.

To quantify the carbon signals, spectra from an active (350-110h) and quasi-deactivated (400-44h) catalyst were measured with a quantitative 90-180° Hahn-Echo pulse sequence with 1 rotor delay and high spinning speed.<sup>23</sup> The spectra are presented in Figure 5.14, with significant differences between samples apparent, indicating differences in the nature of the 'coke' formed in each case.

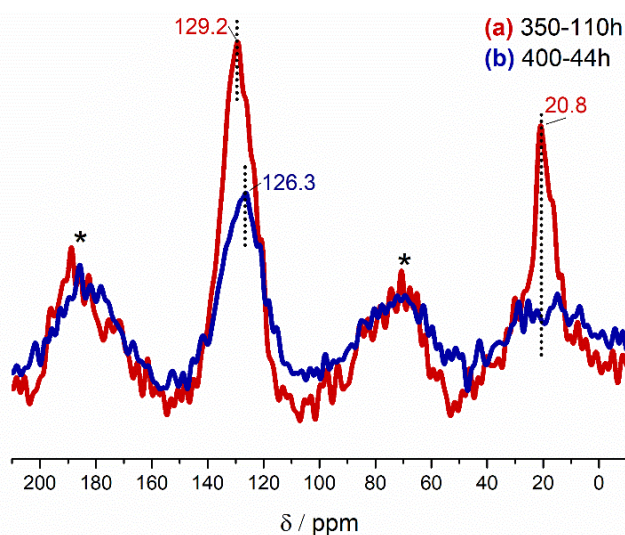


Figure 5.14:  $^{13}\text{C}$ -ssNMR spectra of the reacted ZSM-5 samples of (a) 350°C-110h (red) and (b) 400°C-44h (blue) collected at a spinning speed of 10 KHz.

The peak at 20.8 ppm in the 350-110h spectrum has disappeared in the 400-44h spectrum, whereas the peak at 129.2 ppm has upshifted to 126.3 ppm. The 20.8 ppm peak is assigned to the aliphatic carbon of the methyl carbons of methylated aromatic compounds.<sup>21</sup> The shoulders present at 16.6 ppm and 13.5 ppm are associated with polymethyl substitutions on aromatic compounds.<sup>21</sup> Both peaks at 129.2 ppm and 126.3 ppm are typical of aromatic carbons, both being close in chemical shift to that of methylated benzenes and polycyclics,<sup>22,23</sup> and both spectra contain strong spinning side bands (marked \*) due to the anisotropic aromatic chemical shift. Although it is not possible to assign the peaks to a particular hydrocarbon, both peaks in the two samples are broad with a range of shoulders suggesting different levels of methyl substitution. The quasi-deactivated catalyst contains significantly fewer methyl groups than the active catalyst.

For this pulse sequence, the integrated intensity is directly proportional to the number of carbon atoms present,<sup>25</sup> and Figure 5.14 shows the 400-44h spectrum to possess less carbon than the 350-110h sample. This outcome contrasts with the TPO analysis (Table 5.2) that indicates an opposite trend. This apparent contradiction is understood in terms of graphitic carbon and amorphous coke being NMR invisible.<sup>21,23</sup> An increasing fraction of NMR invisible carbon with increasing coke content was also observed by Meinhold and Bibby.<sup>21</sup>

#### 5.4.1.2 <sup>27</sup>Al NMR spectroscopy

Figure 5.14 presents the <sup>27</sup>Al NMR spectra for the short and long run MTH spectra recorded over a range of temperatures. The 51 ppm resonance is assigned to tetrahedral ( $T_d$ ) aluminium and the 3 ppm resonance is attributed to octahedral ( $O_h$ ) aluminium present in the framework.<sup>26</sup> The  $O_h$  Al signal is completely gone at the long reaction samples (Figure 5.15.c and 5.15.e) and there is also a slight shift in the  $T_d$  Al signal to a higher field. A similar outcome is reported for heavily coked samples when DME is used as feedstock (it will also be discussed further in chapter 7).<sup>[11]</sup> In comparison to the unreacted ZSM-5 (Figure 5.15.a), the overall signal intensity is decreased even at the short reaction times. This is attributed to displacement of adsorbed water around tetrahedral Al sites by hydrocarbon molecules increasing the transverse relaxation time ( $T_2$ ) and second order quadrupolar broadening term.<sup>23</sup>

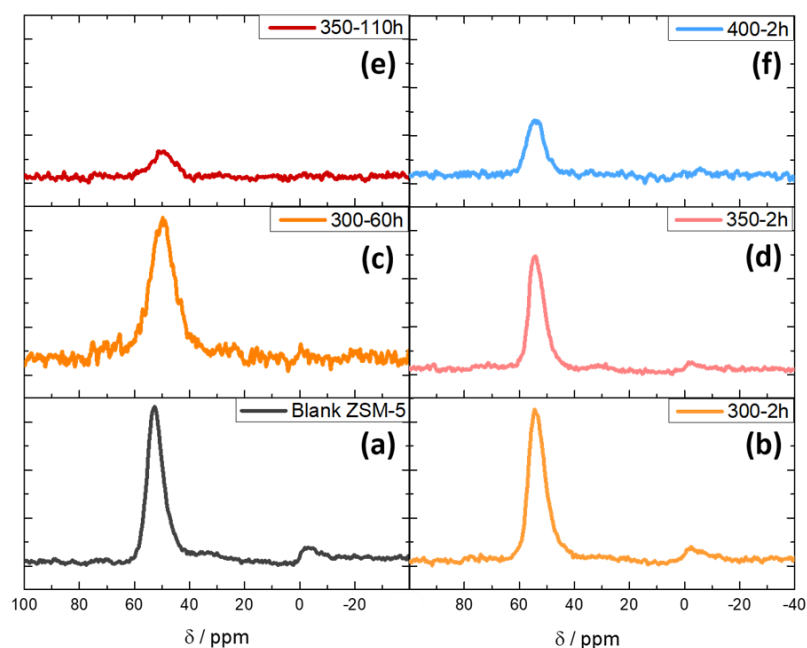


Figure 5.15: <sup>27</sup>Al-NMR Spectra ( $B_0 = 9.4$  T) of the MTH reacted samples contrasted against unreacted ZSM-5: short reaction times; and extended reaction times. (a) unreacted ZSM-5; (b) 300-2h; (c) 300-60h; (d) 350-2h; (e) 350-110h; (f) 400-2h.

### 5.4.1.3 $^{29}\text{Si}$ -NMR spectroscopy

Figure 5.15 presents the  $^{29}\text{Si}$  NMR spectra for the short and long run MTH spectra recorded over a range of temperatures. The signal at -113 ppm is due to  $\text{Si}(\text{OSi})_4$  in the framework, with the -107 ppm signal assigned to  $\text{Si}(\text{OSi})_3(\text{OAl})$ .<sup>[11]</sup> Compared to the unreacted ZSM-5 (Figure 5.16.a), there is a progressive decrease in the -107 ppm signal, even with the 2 hour reactions, which suggests that framework dealumination is taking place. Framework dealumination has previously been linked to steam production in the initial stages of the reaction.<sup>27</sup>

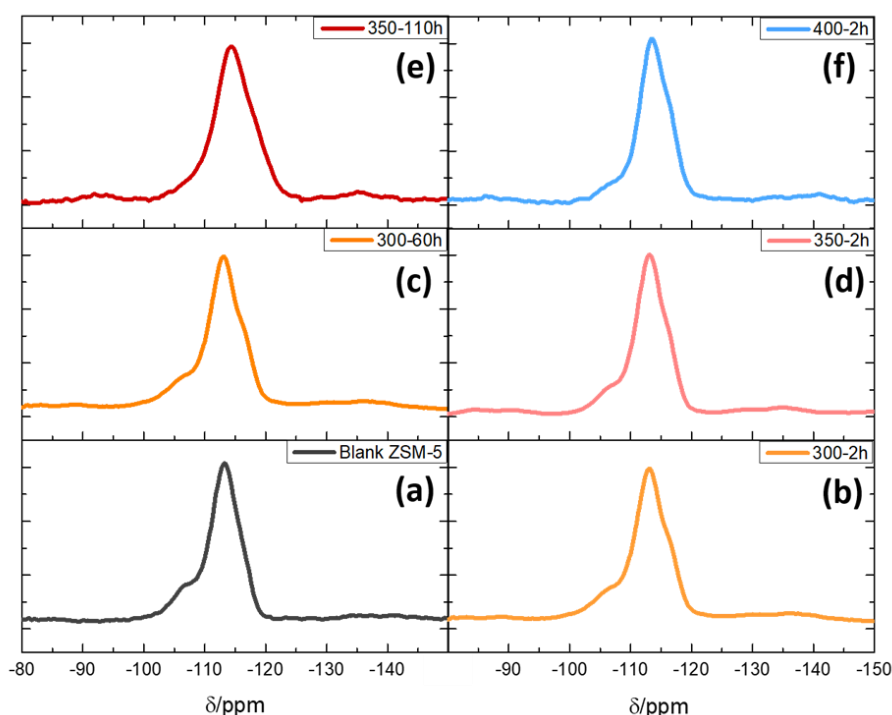


Figure 5.16:  $^{29}\text{Si}$ -NMR spectra ( $B_0 = 9.4 \text{ T}$ ) of the MTH reacted samples contrasted against unreacted ZSM-5. (a) unreacted ZSM-5; (b) 300-2h; (c) 300-60h; (d) 350-2h; (e) 350-110h; (f) 400-2h.

The  $^{29}\text{Si}$  NMR spectra recorded at a magnetic field strength of 9.4 T (Figure 5.16) indicate dealumination to be active at the higher temperatures for the short run samples. Figure 5.15.c shows the -107 ppm signal ( $\text{Si}(\text{OSi})_3(\text{OAl})$ ) to be almost absent for the long-run 350°C sample (350-110h). Figure 5.17 presents the spectra, of the 400-44h and 350-110h sample which were collected with the 600 MHz spectrometer at an elevated magnetic field strength of 14.1 T. The intensity of the 400 °C spectrum has been normalised to the peak intensity of the 350 °C spectrum. The spectra overlap almost completely, indicating that the silica-to-alumina ratio of the two samples are comparable.

This series of measurements shows that the dealumination process is most prominent during the initial stages of reaction.<sup>27</sup>

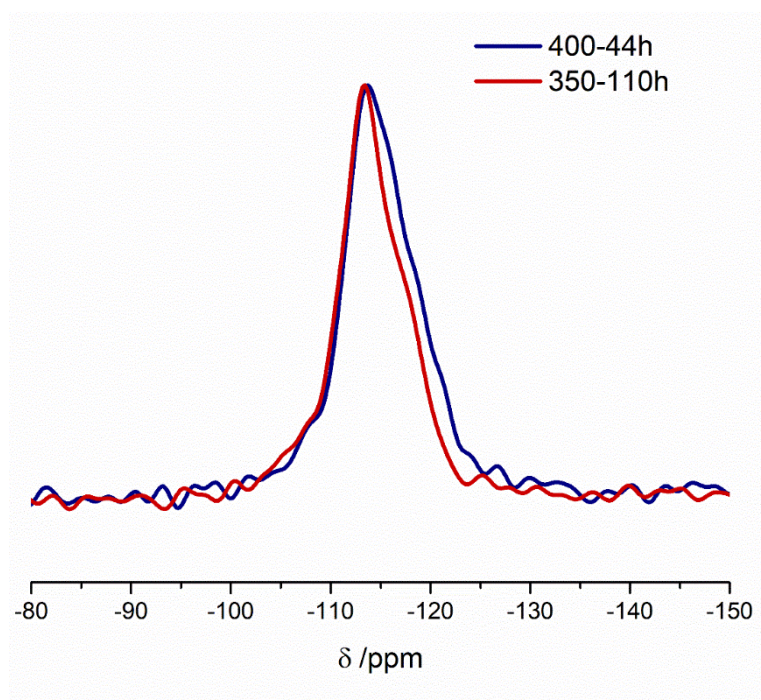


Figure 5.17: Solid state  $^{29}\text{Si}$  MAS NMR Spectra ( $B_0 = 14.1$  T) of (a) 350-110h sample and (b) 400-44h sample. The peak maximum for (b) is scaled with respect to (a).

### 5.4.2 DRIFTS

Figure 5.18 shows a stack plot of the DRIFTS data collected of the short reaction samples at the three reaction temperatures. The energy range is between  $2500 - 4000 \text{ cm}^{-1}$  because the lower region is obstructed by strong framework bands of the zeolite. Figure 5.18.a shows the unreacted ZSM-5 to exhibit three major OH environments: (i) Brønsted acid sites ( $3595 \text{ cm}^{-1}$ ); (ii) extra-framework aluminium (Al-OH) ( $3653 \text{ cm}^{-1}$ ); (iii) silanol groups located at the external surface of the zeolite ( $3736 \text{ cm}^{-1}$ ).<sup>12,28,29</sup>

Upon reaction, Figure 5.18(b-d) show that increasing temperature changes the intensity ratio between the three OH peaks. Increasing the temperature progressively diminishes the relative intensity of the Brønsted acid sites, whilst there is a relative increase in the AlOH band intensity; this scenario is suggestive of hydrolysis of the acid sites at elevated temperatures.

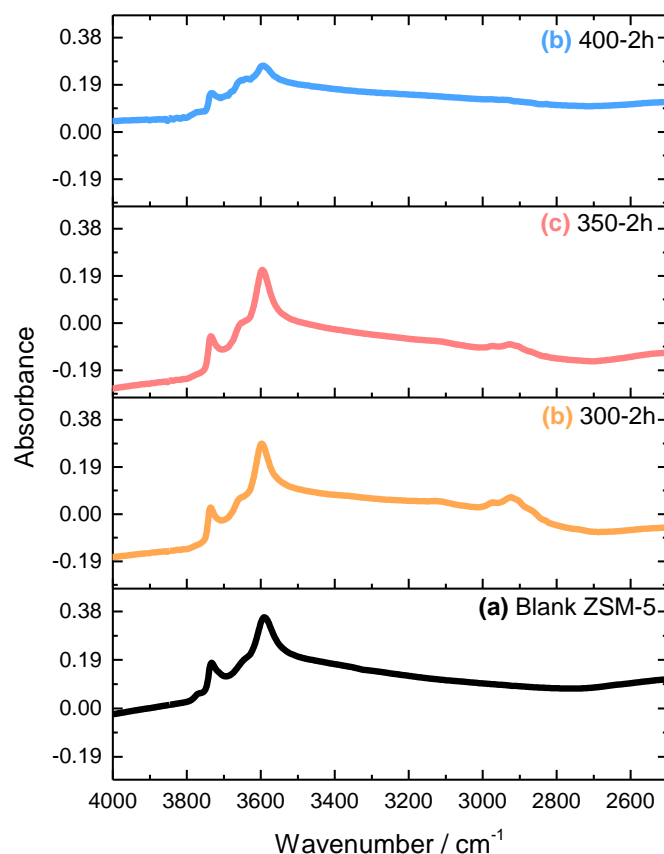


Figure 5.18: DRIFTS spectra ( $4000\text{-}2500\text{ cm}^{-1}$ ) of the ZSM-5 catalyst post-reaction after 2 h T-o-S at the following reaction temperatures: (b) 300, (c) 350 and (d) 400 °C. The spectra were recorded at the reaction temperatures, and normalised on the zeolite overtone at  $1864\text{ cm}^{-1}$ . Spectrum (a) corresponds to an activated but unreacted sample of ZSM-5 recorded at 350 °C.

Wide-scan DRIFTS spectra for the extended run samples are presented in Figure 5.19. This format is selected in order to illustrate difficulties that may be encountered when using infrared spectroscopy to examine heterogeneous catalysts for extended periods of T-o-S. Compared to Figure 5.18, a significant broadening of the OH region is observed, making it difficult to distinguish the different OH environments. This loss of spectral identity in the diagnostic  $4000\text{-}2500\text{ cm}^{-1}$  region of the spectrum could arise from two factors: (i) a loss of Brønsted acid sites and/or (ii) a loss of diffuse reflectivity due to the sample colour becoming progressively darker at the longer reaction times. Although the  $\nu(\text{C-H})$  modes of the HCP are visible for the 300 and 350 °C spectra (Figure 5.19.b and 5.19.c), with the peaks resembling the coke bands seen for catalysts previously used for methanol conversion at 350 °C over three days,<sup>12</sup> there is an almost complete loss of diffuse reflectivity for the 400 °C sample (Figure 5.19.d). Indeed, it is possible that (i) and (ii) could be coincident events: Table 5.2 shows the long-run 400 °C sample to possess the highest coke content and neither  $\nu(\text{C-H})$  or  $\nu(\text{O-H})$  modes are detectable in Figure 5.19.d. Moreover,

the fact that Figure 5.19 shows a progressive increase in the baseline of the infrared spectrum for increasing reaction temperature (signifying greater advancement of the reaction coordinate) illustrates a limitation of IR spectroscopy to characterise and interrogate aged heterogeneous catalysts. Against this background, it was deemed profitable to employ the technique of inelastic neutron scattering (INS) spectroscopy to access the vibrational spectrum of aged MTH catalysts.

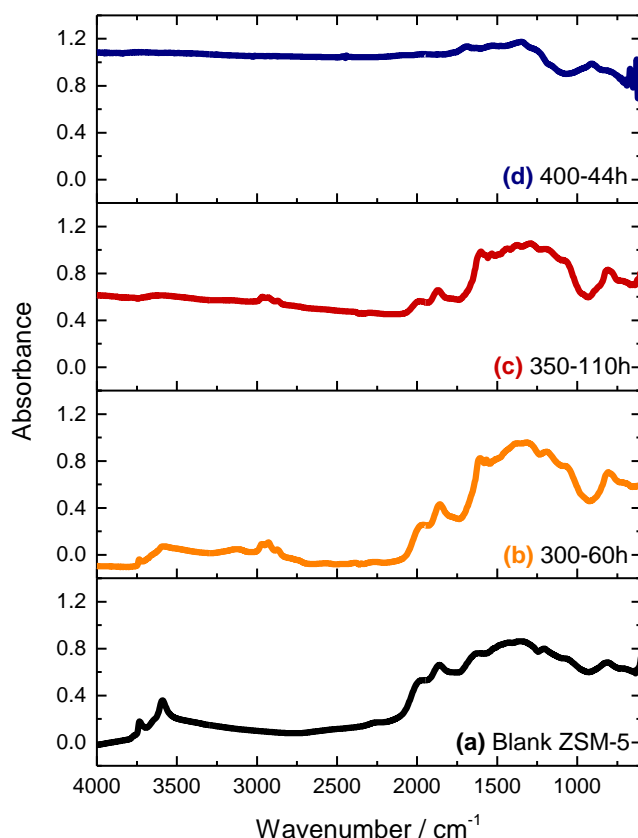


Figure 5.19: DRIFTS spectra (4000-500  $\text{cm}^{-1}$ ) of the ZSM-5 catalyst post-reaction after extended T-o-S at the following reaction temperatures: (b) 300-60h (c) 350-110h and (d) 400-44h. The spectra were recorded at their reaction temperature. Spectrum (a) corresponds to an activated but unreacted sample of ZSM-5 recorded at 350°C.

### 5.4.3 INS

Compared to optical spectroscopic probes such as IR spectroscopy, INS is a relatively insensitive technique.<sup>2</sup> This makes the initiation stage of the MTH reaction difficult to observe by INS. A reaction time of 2 h is representative of the later stages of catalyst conditioning and the early stages of steady-state operation. Figure 5.20 presents the INS spectra for T-o-S = 2 h as a function of reaction temperature. The spectra are of low intensity indicating relatively little hydrogenous material to be present. They are complex and insufficiently

distinct for absolute assignments to be made. This is because the HCP is still in the process of being established. Many of the preliminary products and starting hydrocarbons of the HCP are present in small quantities but with no one species or functional group dominating the composition. The mixture of hydrocarbons leads to the peak broadening observed. The ratio between the intensities of the different broadened peaks is changing with temperature, suggesting that the hydrocarbon pool progression is different at the three temperatures studied from the initial stages of the reaction. The  $^{13}\text{C}$  NMR spectra of the 350 and 400 °C samples indicate unreacted methanol and DME to be present (Fig 5.12), no bands directly attributable to these entities are observable in Figure 5.20. The lack of definition of the bands indicates an absence of discrete molecular entities; with the profile being consistent with a mixture of species. The conclusion is that the hydrocarbon pool is not fully developed after T-o-S = 2 h.

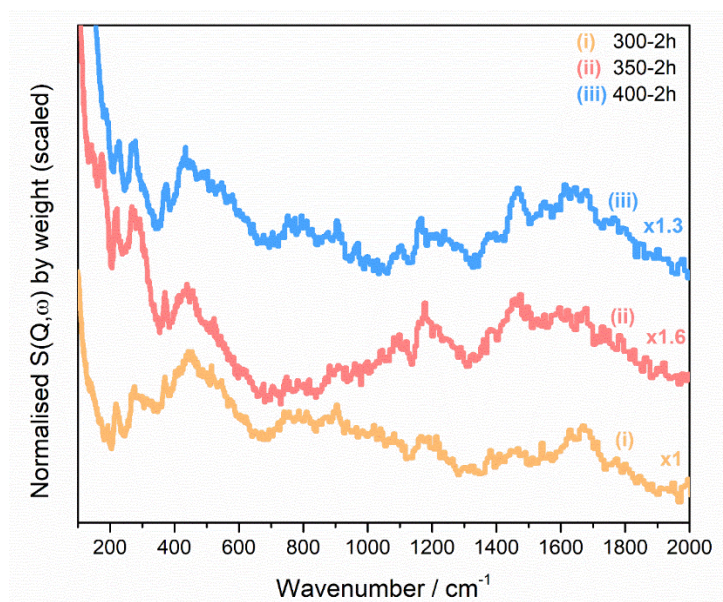


Figure 5.20: INS spectra collected with the TOSCA spectrometer for the short reaction times (2 h) as a function of reaction temperature: (i) 300, (ii) 350 and (iii) 400 °C.

The INS spectra for the long-run samples that correspond to mature steady-state and quasi-deactivation regimes are presented in Figure 5.21. In contrast to the short run spectra, well-defined INS spectra are observed. Two different INS spectrometers were used to obtain spectra in the range 20-4000  $\text{cm}^{-1}$  at favourable resolution. Figure 5.21.a presents spectra in the range 0-2000  $\text{cm}^{-1}$  that were recorded using the TOSCA spectrometer,<sup>2,30,31</sup> whereas, Figure 5.21.b shows the spectral response over the energy range 2000-4000  $\text{cm}^{-1}$  that was recorded using the MAPS spectrometer.<sup>2,32</sup> Figure 5.21 defines the vibrational fingerprint of the HCP for the extended duration variable

temperature runs. This is the first time that vibrational spectra of this specification (energy range and resolution) for MTH catalysts operative over such a wide range of conditions have been reported.

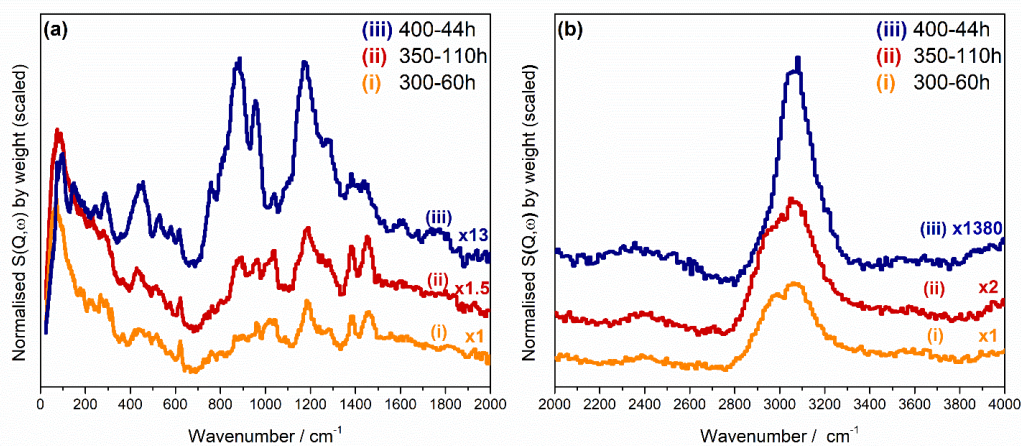


Figure 5.21: INS spectra of the MTH reacted ZSM-5: (i) 300°C for 60 h; (ii) 350°C for 110 h; (iii) 400°C for 44 h. The spectra are normalised to sample mass and scaled by the factors shown. (a) Spectra collected using the TOSCA spectrometer;<sup>2,30,31</sup> (b) spectra collected with the MAPS spectrometer at an incident energy of 5244 cm<sup>-1</sup> using the A-chopper package.<sup>2,32</sup>

The spectra for the 300 (i) and 350 °C (ii) runs in Figure 5.21. are comparable and exhibit a similar pattern to previously reported ZSM-5/MTH HCP INS spectra.<sup>12,13</sup> The general profile observed for both samples also closely resembles the spectrum of ZSM-5 upon exposure to dimethyl ether at elevated temperatures, which will be discussed in Chapter 7. The same pattern has also been observed when a range of methyl acetate/methanol solutions has been used as feedstock under MTH reaction conditions (Chapter 7). Both of those cases will be discussed further in Chapter 7. From the variety of spectral features present in Figure 5.21.a (i and ii), no single molecular entity is deemed to be present; the spectra represent a mixture of hydrocarbon species. Figure 5.21.a (iii) shows significant changes on progressing to the 400°C sample. As considered above, the 400-44h sample has experienced a degree of deactivation; inspection of Figure 5.21.a (iii) shows that this has altered the composition and form of the hydrocarbonaceous entities retained within the porous network of the zeolite, *i.e.* the all-important HCP.

Figure 5.21.b presents the spectra in the C-H stretching region of the spectrum and indicates the reaction temperature to affect the distribution of sp<sup>3</sup> hybridized C-H modes (*i.e.* aliphatic C-H) and sp<sup>2</sup> hybridized C-H modes (*i.e.* olefinic and/or aromatic C-H). INS spectroscopy is a quantitative technique, where the scattering intensity is proportional to the number of oscillators and

the amplitude of motion that the hydrogen experiences within a specific mode.<sup>2,4</sup> This means that curve fitting can be used to determine the ratio of aliphatic: olefinic/aromatic C-H modes for any given spectrum.

Figure 5.22 present curve fitting outcomes for the spectra shown in Figure 5.21.b. The ratio of  $sp^3$  :  $sp^2$   $\nu(C-H)$  modes for the 300 °C sample is 1: 1.35, which decreases to 1: 1.14 for the 350 °C sample. The  $sp^3$  hybridized  $\nu(C-H)$  signal is absent in the case of the 400 °C sample (Figure 5.20.b(iii)). Thus, for the long run samples, increasing temperature leads to a diminution of the aliphatic component of the HCP. Moreover, the scaling factors illustrated in Figure 5.21.b reveal a further facet of modifications extant within the HCP as a function of temperature and T-o-S. Namely, the quasi-deactivated sample contains significantly less hydrogen than that seen for steady-state operation, as represented by the spectrum of the 350 °C sample (Figure 5.21.b(ii)). Collectively, Figure 5.21.b signifies the presence of a dehydrogenation pathway within the hydrocarbon pool as the catalyst evolves towards a deactivation regime. The spectrum of the 400-44h sample closely resembles that of amorphous carbon, with hydrogen termination of the graphene planes.<sup>33–35</sup> The low energy spectra (Figure 5.21.a) are consistent with this deduction, this will be discussed further in the following section.

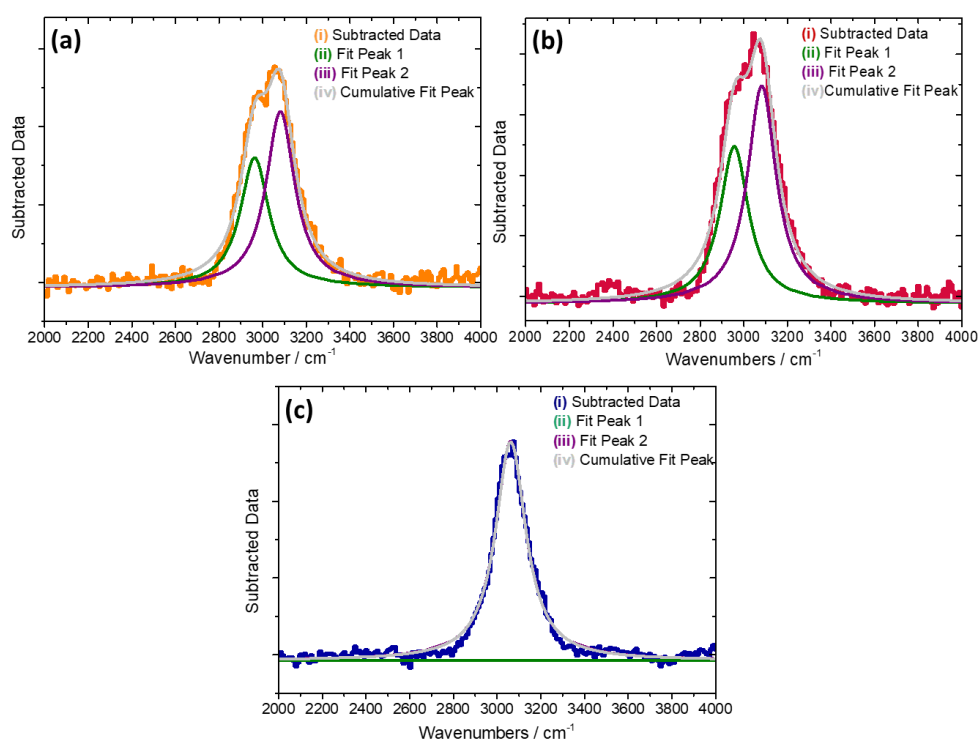


Figure 5.22: Peak fitting of (a) 300-60h (b) 350-110h (c) 400-44h samples. (i) background subtracted experimental dataset, (ii)  $sp^3$  hybridised  $\nu(C-H)$  peak, (iii)  $sp^2$  hybridised  $\nu(C-H)$  peak, (iv) cumulative fit, i.e. (ii) + (iii).

#### 5.4.4 INS Assignments

As has been discussed in Chapter 3, the INS spectra of a variety of hydrocarbons have been acquired and analysed. The molecules examined included cyclic and polycyclic unsaturated compounds (including all 13 methylated benzenes), that are considered to be candidate molecules that could contribute to the HCP. Synthetic spectra were generated by adding spectra of the model compounds in an equimolar ratio; similar hydrocarbons were added together in order to highlight common spectral features. The results of this process is shown in Figure 5.23 where the simulated spectra are compared to the spectrum for the long-run steady-state sample (350-110h, Figure 5.20.a(ii)).

A doublet of peaks at  $1354\text{ cm}^{-1}$  and  $1458\text{ cm}^{-1}$  are evident in all plots in Figure 5.21(a), with reference to Figure 5.23.a they are assigned to symmetric and asymmetric  $\text{CH}_3$  bending modes of highly methylated benzenes ( $\geq 4$  methyl groups). The same doublet is also seen in methylated polycyclic aromatic molecules (Figure 5.23.b), therefore some of the intensity could correspond to those hydrocarbons as well. This is indicative of high levels of methylation happening within the HCP. Peaks about  $1200\text{ cm}^{-1}$  are observed in the simulated spectra of polycyclic molecules (Figure 5.23.b) but these features are absent in the spectra of methylated benzenes (Figure 5.23.a). On this basis, the strong peak at  $1200\text{ cm}^{-1}$  with a high energy shoulder at  $1246\text{ cm}^{-1}$  is assigned to C-H bending modes of polycyclic molecules such as naphthalene.<sup>36,37</sup> When inspecting the ratio of the  $1200\text{ cm}^{-1}$  peak with other peaks in the reference compounds, it is seen that for all the polycyclic hydrocarbons it has approximately the same intensity as the peak found at  $960\text{ cm}^{-1}$  that corresponds to a CH wag.<sup>36</sup> However, in the steady-state MTH spectrum (Figure 5.23) the relative intensity of the two peaks ( $1200\text{ cm}^{-1}$  and  $960\text{ cm}^{-1}$ ) is different, with the  $1200\text{ cm}^{-1}$  peak being significantly more intense. This suggests that there is an additional species that is also contributing to the intensity of the  $1200\text{ cm}^{-1}$  peak.

In the MTH spectrum (Figure 5.23(i)) a sharp band is located at  $600\text{ cm}^{-1}$ . This band is only present in the spectra of naphthalene model compounds and, consequently, it is assigned to the double aromatic ring distortion of naphthalenes.<sup>37</sup> The broad peaks below  $400\text{ cm}^{-1}$  are largely attributed to the methyl torsions of the methylated benzenes and the polycyclic species. It was

shown that the degree of methyl substitution on the aromatic rings and the local environment both strongly influence the methyl torsion transition energies (Chapter 3). This helps explain why there are no distinct methyl torsion peaks present in the HCP spectrum (Figure 5.23(i)).

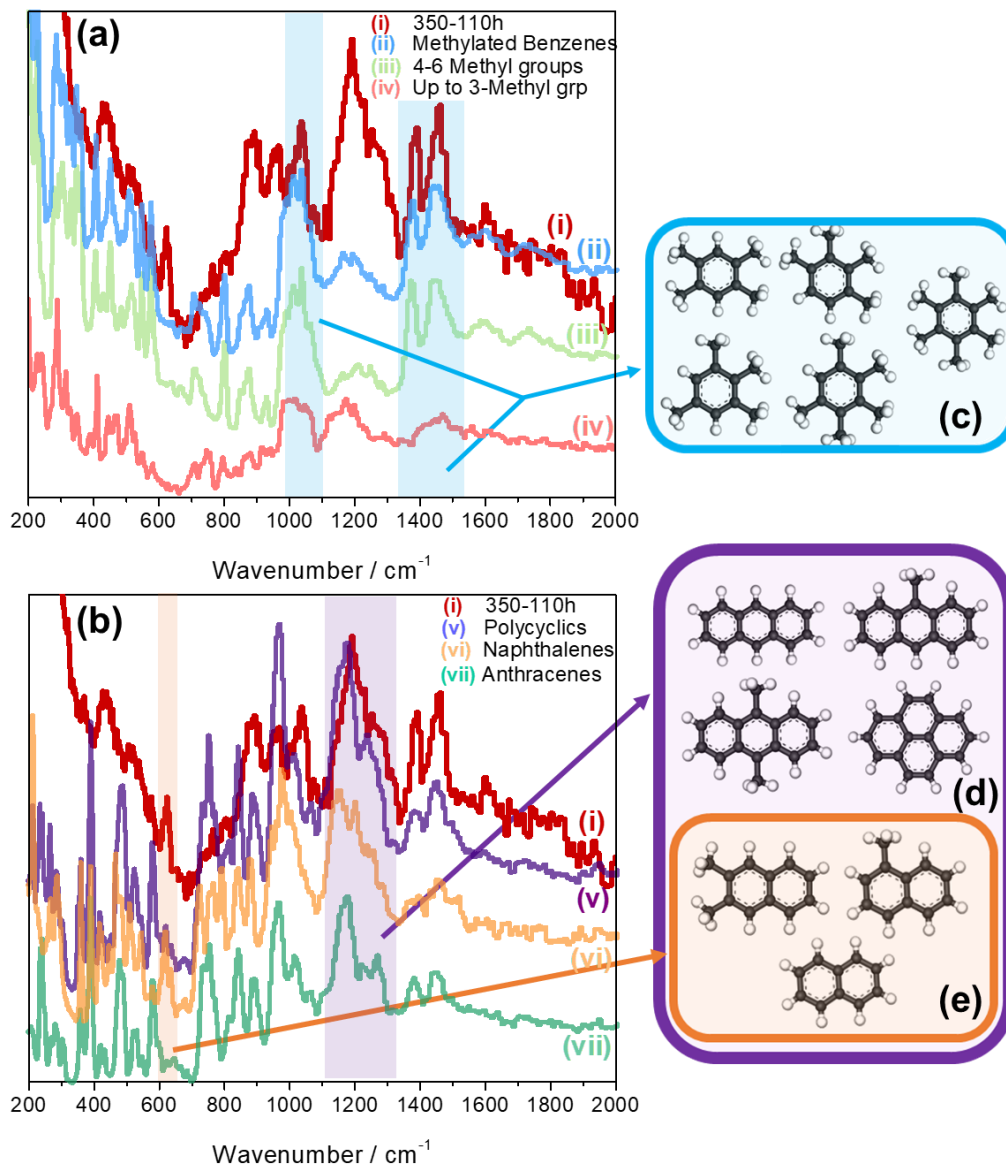


Figure 5.23: Experimental 350-110h spectrum (i) compared with the generated addition spectra (equimolar additions of model compound spectra). The colour coding highlights regions which are characteristic of the different hydrocarbons. (a) Comparison with methylated benzenes: (ii) all of the methylated benzenes; (iii) methylated benzenes with more than 4 substitutions; (iv) methylated benzenes with up to 3 methyl substitutions. (b) Comparison with polycyclic aromatic molecules: (v) all polycyclics, (vi) naphthalenes and (vii) anthracenes. Sections (c)-(d) illustrate the principal contributors to the spectra: (c) methylated benzenes with  $\geq 4$  methyl groups; (d) anthracenes and pyrene; (e) naphthalenes

As discussed above, the spectrum for the long-run 400 °C sample (400-44h, Figure 5.21) is representative of a sample approaching deactivation. Interestingly, the INS spectrum closely matches that reported for activated carbon and glassy carbon.<sup>33,34</sup> To illustrate this point, Figure 5.24 compares the INS spectrum of the quasi-deactivated HCP alongside that of reference spectra for graphite<sup>34</sup> and glassy carbon<sup>33</sup>. Glassy carbon is a type of amorphous carbon with no long-range crystalline order.<sup>38,39</sup> The graphite spectrum (Figure 5.24(iii)) does not share any of the spectral features with the 400-44h sample, whereas the glassy carbon (Figure 5.24(ii)) provides a close match. This outcome suggests that the coke that forms on the surface of the zeolite as the catalyst deactivates, (Figure 5.2) is irregular and closer to glassy carbon than structured graphite. The major peak at  $\sim 880\text{ cm}^{-1}$  is indicative of isolated hydrogen atoms at carbon edge termination points.<sup>33,35</sup> It is presumed that a phase of the HCP evolution involves polycyclic aromatics continuing to grow within the zeolite pores until they reach another set, which leads to termination. Chua and Stair suggested from UV-Raman spectroscopy that the amorphous carbon present is not 2 dimensional but rather closer to a chain-like topology.<sup>40</sup> This agrees with the INS observation of the amorphous carbon being similar to glassy carbon in structure and looking nothing like graphite.

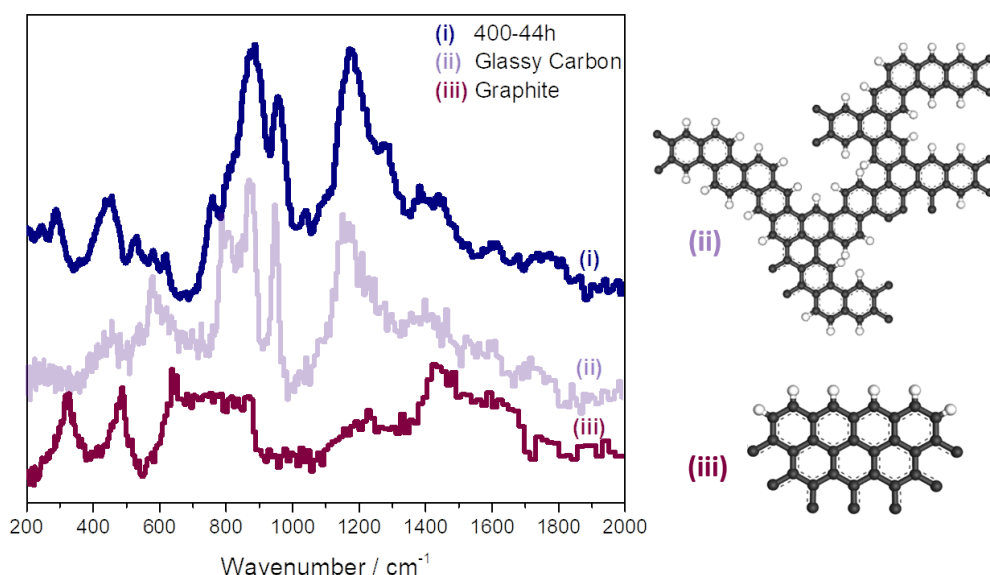


Figure 5. 24: Experimental 400-44h spectrum (i) compared with model compounds: (ii) glassy carbon<sup>33</sup>; (iii) graphite<sup>34</sup>. (Glassy carbon and graphite molecule schematics are a schematic representation and not specific molecular models).

The doublet at  $1354\text{ cm}^{-1}$  and  $1458\text{ cm}^{-1}$  is still present in the 400-44h spectrum, which suggests that the HCP pool products are still present, but at a much

lower degree, as the spectrum is dominated by amorphous carbon. The presence of amorphous carbon also explains the anomalous intensity of the  $1200\text{ cm}^{-1}$  peak in the spectra of the 300 and 350°C samples, showing that coke is already present in a working, steady-state catalyst (consistent with the TPO data, Figure 5.10). This is not however the dominant form of deactivation in those samples as seen from the TPO data (Figure 5.10) and the higher visibility of the HCP peaks in their INS spectra (Figure 5.21). This is consistent with literature that suggests that at lower temperatures the dominant deactivation pathway is due to polycyclic methylated aromatic build up within the pores, whereas at higher temperatures the major pathway of deactivation is pore blockage due to external coke.<sup>5,7,41,42</sup>

The presence of coke also explains the apparent contradiction that on increasing T-o-S the degree of methylation increases (see catch-pot analysis, Figure 5.3), which requires the presence of  $\text{sp}^3$  hybridised  $\nu(\text{C-H})$ , but the ratio of  $\text{sp}^3:\text{sp}^2$  C-H decreases with time, *i.e.* the processes of ring methylation and dehydrogenation are occurring in parallel. This also explains the difference in NMR visible carbon which was observed in the  $^{13}\text{C}$ -NMR spectra (Fig. 5.12) and shows that the  $^{13}\text{C}$ -NMR measurements are supportive of the INS-derived concept of the evolving nature of the HCP, which is influenced by temperature and time.

## 5.5 Changing the Contact Time

### 5.5.1 Reaction Monitoring

For the sample 400-Frt (see Table 5.1), the contact time was changed from 0.0064 h to 0.0048 h whilst keeping the WHSV the same as the 400-44h sample explored before. The reduced contact time means that the methanol moves through the sample faster. Due to complications with the online monitoring, the catch-pot sampling was changed from every 12 hours to every 2 hours which allowed for the monitoring of the reaction via the liquid products and GC-MS. The percentage peak areas change over the time on stream can be seen in Figure 5.25.

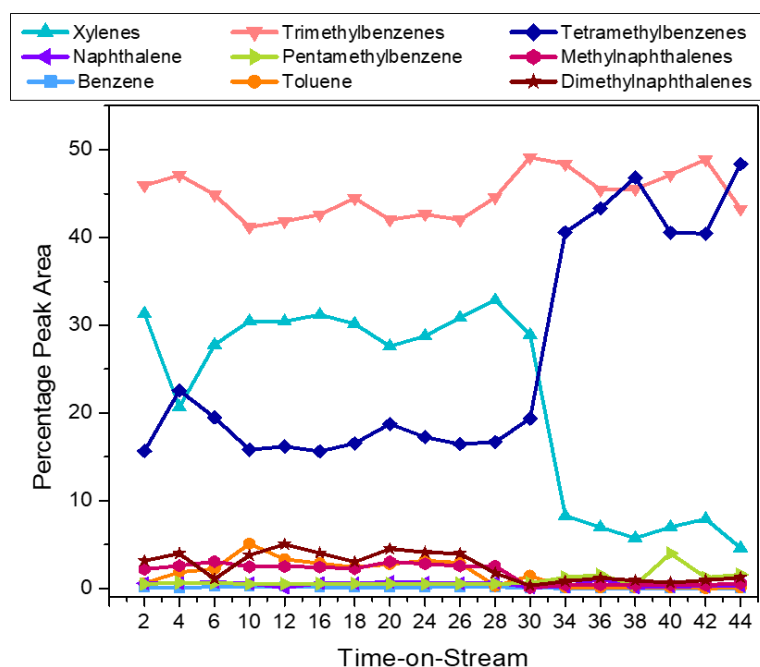


Figure 5.25: Percentage peak areas of the GC-MS liquid product analysis plotted against time-on-stream for the reactions of sample 400-44h-Frt

As can be seen from Figure 5.25, the trends observable in Figure 5.4.c are also seen here. Namely, a relatively stable trimethylbenzene production with a gradual increase in tetramethylbenzenes and a drop in xylene production. This trend looks to happen a lot more sharply than seen in Figure 5.4.c which could be because the catch-pot products of +32hrs and over, were analysed on a different day after the filament of the GC-MS was changed. Unfortunately, re analysing the whole batch turned out to be problematic and could not be done. The samples analysed with the new filament, have a little bit more intensity than the previous ones, however, as we are looking it as a percentage of total peak areas, it should not make a difference.

### 5.5.2 Post Reaction Analysis

The 400-44h-Frt sample was analysed with the same techniques as above with the post reaction characterisation data summarised in Table 5.3. The post reaction analysis of this sample suggests that the 400-44h-Frt sample is not as deactivated as the 400-44h sample. The coke content is significantly smaller compared to the 20.2 wt% coke present in the 400-44h sample. The TPO profile of the 400-44-Frt sample can be found in Figure 5.26. The peak looks to be asymmetrical in shape, with a peak maximum at 575 °C, suggesting that very little Type I coke is present within the sample.

Table 5.3: Nitrogen adsorption data and coke content for the 400-44h-Frt sample prepared using the ISIS/Glasgow reactor. The 400-44h sample data taken from Table 5.2 are shown for easy reference

400-44h-Frt			400-44h	
$S_{\text{BET}}$	$\text{m}^2\text{g}^{-1}$	202		38
$V_{\text{miropore}}$	$\text{cm}^3\text{g}^{-1}$	0.007		0.011
$S_{\text{external}}$	$\text{m}^2\text{g}^{-1}$	32.1		12.2
Coke Content	wt%	8.45		20.20

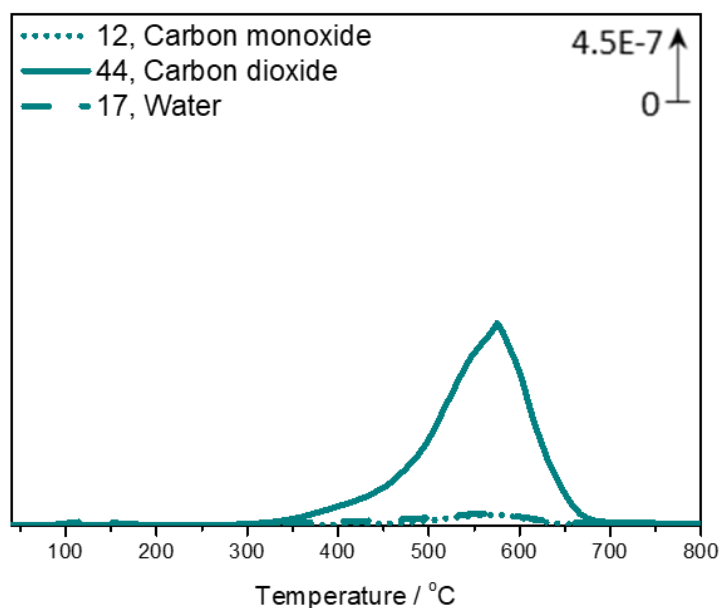


Figure 5.26: TPO profile of sample 400-44-Frt

Figure 5.27 shows the ss-NMR spectra of the 400-44h-Frt sample. The  $^{13}\text{C}$ -NMR sample shows the aliphatic peak to have a lot of fine structure, suggesting a range of aliphatic carbons present. As has been discussed in section 5.4.1.1, the peak maxima and the shoulder peaks have been associated with multiple methyl substituted aromatic compounds.<sup>22,23</sup> It must be noted that the 400-44h sample shows almost no aliphatic carbon whereas the 400-44h-Frt shows a  $^{13}\text{C}$ -NMR spectrum closer to that of the 350-110h and 300-60h spectra than the 400-44h sample. This again implies that even though the sample was completed at the same temperature and time-on-stream, the difference in contact time affected how far the reaction progressed. The silicon and aluminium spectra do not show anything new, with the  $^{27}\text{Al}$ -NMR showing comparable intensities with the 350-110h sample.

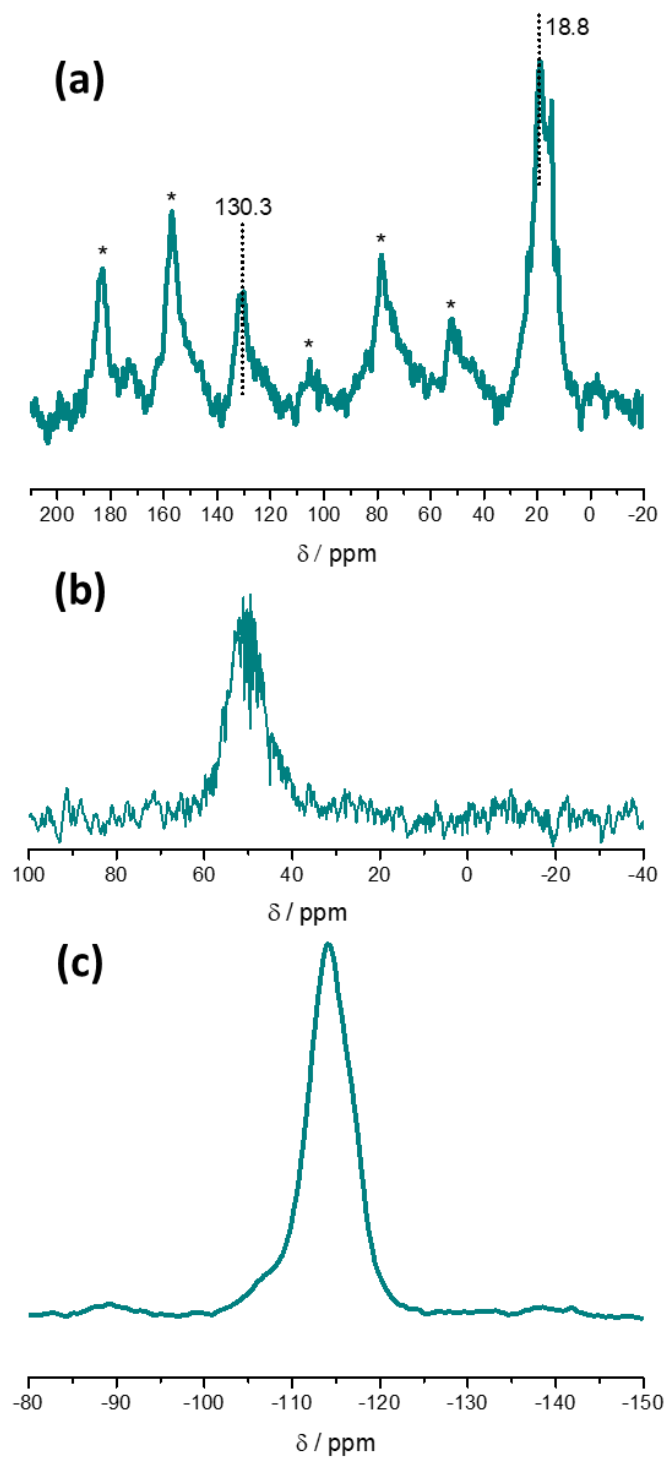


Figure 5. 27: ssNMR of the 400-44h-Frt sample completed with the 400 MHz Spectrometer. (a)  $^{13}\text{C}$ -NMR (b)  $^{27}\text{Al}$ -NMR and (c)  $^{29}\text{Si}$ -NMR

The DRIFTS spectra shown in Figure 5.28, are a comparison between the DRIFTS spectrum of 400-44h-FRt with both the 350-110h and 400-44h spectra. The spectra show that the 400-44h-Frt sample is closer to the 350-110h sample than it is to the 400-44h sample. There is still some distinguishable features in the acid site region, with all three OH peaks being identifiable. The difference

between the two 400 samples is very prominent, as the 400-44h sample the zeolite framework modes are hard to see with IR due to the colour of the sample.

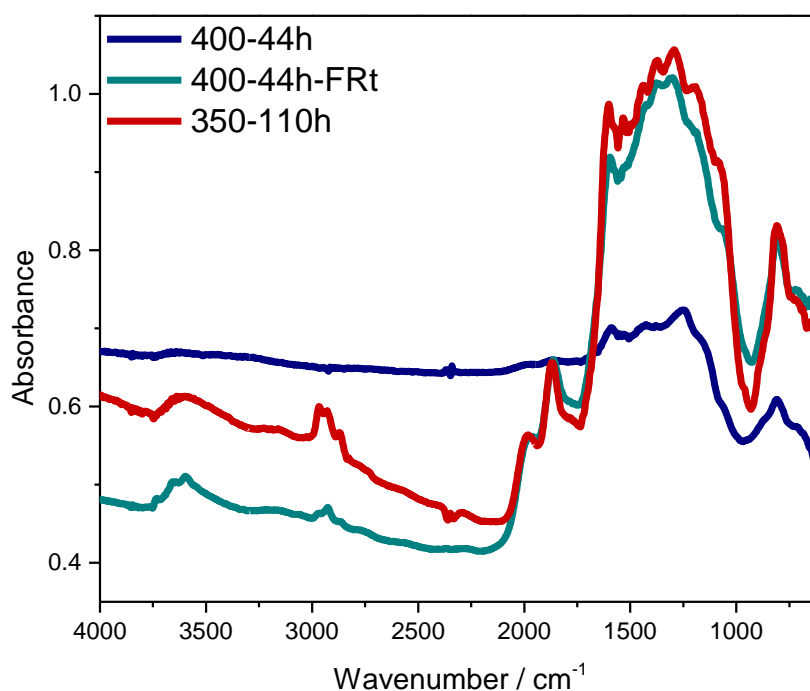


Figure 5.28: DRIFTS spectra of the 400-44h sample (blue), the 350-110h sample (red) and 400-44h-Frt sample (cyan)

The INS spectrum of the 400-44h-Frt sample can be found in Figure 5.29. The pattern shown in Fig. 5.29.a is the same pattern which was observed with the 300-60h and 350-110h samples. The pattern has been identified as the vibrational fingerprint of the hydrocarbon pool within a still working catalyst. The INS spectrum is a clear indication that the two 400 °C samples are in completely different stages within the MTH catalytic cycle. Figure 5.29.b shows the high energy spectrum of the sample. The peak shape suggests that both  $sp^3$  and  $sp^2$  carbon is present within this sample, in contrast with the 400-44h sample where no  $sp^3$  contribution was found. Figure 5.30 shows the peak fitting for the spectrum seen in Fig. 5.29.b. The ratio of  $sp^3:sp^2$  is 1:2.41. This means that this sample has a lot more  $sp^2$  carbon than  $sp^3$ , and even though the coke content suggests that it should be along the same lines as the 300-60h sample, the INS ratio suggests that there is a lot more aromatic carbon in this sample than there is in either the 300-60h or the 350-110h samples.

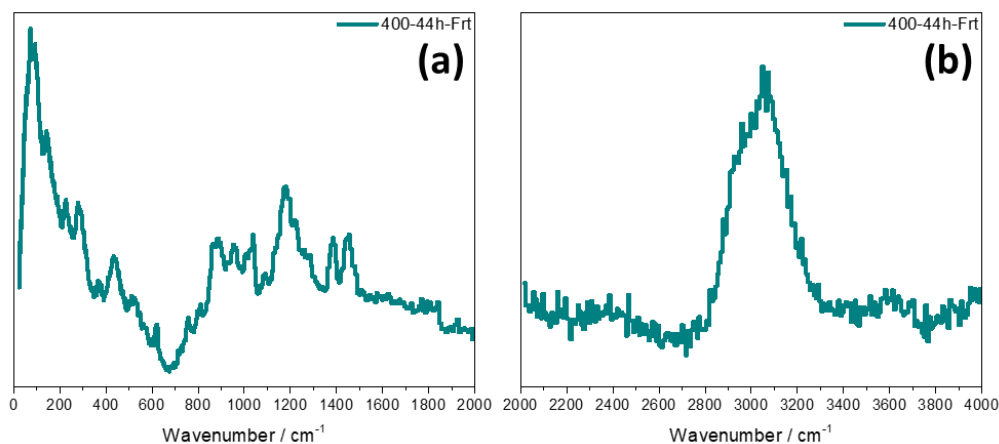


Figure 5.29: The INS spectra of the 400-44h-Frt sample collected via (a) TOSCA (b) MAPS using the A-chopper package at an incident energy of  $5244 \text{ cm}^{-1}$ .

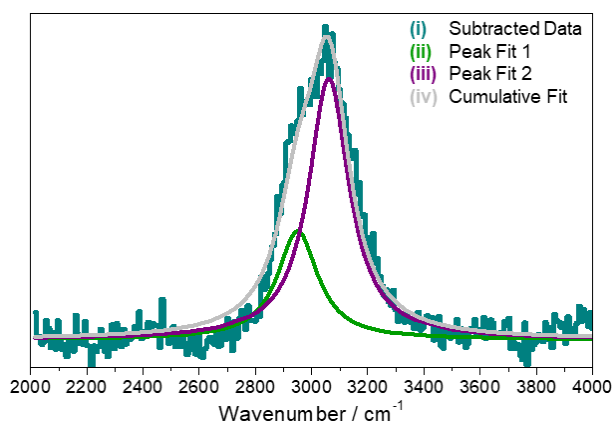


Figure 5.30: Peak fitting of 400-44h-Frt sample. (i) background subtracted experimental dataset, (ii)  $sp^3$  hybridised  $\nu(\text{C-H})$  peak, (iii)  $sp^2$  hybridised  $\nu(\text{C-H})$  peak, (iv) cumulative fit, i.e. (ii) + (iii).

Changing the contact time of the methanol in this reaction has proven to slow down the deactivation of the sample. The temperature and time-on-stream remained the same. This is something that has been explored in literature as well, with the suggestion that longer contact times promote the accumulation of aromatic species whereas decreasing contact time could enhance olefin production.<sup>43,44</sup> Due to lack of reaction monitoring, we were unable to see if the shorter contact time enhanced olefin production.

## 5.6 Conclusions

INS spectroscopy has been used as the principal probe to interrogate the ZSM-5/MTH reaction system, with an emphasis on the form of the hydrocarbon pool. Reactions in the temperature range  $300\text{-}400^\circ\text{C}$  were studied at short (2 h) and extended ( $t \geq 44$  h) time domains. The following conclusions have been drawn.

At short reaction times the INS spectra indicate a mixture of hydrocarbons to be present but with no singular molecular entity dominant (Figure 5.19). The changing ratios in the INS intensities within those spectra also suggest that there are different chemistries occurring between the three temperatures at the initial stages of the reaction. The INS spectra for longer run samples recorded at 300 and 350 °C exhibit the same spectral pattern as previously reported (Figure 5.20) and may be characterised as the vibrational fingerprint of the working hydrocarbon pool (HCP). Vibrational assignment reveals this variant of the HCP to comprise polycyclic aromatics, polymethylated benzenes and amorphous coke (Figure 5.21). The INS analysis on these larger scale working catalysts is validated by comparison with other spectroscopies.

The amorphous coke present is at much lower quantities in these two temperatures, suggesting that any degree of deactivation being observed (drop in methanol conversion) to be due to pore filling rather than pore blockage from external coke. Polycyclic aromatics and polymethylated benzenes are found to be the dominant species within the HCP at this stage of the catalytic lifetime in agreement with literature despite the increased sample size required for the INS samples. The assignment of the doublet (1354 and 1458  $\text{cm}^{-1}$ ) in the INS spectra to aromatic molecules substituted with more than 4 methyl groups is indicative of a fast rate of methylation occurring at the 300 and 350°C reaction. The presence of a relatively intense 600  $\text{cm}^{-1}$  which has been assigned to naphthalenic species, as well as the intense 1200  $\text{cm}^{-1}$  peak is indicative of hydride transfer and cyclisation reactions to form polycyclic molecules.

The reaction profile of the longer run higher temperature sample indicates the catalyst to be approaching a deactivation regime (Figure 5.2). The INS spectrum of this sample is distinct and noticeably different to the catalyst operating under steady-state conditions (Figure 5.20). The spectrum closely corresponds to that of glassy carbon (Figure 5.23), a form of amorphous carbon with no long-range crystalline order and isolated hydrogen atoms at carbon edge termination points. This moiety is the dominant species, although residual traces of the HCP are also present. This suggests that the degree of deactivation being observed is due to external pore blocking and not due to pore filling or because of loss of acid sites. The shift in the  $\text{sp}^3:\text{sp}^2$  ratio of the high energy INS spectra suggests that the HCP present is relatively little in comparison with the amorphous coke build up as there is no detectable amount of  $\text{sp}^3$  C-H stretch present through peak fitting. The small contribution from the

HCP observed in the lower energy 400-44h sample could still be there but masked from the heavy contribution of  $sp^2$  C-H. The intensity of the 400-44h sample in comparison with the 300 and 350 °C sample spectra must also be acknowledged. There is a large intensity difference between them, with a large loss of INS intensity being observed in the 400-44h sample. This suggests a large degree of dehydrogenation and carbon retention at higher temperatures.

Changing the contact time of the reaction to make it faster (decreased contact time), seems to slow down the catalyst deactivation, keeping it at steady state for longer periods of time despite the higher temperature. The INS spectrum observed for the 400-Frt sample being similar to that obtained from the 300 and 350 °C reactions. Although, the GC-MS has suggested that methylation is one of the dominant reaction pathways within this regime, it is seen from the MAPS data and the higher  $sp^2$  to  $sp^3$  C-H presence in the data, that it is happening at a lower extent than the 300 and 350°C samples.

The INS spectra provide molecular information on the form of the HCP during (i) its evolutionary phase, (ii) mature steady-state operation and (iii) a quasi-deactivation phase. The latter is approached by a process of dehydrogenation and carbon retention within the zeolite pore network. TPO, DRIFTS and  $^{13}C$  solid-state NMR spectroscopic measurements are consistent with the INS-derived findings. The increased sample sized required for the INS measurements does not show any difference in the HCP build up or on the temperature dependent pathways of deactivation compared with the micro-sampling of other spectroscopic methods shown in literature. The INS technique has been shown to be particularly powerful for observing the deactivation stage of MTH catalysis.

## 5.7 References

- 1 M. D. Argyle and C. H. Bartholomew, *Catalysts*, 2015, **5**, 145–269.
- 2 S. F. Parker, D. Lennon and P. W. Albers, *Appl. Spectrosc.*, 2011, **65**, 1325–1341.
- 3 S. F. Parker and P. Collier, *Johnson Matthey Technol. Rev.*, 2016, **60**, 132–144.
- 4 P. C. H. Mitchell, S. F. Parker, A. J. Ramirez-Cuesta and J. Tomkinson, *Vibrational spectroscopy with neutrons with applications in chemistry*,

- World Scientific, Singapore, 2005.
- 5 H. Schulz, *Catal. Today*, 2010, **154**, 183–194.
  - 6 B. A. Sexton, A. E. Hughes and D. M. Bibby, *J. Catal.*, 1988, **109**, 126–131.
  - 7 D. Mores, J. Kornatowski, U. Olsbye, B. M. Weckhuysen, J. Kornatowski, U. Olsbye and B. M. Weckhuysen, *Chem. - A Eur. J.*, 2011, **17**, 2874–2884.
  - 8 U. Olsbye, S. Svelle, K. P. Lillerud, Z. H. Wei, Y. Y. Chen, J. F. Li, J. G. Wang and W. B. Fan, *Chem. Soc. Rev.*, 2015, **44**, 7155–7176.
  - 9 K. Hemelsoet, J. Van Der Mynsbrugge, K. De Wispelaere, M. Waroquier and V. Van Speybroeck, *ChemPhysChem*, 2013, **14**, 1526–1545.
  - 10 C. D. Chang, *Catal. Rev.*, 1983, **25**, 1–118.
  - 11 R. Warringham, D. Bellaire, S. F. Parker, J. Taylor, R. A. Ewings, C. M. Goodway, M. Kibble, S. R. Wakefield, M. Jura, M. P. Dudman, R. P. Tooze, P. B. Webb and D. Lennon, in *Journal of Physics: Conference Series*, 2014, vol. 554.
  - 12 Suwardiyanto, R. F. Howe, R. C. A. Catlow, E. K. Gibson, A. Hameed, J. McGregor, P. Collier, S. F. Parker and D. Lennon, *Faraday Discuss.*, 2017, **197**, 447–472.
  - 13 R. F. Howe, J. McGregor, S. F. Parker, P. Collier and D. Lennon, *Catal. Letters*, 2016, **146**, 1242–1248.
  - 14 I. Yarulina, A. D. Chowdhury, F. Meirer, B. M. Weckhuysen and J. Gascon, *Recent trends and fundamental insights in the methanol-to-hydrocarbons process*, Nature Publishing Group, 2018, vol. 1.
  - 15 M. Bjørgen, F. Joensen, K.-P. Lillerud, U. Olsbye, S. Svelle, M. Bjørgen, F. Joensen, K.-P. Lillerud, U. Olsbye and S. Svelle, *Catal. Today*, 2009, **142**, 90–97.
  - 16 D. M. Bibby, N. B. Milestone, J. E. Patterson and L. P. Aldridge, *J. Catal.*, 1986, **97**, 493–502.
  - 17 S. Müller, Y. Liu, M. Vishnuvarthan, X. Sun, A. C. Van Veen, G. L.

- Haller, M. Sanchez-Sanchez and J. A. Lercher, *J. Catal.*, 2015, **325**, 48–59.
- 18 M. Bjørgen, S. Svelle, F. Joensen, J. Nerlov, S. Kolboe, F. Bonino, L. Palumbo, S. Bordiga and U. Olsbye, *J. Catal.*, 2007, **249**, 195–207.
- 19 S. Teketel, L. F. Lundegaard, W. Skistad, S. M. Chavan, U. Olsbye, K. P. Lillerud, P. Beato and S. Svelle, *J. Catal.*, 2015, **327**, 22–32.
- 20 K. S. W. Sing, D. H. Everett, R. A. W. Haul, L. Moscou, R. A. Pierotti, J. Rouguerol and T. Siemieniowska, *Pure Appl. Chem.*, 1985, **57**, 603–619.
- 21 R. H. Meinhold and D. M. Bibby, *Zeolites*, 1990, **10**, 121–130.
- 22 R. S. Ozubko, G. W. Buchanan and I. C. P. Smith, *Can. J. Chem.*, 1974, **52**, 2493–2501.
- 23 K. Barbera, S. Sorensen, S. Bordiga, J. Skibsted, H. Fordsmand, P. Beato and T. V. W. Janssens, *Catal. Sci. Technol.*, 2012, **2**, 1196–1206.
- 24 D. M. Grant and B. V. Cheney, *Physical and Inorganic Chemistry Carbon-13 Magnetic Resonance. VII.1 Steric Perturbation of the Carbon-13 Chemical Shift of the H<sup>1</sup>H and HC<sup>13</sup> angle for each of the*, 1967, vol. 89.
- 25 J. D. Mao and K. Schmidt-Rohr, *Environ. Sci. Technol.*, 2004, **38**, 2680–2684.
- 26 Y. Jiang, W. Wang, V. R. Reddy Marthala, J. Huang, B. Sulikowski and M. Hunger, *J. Catal.*, 2006, **238**, 21–27.
- 27 S. K. Matam, A. J. O'Malley, C. R. A. Catlow, S. Suwardiyanto, P. Collier, A. P. Hawkins, A. Zachariou, D. Lennon, I. Silverwood, S. F. Parker and R. F. Howe, *Catal. Sci. Technol.*, 2018, **8**, 3304–3312.
- 28 P. A. Jacobs and R. Von Ballmoos, *J. Phys. Chem*, 1982, **86**, 3050–3052.
- 29 L. Kubelková, J. Nováková and K. Nedomová, *J. Catal.*, 1990, **124**, 441–450.
- 30 D. Colognesi, M. Celli, F. Cilloco, R. J. Newport, S. F. Parker, V. Rossi-

- Albertini, F. Sacchetti, J. Tomkinson and M. Zoppi, *Appl. Phys. A Mater. Sci. Process.*, 2002, **74**, 64–66.
- 31 R. S. Pinna, S. Rudić, S. F. Parker, J. Armstrong, M. Zanetti, G. Škoro, S. P. Waller, D. Zacek, C. A. Smith, M. J. Capstick, D. J. McPhail, D. E. Pooley, G. D. Howells, G. Gorini and F. Fernandez-Alonso, *Nucl. Instruments Methods Phys. Res. Sect. A Accel. Spectrometers, Detect. Assoc. Equip.*, 2018, **896**, 68–74.
- 32 Science Technology and Facilities Council, MAPS Instrument, <https://www.isis.stfc.ac.uk/Pages/maps.aspx>, (accessed 16 April 2020).
- 33 S. F. Parker, S. Imberti, S. K. Callear and P. W. Albers, *Chem. Phys.*, 2013, **427**, 44–48.
- 34 J. K. Walters, R. J. Newport, S. F. Parker and W. S. Howells, *J. Phys. Condens. Matter*, 1995, **7**, 10059–10073.
- 35 P. W. Albers, W. Weber, K. Möbus, S. D. Wieland and S. F. Parker, *Carbon N. Y.*, 2016, **109**, 239–245.
- 36 D. Lin-Vien, N. B. Colthup, W. G. Fateley and J. G. Grasselli, *The Handbook of Infrared and Raman Characteristic Frequencies of Organic Molecules*, 1991.
- 37 E. R. Lippincott and E. J. O'Reilly, *J. Chem. Phys.*, 1955, **23**, 238–244.
- 38 E. Fitzer, K. H. Kochling, H. P. Boehm, H. Marsh and I. U. of P. and A. C. IUPAC, *Pure Appl. Chem.*, 1995, **67**, 473–506.
- 39 D. F. . Mildner and J. M. Carpenter, *J. Non. Cryst. Solids*, 1982, **47**, 391–402.
- 40 Y. T. Chua and P. C. Stair, *J. Catal.*, 2003, **213**, 39–46.
- 41 E. Borodina, F. Meirer, I. Lezcano-González, M. Mokhtar, A. M. Asiri, S. A. Al-Thabaiti, S. N. Basahel, J. Ruiz-Martinez and B. M. Weckhuysen, *ACS Catal.*, 2015, **5**, 992–1003.
- 42 D. Mores, E. Stavitski, M. H. F. Kox, J. Kornatowski, U. Olsbye and B. M. Weckhuysen, *Chem. - A Eur. J.*, 2008, **14**, 11320–11327.
- 43 M. Zhang, S. Xu, Y. Wei, J. Li, J. Wang, W. Zhang, S. Gao and Z. Liu, *Chinese J. Catal.*, 2016, **37**, 1413–1422.

44 C. D. Chang, *CATAL. REV.-SCI. ENG.*, 1984, **26**, 323–345.

# Chapter 6

## Methane Diffusion Through Coked Samples

---

This chapter will focus on studying methane diffusion through the fresh ZSM-5 catalyst and through the coked samples investigated in Chapter 5. Methane diffusion will be studied by QENS. The work presented in this chapter was carried out in collaboration with Mr. Alex P. Hawkins whose molecular dynamic simulations on the system which can be found in his thesis.

### 6.1 Introduction

In the previous chapter, the study of MTH reacted samples with INS was reported. During the MTH reaction, there is a build-up of aromatics and olefins within the ZSM-5 structure. This will affect the diffusion of both reactant and products through the zeolite channels, with the diffusion constraints becoming larger with increased time-on-stream. However, how exactly the diffusion is affected with the build-up of 'coke' remains poorly understood. In heterogeneous catalysts, QENS has only been recently used in order to study the effect of deactivation in molecule diffusion.<sup>1-3</sup> The use of QENS in this way is relatively new, and has challenges that need to be overcome in order to be able to study real industrial samples.

A first attempt at studying the effect of the retained hydrocarbons on the methanol diffusion using QENS has been published by Matam et al.<sup>3</sup> In this QENS study, methanol was used as the probe molecule on a blank ZSM-5 catalyst, an MTH catalyst reacted at 350 °C and one at 400 °C. However, the study showed that the methanol looks to be immobile in both the clean zeolite, and the reacted zeolite sample at 350 °C. The methanol showed isotropic rotation within the zeolite pore, when introduced in the MTH reacted sample at 400 °C. The increased reaction temperature also induced some mesoporosity in the zeolite, which caused the methanol rotational movement to be visible within the QENS time frame. The immobility of the methanol could be either because it was moving too slow for detection or because it was interacting with

the hydrocarbons already present. As was already discussed in Chapter 4, methanol in ZSM-5 is quite challenging to observe. This study considers a role for methane as a probe molecule.

A QENS study using methane as the probe was designed. Methane was chosen as it is believed to be unreactive within the zeolite framework, and should be able to move unhindered by the presence of acid sites or the hydrocarbons present. Therefore, only steric contributions would affect its movement through the zeolite. A complementary molecular dynamics study has been recently completed using methane as the diffusion molecule through a ZSM-5 with varying levels of coke present.<sup>4</sup> The coke was simulated by having two different models for coke deposition, a uniform deposition which is what has been assumed happens at the early stages of the reaction and uneven deposition when larger amounts of coke are used. It was found that a uniform deposition of coke has little to no effect on methane diffusion and when random deposition of coke happened, the methane self-diffusion coefficient dropped. The simulated self-diffusion coefficients of methane were in the  $\times 10^{-9} \text{ m}^2\text{s}^{-1}$  regime, which suggests that methane diffusion will be visible within the usual QENS timescales.

This chapter will focus on trying to understand the motions of methane in the empty ZSM-5 catalyst as well as within coked samples. Two coked samples from Chapter 5, will be used in this investigation. The 350-2h and 350-110h sample were chosen as two samples that represent the early stage and a mature steady state stage of the MTH reaction respectively. This will help us understand the difference between diffusion in a clean ZSM-5, at the early stages of MTH and at a mature stage in the reaction.

## 6.2 Experimental

The empty ZSM-5 catalyst was calcined under static air at 500 °C for 12 hours, it was then dried under He flow before 3.13 g being loaded into the QENS annular cans with a 1mm diameter. The QENS sample cans are equipped with gas handling capabilities. The experimental details for creating the MTH reacted samples as well as their full characterisation can be found in Chapter 5. The samples used for this chapter are the 350-2h and 350-110h, renamed in this chapter as MTH-2h and MTH-110h respectively. The major sample details are summarised in Table 6.1. The samples were kept under inert

atmosphere in-between the INS and QENS experiments, therefore no drying was needed for these samples before being loaded in the QENS annular cans.

The QENS experiments were carried out using the IRIS spectrometer, located at the ISIS Muon and Neutron Source. The temperature range investigated was from base temperature (set to start measuring below 5K) to 373 K. 375 K is the maximum rated temperature the cryostat could go to, therefore, the final temperature was lowered in order to not exceed that temperature. Elastic fixed window scans (elwin) were done at 25 K intervals with high resolution QENS spectra being measured at base temperature, 225, 275, 325 and 373 K. The QENS measurements were done both for the blank samples and for the loaded methane samples. The methane dosing was done whilst the sample was in the IRIS spectrometer at room temperature with the procedure being described in Section 2.1.3.2. The experimental loadings can be found in Table 6.1.

Table 6.1: Sample experimental and characterisation details.

		ZSM-5	MTH-2h	MTH-110h
<i>Chapter 5 Equivalent</i>		<i>(Fresh)</i>	<i>350-2h</i>	<i>350-110h</i>
<b>Reaction Time</b>	<b>(h)</b>	0	2	110
<b>Coke</b>	<b>(wt%)</b>	0	2.58	14.20
<b>S<sub>BET</sub></b>	<b>(m<sup>2</sup>g<sup>-1</sup>)</b>	404	397	46
<b>V<sub>micropore</sub></b>	<b>(cm<sup>3</sup>g<sup>-1</sup>)</b>	0.16	0.15	0.01
<b>QENS Weight</b>	<b>(g)</b>	3.13	3.75	4.02
<b>ZSM-5 Estimate Weight</b>	<b>(g)</b>	3.13	3.65	3.45
<b>Final Loading Pressure</b>	<b>(mBar)</b>	877.2	864.2	865.2
<b>Methane</b>	<b>(moles)</b>	2.56x10 <sup>-3</sup>	1.66x10 <sup>-3</sup>	4.17x10 <sup>-4</sup>
<b>Methane Loading</b>	<b>(mol<sub>CH4</sub>/mol<sub>ZSM5</sub>)</b>	4.71	2.62	0.70

### 6.3 Elastic Window Scans

The elastic window scan (elwin) follows the immobility of the sample and is dependent on neutrons being scattered elastically from the sample.<sup>5,6</sup> Figure 6.1 shows the change in elastic intensity as a function of temperature for the three investigated samples, both empty and after methane loading. The total integrated elastic intensity was obtained by integration between -0.0175 and +0.0175 meV, which is twice the instrument resolution.

A decrease in the integrated elastic intensity suggests an increase in sample mobility, whilst the 0 K value of the elwin gives an indication of the number of elastic scatterers present within the sample at the time of the measurement. Assuming that all the methane is within the sample for the empty ZSM-5 (Figure 6.1.a), then the drop in intensities (after the zeolite contribution has been removed) in Figures 6.1.b and c, should correspond to the difference between their methane loadings. The loading drop from ZSM-5 to MTH-110h is within 13% of the expected drop in the initial intensity between the two elwins. However, the drop between ZSM-5 to MTH-2h is not proportional, with the elastic intensity being 40% higher than the expected value from the calculated loading. The methane loading is calculated from the drop of pressure in the manifold, with the assumption that all the methane is diffusing through the zeolite pores in the sample. The manifold is calibrated with helium before the start of each experiment in order to determine the dead volume, corresponding to the lines needed to connect the manifold to the cell. The system is a closed system, so it is therefore unclear where the extra intensity could be coming from other than a possible experimental error. From the intensity of the elwin the methane would correspond to something closer to  $4.3 \text{ mol}_{\text{CH}_4}/\text{mol}_{\text{ZSM-5}}$  than what the calculated methane dosing was from the pressure recorder in the manifold which would give a dosing of  $2.62 \text{ mol}_{\text{CH}_4}/\text{mol}_{\text{ZSM-5}}$ . Nonetheless, despite this uncertainty, the results are presented below.

The graphs shown in Figure 6 all show an increase in mobility with increasing temperature, as expected. For the ZSM-5 and the MTH-2h samples, the elastic intensity of the blank samples and the loaded samples overlap after a temperature of about 300 K is reached. This overlap is seen even earlier for the MTH-110h sample, with it happening above the 125 K temperature mark. The overlap suggests that the methane after that temperature is fully mobile, with methane no longer contributing to the elastic intensity. Methane still contributes to the quasi-elastic intensity, however, the elwins indicate that the temperatures chosen to complete the high resolution scans might be unsuitable, especially for the MTH-110h sample (Figure 6.1c). The high mobility of the methane made fitting the data more complex than initially anticipated.

It must also be mentioned that the melting point of methane is at 91 K with its boiling point being at 111 K. There is a small kink observed in the elwin of the loaded samples in the region between 50K-120K, but it is unclear if it is due to the melting and boiling of methane within the zeolite or not.

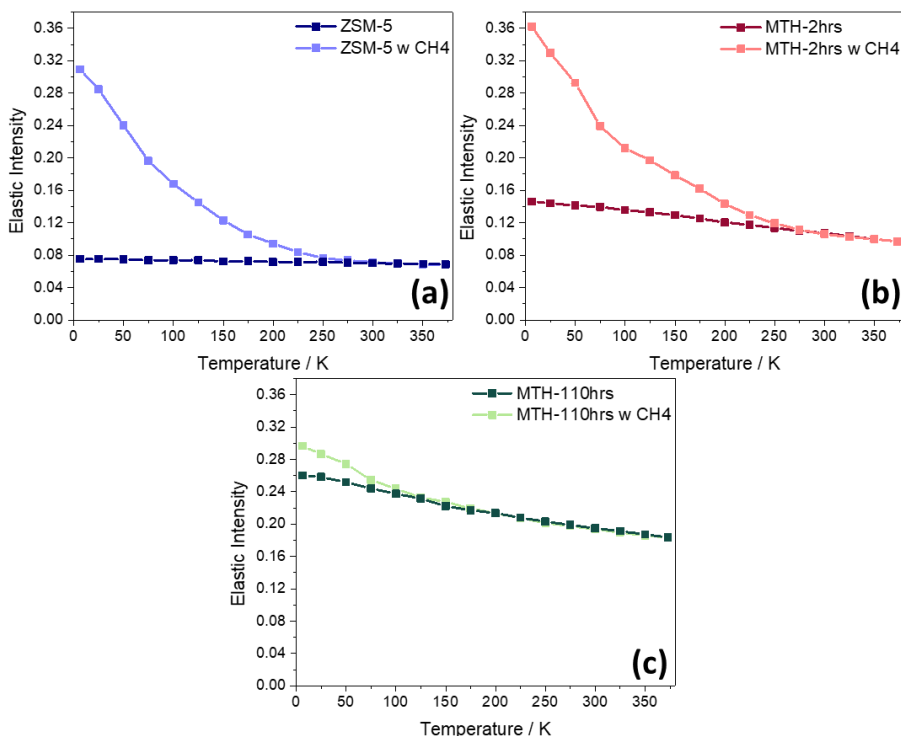


Figure 6.1: Elastic Fixed Window Scan of the empty samples compared with the methane loaded samples (a) ZSM-5 blank (b) MTH-2h and (c) MTH-110h

## 6.4 Quasi-elastic Analysis

The QENS data were analysed using two software packages, MANTID<sup>7</sup> and DAVE<sup>8</sup>, developed by ISIS and NIST respectively. Mantid was used in order to reduce the data, and group the detectors into 17 groups, the DAVE software was used in order to fit the QENS peaks at each grouped Q value. A complication was noticed at the base temperature scans for the methane loaded samples. Figure 6.2 (a-c) shows the QENS spectra at base temperature comparing the blank samples with the methane loaded samples, with (i-iii) being a detailed version of the same spectra.

It was observed that at base temperature, there are extra peaks present other than the elastic peak. Those peaks are associated with rotational methyl tunnelling.<sup>9,10</sup> The base temperature is used as a background because at those low temperatures, no movement should be possible, therefore, the peak seen should be the instrument resolution peak. Due to the presence of methyl tunnelling, the elastic peak becomes broader than the instrument resolution and the extra peaks make it impossible to use the base temperature loaded sample as a resolution file. Therefore, the sample before methane loading at base temperature, was used as the resolution file in all spectra.

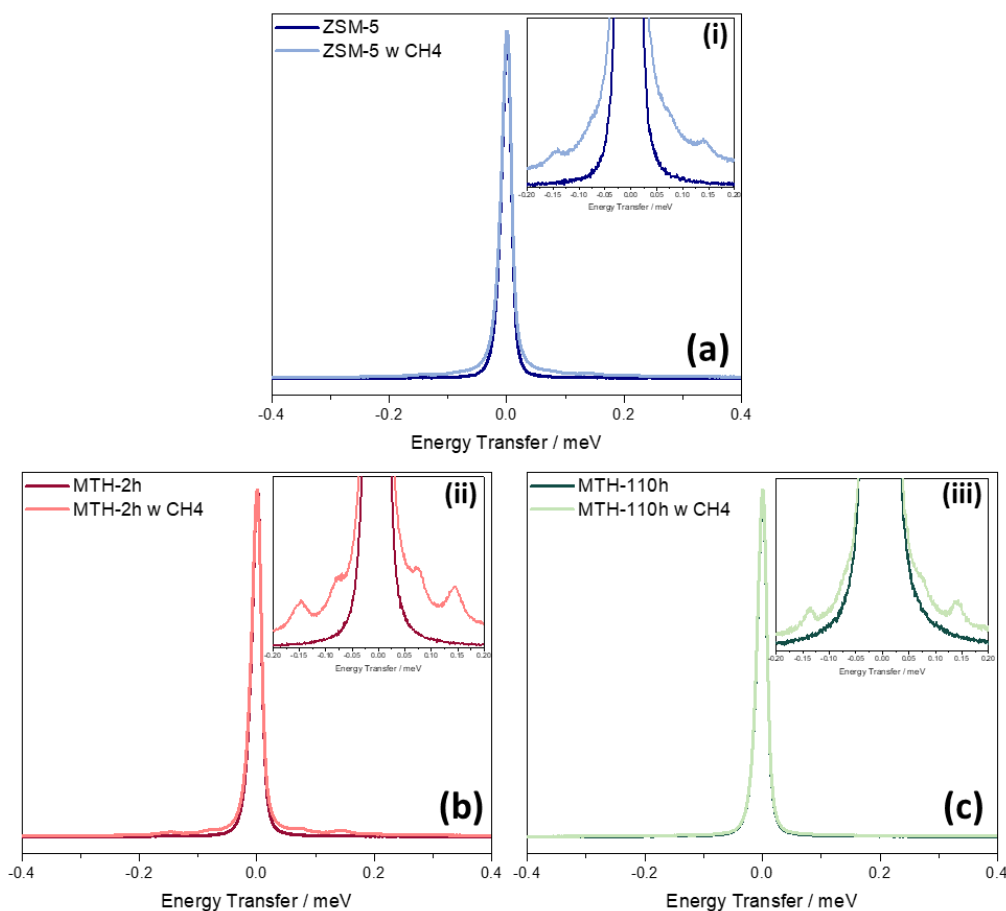


Figure 6.2: QENS spectra at base temperature for the blank samples and their loaded counterparts (all detector groups grouped together). (a) ZSM-5 (b) MTH-2h and (c) MTH-110h. (i),(ii) and (iii) a detail look in the -0.2 to 0.2 meV region of their respective graphs.

#### 6.4.1 ZSM-5 Blank/ZSM-5 with Methane

The data were fit using a broadened delta peak for the instrument resolution, 1 Lorentzian peak to model the quasi-elastic broadening plus a background. The broadened delta is the base temperature scan of the blank ZSM-5. The QENS spectra with respect to  $Q$  are complicated by the contribution of coherent Bragg scattering from the zeolite framework. However, attempting to subtract the empty zeolite from the methanol dosed sample data resulted in negative peaks, therefore the fits were made with the zeolite still present.

Four diffusion models were tested in order to fit the data. Each model describes jump-type diffusion behaviour and relates the half-width at half-maximum (HWHM) of the Lorentzian broadening at a given  $Q$  value,  $\Delta\omega(Q)$ , to the residence time of the diffusing molecule between jumps,  $\tau$ , and the length of each jump. The model of Chudley and Elliott (CE)<sup>11</sup> assumes a constant jump

distance of length  $d$  resulting in the relationship described by Equation 6.1. The models of Hall and Ross (HR)<sup>12</sup>, and Singwi and Sjölander (SS)<sup>13</sup> assume a distribution of jump lengths, of a different form in each case, and link the broadening to the mean squared jump distance,  $\langle r^2 \rangle$ , by the relationships in Equations 6.2 and 6.3 respectively. Finally, a model proposed by Jobic<sup>14</sup> models differences in jump lengths by reference to terms for the average jump length,  $d_0$ , and the degree of delocalisation of the molecule between jumps,  $r_0$ , in the relationship in Equation 6.4.

$$\Delta\omega(Q) = \frac{1}{\tau} - \left[ \frac{\sin Qd_0}{Qd_0} \exp\left(-\frac{Q^2\langle r_0^2 \rangle}{2}\right) \right] \quad (\text{Equation 6.1})$$

$$\Delta\omega(Q) = \frac{1}{\tau} - \left[ \frac{\sin Qd_0}{Qd_0} \exp\left(-\frac{Q^2\langle r_0^2 \rangle}{2}\right) \right] \quad (\text{Equation 6.2})$$

$$\Delta\omega(Q) = \frac{1}{6\tau} \frac{Q^2\langle r^2 \rangle}{1+Q^2\langle r^2 \rangle/6} \quad (\text{Equation 6.3})$$

$$\Delta\omega(Q) = \frac{1}{\tau} - \left[ \frac{\sin Qd_0}{Qd_0} \exp\left(-\frac{Q^2\langle r_0^2 \rangle}{2}\right) \right] \quad (\text{Equation 6.4})$$

In each case, once the experimental data is fit to the models in Equations 6.1-6.4, the predicted methane self-diffusion constant ( $D_s$ ) can be derived from the fitted values for (average) jump length and residence time by means of the relationship  $D_s = \langle r^2 \rangle / 6\tau$ . The natural log of these diffusion coefficients can then be plotted against inverse temperature which follows a linear Arrhenius behaviour. The Arrhenius relationship can be described in Equation 6.5, where the  $D_s$  is the derived diffusion coefficient from the models above for each motion,  $E_A$  is the activation energy,  $R$  is the ideal gas constant,  $T$  is temperature and  $A$  is the pre-exponential factor. This allows the plotting of a straight line where the gradient of that line gives the activation energy for the motion observed.

$$\ln D_s = \left(-\frac{E_A}{R}\right)\left(\frac{1}{T}\right) + \ln A \quad (\text{Equation 6.5})$$

Figure 6.3 shows the Full Width Half Max (FWHM,  $\Gamma$ ) derived from fitting the experimental data compared with the  $\Gamma$  of the four jump diffusion models. Table 6.2, shows the parameters used for each of the different models and the calculated diffusion coefficient for each one. The fit error shown in Table 6.2, is

calculated from the standard deviation of the residual fits, and is showing how well the data fit the model used. The fit error is converted from (meV and Å units to  $s^{-1}$  and m units respectively) When trying to establish what model fits the data better, the different constraints were left to float. However, the mean square jump seemed to change without a noticeable trend. The  $\langle r^2 \rangle$  value was then limited to the value obtained for the lower temperature. This did not seem to noticeably change the fit of the models for the 225 K, 275 K and 325 K with the  $\langle r^2 \rangle$  value staying within  $\pm 2$  Å. The 373 K data, are difficult to fit with the  $\langle r^2 \rangle$  value for the Jobic model in particular being higher than anticipated. This could be due to the mobility of the methane becoming so fast that the data are too noisy for a proper fit. From Figure 6.3, it is apparent that the models seem to have a better fit at low  $Q$  values, with the fit deviating at higher  $Q$  values ( $Q^2 \leq 1.5$ ). Literature values for the diffusion coefficient of methane in NaZSM-5 at 200 K and 250 K are  $2.7 \times 10^{-9} \text{ m}^2\text{s}^{-1}$  and  $5.5 \times 10^{-9} \text{ m}^2\text{s}^{-1}$  respectively.<sup>15</sup> The literature values in NaZSM-5 are within acceptable limits of the diffusion coefficients calculated with the Chudley-Elliot, Hall-Ross and Jobic models, with the Singwi-Sjölander model showing a higher diffusion coefficient than anticipated.

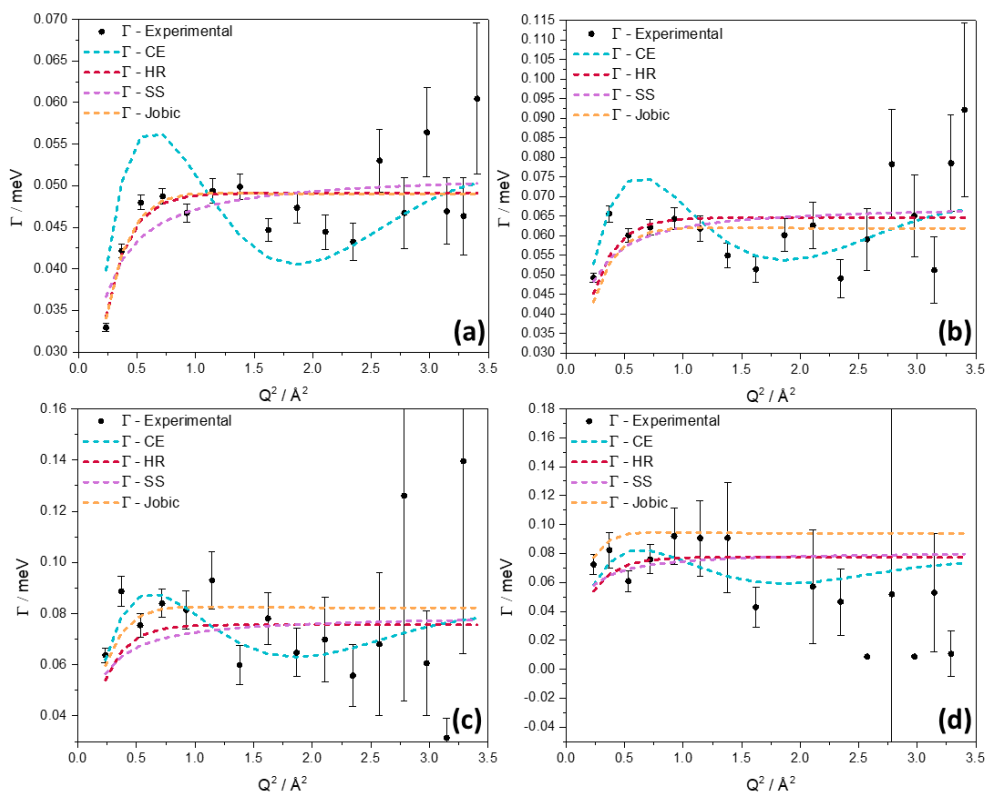


Figure 6.3: HWHM ( $\Gamma$ ) vs.  $Q^2$  for the Lorentzian fit on each temperature for the fresh ZSM-5 with methane (a) 225 K, (b) 275 K, (c) 325 K and (d) 373 K.

Table 6.2: Diffusion coefficients ( $D$ ), residence times ( $\tau$ ) and mean square jump lengths ( $\langle r^2 \rangle$ ), calculated using the four different jump models

Temperature (K)	Models	Parameters			
		D (m <sup>2</sup> s <sup>-1</sup> )	Fit Error (±)	$\tau$ (ps)	$\langle r^2 \rangle$ (Å <sup>2</sup> )
225	<i>CE</i>	3.78x10 <sup>-9</sup>	1.7x10 <sup>-12</sup>	14.16	32.1
	<i>HR</i>	3.82x10 <sup>-9</sup>	9.5x10 <sup>-13</sup>	13.40	30.8
	<i>SS</i>	8.20x10 <sup>-9</sup>	8.3x10 <sup>-13</sup>	12.74	62.7
	<i>Jobic</i>	3.66x10 <sup>-9</sup>	9.2x10 <sup>-13</sup>	13.44	29.6
275	<i>CE</i>	5.00x10 <sup>-9</sup>	2.2x10 <sup>-12</sup>	10.69	32.1
	<i>HR</i>	5.03x10 <sup>-9</sup>	1.8x10 <sup>-12</sup>	10.20	30.8
	<i>SS</i>	1.08x10 <sup>-8</sup>	1.7x10 <sup>-12</sup>	9.68	62.7
	<i>Jobic</i>	4.63x10 <sup>-9</sup>	1.8x10 <sup>-12</sup>	10.64	29.6
325	<i>CE</i>	5.87x10 <sup>-9</sup>	1.5x10 <sup>-12</sup>	9.11	32.1
	<i>HR</i>	6.15x10 <sup>-9</sup>	1.0x10 <sup>-12</sup>	8.70	32.1
	<i>SS</i>	1.26x10 <sup>-8</sup>	1.3x10 <sup>-12</sup>	8.27	62.7
	<i>Jobic</i>	6.60x10 <sup>-9</sup>	7.9x10 <sup>-13</sup>	8.00	31.7
373	<i>CE</i>	5.51x10 <sup>-9</sup>	2.3x10 <sup>-12</sup>	9.70	32.1
	<i>HR</i>	7.00x10 <sup>-9</sup>	2.2x10 <sup>-12</sup>	8.50	35.7
	<i>SS</i>	1.30x10 <sup>-8</sup>	2.5x10 <sup>-12</sup>	8.06	62.7
	<i>Jobic</i>	9.76x10 <sup>-9</sup>	2.4x10 <sup>-12</sup>	7.00	40.9

As mentioned, there is an Arrhenius relationship between the natural logarithm of the diffusion coefficients and the inverse of temperature which is plotted in Figure 6.4. Table 6.3 shows the derived activation energies of the motions which the different jump diffusion models are describing. The Jobic model is seen to be the closest fit when comparing the activation energies with literature values. Literature values were recorded with different Si/Al of ZSM-5 and a different cation present (Na). The difference in Si/Al ratio of a zeolite, as well as the presence of a different cation could potentially change the activation energy of the methane motions within the zeolite. To the best knowledge of the author, neither the effect of changing the Si/Al ratio nor of different cations on the effect of motion of an inert probe molecule within the zeolite pores have been investigated so far.

Table 6.3: Table of activation energies calculated from Figure 6.5

Jump Diffusion Models	Activation Energy KJ mol <sup>-1</sup>	Fit Error (±)
<i>Chudley Elliot</i>	10.45	7.7x10 <sup>-4</sup>
<i>Hall Ross</i>	2.86	2.9x10 <sup>-6</sup>
<i>Singwi Sjolander</i>	2.24	4.0x10 <sup>-5</sup>
<i>Jobic</i>	4.49	1.1x10 <sup>-4</sup>
<i>Literature – CH<sub>4</sub> in Silicalite<sup>16</sup></i>	4.3±1	
<i>Literature – CH<sub>4</sub> in Na-ZSM-5<sup>15</sup></i>	4.7±0.7	

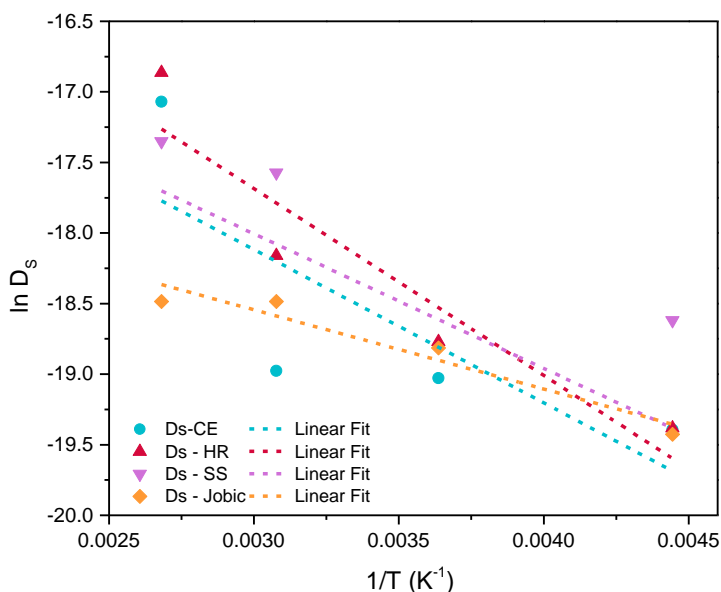


Figure 6.4: Arrhenius plot of the natural log of the diffusion coefficient over the inverse of temperature, for the ZSM-5 with methane

### 6.4.2 Coked Samples

The QENS analysis for the coked samples was carried out in the same way as above. Due to the presence of coke, both the empty/blank samples and the loaded samples were analysed. This is because the coke present contains hydrogen atoms, which have their own motions. Due to the degree of coking, and the fact that the samples were flushed before the QENS measurement, it is assumed that the coke present would only be able to have localised motions. This is because the only coke left within the zeolite should be either adsorbed on the zeolite surface or trapped within a pore.

Localised motions or rotations can be identified using the elastic incoherent structure factor (EISF,  $A_0(Q)$ ), which is a measure of the elastic components as a function of  $Q$  (Equation 6.6).

$$A_0(Q) = \frac{I_{Elastic}}{I_{Elastic} + I_{QENS}} \quad (\text{Equation 6.6})$$

How the EISF can be modelled depends on the probe molecule used in the QENS experiment. Previous work on using methanol as a probe to study diffusional constraints over the same ZSM-5 we are using in this study has been completed by S. Matam et al.<sup>3</sup> Jobic and co-workers in two separate studies used methanol and methane as probe molecules to study the motions in an

unreacted ZSM-5 zeolite.<sup>15,17</sup> The models from all three of the studies have been used in order to find the best fit model for the experimental EISF.

There are four main models which have been used to fit the motion of hydrocarbons within a zeolite pore. The first one is isotropic rotation, where the molecule is assumed to be a sphere, with the atoms in the molecule not thought to have a time averaged preferred orientation. The EISF for the isotropic rotation can be calculated by Equation 6.7.

$$A_0(Q) = j_0^2(Qr) \quad (\text{Equation 6.7})$$

Where  $j_0$  is the 0<sup>th</sup> order spherical Bessel function and  $r$  is the radius of the molecule.<sup>18</sup> If the molecule is cylindrical in shape, i.e. a longer chain hydrocarbon, then the same equation as Equation 6.7 can be used, but instead of the spherical Bessel function, a cylindrical one is used in order to account for the cylindrical shape of the molecule. When a spherical Bessel function is used the model is referred to as isotropic rotation on a spherical surface, when a cylindrical Bessel function is used, the model is referred to as isotropic planar rotation.

Model two was adapted from Volino and Dianoux<sup>19</sup> and it assumes that the molecule is undergoing small translational motions in a confined spherical volume, which in our case is the zeolite pore (pore diameter  $\sim 5.5$  Å, radius used  $\sim 2.75$  Å). The EISF is given by Equation 6.8 and the model is referred to as translation in a sphere.

$$A_0(Q) = \left[ \frac{3j_1(Qr)}{Qr} \right]^2 \quad (\text{Equation 6.8})$$

Where  $j_1$  is the 1<sup>st</sup> order spherical Bessel function and  $r$  is the radius of the zeolite pore.

Models three and four consist of a series of rotations around the carbon atom with only the hydrogen atoms moving in a circular motion. Either in a two-way exchange (2 site rotation) seen in Equation 6.9 or a three-way re-orientation around the carbon atom (3 site rotation) seen in Equation 6.10.

$$A_0(Q) = \frac{1}{2} [1 + j_0(Qr)] \quad (\text{Equation 6.9})$$

Where  $r$  in this case is the distance between the two hydrogen atoms in the exchange.

$$A_0(Q) = \frac{1}{3} [1 + 2j_0(Qr\sqrt{3})] \quad (\text{Equation 6.10})$$

Where  $r$  in this case is the C-H bond length (1.087 Å), as the movement of the three hydrogens would be around the C-atom.

In order to account for the coke's immobile hydrogen atoms, for each model an immobility factor can be incorporated. The immobility factor can be calculated using Equation 6.11.

$$N_{SQ} = P_i + P_m A_0(Q) \quad (\text{Equation 6.11})$$

Where  $N_{SQ}$  is the new scattering intensity,  $P_i$  is the immobile fraction,  $P_m$  is the mobile fraction and  $A_0(Q)$  is the scattering intensity of the different models. The addition of  $P_i$  and  $P_m$  is equal to 1.

When it comes to fitting the coke component, the analysis becomes complicated because of the complex nature of the hydrocarbon pool. There are many different molecules present within the zeolite, which makes predicting the kind of movement expected a lot more difficult. The fitting of the experimental data has been done without adding any constraints to the models. The  $r$  values were left to float, so as to find the best fit possible.

#### 6.4.2.1 Fitting of the MTH-2h

The MTH-2h data were fitted using a broadened delta peak for the instrument resolution, 1 Lorentzian peak to model the quasi-elastic broadening of the QENS peak plus a background to account for the increased intensity in the baseline. The resolution file used for creating the broadened delta was the MTH-2h scan at base temperature. From those fits, the EISF values were extracted, showing a decreasing trend over increasing  $Q$ , which is indicative of constrained rotational motion. Figure 6.7 shows the EISF as a function of  $Q$  for the four different temperature scans, with the different fitted models. As mentioned above, owing to the variety of hydrocarbons present, especially for the MTH-2h sample, where no assignment could be made of the INS spectra, the  $r$ -values were left to float. This should allow the  $r$ -value to settle to a number that would closely represent the average rotational distance. The parameters for the fits found in Figure 6.7 are given in Table 6.4. Unfortunately, the scatter in the data is too large to allow a definite conclusion as to which model best fits the data.

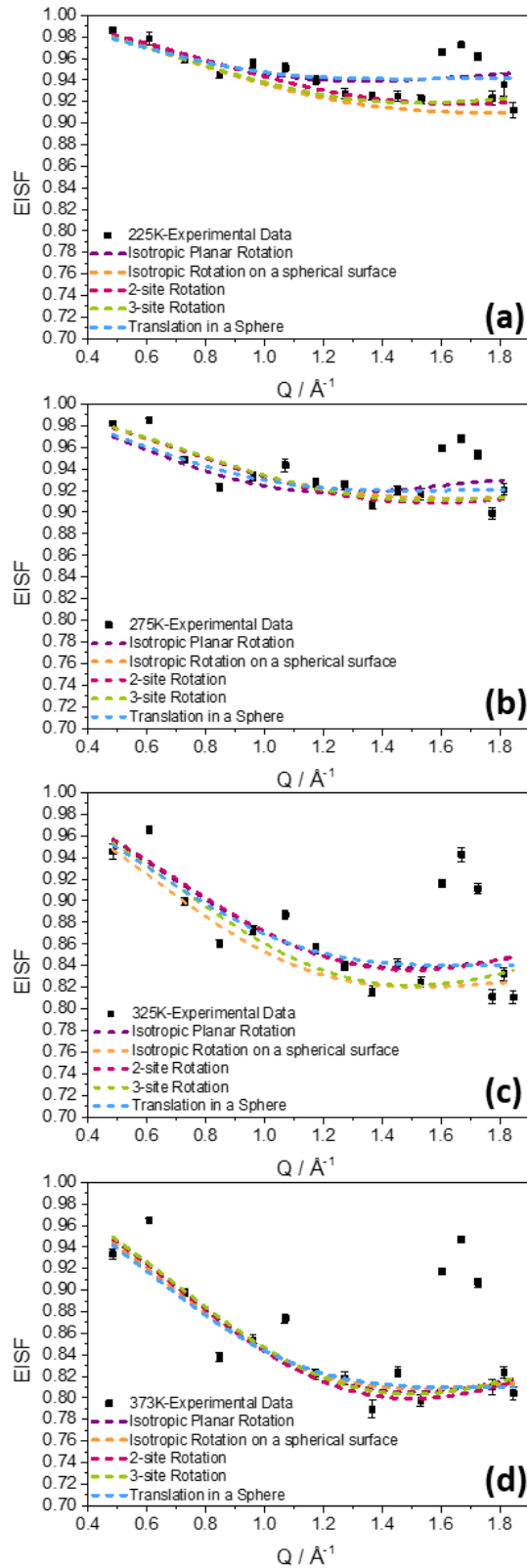


Figure 6.5: EISF experimental data of the MTH-2h sample fit with rotational models. Isotropic planar rotation (purple dashed line), isotropic rotation on a spherical surface (orange dashed line), 2-site rotation (pink dashed line), 3-site rotation (green dashed line) and translation in a sphere (blue dashed line). The QENS EISF data fit were recorded at (a) 225 K, (b) 275 K, (c) 325 K and (d) 373 K.

Table 6.4: Fitting parameters for rotational fitting models for MTH-2h

		QENS Temperatures				
		225K	275K	325K	373K	
Rotational Fitting Models	Isotropic Planar Rotation	r (Å)	1.99	1.99	1.61	1.60
		Pi (%)	94	92	84	81
	Isotropic Rotation Spherical	r (Å)	1.80	1.92	2.07	2.05
		Pi (%)	91	91	82	81
	2-site Rotation	r (Å)	2.70	2.86	3.00	3.00
		Pi (%)	87	85	73	67
	3-site Rotation	r (Å)	1.70	1.65	1.73	1.73
		Pi (%)	90	89	78	76
	Translation in a Sphere	r (Å)	3.08	3.00	2.74	2.75
		Pi (%)	94	92	84	81

The r-values for the model of rotation could be due to the whole molecule rotating or because part of the molecule is rotating. As the samples were flushed with He before the QENS measurements, the most likely scenario is that the majority of the hydrocarbons are adsorbed on the zeolite surface with part of them free to rotate. The r-values obtained for isotropic rotations, both spherical and planar, lie between 1.6 – 2.1 Å. The values are too small for it to be due to a free benzene ring motion which has an r-value of ~2.5 - 3Å.<sup>20,21</sup> Therefore, free isotropic rotation of the methylated aromatics is unlikely. Translation in a sphere could also be a possibility with a reduced pore size of 3 Å, assuming the molecule that is moving is small enough to be able to do so. The immobile fraction of the samples in all rotational models are quite high, which fits with the expectation of most hydrocarbons being adsorbed to the zeolite surface. However, it must be noted that the QENS data also required a background in order for the fit to work. Background intensity is usually related to fast motions, faster than the instrument is able to detect which broaden out the QENS peak to the baseline. What could cause such movement is still unknown.

#### 6.4.2.2 Fitting of the MTH-110h

The QENS measurements obtained for the MTH-110h blank sample were analysed using the same methods as the MTH-2h, with the peak fit being one Lorentzian, a broadened delta resolution function and a background. The fits show a decreasing EISF, which as was discussed above, is characteristic of constrained rotational motion. In Figure 6.8, the experimental EISF data points

are fit using the different localised motion models found in Equations 6.5-6.9, with the immobility factor being calculated from Equation 6.10. The r-value and immobility were left to float for the same reasons as discussed previously. The model fit parameters can be found in Table 6.5. The immobile fraction is large for all models, suggesting that a large number of hydrogen atoms are immobile. The immobile fraction does not decrease with temperature, as was observed in the MTH-2h sample. This could suggest that the immobile hydrogen atoms are hydrogen atoms at the edges of large polycyclic aromatics or the amorphous coke, which would be expected to be immobile. This is consistent with what we know of the amorphous coke present within a zeolite coked to such an extent.

All the models seen in Figure 6.8 seem to fit the data well, especially at low temperatures. The translation in the sphere fails at higher temperatures: the fit cannot get close to the experimental data, even with no constraints. This is to be expected, as the motions observed are most likely due to anchored hydrogens. Isotropic rotations show a good fit at all temperatures, the r-values are too small for benzene, methylated benzenes or polycyclic rotation. The r-value of the three site jump rotation ranges from 1.28 – 1.54 Å, this is closest to a hydrogen three jump in a methyl atom that is anchored which is 1.48 Å.<sup>3</sup> The r-values for that need to be adjusted slightly but the shape of the curve should remain the same. If that is the case, then the EISF could possibly be observing methyl rotation of the methyl groups attached to the methyl aromatics stuck within the zeolite pores.

Table 6.5: Fitting parameters for rotational fitting models for MTH-110h

		QENS Temperatures				
		225K	275K	325K	373K	
Rotational Fitting Models	Isotropic Planar Rotation	r (Å)	1.20	1.20	1.30	1.28
		Pi (%)	90	89	89	89
	Isotropic Rotation Spherical	r (Å)	1.48	1.48	1.60	1.48
		Pi (%)	90	89	89	89
	2-site Rotation	r (Å)	2.20	2.21	2.67	2.36
		Pi (%)	83	82	84	83
	3-site Rotation	r (Å)	1.30	1.28	1.54	1.37
		Pi (%)	88	87	87	87
	Translation in a Sphere	r (Å)	1.80	1.82	1.91	1.90
		Pi (%)	90	88	87	87

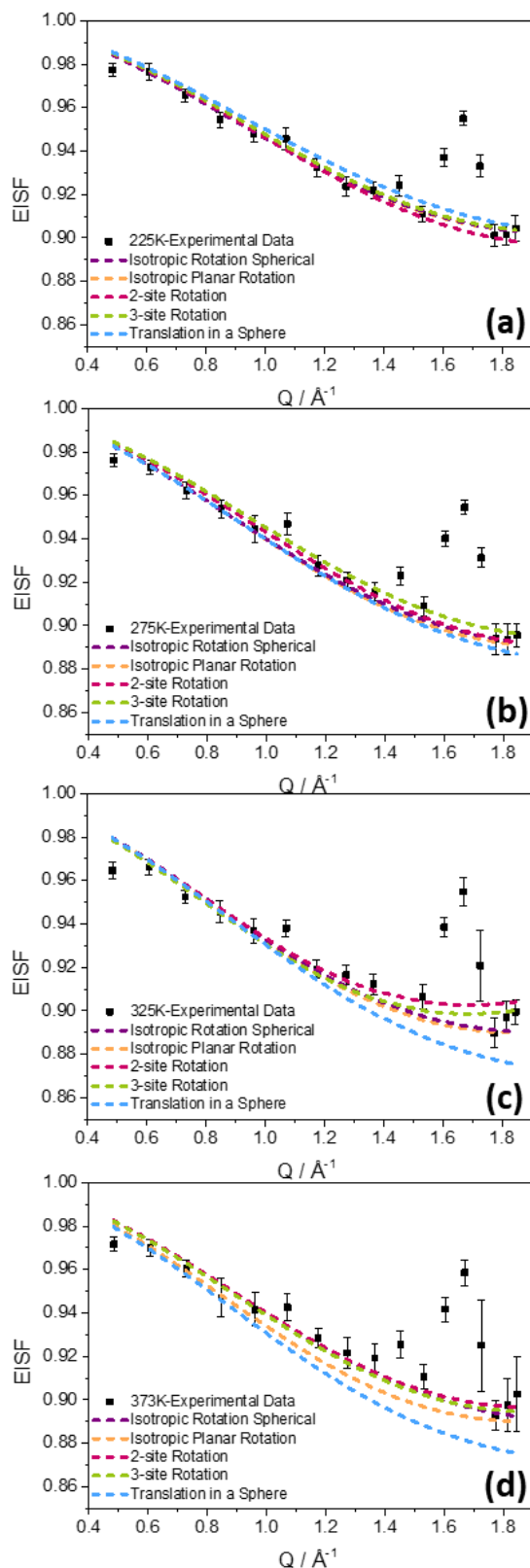


Figure 6.6: EISF experimental data of the MTH-110h sample fitted with rotational models. Isotropic planar rotation (purple dashed line), isotropic rotation on a spherical surface (orange dashed line), 2-site rotation (pink dashed line), 3-site rotation (green dashed line) and translation in a sphere (blue dashed line). QENS EISF data fitted were recorded at (a) 225 K, (b) 275 K, (c) 325 K and (d) 373 K.

### 6.4.3 Methane Loaded Coked Samples

The methane loaded samples have a lot more complexity than previously anticipated. Attempting to remove the blank samples from the loaded ones before fitting, turned out to be problematic as at some Q values it resulted in negative peaks. This caused further complications due to the coke being hydrogenous in nature.

#### 6.4.3.1 Fitting of the Methane Loaded MTH-2h

The fitting of the data was carried out in the same way as described above. The loaded samples, in theory, should have at least two motions associated with them. These are the rotational movement of the coke, observed above, and the movement of the methane. However, the fitting that best fit the data was again a broadened delta resolution function using the base temperature scan of the MTH-2h sample with no methane for the instrumental resolution, one Lorentzian and one background. The fit of a single Lorentzian is surprising, as the movement of the coke has been observed in the empty samples. However, the Lorentzian in this case has different fitting parameters than the empty coked sample and those parameters match loosely with those expected for translational diffusion of methane. The width of the QENS peak observed from the blank sample was small, meaning the rotational motions did not broaden the peak much. When the methane is loaded, which consists of approximately 2.6 methane molecules per unit cell, its motion could dominate the broadness observed in the peak, with the rotational movement being too small to observe when methane has so many more hydrogens present within the zeolite.

Figure 6.7 shows the experimental data with the fitted translational models, which are the same as those used for fitting the fresh ZSM-5 plus methane. The fitting parameters for the translational models can be found in Table 6.6. The experimental data collected at 225 K and 275 K have a better model fit than the higher temperature data. This is expected, as it was seen from the elwin scans in Figure 6.1, that at higher temperatures, the methane loaded samples and the blanks showed their elastic intensities to converge, which suggested that the methane has moved out of the IRIS time window. Although a fit was attempted at the 325 K and 373 K, it might not be correct. The data were fitted with no constraints to start with. However, the  $\langle r^2 \rangle$  value seemed to be shifting again with the changing temperature, and was therefore constrained to the value of the lowest temperature providing a good fit for all models for the

225K and 275K temperatures. However, the  $\langle r^2 \rangle$  value needed to be changed for the higher temperatures. This suggests that the broadening observed in the higher two temperatures is not necessarily from a methane motion.

The fitting parameters show that from all the model data fits at the two lowest temperatures, the Singwi-Sjölander, the Hall-Ross and the Jobic models are the closest fit to the data. The Chudley-Elliott model does not seem to fit the data at all. When comparing the diffusion coefficients of the methane loaded MTH-2h sample with the methane loaded fresh ZSM-5 (Table 6.2), it is seen that the diffusion coefficient derived from the Hall-Ross and Jobic models are roughly the same, with the MTH-2h samples having a slightly faster diffusion coefficient.

The Singwi-Sjölander model shows a diffusion coefficient a lot faster than that of the fresh catalyst. This is surprising as the diffusion should in theory be hindered from the coke present within the zeolite, however, since the Singwi-Sjölander model did not have a good fit in the fresh sample which could have affected the calculated diffusion coefficient. For the Hall-Ross and Jobic models the effect however, is minimal, as the diffusion is only fractionally faster, which suggests that the coke present does not affect the methane diffusion to a great degree. This is something that has already been predicted by Li et al, in a study using molecular dynamic calculations to study methane diffusion through coked samples.<sup>4</sup> At early stages of the reaction, they assumed a uniform coke deposition, which in their calculations showed that this type of coke present in the zeolite does not have a big effect on the methane diffusion. The experimental evidence so far, suggest that their model for coke deposition is correct, and that when coke is uniformly distributed, it has little effect on the diffusion of methane. In all temperatures all models are limited in their fits, which could have an effect in the calculated diffusion coefficient.

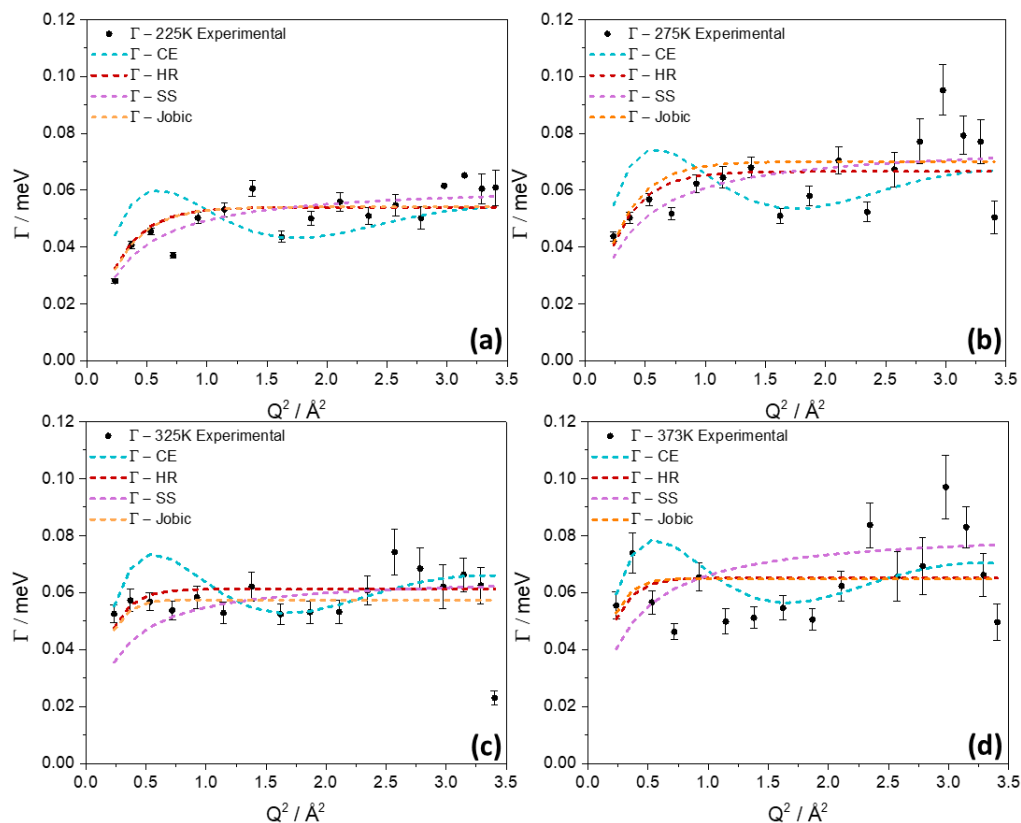


Figure 6.7: HWHM over  $Q$  for the Lorentzian fit on each temperature for MTH-2h with methane (a) 225K (b) 275K (c) 325K and (d) 373K. Four different jump diffusion models were used to fit the data. CE: Chudley Elliot (green), HR: Hall Ross (red), SS: Singwi Sjolander (pink) and the Jobic (orange) model.

Table 6.6: Diffusion coefficients ( $D$ ), Residence times ( $\tau$ ) and mean square jump lengths ( $\langle r^2 \rangle$ ) for the MTH-2h with methane calculated using four different jump models (HR: Hall Ross, SS: Singwi and Sjolander and Jobic).  $D$ ,  $\tau$  and  $\langle r^2 \rangle$  are calculated for each model at all temperatures.

Temperature (K)	Models	Parameters			
		$D$ ( $\text{m}^2\text{s}^{-1}$ )	Fit Error ( $\pm$ )	$\tau$ (ps)	$\langle r^2 \rangle$ ( $\text{\AA}^2$ )
225	CE	$4.29 \times 10^{-9}$	$1.7 \times 10^{-12}$	13.32	34.3
	HR	$3.24 \times 10^{-9}$	$1.0 \times 10^{-12}$	12.20	23.7
	SS	$3.64 \times 10^{-9}$	$8.3 \times 10^{-12}$	10.58	23.1
	Jobic	$3.14 \times 10^{-9}$	$9.8 \times 10^{-13}$	12.17	22.9
275	CE	$5.32 \times 10^{-9}$	$2.2 \times 10^{-12}$	10.75	34.3
	HR	$4.05 \times 10^{-9}$	$1.8 \times 10^{-12}$	9.89	24.0
	SS	$4.48 \times 10^{-9}$	$1.7 \times 10^{-12}$	8.59	23.1
	Jobic	$4.06 \times 10^{-9}$	$1.8 \times 10^{-12}$	9.40	22.9
325	CE	$5.47 \times 10^{-9}$	$2.1 \times 10^{-12}$	10.89	35.7
	HR	$5.98 \times 10^{-9}$	$1.7 \times 10^{-12}$	10.75	38.6
	SS	$5.00 \times 10^{-9}$	$1.9 \times 10^{-12}$	10.00	30.1
	Jobic	$6.01 \times 10^{-9}$	$1.6 \times 10^{-12}$	11.48	41.4
373	CE	$5.92 \times 10^{-9}$	$2.4 \times 10^{-12}$	10.20	36.2
	HR	$6.37 \times 10^{-9}$	$2.2 \times 10^{-12}$	10.11	38.6
	SS	$5.10 \times 10^{-9}$	$2.5 \times 10^{-12}$	8.00	24.5
	Jobic	$6.79 \times 10^{-9}$	$2.3 \times 10^{-12}$	10.17	41.4

The Arrhenius plot is shown in Figure 6.8 and the derived activation energies in Table 6.7. Comparison with the activation energies seen in Table 6.3, does not show a consistent trend between the models. The Hall-Ross model shows the activation barrier to increase as is expected with coked samples, however, the rest of the models show a decreased activation barrier which is surprising.

Focusing on the Jobic model which was the closest fitted model in the fresh sample, it is shown that the activation energy is  $0.94 \text{ KJ mol}^{-1}$  higher in the fresh sample than in the coked. MD simulations (Alex Hawkins thesis), show that methane-methane interactions play an important role in the diffusion within the zeolite. This was shown by comparing the diffusion coefficients in a simulated ZSM-5 and silicalite, on removing the acid site contribution, the increased loading of methane (9 moles per zeolite cage) kept the diffusion coefficient in the same low value as a lower level of methane (4 moles per zeolite cage). From Liu and et al., it has been discussed that at early stages, the diffusion of methane is undisturbed by the coke. It could therefore be, that the lower loading of methane in the coked sample is causing the activation energy barrier to decrease, since the methane-methane interactions are weaker, it is possible that the activation energy is not as high. It is still unclear if a drop of  $0.94 \text{ KJ mol}^{-1}$  can be completely explained by the drop in methane loading however. However, caution is needed because the activation energy is derived from the higher temperature scans as well. The numbers in Table 6.7 are tentative and could change once QENS experiments with a better temperature range are completed.

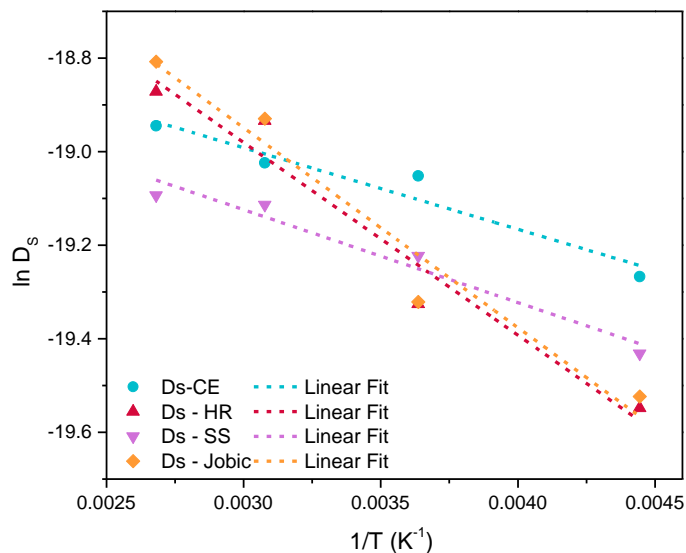
Calculating the activation energy from only two points is not recommended, however, attempting it has shown the diffusional barrier to drop even further than when using all four different temperature scans. The attempt can be seen in Table 6.8.

Table 6.7: Table of activation energies calculated from Figure 6.8 using all temperatures

Jump Diffusion Models	Activation Energy $\text{KJ mol}^{-1}$	Fit Error ( $\pm$ )
<b>Chudley Elliot</b>	1.45	$2.1 \times 10^{-4}$
<b>Hall Ross</b>	3.43	$6.9 \times 10^{-5}$
<b>Singwi Sjolander</b>	1.65	$3.1 \times 10^{-5}$
<b>Jobic</b>	3.55	$7.0 \times 10^{-5}$

Table 6.8: Table of activation energies calculated from using only the 225K and 275K data points

Jump Diffusion Models	Activation Energy KJ mol <sup>-1</sup>	Fit Error (±)
<b>Chudley Elliot</b>	2.21	1.1x10 <sup>-4</sup>
<b>Hall Ross</b>	2.28	1.7x10 <sup>-4</sup>
<b>Singwi Sjolander</b>	2.14	7.0x10 <sup>-5</sup>
<b>Jobic</b>	2.08	2.2x10 <sup>-4</sup>

Figure 6.8: Arrhenius plot of the natural log of the diffusion coefficient over  $1/T$  for the sample of MTH-2h loaded with methane

#### 6.4.3.2 Fitting of the Methane Loaded MTH-110h

The MTH-110h sample was a lot harder to fit. The methane present, as was seen from Figure 6.1, is a lot lower than initially estimated with about 65% of the methane not ending up within the sample at all. This means that the fitting parameters are heavily influenced by the coke. However, the best fit was again one Lorentzian, one broadened delta resolution function derived from the base temperature empty MTH-110h and a background. Attempting to include a second Lorentzian in the fit to the experimental data, gave bad fits with the Lorentzian FWHM either being zero or maximizing at 2 meV, which was the upper limit allowed. Despite the low methane loading, the same assumption is made as was made with the MTH-2h sample, namely that the Lorentzian describes the methane motion, rather than that of the coke despite the small amount of methane loaded in the sample. No jump diffusion models seem to fit the data, with the EISF showing a decrease which is indicative of localised 'rotational' motions. The same rotational models as discussed in 6.4.2 were used. However, the r-values were constrained when taking the methane

molecule into account, with the immobility percentage left to float. The methane motions considered can be seen in Figure 6.9. For the model for the translation in a sphere, which assumes small translational motions within the zeolite pore, the r-value was left to float, converging on the best fit. The fitting parameters can be found in Table 6.12.

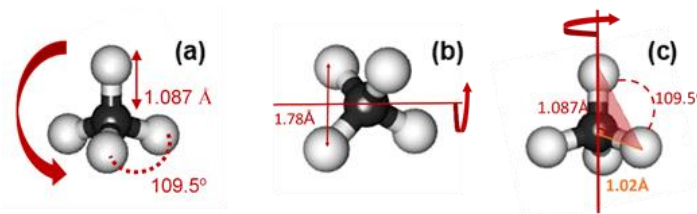


Figure 6.9: Methane molecule rotational models labelled with bond lengths and angles. (a) Isotropic rotation (b) 2-site jump and (c) 3-site jump

Figure 6.10 shows the experimental derived EISF data for the MTH-110h sample loaded with methane, compared with those from the four rotational models. From the plots it is observed that the model that best fits the data is the translation in a sphere, suggesting that the methane is tumbling around within the pores of the zeolite. From Table 6.9, it is seen that the r-value has converged to around 2 Å. The r-value for a fresh ZSM-5 is around 2.75 Å, which indicates that the pore has decreased in size, which is consistent with the loss of micropore volume observed with the nitrogen sorption experiments (Table 6.1). The immobile fraction of the sample remained high, a decrease is observed from 225 K to 275 K, which also shows the most mobility within the sample. At the highest two temperatures it is difficult to say if the motion observed is due to the methane or the coke.

Table 6.9: Fitting parameters for the rotational models for MTH-110 with methane

			QENS Temperatures			
			225K	275K	325K	373K
Rotational Models	Isotropic Rotation Spherical	r (Å)	1.087	1.087	1.087	1.087
		Pi (%)	85	78	84	88
	2-site Rotation	r (Å)	1.78	1.78	1.78	1.78
		Pi (%)	76	57	76	76
	3-site Rotation	r (Å)	1.02	1.02	1.02	1.02
		Pi (%)	82	67	81	82
	Translation in a Sphere	r (Å)	2.00	2.00	2.00	2.00
		Pi (%)	89	79	88	89

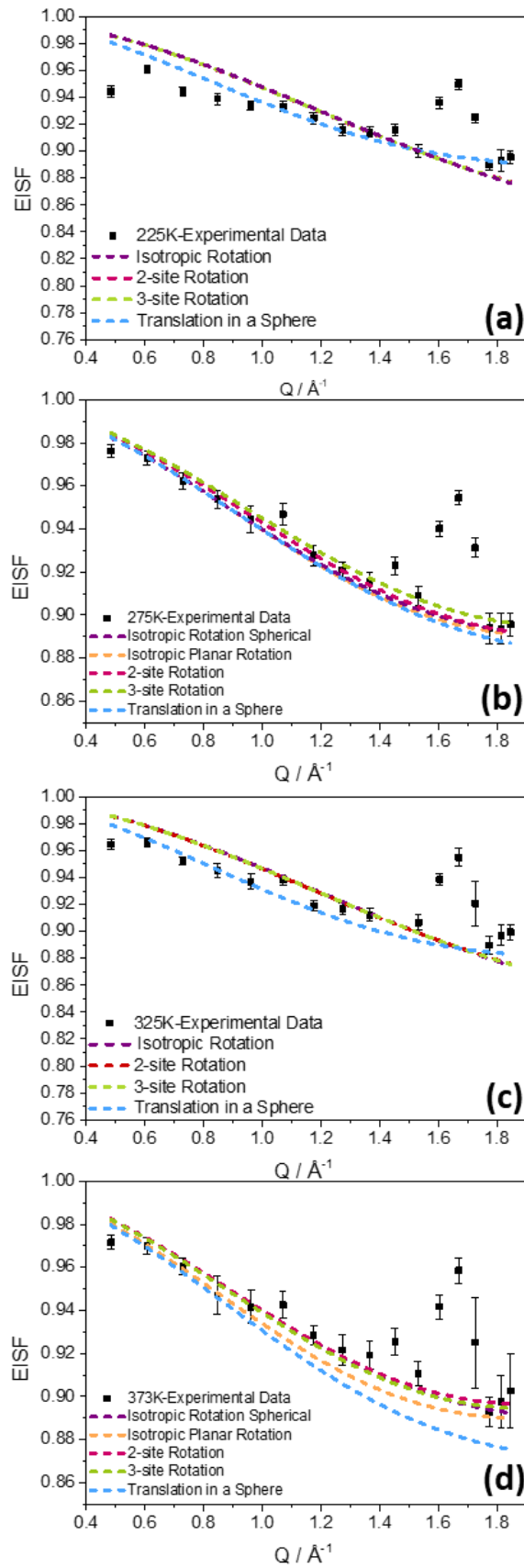


Figure 6.10: EISF Experimental data fitted with rotational models for the MTH-110h with methane (a) 225K (b) 275K (c) 325K and (d) 373K

## 6.5 Conclusions

The diffusion of methane through fresh ZSM-5 and ZSM-5 that has been through an MTH reaction at different times on stream has been studied. A similar study completed at the beginning of this project using methanol as the probe has shown that the methanol – Brønsted acid sites interactions were too strong even in coked catalysts,<sup>3</sup> which made methanol an unsuitable probe for this kind of experiment. The same experiment was then designed, but this time using methane as the probe, which should, in principle, not have any interactions with the sample. The same temperature range that was used with methanol was also used with methane. This caused complications because methane showed increased mobility within the zeolite, causing the methane motions to become too fast after about 250 K within the fresh and early stage MTH reacted sample and even earlier for the heavier coked sample (~200 K) (Figure 6.1).

Methane through a fresh ZSM-5 showed diffusion constants and activation energies closely matching those previously observed with methane in different Si:Al ratio ZSM-5's (Table 6.3). The best fit model for the diffusion of methane through the zeolite was the Jovic model of jump diffusion (Figure 6.3, Table 6.3).

Fitting the coked samples was a lot more complicated than previously anticipated because the blank coked samples could not be subtracted from the methane loaded coked samples. The elwins showed that methane is mobile within the coked samples. The QENS fitting showed that methane diffusion was not affected to a large degree in the early stage MTH sample (MTH-2h), agreeing with the suggestion made in the literature that the coke present is uniform in nature. The slightly lower diffusion coefficients and lower activation barriers observed in the coked sample when compared with the fresh sample are surprising, with the only plausible explanation being the lower methane loading in the coked sample. Methane-methane interactions could be playing a role in limiting the diffusion barrier. Diffusion through the heavier coked sample was severely hindered, with the only model fitting the data being a rotational diffusion model of translation within a sphere, with the zeolite pore size being reduced from 2.75 Å to 2 Å. The methane loading of 0.7 mol<sub>CH<sub>4</sub></sub>/mol<sub>ZSM-5</sub> suggests that very little methane in comparison with the other samples was able to diffuse through the zeolite. The methane went from unrestricted jump

diffusion within the fresh and MTH-2h sample, to small translational movements within a confined volume within the heavier coked sample.

The model fits are not unambiguous because the methane loading is so low that distinguishing between the methane motion and the coke contribution is challenging. The coke within both samples had its own rotational movement, something that caused issues with the data analysis. The rotational motion of the coke is interesting to study, however, owing to the complexity of the coked species, the actual motion could not be determined in either the MTH-2h or the MTH-110h samples. In order for the true movement of methane to be observed, the MTH reaction could be carried out with deuterated methanol. This would create coke that will have deuterium instead of hydrogen, making it virtually invisible to the neutrons and therefore any broadening observed would be from the dosed methane.

The increased mobility of the methane within the samples was also a challenge, although changing the temperature regime might work, there will be limited temperature points where the methane could be observed, with methane freezing at 91 K and as was seen from Figure 6.1 moving too fast above 200 K. This limited time window might cause further problems, therefore an alternative probe molecule might be more suited for the task. Ethane might be a good alternative. Jobic et al., studied ethane diffusion in ZSM-5 at a singular temperature of 300 K at different ethane loadings.<sup>22</sup> Ethane has been shown to be slower than methane at similar loadings ( $3 \times 10^{-9} \text{ m}^2\text{s}^{-1}$  at 300K and 4 molecules per unit cell) and therefore might be a viable alternative to study the diffusion constraints of both the fresh and coked samples.

## 6.6 References

- 1 A. L. Davidson, P. B. Webb, I. P. Silverwood and D. Lennon, *Top. Catal.*, 2020, **63**, 378–385.
- 2 I. P. Silverwood, M. A. Arán, I. L. González, A. Kroner and A. M. Beale, in *AIP Conference Proceedings*, AIP Publishing LLC, 2018, vol. 1969, p. 030002.
- 3 S. K. Matam, A. J. O'Malley, C. R. A. Catlow, S. Suwardiyanto, P. Collier, A. P. Hawkins, A. Zachariou, D. Lennon, I. Silverwood, S. F. Parker and R. F. Howe, *Catal. Sci. Technol.*, 2018, **8**, 3304–3312.

- 4 Y. Li, C. Zhang, C. Li, Z. Liu and W. Ge, *Chem. Eng. J.*, 2017, **320**, 458–467.
- 5 M. Bee, *Quasielastic Neutron Scattering*, Adam Hilger, 1988.
- 6 M. F. Telling, *A Practical Guide to Quasi-Elastic Neutron Scattering*, Royal Society of Chemistry (RSC), 2020.
- 7 O. Arnold, J. C. Bilheux, J. M. Borreguero, A. Buts, S. I. Campbell, L. Chapon, M. Doucet, N. Draper, R. Ferraz Leal, M. A. Gigg, V. E. Lynch, A. Markvardsen, D. J. Mikkelsen, R. L. Mikkelsen, R. Miller, K. Palmén, P. Parker, G. Passos, T. G. Perring, P. F. Peterson, S. Ren, M. A. Reuter, A. T. Savici, J. W. Taylor, R. J. Taylor, R. Tolchenov, W. Zhou and J. Zikovsky, *Nucl. Instruments Methods Phys. Res. Sect. A Accel. Spectrometers, Detect. Assoc. Equip.*, 2014, **764**, 156–166.
- 8 R. T. Azuah, L. R. Kneller, Y. Qiu, P. L. W. Tregenna-Piggott, C. M. Brown, J. R. D. Copley and R. M. Dimeo, *J. Res. Natl. Inst. Stand. Technol.*, 2009, **114**, 341–358.
- 9 S.F. Parker, in *Encyclopedia of Spectroscopy and Spectrometry (Third Edition)*, eds. J. C. Lindon, G. E. Tranter and D. W. Koppenaal, Academic Press Inc., 3rd edn., 2017, pp. 246–256.
- 10 M. Prager and A. Heidemann, *Chem. Rev.*, 1997, **97**, 2933–2966.
- 11 C. T. Chudley and R. J. Elliott, *Proc. Phys. Soc.*, 1961, **77**, 353.
- 12 P. L. Hall and D. K. Ross, *Mol. Phys.*, 1981, **42**, 673–682.
- 13 K. S. Singwi and A. Sjölander, *Phys. Rev.*, 1960, **119**, 863–871.
- 14 H. Jobic and D. N. Theodorou, *Microporous Mesoporous Mater.*, 2007, **102**, 21–50.
- 15 H. Jobic, M. Bee, J. Caro, M. Bulow and J. Karger, *J. Chem. Soc. Faraday Trans. I*, 1989, **85**, 4201–4209.
- 16 J. J. Caro, M. Bülow, W. Schirmer, J. Kärger, W. Heink, H. Pfeifer, S. P. Ždanov, M. Burlow, W. Schirmer, M. Bülow, W. Schirmer, J. Kärger, W. Heink, H. Pfeifer and S. P. Ždanov, *J. Chem. Soc. Faraday Trans. 1 Phys. Chem. Condens. Phases*, 1985, **81**, 2541–2550.
- 17 H. Jobic, A. Renouprez, M. Bee and C. Poinignon, *J. Phys. Chem.*,

- 1986, **90**, 1059–1065.
- 18 Z. Mao and S. B. Sinnott, *J. Phys. Chem. B*, 2001, **105**, 6916–6924.
- 19 F. Volino and A. J. Dianoux, *Mol. Phys.*, 1980, **41**, 271–279.
- 20 H. Jobic, M. Bee and A. Renouprez, *Surf. Sci.*, 1984, **140**, 307–320.
- 21 C. L. Yaws, in *Thermophysical Properties of Chemicals and Hydrocarbons*, Elsevier, 2014, pp. 693–700.
- 22 H. Jobic, M. Bée and G. J. Kearley, *Zeolites*, 1992, **12**, 146–151.

# Chapter 7

## Studying the Effect of Different Reagents as Feedstock for the MTH Reaction

---

This chapter will focus on using two different types of feedstock in order to study their role in the MTH reaction. There was a lot of contribution from different people for data collection and analysis. The DME samples were made before the start of the iCase project by Prof Stewart Parker, Prof Russell Howe, Prof. David Lennon and Dr Suwardiyanto. The MERLIN data presented in this chapter were collected by the same group of people just before the start of the iCase project (September 2016). The GC-MS, TPO data for the DME section were completed by Prof. James McGregor (University of Sheffield). The ss-NMR data for both the DME and methyl acetate sections was completed by Prof. Russell Howe. This chapter concentrates on linking the neutron-based measurements with ancillary characterisation measurements.

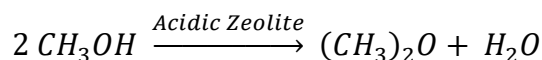
### 7.1 Introduction

Understanding the first steps of the MTH reaction is important in order to help with catalyst optimisation, in order to both optimise efficiency and tune selectivity. In this chapter we have chosen to study two different feedstocks which have been suggested as being important intermediates in the first steps of the reaction.

#### 7.1.1 Dimethyl Ether

It has long been established that in the MTH reaction, dimethyl ether (DME) is the first intermediate.<sup>1,2</sup> In certain variations of the MTH reaction, methanol is not the only feedstock of the reaction. Methanol is first dehydrated to DME and water in a different reactor and then an equilibrium mixture of methanol, DME and water is then introduced into a separate reactor where the MTH reaction takes place.<sup>3,4</sup> Relatively recent studies have suggested that the mechanistic steps of methanol and DME based MTH are not the same.<sup>4-6</sup> Kinetic studies have shown that DME converts faster at lower temperatures than methanol and

deactivation studies have shown that the catalyst deactivates at a faster rate.<sup>4,5,7,8</sup> DME reactions have also shown a higher affinity towards olefinic products.<sup>9</sup>



*Scheme 7.1: Methanol dehydration to DME*

### 7.2.1 Methyl Acetate

Although DME has been proven to be part of the MTH reaction, methyl acetate is a new concept. It has been recently proposed by two different groups, independently, that methyl acetate could be the first intermediate in creating the first carbon-carbon bond.<sup>10,11</sup> The formation of methyl acetate would require carbonylation of methanol or DME to form surface acetate groups. For the carbonylation reaction to be possible, there must be a source of CO readily available. CO has been observed as part of the initial stages of the MTH reaction on both ZSM-5 and SAPO-34 catalysts.<sup>12,13</sup> Lercher et al., suggest that the CO needed for the carbonylation reaction comes either from the dehydrogenation of methanol or methanol decomposition to formaldehyde and CO.<sup>10</sup> Both methanol and DME carbonylation have been reported, although mainly with modernite acid catalysts.<sup>14</sup> It has been recently shown that, at low temperatures, both methanol and DME have reported good selectivity towards methyl acetate with ZSM-5.<sup>2</sup> It must be noted that in studies where the carbonylation of methanol and DME was the main focus, it was reported that water causes the carbonylation rate to decrease due to competitive adsorption of water with CO.<sup>14,15</sup> Since methanol is dehydrated to form DME and water, it is expected that the carbonylation step is the rate limiting step.

## 7.2 Experimental

For the following experiments the same ZSM-5 catalyst has been used as with previous samples, with the catalyst characterisation seen in Chapter 3. The catalyst sample was calcined at 500 °C in static air in order to remove any residual template (tetrapropyl ammonium bromide) and dried under He (100 ml min<sup>-1</sup>, CK Gas >99%) in the ISIS/Glasgow Rig described in Chapter 2, Section 2.3.1.

### 7.2.1 Dimethyl Ether as Feedstock

The DME samples were created using the ISIS/Glasgow Rig described in Section 2.3.1. The DME is introduced into the reactor through the gas panel and diluted with He. There were three samples created in total (DME-1D, DME-2D and DME-3D), with the detailed experimental details found in Table 7.1. The liquid product GC-MS analysis was completed at the University of Sheffield by James McGregor using a Shimadzu QP2010SE (DB-1MS capillary l: 60m, d: 0.25 mm, t: 0.25  $\mu\text{m}$ ) at an initial oven temperature of 40  $^{\circ}\text{C}$  for 2 min, increased at 10  $^{\circ}\text{C min}^{-1}$  to 150  $^{\circ}\text{C}$  held for 3 minutes.

Table 7.1: Experimental details of the DME samples prepared

Sample	Catalyst Mass	DME Flow	He Flow	Duration	WHSV	$\tau$
	g	ml min <sup>-1</sup>	ml min <sup>-1</sup>	h	h <sup>-1</sup>	h
DME-1D	12	50	106	24	0.5	0.00574
DME-2D	12	80	106	48	0.8	0.00481
DME-3D	12	30	106	72	0.3	0.00658

$$[1] \text{ WHSV (Weight Hourly Space Velocity)} = \frac{\text{Reactant feed (g h}^{-1}\text{)}}{\text{Catalyst Mass (g)}} \quad [2] \tau \text{ (contact time)} = \frac{\text{volume of reactor (cm}^3\text{)}}{\text{total gas flow (cm}^3\text{h}^{-1}\text{)}}$$

The post reaction catalyst analysis was conducted using various techniques. The INS spectra were recorded with the TOSCA and MERLIN instruments as described in section 2.1.2.3. The MERLIN incident energies used were 4809 and 2004  $\text{cm}^{-1}$ . DRIFTS spectra were collected as described in Section 2.2.1.1 after the samples were dried at their reaction temperature under a He flow of 20  $\text{ml min}^{-1}$ . The TPO experiments were also done in Sheffield by James McGregor, using a Micromeritics Chemisorb 2720 instrument equipped with a thermal conductivity detector. The TPO samples were kept under argon atmosphere for approximately 4 weeks before the TPO measurements were conducted and for each measurement 5 mg of sample was used. Samples were purged with helium (25  $\text{ml min}^{-1}$ ) before being heated in 5%  $\text{O}_2/\text{He}$  (25  $\text{ml min}^{-1}$ ) at a rate of 10  $^{\circ}\text{C min}^{-1}$  until 800  $^{\circ}\text{C}$  was reached. The final temperature was maintained for 30 minutes to ensure the complete combustion of any carbonaceous species.

The NMR analysis of the samples was done at the University of Aberdeen by Russell F. Howe. The samples were analysed by  $^{13}\text{C}$ -NMR,  $^{27}\text{Al}$ -NMR and  $^{29}\text{Si}$ -NMR with the Varian Infinity Plus 400MHz spectrometer. The experimental details were the same as described in Section 5.2.1.1 in Chapter 5. INS

MERLIN spectra of the reference compounds of o-xylene (Sigma Aldrich, 99.9%), and durene (Sigma Aldrich, 98.7%) were also measured.

### 7.2.1 Methyl Acetate/Methanol as Feedstock

The experiments were conducted in the ISIS/Glasgow Catalysis Rig. The reactant feed was a liquid mixture of methanol and methyl acetate, with molar percentages of 0% MeOAc, 10% MeOAc, 30% MeOAc, 60% MeOAc and 100% MeOAc and all the experimental details can be found in Table 7.2. Online vapour and liquid product analysis were respectively conducted via an online MS and an offline GC-MS as described in Section 2.3.2. The post reaction catalyst samples were analysed via INS using the TOSCA instrument, TPO, DRIFTS and nitrogen sorption experiments with their experimental details being described in their respective sections in Chapter 2. The coke percentage present within the sample was confirmed via the TGA technique as described in section 2.4.4.1.

Table 7.2: Experimental details of the MeOAc/Methanol samples

Sample	Catalyst Mass g	Feed Flow ml min <sup>-1</sup>	He Flow ml min <sup>-1</sup>	Duration h	WHSV h <sup>-1</sup>	$\tau$ h
0% MeOAc	12	0.25	150	6	1	0.064
10% MeOAc	12	0.25	150	6	1	0.064
30% MeOAc	12	0.24	150	6	1	0.064
60% MeOAc	12	0.23	150	6	1	0.064
100% MeOAc	12	0.21	150	6	1	0.064

$$[1] \text{ WHSV (Weight Hourly Space Velocity)} = \frac{\text{Reactant feed (g h}^{-1}\text{)}}{\text{Catalyst Mass (g)}} \quad [2] \tau \text{ (contact time)} = \frac{\text{volume of reactor (cm}^3\text{)}}{\text{total gas flow (cm}^3\text{h}^{-1}\text{)}}$$

## 7.2 Dimethyl Ether as Feedstock

### 7.3.1 Reaction Monitoring

The mass spectrometric analyses of the effluent gases during the two and three day runs are presented in Fig. 7.1. The intensities were normalised with respect to the helium carrier gas signal and smoothed by taking one point in approximately every 20 minutes. This was done in order to eliminate unnecessary noise and to be able to follow the product trends easier. Both DME-2D and DME-3D samples show similar trends. After an initial break-in period of approximately 2 h there is a steady evolution of alkenes and methylaromatic products. This continues for 15–20 hours on stream, after

which DME conversion begins to decrease, as does the yield of alkene and aromatic products. It seems that the catalyst still retains some activity as the product signals do not drop off completely, which means that the catalyst does not become completely deactivated by the end of either reaction. When comparing the DME reacted samples, with those reacted with methanol at the same temperature (see Chapter 5, section 5.3), it is seen that the reaction profiles are quite similar with the only difference being that the DME reaction profile shows deactivation a lot faster than the methanol one. Catalyst deactivation with methanol as feedstock is seen after about 40 hours on stream, whereas for the DME sample, DME breakthrough is seen closer to 15 hours. For the DME-1D run (Figure 7.2), there seemed to be a problem with the helium flow. The helium flow seemed to fluctuate in the mass spec, which could suggest a problem in the overall flow of the reaction. The mass spectrometer profile exhibits inconsistencies and therefore cannot be used.

Off-line GC-MS analysis of the catch-pot samples from each run showed similar reaction products in each case: trimethylbenzenes (30–40%) and tetramethylbenzenes (20–30%) being the major products, followed by lesser amounts of xylenes (typically < 15%) and small amounts of methyl-naphthalenes and unidentified alkanes. This is in agreement with the GC-MS analysis for the methanol reacted samples found in Chapter 5, Section 5.3.

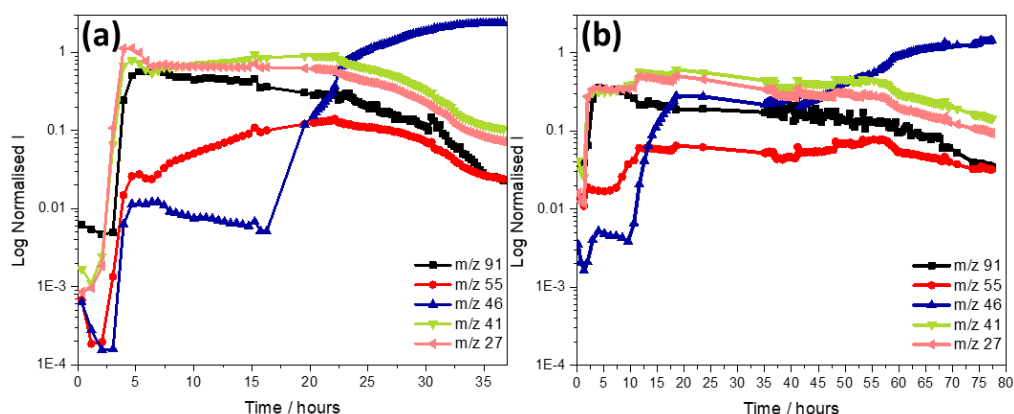


Figure 7.1: Normalised mass spectrometer reaction profiles of gaseous products evolved during DME conversion at 350 °C for (a) DME-2D and (b) DME-3D samples. Tropylium ion indicative of aromatics ( $m/z$  91, black), butene ( $m/z$  55, red), DME ( $m/z$  46, Blue), propene ( $m/z$  41, green), ethene ( $m/z$  27, pink)

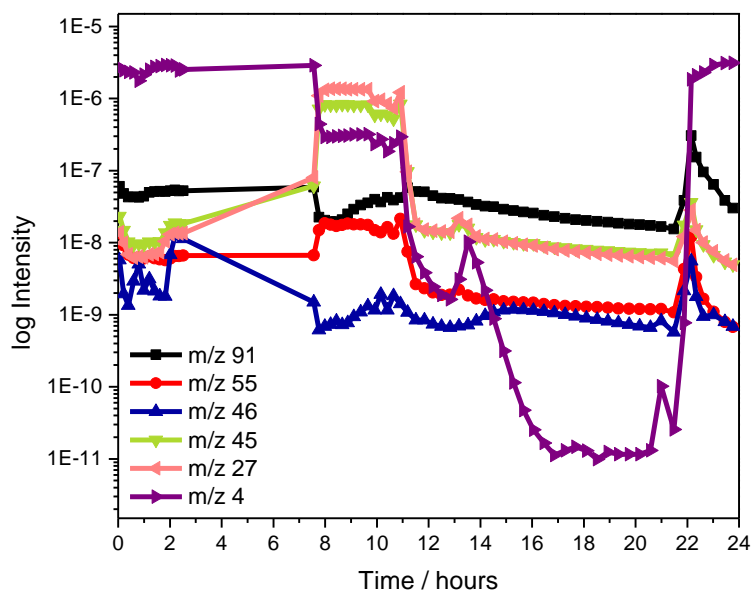


Figure 7.2: Mass spectrometer reaction profiles of gaseous products evolved during DME conversion at 350 °C for the DME-1D sample. Tropylium ion indicative of aromatics (m/z 91, black), butene (m/z 55, red), DME (m/z 46, Blue), propene (m/z 41, green), ethene (m/z 27, pink) and helium (m/z 4, purple).

## 7.2.2 Post Reaction Analysis

TPO analysis was used to characterise the coke percentage present in the reacted catalyst and to confirm the observations of deactivation from the reaction profiles. TPO of the used catalysts after reaction indicate a weight loss between 200 °C–800 °C indicative of CO and CO<sub>2</sub> generation. Table 7.3 shows the coke contents of the three used catalysts determined by TPO along with the nitrogen sorption data.

Table 7.3: Nitrogen sorption data and coke content for the fresh zeolite and DME samples

Catalyst	S <sub>BET</sub> m <sup>2</sup> g <sup>-1</sup>	V <sub>micropore</sub> cm <sup>3</sup> g <sup>-1</sup>	S <sub>external</sub> m <sup>2</sup> g <sup>-1</sup>	Coke content wt %
Fresh catalyst	404.2	0.156	37.6	N/A
DME-1D	176.0	0.047	22.9	8.8
DME-2D	43.7	0.013	14.7	18.7
DME-3D	31.5	0.008	14.6	14.6

The coke content and surface area/micropore data are broadly similar to values reported for the methanol reactions seen in Chapter 5. The DME-2D and DME-3D show coke content and reduced surface area comparable to the methanol reaction at 350 °C for 110 hours. It must be noted that the methanol reaction ran for approximately 62 hrs and 32 hrs longer than the DME-2D and DME-3D

samples respectively. It must also be noted that the samples have a different WHSV and contact time, which as was seen in Chapter 5 could have an effect in how far the reaction progresses. This faster coke build up could be due to the lack of water present in the DME reactions as there is no methanol dehydration step. The water usually present in the MTH attenuates coke formation by competing with the coke precursors for adsorption on the acid sites.<sup>16</sup> With DME, the lack of this competitive adsorption could potentially cause an increase in the formation of coked species. Bibby et al. reported that complete deactivation of methanol conversion occurs at coke levels between about 14 and 18 wt %, depending on the particular zeolite used.<sup>17</sup> The loss of surface area/micropore volume in the used catalysts is also similar to that reported by Bibby et al.<sup>17</sup>

There are some differences between the DME-2D and DME-3D samples. The DME-2D and DME-3D samples were exposed to dimethylether for different times and at different flow rates (Table 7.1). The DME-2D catalyst deactivates more quickly than the DME-3D catalyst, which may be due to the higher DME flow rate, and contains a higher level of coke. There is also a significant difference in the TPO profile for the DME-3D catalyst compared with the two exposed to DME for shorter times (Figure 7.3). The TPO profiles of DME-1D and DME-2D shown in Figure 7.3, are quite symmetrical with a maximum CO/CO<sub>2</sub> desorption at ~ 600 °C. The TPO profile of DME-3D shows a higher maximum temperature of ~ 635 °C. Both types of profile fall into the category of Type II coke assigned by Muller et al to aromatic hydrocarbon species formed in the conversion of methanol to olefins over ZSM-5 at 450 °C.<sup>18</sup> The type I coke with a TPO maximum below 400 °C and attributed by these authors to oxygenated molecules was not seen in any of the samples. Choudhary et al. distinguished between “soft” (TPO maximum < 600 °C) and “hard” (TPO maximum ~ 650 °C) coke formed in the aromatisation of propane over gallosilicate MFI catalysts, and suggested that the “hard” coke is more graphitic in nature with a lower H:C ratio.<sup>19</sup>

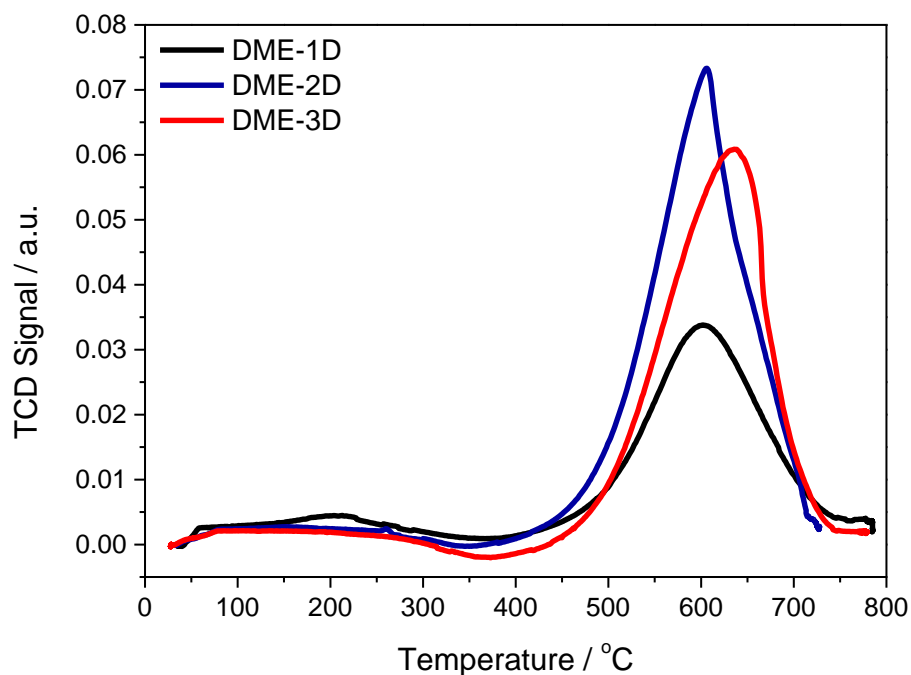


Figure 7.3: TPO profiles of DME-1D (black), DME-2D (blue) and DME-3D (red)

### 7.2.2.1 $^{13}\text{C}$ -NMR Spectroscopy

To further probe the molecular identity of coked species present in the used catalysts,  $^{13}\text{C}$  CP-MAS NMR measurements were also carried out on the used catalysts. Figure 7.4 compares the spectra obtained with that of the same zeolite catalyst used to convert methanol at 350 °C for three days.<sup>20</sup> The NMR spectra were taken from reference 15. There are three regions of interest. Signals around 20 ppm are due to aliphatic carbon, most probably methyl groups.<sup>21</sup> A sharp signal at 60 ppm in the catalyst reacted for only 1 day is due to unreacted (weakly bound) dimethylether.<sup>22</sup> The remaining features are due to aromatic carbons. These give intense spinning side band features separated by the spinning speed employed (between 3 and 4 kHz in the spectra shown here), due to the large chemical shift anisotropy of the aromatic  $^{13}\text{C}$ . The spinning side bands are identified by observing their shifts on changing the spinning speed. The un-shifted peaks are the isotropic chemical shifts of the species concerned.

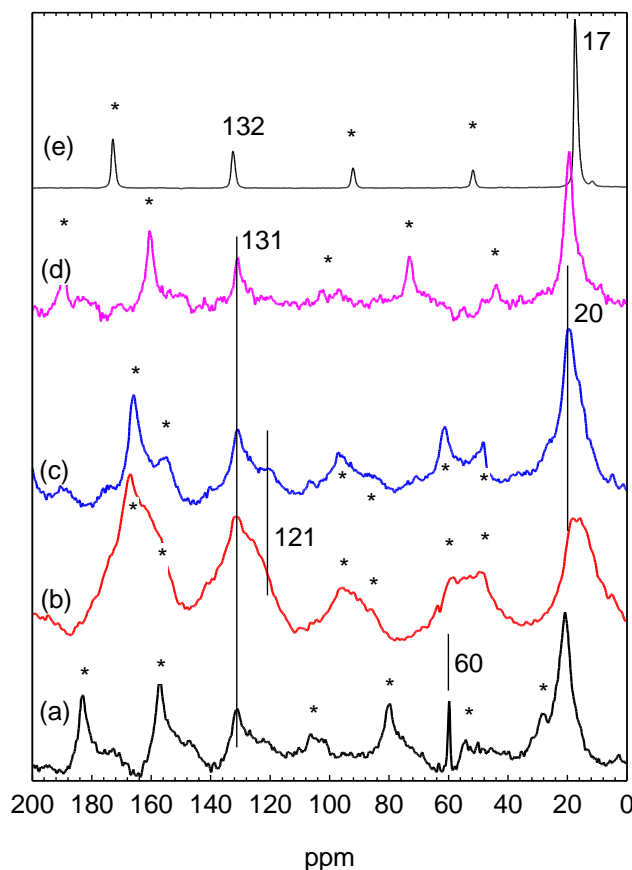


Figure 7.4:  $^{13}\text{C}$  CPMAS spectra of: (a), DME 1D, 2.6 kHz; (b), DME 2D, 3.5 kHz; (c), DME 3D, 3.5 kHz; (d) Zeolite reacted with methanol at 523 K for 3 days, 3.0 kHz [8], (e) hexamethylbenzene, 4.0 kHz. (\*) denote spinning side bands resulting from the spinning speed indicated.

The spectrum shown in Figure 7.4.d of a catalyst reacted with methanol for three days at 350 C (and still active for hydrocarbon formation<sup>20</sup>) shows a single aromatic carbon signal at ~ 131 ppm with its associated spinning side bands. This resembles, but does not match exactly, the spectrum of hexamethylbenzene shown in Figure 7.4.e. The same signal also dominates the spectrum of the catalyst reacted with dimethylether for 1 day (and still active) shown in Figure 7.4.a. The two partially deactivated catalysts (Figure 7.4.b and 7.4.c) show broadening of the 130 ppm signal and the appearance of a definite new component at ~124 ppm. The second aromatic component becomes more apparent in the spinning sidebands, as each spinning side band appears as a doublet. The largest contribution from this component is found in the DME-2D sample which has the highest coke content and the greatest extent of deactivation.

Although there have been extensive  $^{13}\text{C}$  NMR studies reported in the literature of the initial stages of methanol conversion over ZSM-5 there is little prior

information available on deactivated catalysts.<sup>23</sup> Meinhold and Bibby reported NMR evidence for the presence of methylaromatic species in coked ZSM-5 catalysts.<sup>24</sup> In particular, a signal at ~20 ppm was assigned to methyl groups in tetramethylbenzene isomers, significantly shifted from the 17.2 ppm signal of methyl groups in hexamethylbenzene. This difference is also evident in the spectra shown in Figure 7.4. A signal around 130 ppm with strong spinning sidebands was assigned to aromatic carbons, although it was not possible to identify particular species. The 20 ppm and 130 ppm signals from coked ZSM-5 have also been reported more recently by Barbera et al., although both show higher and lower field shoulders suggestive of multiple methyl aromatic species.<sup>25</sup>

For the samples analysed here, we can conclude that the DME-1D sample, as with the sample exposed to methanol for three days at 350 °C, contains mostly tetramethylbenzene species. In the more deactivated samples (DME-2D and DME-3D), there is a growing contribution from other species which may include pentamethylbenzene and methylated naphthalenes. Particularly in the DME-2D, sample there is a much larger ratio of aromatic to aliphatic carbon, although this cannot be quantified without knowing cross-polarisation efficiencies. The TPO profiles suggest that some graphitic carbon might be present. This carbon, as Meinhold and Bibby reported, may be NMR invisible.<sup>24</sup> This was already observed in Chapter 5, where the amorphous carbon present in the deactivated sample which was dominating the INS spectrum, was mostly invisible in the NMR spectrum. Although DME-2D and DME-3D were not deactivated to the same extent of the 400-44h sample in Chapter 5, it is obvious that there is amorphous coke present within both samples, but it is not seen by the NMR.

### **7.3.2.2 <sup>27</sup>Al and <sup>29</sup>Si NMR Spectroscopies**

Figure 7.5 shows <sup>27</sup>Al spectra of the fresh catalyst and the three used DME catalysts. The dominant signal in the fresh catalyst at 51 ppm is due to tetrahedral aluminium in the zeolite framework, while the small signal at ~ -3 ppm is attributed to octahedral Al species not in the framework.<sup>26</sup> There is a dramatic decrease in the amount of NMR visible aluminium in the coked zeolites, and the remaining tetrahedral signal is shifted to higher field (by 2-4 ppm). These effects have been seen before in coked ZSM-5 catalysts, and attributed to interaction of coke species with the AlO<sub>4</sub> framework sites, causing broadening of the signal from quadrupolar <sup>27</sup>Al beyond detection in a one pulse

measurement.<sup>17</sup> Note that the octahedral Al signal is also completely removed. There is no evidence in Figure 7.5 for formation of 5 coordinate extra-framework aluminium. However, the <sup>29</sup>Si NMR spectra in Figure 7.6 show that during reaction some loss of lattice AlO<sub>4</sub> aluminium occurs.

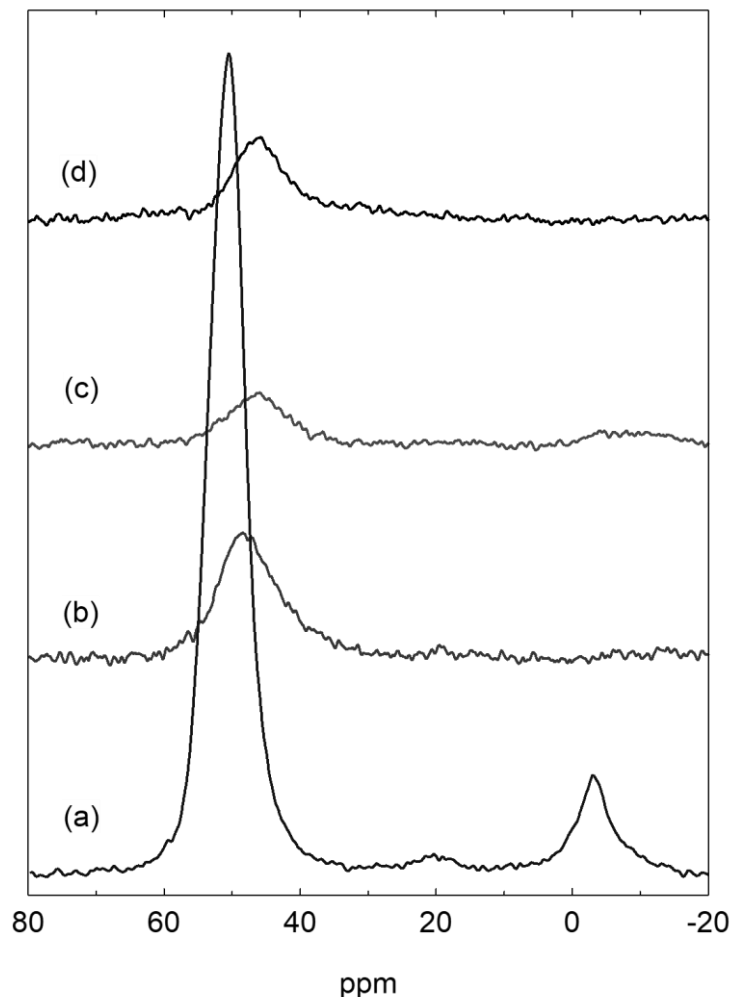


Figure 7.5: <sup>27</sup>Al NMR Spectra of (a) Fresh ZSM-5, (b) DME-1D, (c) DME-2D and (d) DME-3D. All spectra have been normalised to the same S/N to allow an approximate comparison of intensities.

The major <sup>29</sup>Si NMR signal at -113 ppm is due to Q<sub>4</sub> Si(OSi)<sub>4</sub> units in the framework, while the shoulder at -107 ppm is due to Q<sub>3</sub> Si(OSi)<sub>3</sub>(OAl) units. It is clear that even after 1 day of reaction with DME there has been significant framework dealumination, causing a decrease in the -107 ppm signal. It does not appear to decrease further with longer reaction times, although the overall line-width of the <sup>29</sup>Si signal is increased as the coke level rises. This framework dealumination is attributed to the steam produced in the initial stages of the reaction, as reported elsewhere.<sup>27</sup>

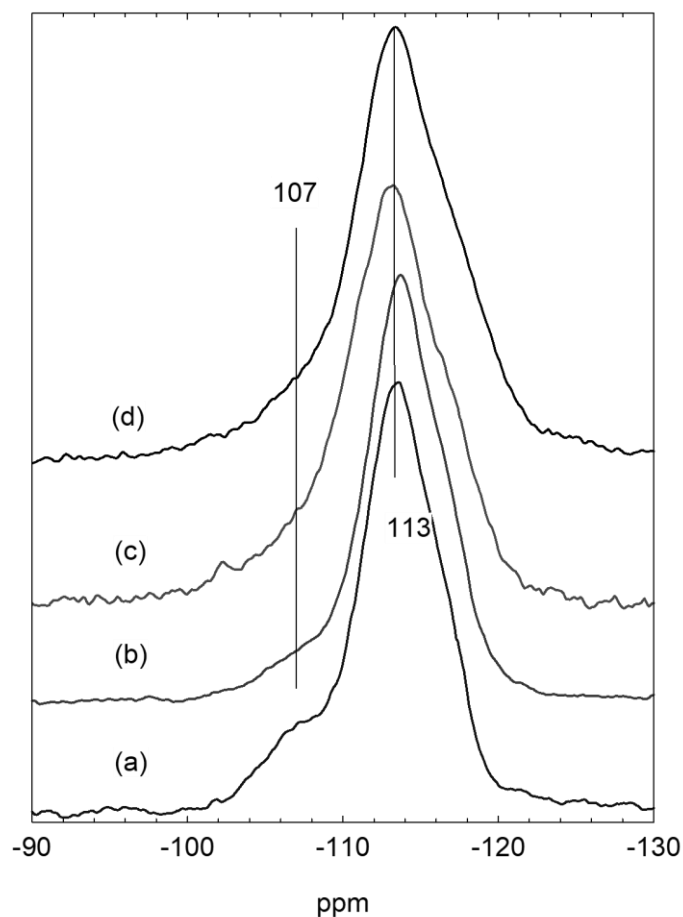


Figure 7.6:  $^{29}\text{Si}$  NMR spectra of (a) fresh catalyst; (b) DME-1D; (c) DME-2D; (d) DME 3D.

### 7.3.2.3 DRIFTS

The DRIFTS spectra found in Figure 7.7 were measured 6 months after the samples were reacted. The samples were not kept in an inert atmosphere, so it is possible that the samples aged in some way. The spectra are on the same absorbance scale (with no offset), and they show a marked decrease in reflectivity (more evident on the framework bands). This was also observed in Chapter 5, Section 5.4.1 where the samples that were reacted for longer seemed to lose spectral identity. Even when some of the spectral identity was lost, with the methanol samples the ones that did not reach complete deactivation, there were still peaks visible in the CH stretch region. With the DME samples only the spectrum in Fig. 7.7.b, which is for DME-1D shows peaks in the CH region. This is probably because the colour of the other two samples were very dark and with low reflectivity. There is not enough resolution to comment on the acid site region, with all samples showing that region broadened out.

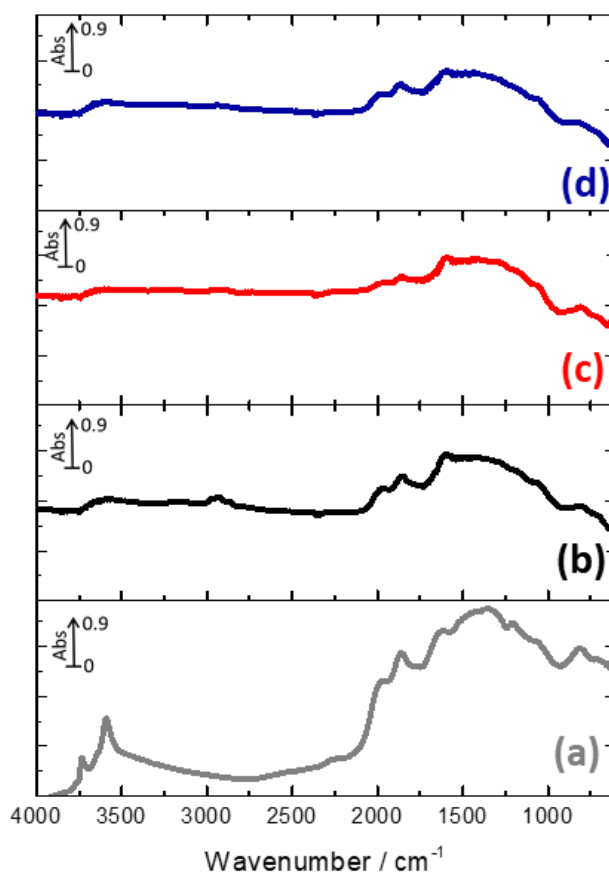


Figure 7.7: DRIFTS spectra of (a) Fresh ZSM-5 (b) DME-1D (c) DME-2D and (c) DME-3D

### 7.2.3.4 INS

The INS spectra of the DME samples obtained with the TOSCA instrument are seen in Figure 7.8. The spectra are stacked and seem to be following the same pattern as observed with the methanol steady state samples. It must be noted that all three DME samples share the same pattern, even at the higher coked sample of 18.7 wt% coke. It is evident that DME as feedstock shows the same INS pattern that methanol does. The DME-3D (Figure 7.8) is almost identical to 350C-110h sample reacted with methanol (Figure 5.21.a) They have the same coke content Table 7.3 and 5.2, so the similarities are not surprising. All samples have the  $600\text{ cm}^{-1}$  peak indicative of naphthalenes and the  $1200\text{ cm}^{-1}$  peak showing the presence of polycyclic aromatics. The ratio between the  $1200\text{ cm}^{-1}$  peak and the  $910\text{ cm}^{-1}$  peak is not at the same intensity in all samples. As discussed in Chapter 5, the intensity difference could be attributed to the presence of amorphous carbon in the sample. From below the  $200\text{ cm}^{-1}$  mark, it is difficult to distinguish between the different methyl torsions, which as was discussed in Chapter 3; the torsional energy shifts depending on the number of methyl substitutions as well as the intermolecular interactions.

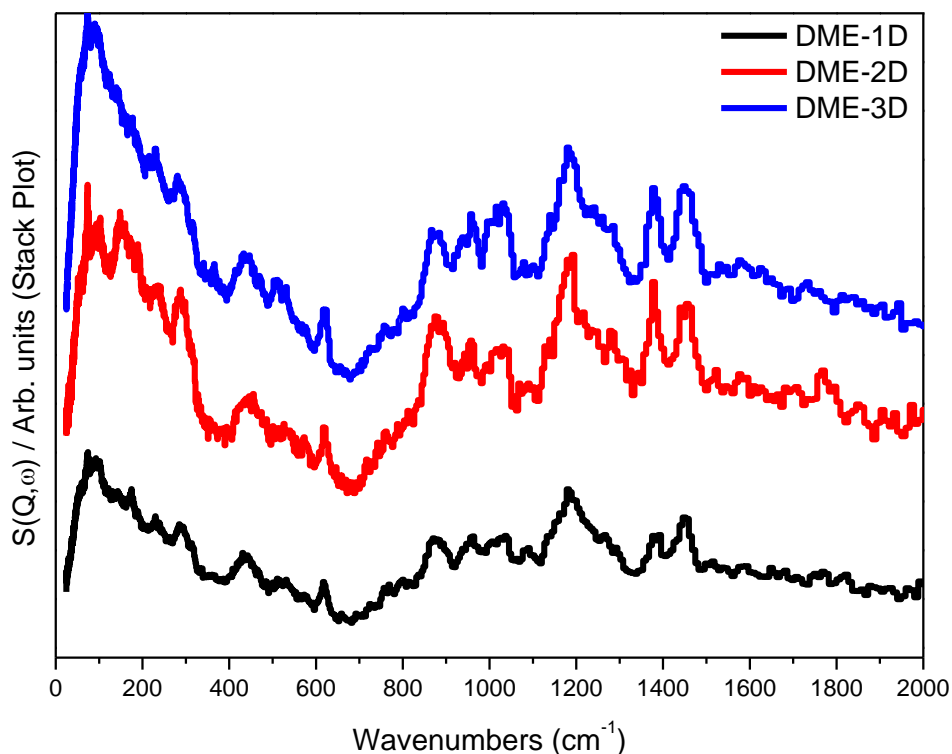


Figure 7.8: Stack plot of INS spectra obtained by the TOSCA instrument of the DME reacted samples

The spectra seen in Figure 7.9 are the MERLIN spectra of the DME reacted samples in the high energy region. The spectra are normalised via the catalyst weight, as the intensity of the INS spectra is directly related to the number of inelastic scatterers in the sample.<sup>28</sup> The intensities seen in Figure 7.9, should scale with the coke determined by TPO analysis, if the coke content is solely hydrocarbonaceous. The DME-2D and DME-3D spectra, with their higher coke content are more intense than DME-1D as expected. However, despite very different coke contents, DME-2D and DME-3D have almost overlapping spectra. The higher coke content in DME-2D sample seen from TPO could be due to a higher level of graphitic or amorphous coke present, which due to the lower hydrogen content, would not be contributing significantly to the INS intensity. As was seen in Chapter 5, although the amorphous coke has a characteristic INS spectrum, the intensity of that spectrum was a lot lower than that of the steady state mature samples (Figure 5.21), independent of the TPO coke. The inelastic cross section of hydrogen is a lot larger than that of carbon, in cases where the coke is dominated by carbon, the INS intensity would be a lot lower.

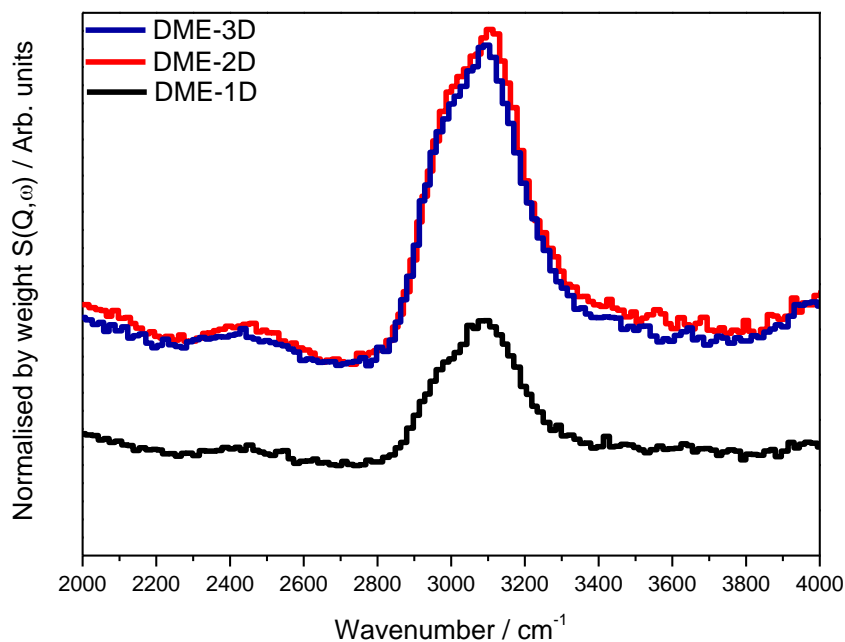


Figure 7.9: INS spectra of the DME reacted samples collected with the MERLIN spectrometer using the A-chopper package at an incident energy of  $4809 \text{ cm}^{-1}$ . Spectra are normalised by sample weight. DME-1D (black), DME-2D (red) and DME-3D (blue).

Because of the quantitative nature of the INS technique, peak fitting can be used to estimate the ratio between the aliphatic and olefinic/aromatic C-H stretch modes seen in Figure 7.9. Figure 7.10 shows the results. The experimental data were peak fitted using Peak Fit Pro (OriginPro 9), with a user defined linear background and Lorentzian peaks constrained to the same width. The ratio of aromatic to aliphatic C-H is considerably higher in all three DME samples than was seen with methanol. With the  $\text{sp}^3:\text{sp}^2$  ratios being 1:1.59 for DME-1D, 1:1.49 for DME-2D and 1:1.32 for DME-3D. It is surprising that the DME-1D has the highest ratio of aromatic contribution considering that it is the one showing the least amount of deactivation. A higher ratio of aromatic character could be a consequence of there being less methylation of the hydrocarbons present within the zeolite. It could also be that as was discussed above, the more deactivated samples could have amorphous coke which would have a lot less intensity when compared to the hydrocarbons retained within the zeolite. It is obvious by both the TOSCA and MERLIN data that the coke present within the DME samples is similar despite their different coke percentages obtained via TPO. The deactivation observed in the DME samples is different than the deactivation observed via the methanol reacted 400-44h sample. Where the methanol deactivated sample is dominated by amorphous coke, the DME-2D sample shows that the amorphous coke does not play a

significant role in its INS spectrum, which highlights the difference between the two feedstocks.

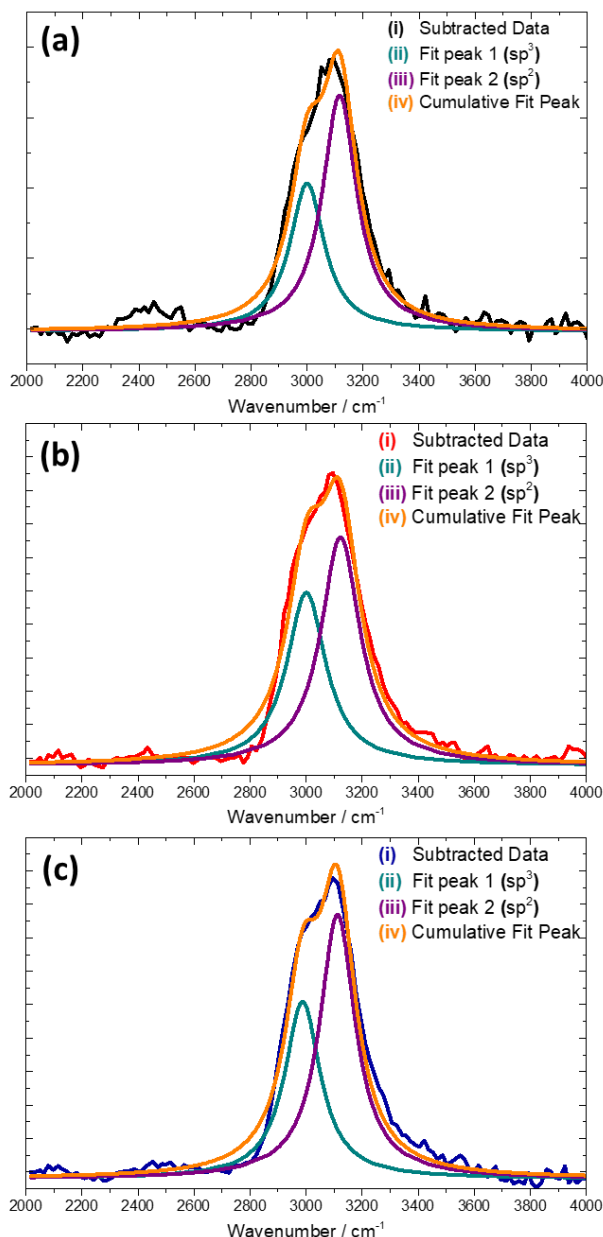


Figure 7.10: Peak fitting of (a) DME-1D (black), (b) DME-2D (red) and (c) DME-3D (blue). (i) background subtracted experimental data set (ii)  $sp^3$  hybridised  $\nu(C-H)$  peak (green) (iii)  $sp^2$  hybridised  $\nu(C-H)$  peak (purple) and (iv) cumulative fit i.e. (ii)+(iii), (orange)

For this experiment, o-xylene and durene were run in the same spectrometer for comparison purposes of the high energy spectra. Figure 7.11 compares the two model compounds with the DME-3D spectrum. The two methylated benzenes were chosen for their  $sp^3:sp^2$  ratio. The  $\nu(CH)$  region for durene contains predominantly contributions from  $sp^3$   $CH_3$  stretching vibrations, since there are 12  $sp^3$  CH bonds compared with its 2 aromatic CH bonds, which vibrate at a higher frequency. In o-xylene, the ratio of  $sp^3$  CH bonds to aromatic

CH bonds is 6 to 4. Since INS intensities depend directly on the number of hydrogen atoms involved, the profile of the  $\nu(\text{CH})$  vibrations shifts to higher wavenumber for *o*-xylene compared with durene. For the DME-3D catalyst, the profile shifts further to higher energy, suggesting that the ratio of  $\text{sp}^3$  CH to aromatic CH is even lower than that in *o*-xylene. This confirms the ratios obtained from the peak fitting, suggesting that there is more aromatic intensity in all three samples. This also shows, that for the DME samples, there could be a difference in the amount of methylation present, with the suggestion being that less methylation is happening.

Polymethylated aromatics are considered to form by sequential methylation steps. Those steps heavily depend on the Brønsted acid sites of the zeolite, as well as the presence of methanol or DME in the sample.<sup>29,30</sup> One major difference between DME and methanol as reactants is the reduced amount of water produced by DME. The higher deactivation rate of DME could be attributed to this lack of water, as methylation reactions are inhibited by the loss of Brønsted acid sites. Due to the lack of water, Brønsted acid sites are not regenerated as fast as with methanol, which could lead to faster deactivation, not by pore blocking as was seen in methanol, but from acid site loss. This faster deactivation with DME was also noted in the literature and was attributed mainly due to the lack of water as well.<sup>4,8</sup> The IR spectra observed (Figure 7.7) are consistent with this scenario.

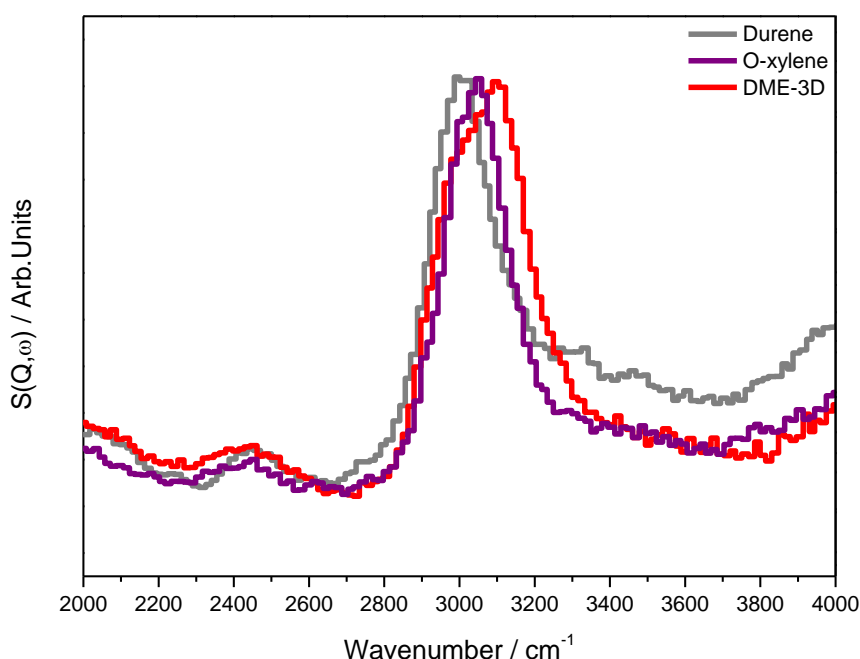


Figure 7.11: INS spectra of the  $\nu(\text{CH})$  region measured with the MERLIN instrument using the A-chopper package at an incident energy of  $4809 \text{ cm}^{-1}$ . Durene (grey), *o*-xylene (purple) and DME-3D (red).

### 7.2.3 Summary

DME formation has been established in the literature as one of the first steps of the MTH reaction. This section has focused on studying DME as the feedstock of the reaction being completed under reaction conditions similar to the methanol reactions. It was shown that the deactivation of the catalyst is faster when DME is used as the feedstock, something that is in agreement with pre-existing literature.<sup>4,7</sup> The deactivation of the catalyst seems to be enhanced at faster space velocities and low contact times. This is in contradiction with the methanol reactions, as it was shown that reducing the contact time also decreased the amount of deactivation present within the sample. However, in the methanol experiments the space velocity was kept the same, something that was not possible for the DME experiments.

The low energy INS spectra of DME and methanol reacted samples at steady state show a similar pattern, with very little differences. The similarities in the spectra solidify the earlier deduction that what is observed with the INS is the vibrational fingerprint of the hydrocarbon pool (Figure 7.8). The INS spectra of the DME samples do not change with the changing conditions or with the increased coke content. None of the DME samples, even if they show signs of deactivation, have shown a similar spectrum to that of the fully deactivated methanol spectrum seen in Chapter 5 (Figure 5.21). In fact, the DME reactions have shown a higher aromatic to aliphatic ratio in all three samples when the high energy INS spectra were analysed (Figure 7.10). This is attributed to the lower levels of water present in DME reactions which has the effect of reducing the regeneration of the acid sites which is needed for the methylation of the aromatic species. The lack of water is also responsible for the faster coke build up observed in the DME samples in comparison with the methanol samples (Table 7.1 and 5.2). Water competitively adsorbs with coke precursors slowing the coke formation within a zeolite. The lack of water in the DME case allows for faster coke formation, with the competitive adsorption happening between the different coked precursors which could also have an effect in the degree of methylation present within the coked species. This difference suggests that the deactivation observed in the DME samples is by loss of acid sites rather than coke build up as is observed with methanol and, as it will be shown later on this chapter, by methyl acetate reactions. From the INS spectra both the low energy and the ratio of  $sp^3:sp^2$  C-H bonds, it can be seen that there is not enough amorphous carbon present in the DME samples in order for the deactivation to

be similar to what has been observed in the methanol 400-44h case (Figure 5.21).

## 7.3 Methyl Acetate/Methanol as Feedstock

### 7.3.1 Reaction Monitoring

Figure 7.12 shows the product profiles versus time on stream for (a) methanol alone, (b) methanol: MeOAc 9:1, (c) methanol: MeOAc 7:3, (d) methanol: MeOAc 4:6 and (e) MeOAc alone. The mass spectrometric analysis is complicated by the contributions from fragmentation of other species but, nonetheless, a number of trends can be identified. For methanol alone, the formation of ethene, propene and aromatic products remains constant over the 6 hour run time. Although there is some increase in the amount of unreacted methanol and DME over this time period, the overall conversion of methanol remains high (>90%).

Figure 7.13 plots the methanol and MeOAc conversions versus time for the different reactant compositions tested. The conversions were calculated from comparison with mass spectral peak intensities measured at time = 0 on bypassing the reactor. Addition of 10% and 30% MeOAc (Figure 7.12.b and c respectively) show the same trends in their product profiles. It must be noted that for the 10% MeOAc, there was an hour and a half where the mass spectrometer was not recording due to software issues. The main difference between them (10% and 30% MeOAc) and the 0% MeOAc is the quick increase of the aromatics signal, which, within an hour of both reactions, becomes the major signal in the mass spectrum. After the  $m/z$  91 increase, the product signals remain constant throughout the duration of the 6 hours, with both MeOH and MeOAc conversions remaining high (Figure 7.13).

At 60% MeOAc a more noticeable deactivation occurs. The methanol conversion falls steadily throughout the run, and although aromatic production continues, the apparent continued production of ethene and propene is largely due to the contributions to  $m/z = 42$  and  $m/z = 27$  from fragmentation of MeOAc. The MeOAc conversion falls steadily with time on stream (Figure 7.13), resulting in larger mass spectrometer signals from MeOAc and its fragmentation products. When the reactant feed was pure MeOAc the initial reaction products are similar to those seen with methanol (Figure 7.12.d), but deactivation occurs much more rapidly, so that after ~ 3 hours on stream the

aromatic signal is seen to steadily decline. There is also a significant increase in the methanol signal, suggesting that hydrolysis of MeOAc may be occurring (Scheme 7.2). It must be noted that in Chapter 5 and the previous section of Chapter 7 where the focus was on DME, the reactions had similar product profiles. One of the main differences is how much more sustainable those reactions are in comparison with the MeOAc reactions. MeOAc/MeOH reactions showed advanced aging of the catalyst in just 6 hours of time-on-stream.

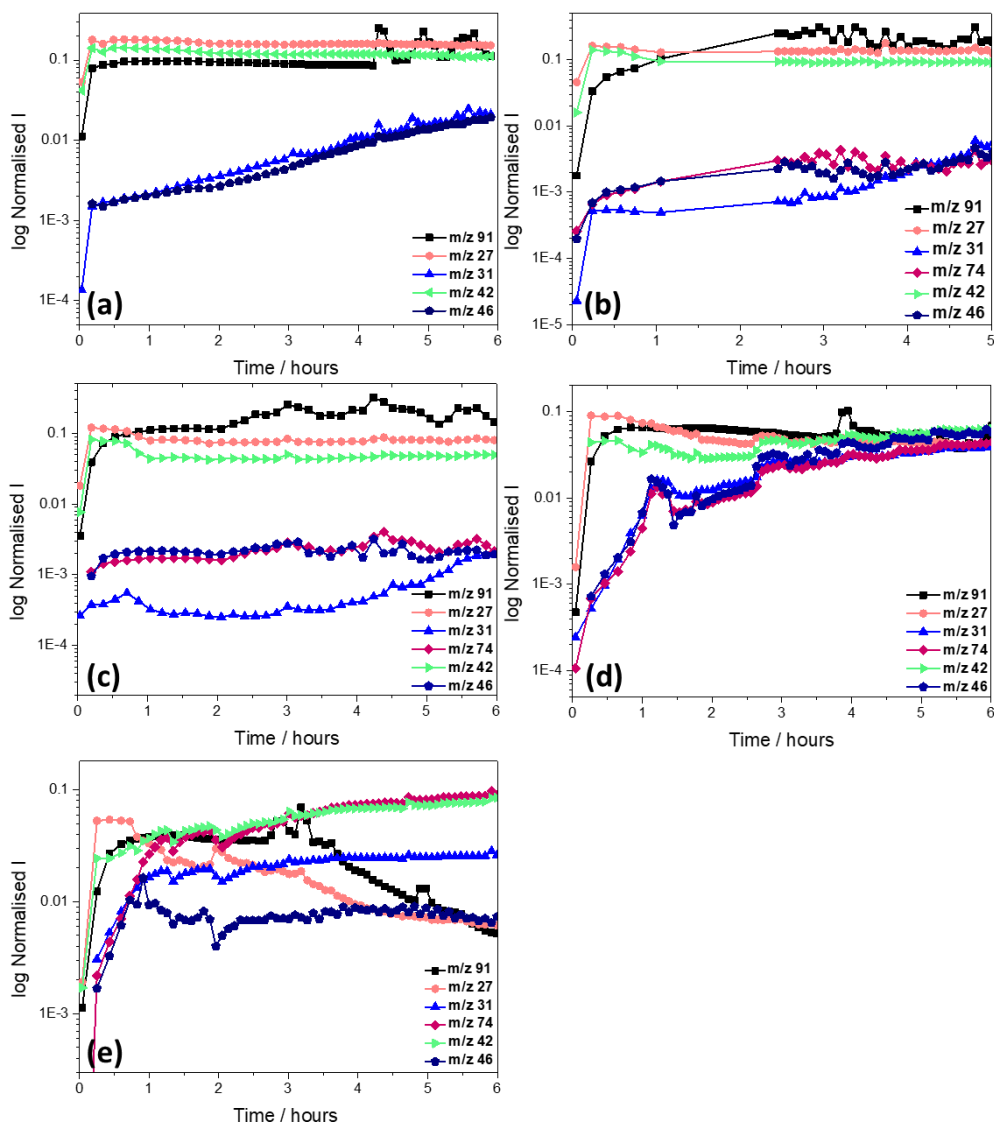


Figure 7.12: Mass spectral analysis of reactor exit gases during MeOH/MeOAc conversion at 350 °C. (a) 0% MeOAc (b) 10% MeOAc (c) 30% MeOAc (d) 60% MeOAc (e) 100% MeOAc. M/z 91 (—■—) signifies the tropylium ion indicating aromatics. m/z 74 (—◆—) signifies methyl acetate, m/z 46 (—◆—) signifies DME, m/z 42 (—▼—) signifies propene, m/z 31 (—▲—) signifies methanol and m/z 27 (—●—) signifies ethene.

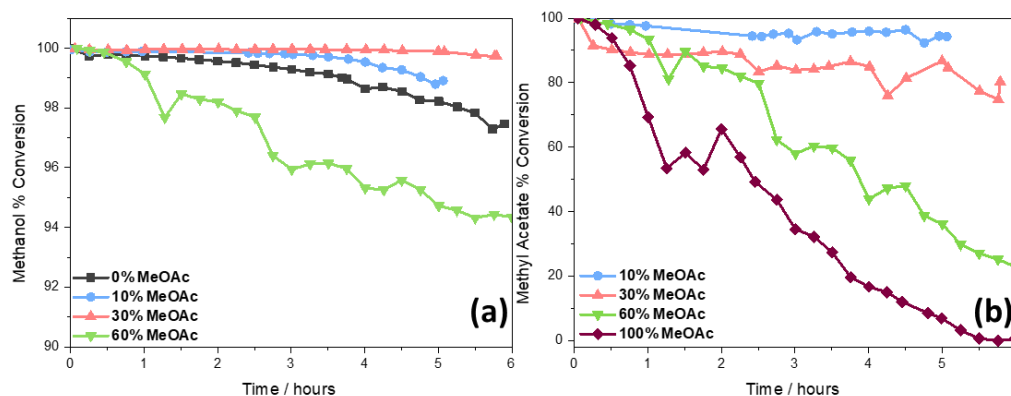
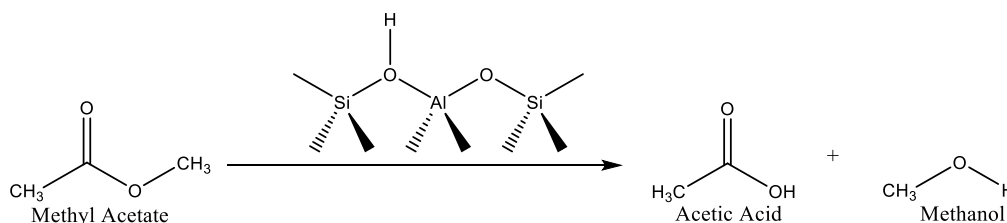


Figure 7.13: Methanol (a) and methyl acetate (b) percentage conversion versus time on stream at 350 °C.



Scheme 7.2: Methyl acetate hydrolysis to acetic acid and methanol.

Figure 7.14 shows GC-MS analysis of the liquid products retained in the reactor catch-pot (total product after 6 hours on stream). For the pure MeOAc reaction, acetic acid is the major liquid product (Scheme 7.2). In all of the reactions, the hydrocarbon products comprise a mixture of xylenes, tri-methylbenzenes, tetra-methylbenzenes and substituted naphthalenes. These products are still present but at much lower levels when pure MeOAc was the reactant. The conversion of MeOAc over SAPO-34 catalysts is reported to give an initial product distribution similar to that formed from methanol, although the production of alkenes falls after only 10 minutes on stream at 400 °C.<sup>31</sup> To the best knowledge of the author, there is no comparable study of MeOAc conversion over ZSM-5, although it must be noted that coupling of CO and methanol over ZSM-5 is reported to form aromatic products, presumably via MeOAc.<sup>32</sup>

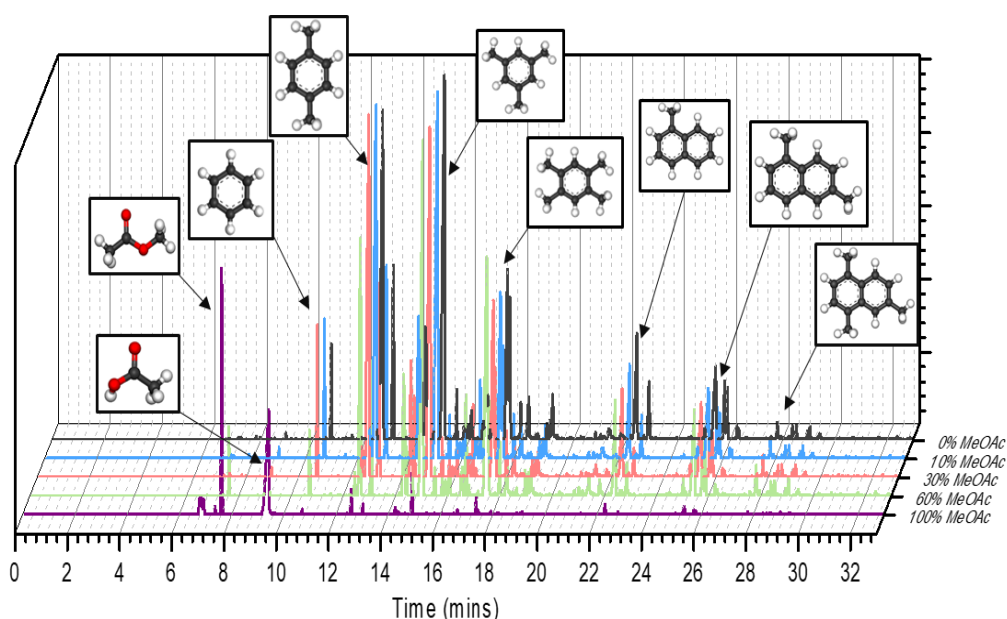


Figure 7.14: Catch-pot analysis via GC-MS of liquid products accumulated during 6 hours on stream at 350 °C.

### 7.3.2 Post-Reaction Catalyst Characterisation

The results presented above suggest that the major effect of MeOAc is to promote catalyst deactivation. Consistent with the suggested role of MeOAc in promoting catalyst deactivation, the coke content of the used catalysts increased with increasing MeOAc content of the reaction feed, as shown in Table 7.4. There is a corresponding loss of surface area, principally micropore volume, which correlates with the increasing coke content. These data are consistent with earlier reports that initial coke formation in methanol conversion over ZSM-5 occurs within the micropores of the zeolites.<sup>33,34</sup> The coke content reported for just 6 hour reactions show the reactions of 60% MeOAc and 100% MeOAc to be high enough to be considered under normal MTH conditions as nearing deactivation.

Table 7.4: Coke content and nitrogen sorption data for the used catalysts

Reaction feed	$S_{\text{BET}}$ / $\text{m}^2\text{g}^{-1}$	$V_{\text{micropore}}$ / $\text{cm}^3\text{g}^{-1}$	$S_{\text{ext}}$ $\text{m}^2\text{g}^{-1}$	Coke content / wt %
Fresh ZSM-5	450.1	0.148	36.9	N/A
0% MeOAc	302	0.112	34.5	2.53
10% MeOAc	327	0.121	34.5	2.81
30% MeOAc	155	0.054	22.9	7.55
60% MeOAc	40.6	0.009	19.8	9.33
100% MeOAc	22.1	0.003	15.3	9.76

The TPO measurements reveal that the addition of MeOAc to the reaction feed causes some change in the nature of the coke species (Figure 7.15). There is a significant shift to higher temperature in the peak maximum in the TPO profile of the used catalysts when MeOAc is added to the feed, from approximately 520 to 580 °C. This shift is observed even when only 10% MeOAc is added to the methanol feed. This suggests that in the presence of MeOAc, the coke deposits have a lower H:C ratio than that formed from methanol alone. The TPO curves show that some of the coke needs a higher temperature of 600°C in order to burn, however it is not a large proportion of curve overall it could suggest that there is some hard coke present.<sup>19</sup> There no evidence for the presence of “hard” or graphitic coke dominating the nature of the coked species however, even with a pure MeOAc feed at 350 °C.<sup>19</sup> The peak shift is consistent with an increased presence of aromatics when methyl acetate is added to the methanol feed, as also observed from the reaction profiles.

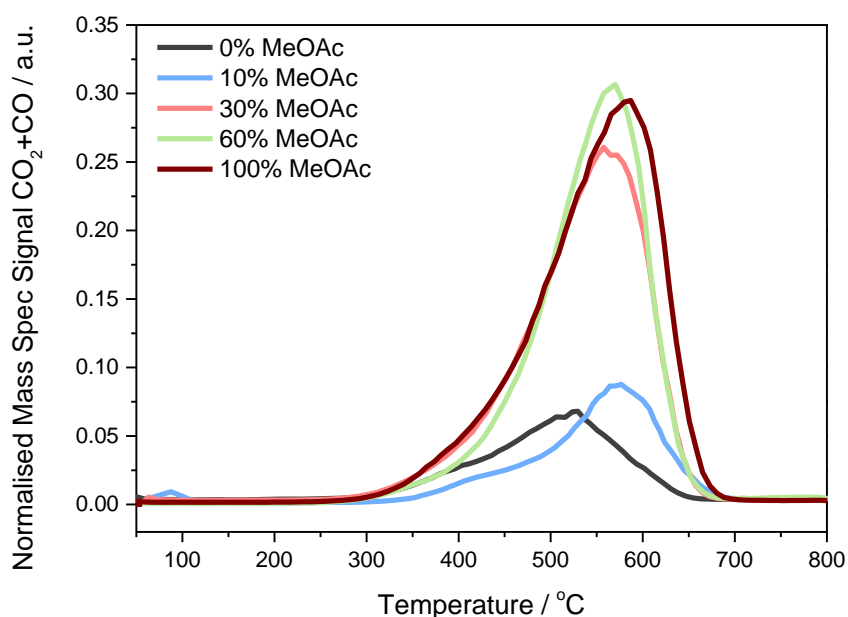


Figure 7.15: TPO profiles of the reacted ZSM-5 zeolites with MeOAc.

### 7.3.2.1 DRIFTS

Figure 5 shows the DRIFTS spectra of the used catalysts in the 4000-2200  $\text{cm}^{-1}$  region, in all cases recorded at 350 °C in flowing helium. As was shown in Chapter 3, the blank zeolite dehydrated at 350 °C shows two characteristic  $\nu(\text{OH})$  bands at 3735 and 3596  $\text{cm}^{-1}$  assigned respectively to SiOH groups on the external surface or in defects and to Si(OH)Al Brønsted acid sites,<sup>35,36</sup> and an additional weak shoulder at 3650  $\text{cm}^{-1}$  allocated to extra-framework AlOH groups.<sup>21,22</sup> All used catalysts spectra show attenuation of the Brønsted acid peak which becomes more attenuated as the MeOAc content in the feed

increases. At higher MeOAc concentrations, the silanol and extra-framework AlOH bands are also attenuated. This reduction of the number of acid sites has also been observed when methanol and DME were used as feedstocks as seen in Chapter 5, and earlier in Chapter 7, as well as with previous work in the literature.<sup>20</sup>

In the  $\nu(\text{CH})$  region the four bands appearing at 3121, 2971, 2926 and 2869  $\text{cm}^{-1}$  closely resemble those reported by Suwardiyanto *et al.* and have been assigned to methylated aromatic hydrocarbon species trapped in the zeolite pores.<sup>20</sup> The intensities of these bands increase with MeOAc content of the feed, as does the coke content, however, from this region of the infrared spectrum we cannot identify any differences in the nature of the coke species formed from methanol versus MeOAc.

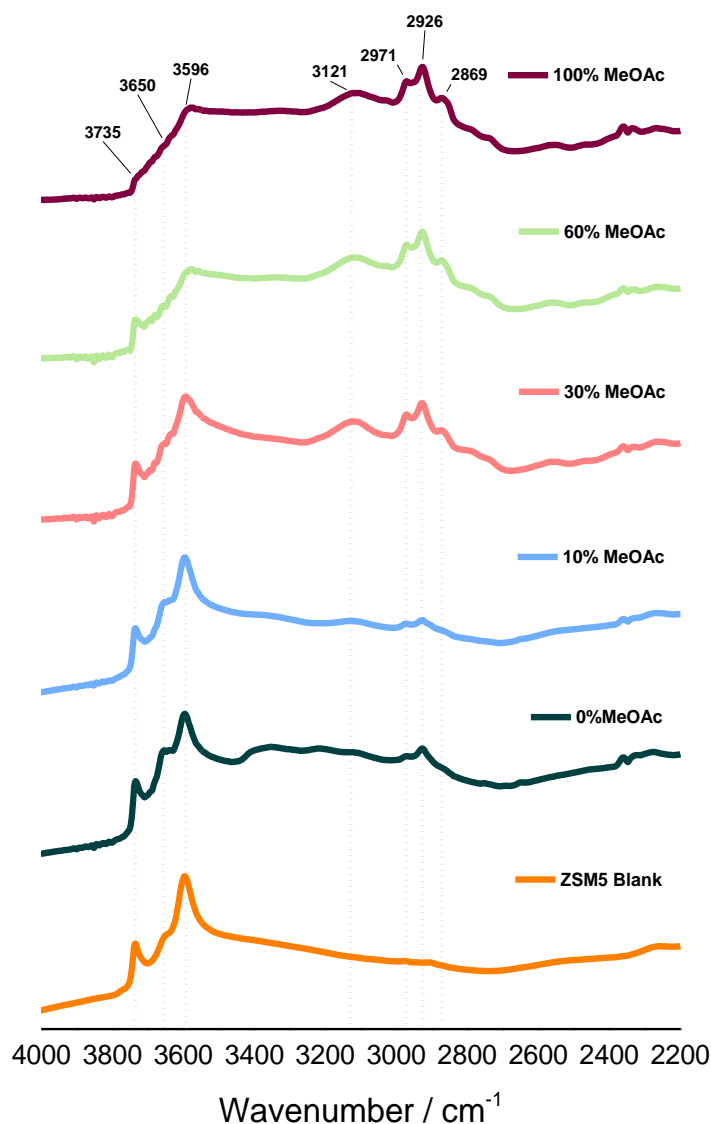


Figure 7.16: DRIFTS Spectra of the reacted samples. Spectra were normalised with respect to the zeolite framework peaks at 1864  $\text{cm}^{-1}$  and 1972  $\text{cm}^{-1}$

### 7.4.2.2 INS

Figure 7.17 shows the INS spectra of the blank zeolite, the zeolite containing MeOAc adsorbed at room temperature, and a sample of pure MeOAc. The spectra are normalised with respect to the weight of the sample. The dosed MeOAc on ZSM-5 shows that the MeOAc remains intact on the ZSM-5 with all the major peaks distinguishable. The peaks become broadened and less intense, which could be attributed to the confinement effects of the MeOAc inside the zeolite structure. The methyl torsion peaks have shifted in the zeolite; this is not a surprise as it was seen in Chapter 3 methyl torsion energy is sensitive to the surrounding environment. The peak present at  $853\text{ cm}^{-1}$  is seen to have broadened out considerably more than all other peaks in the zeolite. The peak is assigned to the  $\text{CH}_3\text{-O}$  stretch of methyl acetate.<sup>37</sup> The reason for the increased broadening occurring on that peak alone is still unclear, however since all other peaks are still present it is believed that the methyl acetate is intact within the zeolite. The blank ZSM-5 spectrum is shown as a reference, showing that the zeolite contribution to the spectra is minimal, which is why INS is advantageous when it comes to studying this region of the spectrum.

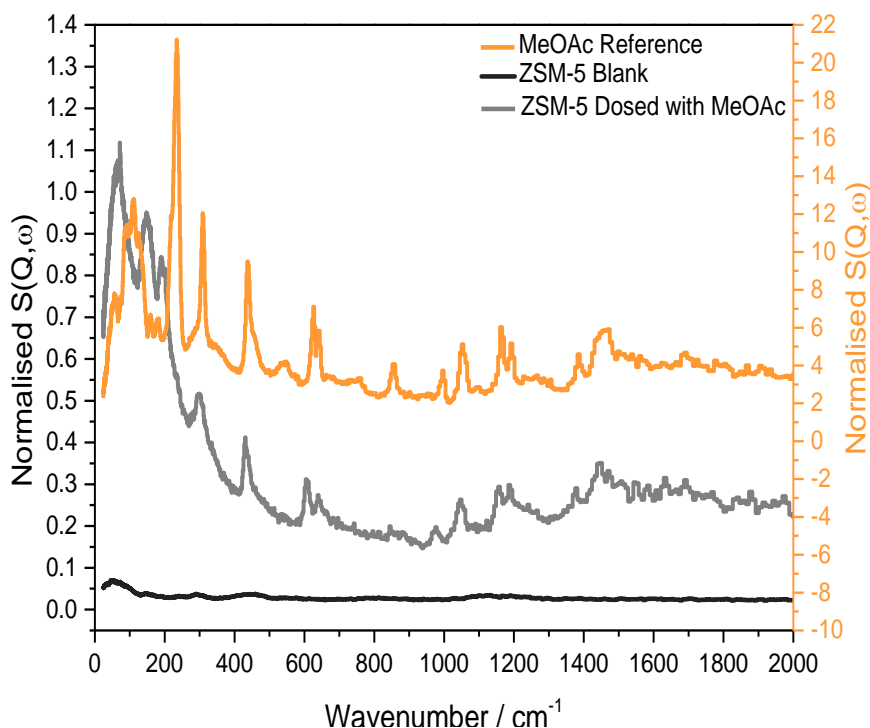


Figure 7.17: INS Spectra of the blank zeolite (black), methyl acetate (orange) and methyl acetate exposed to ZSM-5 at ambient temperature (grey).

Figure 7.18 shows the spectra recorded over the same energy range for the used catalyst samples. As with the infrared spectra in Figure 7.16, the intensities of the bands assigned to hydrocarbon coke species increase with

increasing MeOAc content in the feed. There is no evidence of features that could be attributed to surface bound methyl acetate in either the INS or the IR spectra. The 10% MeOAc does not show any significant difference between the spectrum of 0% MeOAc. The 0% and 10% MeOAc spectra show very broad features and with no dominant characteristics. The differences in the spectra of the 0% MeOAc and the spectra of the reacted samples with 30% MeOAc and above, is striking. Within the 6 hours time-on-stream, MeOAc has pushed the catalyst into a mature steady state/deactivated state. The spectra measured from catalysts exposed to 30% or more MeOAc have strong defined peaks, and interestingly they resemble those previously reported for ZSM-5 zeolite catalysts reacted with DME at 350 °C (Figure 7.8) and have no correspondence with the spectrum of adsorbed MeOAc (Figure 7.17).

From the investigation of the reference compounds completed in Chapter 3, some assignments of the observed peaks can be made. The spectra feature similar peaks to those observed with the DME and methanol at mature steady state spectra. The doublet at 1370 and 1448  $\text{cm}^{-1}$  is assigned to  $\text{CH}_3$  symmetric and asymmetric bending modes, respectively, of methyl groups attached to aromatic rings and both features are present in all of the spectra except that of the 0% MeOAc catalyst. The 1448  $\text{cm}^{-1}$  peak is shifted a little bit lower than the observed 1458  $\text{cm}^{-1}$  observed for the methanol and DME reactions, as well as the methylated aromatics and polycyclic peak. The shift is small, but it could indicate some unreacted MeOAc present in the sample even after flushing. The presence of unreacted MeOAc could also explain the uneven ratio between the doublet peaks at the higher MeOAc concentrations (60%, 100%).

The doublet present in the MeOAc at 605 and 640  $\text{cm}^{-1}$  is no longer present, and a single peak is shown at 620  $\text{cm}^{-1}$ . This is also present in the DME spectra (Figure 7.8) and the methanol mature steady state spectra seen in Chapter 5 (Figure 5.21). The peak is assigned to the double aromatic ring distortion of naphthalenes.<sup>38</sup> The 1186  $\text{cm}^{-1}$  assigned to the C-H bending mode of polycyclic aromatics is present in all spectra and appears to grow together with the 1370, 1448  $\text{cm}^{-1}$  doublet.

The lower frequency bands are also similar to those seen with both dimethylether and methanol as the reactant. There are some small differences in the relative intensity of some peaks, especially evident in the region 800 and 1000  $\text{cm}^{-1}$ . The ratio between the three peaks is evidently different than that

previously observed in DME and methanol reactions. The  $1033\text{ cm}^{-1}$  band due to  $\text{CH}_3$  rocking modes is a lot more intense than the  $960\text{ cm}^{-1}$  band attributed to the CH wag of polycyclic hydrocarbons. Whereas the still unassigned peak at  $878\text{ cm}^{-1}$  is almost non-existent. The band could be the in-plane CH bending mode present in polycyclic aromatic molecules. These observed differences are attributed to a greater degree of methylation of the aromatic rings in the presence of MeOAc. Highly methylated aromatics have been linked with ZSM-5 deactivation, which could explain why the increase in MeOAc has also nudged the catalyst into a deactivation stage earlier than is seen with either methanol or DME.<sup>34,39</sup> This enhanced extent of methylation in the adsorbed aromatic hydrocarbons appears to be the only significant difference in the INS spectra between the coke deposits formed in the presence and absence of MeOAc. It must also be noted that just like the DME and methanol reacted samples, the  $960\text{ cm}^{-1}$  and the  $\sim 1200\text{ cm}^{-1}$  peak, which is present in polycyclic molecules is usually of the same ratio, is uneven in the MeOAc samples. The  $1186\text{ cm}^{-1}$  band is a lot more intense, something that has been shown in Chapter 5 to be attributed to the build-up of amorphous coke. This means that there is some amorphous coke within the MeOAc samples as early as 6 hours in the reaction.

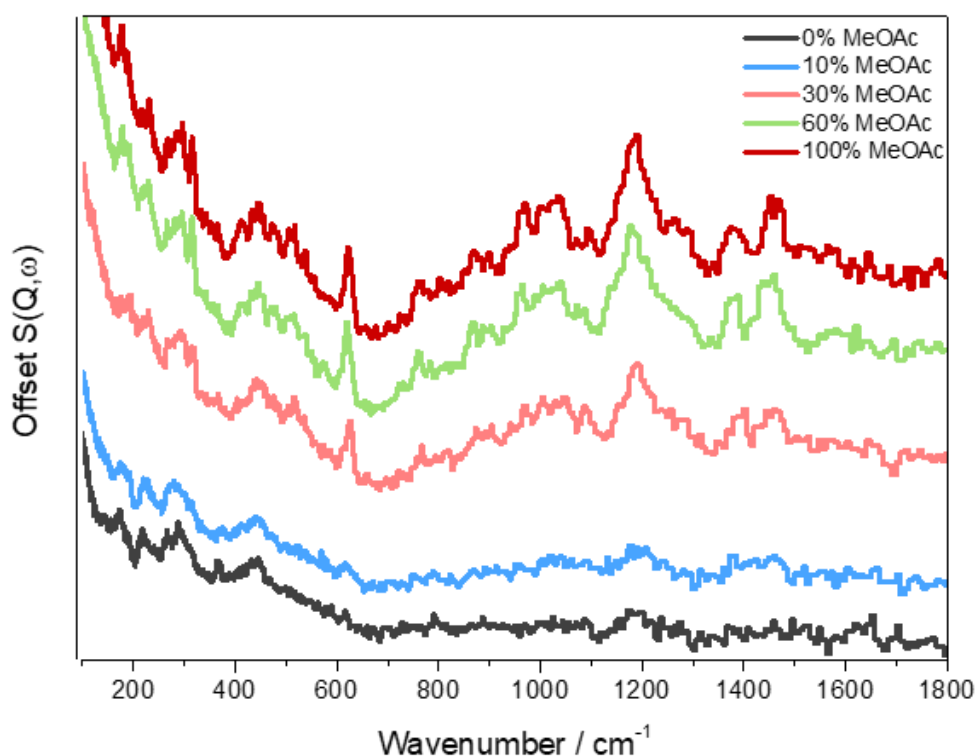


Figure 7.18: INS spectra of ZSM-5 samples reacted at 350 °C with a feed of 0% MeOAc (black), 10% MeOAc (light blue), 30% MeOAc (pink), 60% MeOAc (green) and 100% MeOAc (red)

### 7.3.3 Summary

This section focused on using various percentages of MeOAc in the methanol feed of a reaction in order to observe any differences that it might cause in the vibrational fingerprint of the MTH reaction. The only thing changing in the reactions is the methyl acetate concentration, keeping the temperature, time-on-stream, space velocity and contact time the same. The presence of MeOAc is shown to have influenced the product distribution of both the olefinic and aromatic components. It appears that addition of methyl acetate accelerates catalyst deactivation by enhancing the formation of methylated aromatics, which block the active sites within the zeolite.

Müller et al. have suggested that initial coke formation in ZSM-5 is enhanced by the presence of oxygenated compounds.<sup>18</sup> The vibrational spectroscopic data show no evidence for the presence of anything other than methylated aromatics in the used catalysts studied here. The TPO data show no sign of the Type I coke observed in reference 17. Another possible origin for the deactivation trends observed could be that the presence of methyl acetate in the feed stream leads to a constrained supply of water molecules in the reaction zone (formed as a product in the dimerization of methanol to produce dimethyl ether), which would otherwise facilitate regeneration of the active sites (Brønsted acid sites). Therefore, some of the enhanced deactivation seen could be due to loss of acid sites, as in the DME reactions, which could explain why there is no evidence of heavy coke being a dominant factor in either the TPO's or INS spectra recorded.

## 7.5 Concluding Remarks

The chapter focused on studying the effect of two different feedstocks under MTH conditions with the ZSM-5 catalyst previously used with methanol. DME was chosen due to it being the first major intermediate in the MTH reaction as has been shown in literature.<sup>3,6</sup> Whereas, methyl acetate was chosen due to new literature suggesting that it is the first intermediate with a C-C bond present.<sup>10,11,40</sup> When compared to methanol reactions, it was shown that DME shows similar hydrocarbon build up, but seems to have entered the deactivation stage a lot faster than methanol reacted at the same temperature. The DME has shown a difference in how it deactivates the catalyst, seeming to attenuate the conversion of DME by loss of acid sites. This was attributed to

the lack of water which minimises acid site regeneration. The same has been observed with methyl acetate to a degree. However, addition of methyl acetate has shown that the type of hydrocarbons has changed, and that with the addition of enough MeOAc (above 30%), the catalyst is showing deactivation signs as early as the 6 hour reactions completed here. If MeOAc is the first C-C intermediate, it needs to be the limiting factor of the reaction as presence of high levels of MeOAc cause rapid deactivation. Although not unlikely that methyl acetate could play a role in the hydrocarbon pool, the fast deactivation observed here makes it unlikely to be the only pathway towards the build-up of the hydrocarbons needed for the catalyst to enter its autocatalytic state.

## 7.6 References

- 1 C. D. Chang, *Catal. Rev.*, 1983, **25**, 1–118.
- 2 S. Wang, S. Li, L. Zhang, Z. Qin, Y. Chen, M. Dong, J. Li, W. Fan and J. Wang, *Catal. Sci. Technol.*, 2018, **8**, 3193–3204.
- 3 M. Stöcker, *Microporous Mesoporous Mater.*, 1999, **29**, 3–48.
- 4 P. Pérez-Urriarte, A. Ateka, A. G. Gayubo, T. Cordero-Lanzac, A. T. Aguayo and J. Bilbao, *Chem. Eng. J.*, 2017, **311**, 367–377.
- 5 P. Perez-Urriarte, A. Ateka, M. Gamero, A. T. Aguayo and J. Bilbao, *Ind. Eng. Chem. Res.*, 2016, **55**, 6569–6578.
- 6 J. S. Martinez-Espin, M. Mortén, T. V. W. Janssens, S. Svelle, P. Beato and U. Olsbye, *Catal. Sci. Technol.*, 2017, **7**, 2700–2716.
- 7 P. Pérez-Urriarte, A. Ateka, A. T. Aguayo, A. G. Gayubo and J. Bilbao, *Chem. Eng. J.*, 2016, **302**, 801–810.
- 8 P. Pérez-Urriarte, M. Gamero, A. Ateka, M. Díaz, A. T. Aguayo and J. Bilbao, *Ind. Eng. Chem. Res.*, 2016, **55**, 1513–1521.
- 9 A. S. Al-Dughaiter and H. de Lasa, *Fuel*, 2014, **138**, 52–64.
- 10 Y. Liu, S. Müller, D. Berger, J. Jelic, K. Reuter, M. Tonigold, M. Sanchez-sanchez and J. A. Lercher, *Angew. Chem., Int. Ed*, 2016, **55**, 5723–5726.

- 11 A. D. Chowdhury, K. Houben, G. T. Whiting, M. Mokhtar, A. M. Asiri, S. A. Al-Thabaiti, S. N. Basahel, M. Baldus and B. M. Weckhuysen, *Angew. Chemie - Int. Ed.*, 2016, **55**, 15840–15845.
- 12 A. Haas, C. Hauber and M. Kirchmann, *ACS Catal.*, 2019, **9**, 5679–5691.
- 13 M. W. Anderson and J. Klinowski, *Nature*, 1989, **339**, 200–203.
- 14 P. Cheung, A. Bhan, G. J. Sunley and E. Iglesia, *Angew. Chemie Int. Ed.*, 2006, **45**, 1617–1620.
- 15 Y. Jiang, M. Hunger and W. Wang, *J. Am. Chem. Soc.*, 2006, **128**, 11679–11692.
- 16 A. G. Gayubo, A. T. Aguayo, A. L. Morán, M. Olazar and J. Bilbao, *AIChE J.*, 2002, **48**, 1561–1571.
- 17 D. M. Bibby, N. B. Milestone, J. E. Patterson and L. P. Aldridge, *J. Catal.*, 1986, **97**, 493–502.
- 18 S. Müller, Y. Liu, M. Vishnuvarthan, X. Sun, A. C. Van Veen, G. L. Haller, M. Sanchez-Sanchez and J. A. Lercher, *J. Catal.*, 2015, **325**, 48–59.
- 19 V. R. Choudhary, P. Devadas, S. D. Sansare and M. Guisnet, *J. Catal.*, 1997, **166**, 236–243.
- 20 Suwardiyanto, R. F. Howe, R. C. A. Catlow, E. K. Gibson, A. Hameed, J. McGregor, P. Collier, S. F. Parker and D. Lennon, *Faraday Discuss.*, 2017, **197**, 447–472.
- 21 L. Kubelková, J. Nováková and K. Nedomová, *J. Catal.*, 1990, **124**, 441–450.
- 22 S. M. Campbell, D. M. Bibby, J. M. Coddington, R. F. Howe and R. H. Meinhold, *J. Catal.*, 1996, **161**, 338–349.
- 23 U. Olsbye, S. Svelle, K. P. Lillerud, Z. H. Wei, Y. Y. Chen, J. F. Li, J. G. Wang and W. B. Fan, *Chem. Soc. Rev.*, 2015, **44**, 7155–7176.
- 24 R. H. Meinhold and D. M. Bibby, *Zeolites*, 1990, **10**, 121–130.
- 25 K. Barbera, S. Sorensen, S. Bordiga, J. Skibsted, H. Fordsmand, P. Beato and T. V. W. Janssens, *Catal. Sci. Technol.*, 2012, **2**, 1196–

- 1206.
- 26 J. Jiao, W. Wang, B. Sulikowski, J. Weitkamp and M. Hunger, *Microporous Mesoporous Mater.*, 2006, **90**, 246–250.
- 27 S. K. Matam, A. J. O'Malley, C. R. A. Catlow, S. Suwardiyanto, P. Collier, A. P. Hawkins, A. Zachariou, D. Lennon, I. Silverwood, S. F. Parker and R. F. Howe, *Catal. Sci. Technol.*, 2018, **8**, 3304–3312.
- 28 P. C. H. Mitchell, S. F. Parker, A. J. Ramirez-Cuesta and J. Tomkinson, *Vibrational spectroscopy with neutrons with applications in chemistry*, World Scientific, Singapore, 2005.
- 29 M. Bjørgen, S. Svelle, F. Joensen, J. Nerlov, S. Kolboe, F. Bonino, L. Palumbo, S. Bordiga and U. Olsbye, *J. Catal.*, 2007, **249**, 195–207.
- 30 S. Ilias and A. Bhan, *ACS Catal.*, 2013, **3**, 18–31.
- 31 A. D. Chowdhury, A. L. Paioni, K. Houben, G. T. Whiting, M. Baldus and B. M. Weckhuysen, *Angew. Chemie - Int. Ed.*, 2018, **57**, 8095–8099.
- 32 Z. Chen, Y. Ni, Y. Zhi, F. Wen, Z. Zhou, Y. Wei, W. Zhu and Z. Liu, *Angew. Chemie Int. Ed.*, 2018, **57**, 12549–12553.
- 33 D. M. Bibby and C. G. Pomt, *J. Catal.*, 1989, **116**, 407–414.
- 34 D. M. Bibby, R. F. Howe and G. D. McLellan, *Appl. Catal. A, Gen.*, 1992, **93**, 1–34.
- 35 P. A. Jacobs and R. Von Ballmoos, *J. Phys. Chem*, 1982, **86**, 3050–3052.
- 36 J. C. Vedrine, A. Auroux and G. Coudurier, in *ACS Symposium Series*, 1984, pp. 254–273.
- 37 W. O. George, T. E. Houston and W. C. Harris, *Spectrochem. Acta*, 1974, **30A**, 1003–1057.
- 38 E. R. Lippincott and E. J. O'Reilly, *J. Chem. Phys.*, 1955, **23**, 238–244.
- 39 D. Rojo-Gama, M. Nielsen, D. S. Wragg, M. Dyballa, J. Holzinger, H. Falsig, L. F. Lundegaard, P. Beato, R. Y. Brogaard, K. P. Lillerud, U. Olsbye and S. Svelle, *ACS Catal.*, 2017, **7**, 8235–8246.

- 40 I. Yarulina, A. D. Chowdhury, F. Meirer, B. M. Weckhuysen and J. Gascon, *Recent trends and fundamental insights in the methanol-to-hydrocarbons process*, Nature Publishing Group, 2018, vol. 1.

# Chapter 8

## Conclusions and Future Work

---

### 8.1 Conclusions

This project has focused on using neutron spectroscopic techniques to study the changing nature of the ZSM-5 acid zeolite catalyst in the Methanol-to-Hydrocarbons reaction. The same zeolite catalyst has been used throughout this investigation. The Si:Al ratio of the zeolite was investigated with a variety of techniques with the average being approximately 30 (varying from 24-36), with an approximate number of Brønsted acid sites being around 3 per unit cell. The zeolite also showed a substantial amount of framework Al present, as evidenced by the INS direct hydroxyl quantification and via IR. This extra framework Al is also what has caused complications in the neutron diffraction analysis of the ZSM-5 sample.

The interaction of methanol with ZSM-5 at room temperature has also been investigated. Is room temperature methoxylation really possible? The apparent loss of OH functionality was observed by INS when methanol was exposed to the ZSM-5 at room temperature. This contradicted results obtained from both IR and ssNMR, which showed that methanol strongly hydrogen bonds to the acid sites but that methoxylation requires activation by application of elevated temperatures. A series of scenarios were investigated which showed that although the Fermi resonance ABC structure of hydrogen bonded methanol could potentially obscure the methoxy species in the IR, ssNMR shows no methoxy present within the spectra. A comparison of all three techniques on the same sample showed that the degree of methoxylation, if at all present, would be less than 1% based on the signal to noise ratio of the  $^{13}\text{C}$ -NMR spectrum. A methanol-OD exchange with methanol-OH within the zeolite sample showed a raised baseline as well as the shift in frequency between the  $\text{CH}_3$  rocking modes, which demonstrated that the methanol present within the

zeolite is intact and not methoxylated. The shift in the rocking modes would not have happened if the OH functionality was lost.

A study of the MTH reaction at different temperatures and times-on-stream was also completed. In the initial stages of the reaction the INS spectra do not show a dominant species present, which suggests that the initial steps of the reaction are not dominated by the formation of one intermediate. It must be noted that the first steps of the reaction are thought to be rapid, this means that INS might not be best suited for studying catalysts in their initial stages of reaction. The INS vibrational fingerprint of the hydrocarbon pool within a working catalyst has been obtained (Figure 5.21). The spectra are complex and show that there is no singular molecular entity that dominates the spectra, which mean the assignment of the spectral features is not straightforward.

The spectra have been compared against those of potential hydrocarbon pool products (Figure 5.22), with some of the spectral features being assigned. It is important to note that INS is quantitative, therefore the species dominating the INS spectra are also the dominating species within the HCP pool. Although different hydrocarbons could also be present within the HCP, it is suggested that the dominant species are (i) polymethylated benzenes of more than 4 methyl substitutions, (ii) naphthalenes and (iii) anthracenes. The ratio of the peaks alludes to amorphous coke being present within the sample from the steady state stages, however, the quantity of the hydrocarbons exceeds the intensity contribution of that coke. At the 350 °C reaction it has been shown that some degree of deactivation can be seen due to the drop in methanol intensity in the mass spectrometer and the increased presence of DME towards the end of the reaction. The deactivation seen here is not from the build-up of amorphous coke but rather from the build-up of aromatics within the zeolite pores. At this temperature (350 °C), the  $sp^3$  to  $sp^2$  ratio is close to 1:1.14, which suggests most of the hydrocarbons present within the zeolite are methylated, with the methylation being higher than that observed at the other two temperatures.

At an increased temperature of 400 °C, the amorphous coke dominates the spectra, even though less time-on-stream was needed for the catalyst to reach deactivation. This showed that the catalyst pores were blocked from the external surface area, where the 'amorphous' coke seems to have the space to form. The vibrational spectra of the coked species have been obtained for

the first time. When comparing the spectra with literature, it is seen that the coke resembles 'glassy-like' carbon. This suggests that the coke is being continually added to in order to form the 'glassy-like' carbon structure. The speculation being that the 'glassy-like' structure is created with the continuous growth of polycyclics on the surface of the catalyst at different places. The larger polycyclic species grow until they meet another and condense via a dehydrogenation reaction into a larger molecule which no longer has a 2-D graphene-like structure but the 'glassy-like' carbon structure. High energy INS spectra showed almost no visible contribution from the  $sp^3$  hybridised C-H stretch.

The diffusion of methane on coked samples was also attempted using QENS. Although the right probe molecule was used to study this system, the QENS scans were measured in the wrong temperature range, with the methane diffusing too fast at the temperatures chosen. The attempted fits of the empty zeolite with methane showed that the diffusion constants and activation energy of the Jovic diffusion model were the closest to results reported in the literature.

The coked samples had the additional complication of having the retained hydrocarbons still present. Due to the coke being hydrocarbonaceous in nature, the motion of the coke is detected within the zeolite. This is consistent with rotational diffusion, although the actual motion has not been identified. The low coke sample showed similar methane diffusion constants and activation energies to the fresh ZSM-5. This suggests that the coke present does not affect the diffusion of the methane and that it is possible that the coke present is evenly distributed. The most heavily coked sample showed that the rotational motion of the coke largely dominated the spectra and no clear conclusions could be drawn, other than that the methane diffusion is extremely hindered by the coke, since the methane loading was a lot less within this sample (methane was unable to diffuse in the sample to begin with).

The MTH reaction was also studied with different feedstocks. Dimethyl ether as feedstock showed that the catalyst entered the mature steady state a lot faster than with the methanol feedstock. The INS spectra (Figure 7.8) were similar to that of the MTH mature state at 350 and 300 °C (Figure 5.21). A higher aromatic to aliphatic ratio was observed, this has been attributed to the lower levels of water present with DME as the feedstock. Lower levels of water reduced the acid site regeneration, reducing the methylation pathway. This

could also indicate that the deactivation observed in the mass spectra is due to loss of the acid sites, rather than coke build-up, as was the case in the methanol reactions.

The increased presence of methyl acetate in the feedstock, showed an acceleration of deactivation in the reaction profiles. However, the deactivation observed is different than that of DME. The increased methyl acetate appears to accelerate catalyst deactivation by the formation of methylated aromatic molecules, which block the zeolite pores. The INS spectra (Figure 7.18) strongly resemble the mature MTH steady state spectra of methanol (Figure 7.8) and dimethyl ether (Figure 5.21). This is surprising, as the spectra were obtained within 6 hours of reaction when in the presence of methyl acetate. The coke content build-up on the zeolite when 100% methyl acetate was used is comparable with 110 hours of reaction with methanol under the same exact conditions. This shows that there is an increased rate of hydrocarbon build up when methyl acetate is used as feedstock. Although there is not enough information for a full mechanistic study of the repercussions of this observation, the fast deactivation observed here suggests that if methyl acetate is the first C-C bond intermediate it is unlikely to be the only precursor to the hydrocarbon pool. If methyl acetate is the first C-C intermediate, its formation will need to be the rate limiting step of the reaction, as presence of high levels of methyl acetate cause rapid deactivation.

Overall, it has been shown that INS can be used successfully in studying the MTH reaction. Despite the increased sample size needed for the INS experiments, it has been shown that the hydrocarbon pool build-up is similar to what has already been shown in literature. Using neutron techniques in order to study this samples has proven important especially in heavily deactivated samples.

## 8.2 Future Work

In the duration of this project, an attempt was made to use neutron diffraction in order to find the location of the acid sites. The Rietveld refinement of this dataset is still being completed, as the analysis proved to be more complex than anticipated.

This project also focused on understanding the methanol interaction within the ZSM-5 zeolite at room temperature. This was able to be resolved with using a

combination of INS, DRIFTS and NMR techniques, A QENS experiment is being designed in order to try and observe methanol motion within the ZSM-5. Previous attempts at completing a QENS experiment using methanol and ZSM-5 failed to show any motion with the ISIS spectrometers. There is a possibility that the methanol movement is so slow, that a spectrometer with a different timescale is needed in order to observe it. An application has been accepted by the Institute Laue-Langevin for the use of the WASP spectrometer which is a high intensity spin-echo spectrometer which can access the temporal range of 0.6 – 18 000 ps (Q range: 0.06 - 3.6 Å<sup>-1</sup>). Hence, the WASP spectrometer is able to detect slower motions than the IRIS/OSIRIS spectrometers (range 1.6 – 38 ps, Q range: 0.18 – 1.85 Å<sup>-1</sup>), therefore, if the reason for the failed methanol motion detection was because it was too slow for the instruments to observe it, then WASP measurements should reveal that prospect.

The project has also attempted to study the diffusional constraints through coked samples through QENS using methane as the probe molecule. The experiment should be completed in the right temperature range, however, this may not be enough since some of the complications occurred by the inability to remove the coke contributions from the QENS spectra successfully. An enhancement to the experimental would be to use deuterated methanol in the MTH reaction, which will create a deuterated coke. Deuterium will not have any contribution on the elastic intensity, with any broadness observed coming from the hydrogens in the methane.

This project has completed its main aim, which was to study the changing nature of the ZSM-5 catalyst on reaction with methanol and related reagents. The HCP vibrational fingerprint of both a working and a deactivated catalyst have been obtained. It was demonstrated that INS is not very suitable for studying the initial stages of the reaction directly. The pseudo-deactivation of the catalyst however, still has a lot to be explored. The deactivation that has been observed is from coke build up and not from acid site degeneration. The coke build up can be burned off and regenerated, which is what is being done in industry where the catalyst may be regenerated after each cycle. INS has demonstrated the capability of quantifying the acid sites directly, this can provide accurate, quantifiable data on what happens to acid sites after regeneration. Having the ZSM-5 go through regeneration cycles/MTH reactions for multiple times, could possibly have an effect on the hydrocarbons retained within the zeolite. Now that the INS vibrational fingerprint has been identified,

any changes in the vibrational spectra could help in identifying those changes. Completing various regeneration cycles and MTH reactions would provide information about the catalyst activity under true deactivation conditions.

The same methodology developed here, could be used with different Si:Al ratios of ZSM-5, as well as with the SAPO-34 zeolite catalyst, which strongly favours olefin production. The change in acid site density and topology could heavily influence the retained hydrocarbons and thus change the vibrational fingerprint which has been shown for this specific ZSM-5 catalyst. The possibility of using neutrons to characterise the hydrogen partitioning within MTH reacted zeolites has been shown with this project, and it has demonstrated the advantages of using neutrons to achieve it. The possibility of using the neutron techniques quantitative nature in order to quantify the different species of hydrocarbons present would also be possible with further calibration measurements. Overall, this project can be used as a benchmark in order to study the MTH reaction further, and has shown a new way in which the zeolite deactivation can be studied and further understood. The formation of polycyclic aromatics and amorphous coke is an important hindrance to the MTH reaction, and information about how they are formed, as revealed by neutron spectroscopy, is beneficial in catalyst optimisation strategies.

## Appendix: Chapter 3

- **ZSM-5 INS Before Drying**

The INS of dried ZSM-5 allows for the identification of acid sites as well as offers an almost blank background in order to be able to have no contribution from the framework modes in the reacted samples. Before drying however, there are broad hydrogen bonded peaks of water obscuring the spectra as seen in the following Figure. Therefore, drying the ZSM-5 is important in order to dislodge the water adsorbed within the zeolite as well as the water peaks appearing in the spectra.

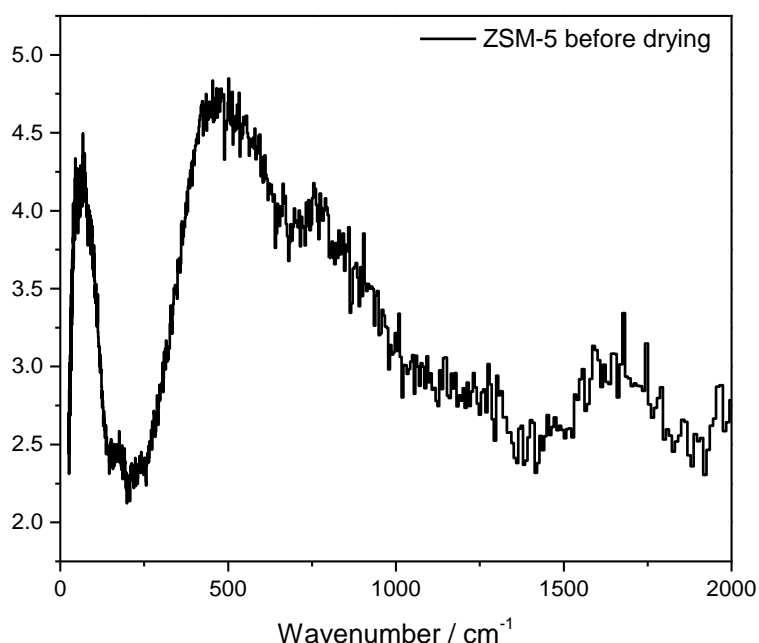


Figure A.1: INS spectrum of ZSM-5 before drying using the TOSCA spectrometer

- **TPD Si:Al Calculation**

The moles of ammonia are all calculated within the instrument software. The ammonia calibration of the ChemBET is contained within the software of the instrument. The volume of ammonia is calculated from the fitted Brønsted peak area seen in Chapter 3, Figure 3.6 against the calibration peaks of known ammonia volumes. The volume of ammonia for 0.087 grams of zeolite was 820.22  $\mu\text{l}$ . This value is normalised to 1 g of ZSM-5 giving 9427.8  $\mu\text{l}_{\text{NH}_3}/\text{g}_{\text{ZSM-5}}$ . The software has all the information needed to use the ideal gas law ( $PV=nRT$ )

in order to calculate the moles of ammonia per gram of ZSM-5 giving  $0.000421 \text{ mol}_{\text{NH}_3}/\text{g}_{\text{ZSM-5}}$ .

To start the calculation of finding the Si:Al ratio, the molecular formula for the MFI unit cell (dry) taken from the IZA website is used ( $\text{H}_n\text{Al}_n\text{Si}_{96-n}\text{O}_{192}$ ). The assumption is made that there is no Al present.

$$n = 0$$

$$M_{\text{ZSM-5}} = (n \times 1.007) + (n \times 26.981) + ((96 - n) \times 28.085) + (192 \times 15.999)$$

$$M_{\text{ZSM-5}} = 5767.968 \text{ g/mol}$$

Therefore, since we have the moles of ammonia per gram of ZSM-5 it can be converted to ammonia per unit cell using the  $M_{\text{ZSM-5}}$  value.

$$0.000421 \text{ mol}_{\text{NH}_3}/\text{g}_{\text{ZSM5}} \times 5767.968 \text{ g}_{\text{ZSM5}}/\text{mol}_{\text{ZSM-5}} = 2.43 \text{ mol}_{\text{NH}_3}/\text{mol}_{\text{ZSM5}}$$

Assuming that 1 mole of ammonia is needed per acid site, this suggests that there is 2.43 acid sites per unit cell. Therefore, the  $M_{\text{ZSM-5}}$  can now be recalculated using 2.43 as the new Al number in the molecular formula ( $\text{H}_n\text{Al}_n\text{Si}_{96-n}\text{O}_{192}$ ).

$$n = 2.43$$

$$M_{\text{ZSM-5}} = (n \times 1.007) + (n \times 26.981) + ((96 - n) \times 28.085) + (192 \times 15.999)$$

$$M_{\text{ZSM-5}} = 5762.85 \text{ g/mol}$$

The Si:Al ratio can now be calculated from the relationship of  $n\text{Al} = 96-n\text{Si}$ .

$$\text{Al} = 2.43$$

$$\text{Si} = 93.57$$

Therefore, the Si:Al ratio is: 38.5:1

### • OH Quantification Using INS Calculations

The OH quantification using the MAPS spectrometer at ISIS was completed by using Brucite in order to calibrate the instrument. The OH mg concentration of brucite was calculated from its molecular formula ( $\text{Mg}(\text{OH})_2$ ) and the known weight of the brucite which was measured with the OH concentration stated in table 3.5 in Chapter 3. The ZSM-5 OH peaks were then fitted with the exact

same way, and their peak areas of the three OH sites were compared against the calibration plot found in Figure 3.8, with the results shown in Table 3.6. The OH Concentration found in Table 3.6 is normalised with the weight of the zeolite sample which was 9.62 g.

Table A3.1: The quantification of the OH sites in ZSM-5 (extension of Table 3.6 in Chapter 3)

OH Site	Peak Area	OH Concentration mg/g <sub>sample</sub>	OH Concentration mg/g <sub>ZSM-5</sub>
<b>Brønsted</b>	80.51	93.99	9.77
<b>Extra Framework Al</b>	26.74	31.95	3.32
<b>Silanol</b>	15.61	19.10	1.98

In order to calculate the OH sites per unit cell, the  $M_{ZSM-5}$  was calculated with the assumption that no Al is present ( $H_nAl_nSi_{96-n}O_{192}$ ).

$$n = 0$$

$$M_{ZSM-5} = (n \times 1.007) + (n \times 26.981) + ((96 - n) \times 28.085) + (192 \times 15.999)$$

$$M_{ZSM-5} = 5767.968 \text{ g/mol}$$

From the calibration, it is known that the ZSM-5 contains 9.77 mg<sub>OH</sub>/g<sub>ZSM-5</sub> therefore, it can be converted to OH concentration per unit cell.

$$9.77 \text{ mg}_{OH}/g_{ZSM-5} = 0.00977 \text{ g}_{OH}/g_{ZSM-5}$$

$$0.00977 \text{ g}_{OH}/g_{ZSM-5} \times 5767.968 \text{ g/mol} = 55.45 \text{ g}_{OH}/\text{mol}_{ZSM-5}$$

Using the OH molecular formula (17 g/mol), then 55.45 g<sub>OH</sub>/mol<sub>ZSM-5</sub> are 3.26 mol<sub>OH</sub>/mol<sub>ZSM-5</sub>. The same calculation is then repeated for the extra framework Al and silanols sites. The Si:Al ratio is calculated from the Brønsted OH population. Since a Brønsted acid site has one Al, the assumption is that 3.26 mol<sub>OH</sub>/mol<sub>ZSM-5</sub> are equal to 1 Brønsted acid site which means 1 Al. Therefore, using the MFI formula ( $H_nAl_nSi_{96-n}O_{192}$ ) Si and Al relationship are:

$$n \text{ Al} = (96 - n) \text{ Si}$$

$$n = 3.26$$

$$\text{Si} = 96 - 3.26 = 92.74$$

The Si:Al ratio is therefore: 28.4:1

- Fitting of the Pyridine and Pyridinium Chloride Spectra**

The spectra for the pyridine and pyridinium chloride used for the one-point calibration of the pyridine adsorbed and desorbed INS MAPS spectra in Chapter 3 can be found in the following Figures. The peak fitting software used was the OriginPro Peak Analyser, with the constraint of not having a negative area. Lorentzian functions were used for peak fitting the data. The integrated area is 985.067 for 1 g of pyridinium chloride and 795.87 for 1 g of pyridine.

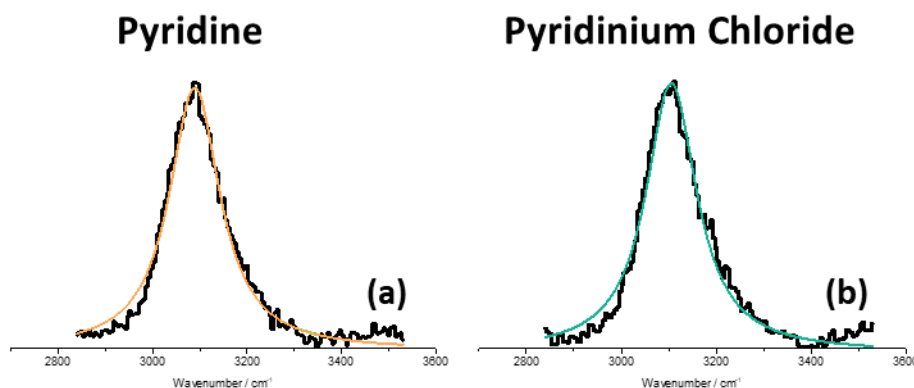


Figure A.2: (a) Pyridine spectrum (black) fitted with one Lorentzian (orange) at a peak max of  $3089\text{ cm}^{-1}$  (b) Pyridinium chloride (black) fitted with one Lorentzian (green) at a peak maximum of  $3110\text{ cm}^{-1}$ .

- Dosed ZSM-5 with Reference Samples**

Some model compounds were chosen in order to see if the vibrational spectrum of their liquid molecular forms changed when added in the zeolite framework. Some dosings were successful others were not.

**ZSM-5 and Toluene:** Dosing toluene in the zeolite was completed successfully with the toluene remaining intact within the zeolite framework. The toluene was dosed using a bubbler arrangement at room temperature. Dried zeolite was 12.32 g and the final loading of toluene was 1.33 g which suggest 6.75 moles of toluene for every ZSM-5 unit cell. There was 91% mass recovery when the sample was transferred to a flat Al can. The pure toluene mass was 1.15g. The spectra intensity of the pure compound and when loaded in the zeolite do not match up, with the intensity dropping when toluene is loaded in the zeolite. The vibrational spectra of the pure toluene with the zeolite loaded toluene look very similar with the only difference being the phonon structure modes in the low

energy region are gone. This suggests that the toluene is adsorbed on the surface of the zeolite and it's not a crystalline frozen liquid. The adsorbed toluene does not show any differences from the pure liquid therefore adsorption on the zeolite does not cause a significant shift in toluene's vibrational frequencies

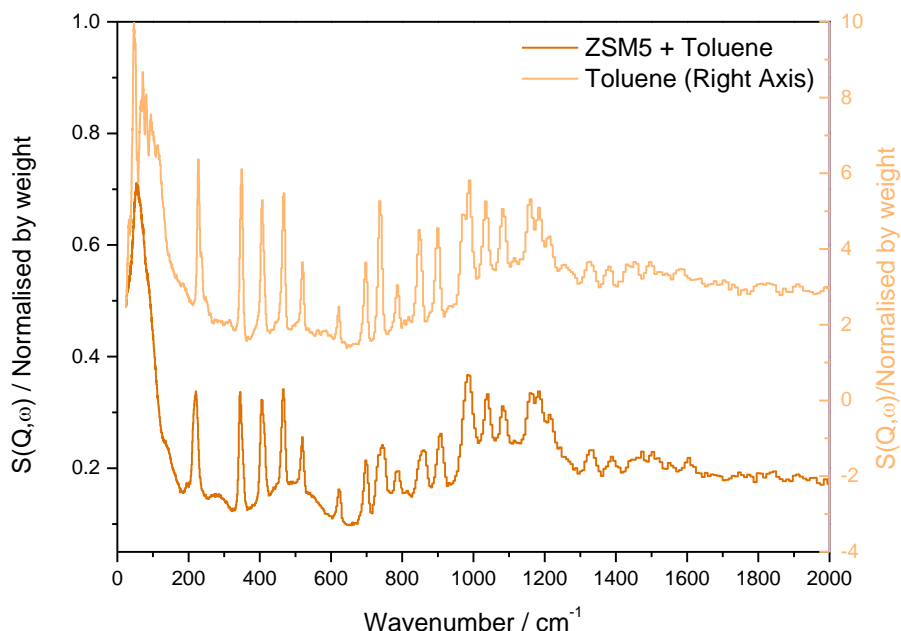


Figure A.3: Toluene dosed in ZSM-5 and toluene model compound as reference

**ZSM-5 and p-Xylene:** Dosing p-xylene in the zeolite again with a bubbler turned out to be tricky as well. The dried ZSM-5 used was 11.22g and the final loading of p-xylene was 1.33g. This suggests a loading of 6.43 moles of xylene per ZSM-5 unit cell. There was an 88% mass recovery when transferring the sample from the dosing can to the flat Al can used for the TOSCA measurements. The pure p-xylene mass was 1.38 g. The intensities of the spectra were normalised with the mass of sample going in the beam. It is obvious that the intensity drops when the xylene is in the pores of the zeolite. Some broadening is observed in the spectrum of the dosed sample with the methyl torsion peak at  $110\text{ cm}^{-1}$  shifting downwards when in the zeolite. However, the structure observed in the phonon region below  $200\text{ cm}^{-1}$ , in the dosed spectrum, suggests that the xylene did not fully diffuse through the zeolite, or it could also be that the zeolite was oversaturated with some of the liquid xylene pooling on the sides of the cell. Either way, the presence of liquid (frozen) xylene in the spectrum complicates any deductions that can be made

on the xylene interaction with the ZSM-5. Therefore, no clear conclusions can be made on the xylene interaction with the zeolite.

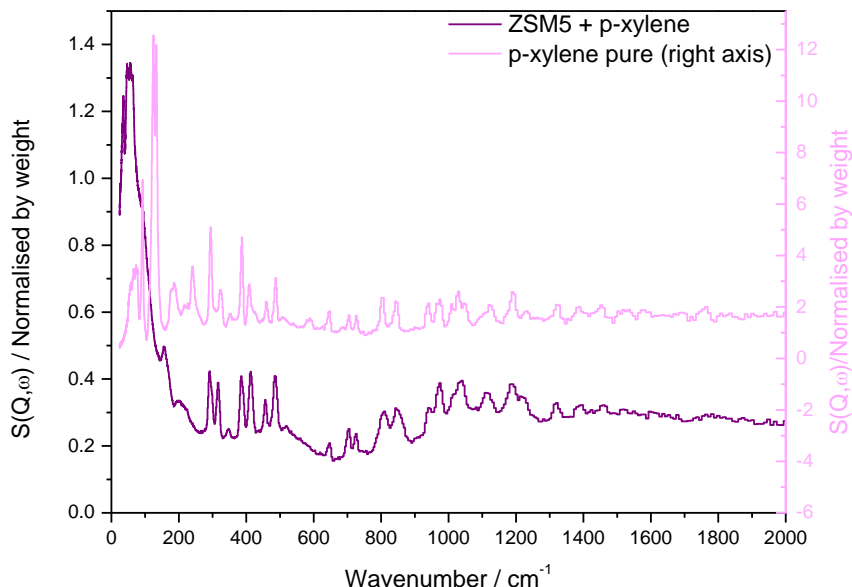


Figure A. 4: *p*-Xylene dosed in ZSM-5 and pure *p*-xylene used as a reference

**ZSM-5 and Durene:** Dosing durene in the zeolite was challenging. Durene is solid at room temperature and it needs to be in the right orientation in order to enter into the zeolite pore. The dosing equipment was modified in order to dose solid into the zeolite. Durene was loaded on the zeolite using the phenol rig. The rig was designed to load solid compounds on samples. The sample is loaded in a vial and placed in a gas tight furnace with an inlet and outlet. The furnace is then heated to a temperature where the solid melts. The gas is flown through the bottom and out the top carrying any vapours produced from the melted solid through heated lines to the inlet of the cell hooked up at the end. The cell is sitting in a tube furnace with the ability to heat it if needed. For durene, the small furnace used to melt durene was kept at 140 °C with the heated lines being kept between 80°C-140 °C. The furnace around the cell was at 140°C with the cell temperature being between 80 °C-100 °C. When trying to keep the cell at room temperature, durene would condense on the inlet pipe and block the lines therefore heating the cell was essential. The dried zeolite used was 11.8 g with the final loading of durene being 1.6 g (5.8 moles of durene for every ZSM- 5 unit cell). When transferring the loaded sample to the flat cans, it was noted that there was some durene condensed at the bottom of the cell. Therefore, the loading of the durene might be less. There was 90%

sample recovery when transferring the sample. Unfortunately, even with the lines heated, there were some cold spots which caused durene to condense and block the lines. This was dissolved using ethanol, but the ethanol was trapped into those lines even after flushing it out. This meant that ethanol was dosed on the zeolite rather than durene, therefore, this attempt was unsuccessful. Unfortunately, due to the time constraints of the beam time, the experiment could not be repeated.

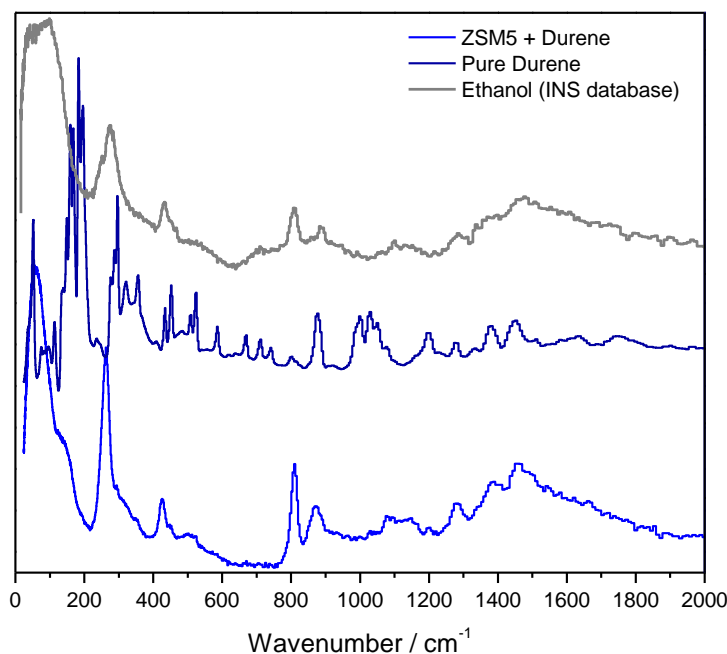


Figure A. 5: Durene dosed in ZSM-5, pure durene as reference and pure ethanol as reference taken from the INS database (<http://www.isis.rl.ac.uk/INSdatabase/Results.asp?Ethanol>)

**ZSM-5 with 1,2,3,4-Tetramethyl-1,3-cyclopentadiene:** This was purchased as an 85% 1,2,3,4-tetramethyl-1,3-cyclopentadiene and the rest a mixture of isomers. The phenol rig was used to load it on the zeolite even if it is a liquid. The reason for that was due to having only 5 g of the compound which was not enough to load it using the usual bubbler arrangement. The amount of dried zeolite used was 10.72 g with a total mass of tetramethylcyclopentadiene at 0.16 g (0.7 moles/unit cell). There was 91% recovery of the sample when transferring it to an Al flat can. The loaded spectrum of the tetramethylcyclopentadiene in the zeolite show a different spectrum than the pure compound. This suggests that at room temperature there is an interaction of the tetramethylcyclopentadiene with the zeolite and that it does not remain intact when in contact with the zeolite. This could be complicated when trying to assign peaks to tetramethylcyclopentadiene in the zeolite as it would not stay

in the same form inside the zeolite. What happened to tetramethylcyclopentadiene is still unclear.

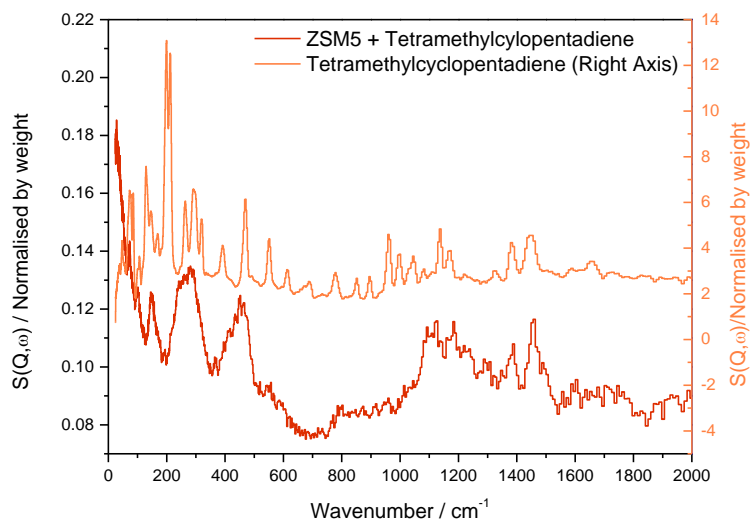


Figure A. 6: Tetramethylcyclopentadiene dosed in ZSM-5 and the pure compound shown as a reference

**ZSM-5 and 4-Methylcyclohexene:** 4-Methylcyclohexene was loaded on the zeolite using the bubbler arrangement at room temperature. 0.71 g of 4-methylcyclohexene were loaded on 12.65 g of dried ZSM-5 which implies that the loading was 3.4 moles of 4-methylcyclohexene per 1 ZSM-5 unit cell. There was 91.9% recovery when the sample was transferred in the Al can. From comparing the pure spectra and the methylcyclohexene loaded on the zeolite, it seems that some sort of reaction has taken place. Again, it is unknown what actually happened within the zeolite.

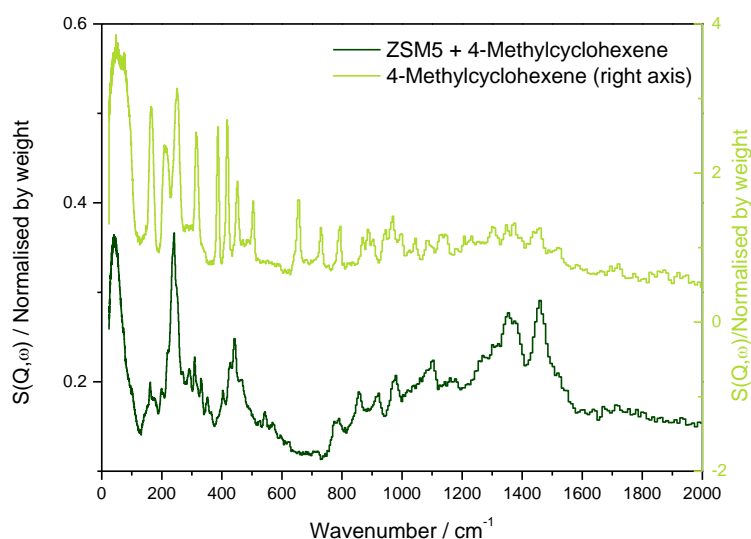


Figure A.7: 4-Methylcyclohexene dosed within the ZSM-5 and the pure compound used as reference

**ZSM-5 and Cyclohexene:** Cyclohexene was loaded on dried ZSM-5 zeolite using the bubbler arrangement at room temperature. The mass of the dried zeolite was 11.71 g and the final loading of cyclohexene was 1.06 g which suggests that there are 6.335 moles of cyclohexene per ZSM-5 unit cell. There was 92.5% mass recovered when transferring the sample to an Al can. After the INS spectra were collected, the sample was heated for 60 °C for 90 minutes (the can was sealed and not opened to air). The INS spectra after the heating were also collected. Figure A.8.a shows the comparison between the pure compound and the compound loaded on the zeolite. The spectra look different suggesting that being adsorbed on the zeolite surface is affecting the vibrational spectra of the cyclohexene. When the loaded sample was heated at 60 °C, the peak at 300  $\text{cm}^{-1}$  is no longer present although it might have shifted and merged with the peak present at 250  $\text{cm}^{-1}$ . A peak at 650  $\text{cm}^{-1}$  is no longer visible, with the peak at 1300  $\text{cm}^{-1}$  becoming much broader. Other than these slight changes nothing else seems to have changed in the spectra. It is still unknown what actually happened to the cyclohexene spectra when adsorbed on the zeolite at room temperature. When the sample was heated, additional changes in the vibrational spectrum could be contributed to a degree of dissociation happening when heat is applied.

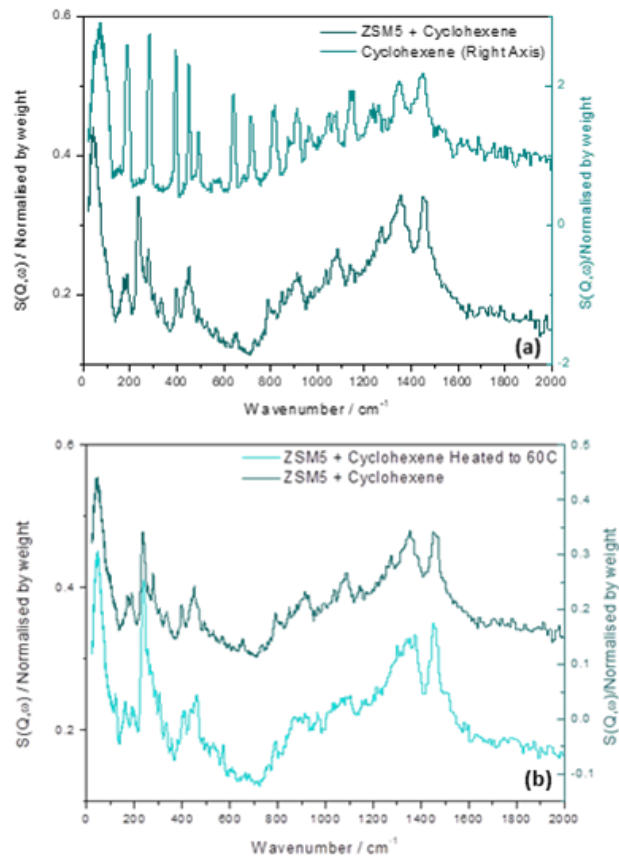


Figure A.8 (a) ZSM-5 dosed with cyclohexene with cyclohexene pure compound as a reference  
(b) ZSM-5 dosed with cyclohexene at room temperature and then after heated to 60 °C.

## Appendix: Chapter 4

- **Mass Spectrometry Traces for DRIFTS data**

The mass spectrometry profile for Figure 4.6 can be found in Figure A.9 and for Figure 4.10 in Figure A. 10. The mass followed for methanol was 31 whereas the mass followed for water was 17.

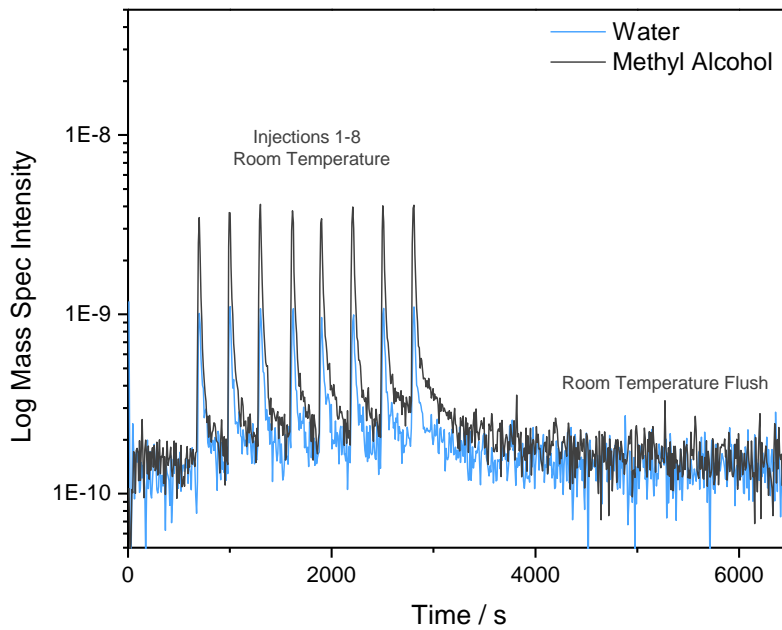


Figure A.9: Mass spectrometry profile for Figure 4.6 in Chapter 4

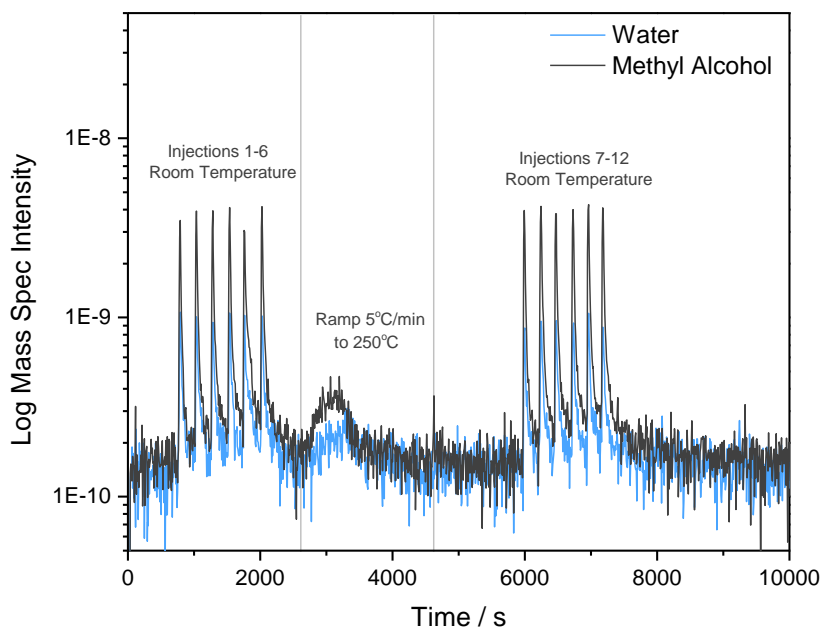


Figure A. 10: Mass spectrometry profile for Figure 4.10 in Chapter 4

- **Comparison with Liquid and Methanol Vapour of the Flushed Spectrum in Figure 4.6**

Figure 4.6 in Chapter 4 shows the difference spectra of the methanol injections right after they were injected and then after flushing with nitrogen. There are some peaks in the freshly injected samples which look like they could be due to methanol in vapour form. In order to confirm what is removed from the zeolite during flushing, the final flushed spectrum was subtracted from the freshly methanol injected spectrum seen in Figure 4.6. This gave the difference spectrum seen in Figure A. 11. The difference spectrum is then compared with the vapour and liquid spectrum of methanol with the liquid methanol spectrum being obtained from the NIST website.<sup>1</sup> The difference spectrum looks to be a combination of liquid and vapour methanol.

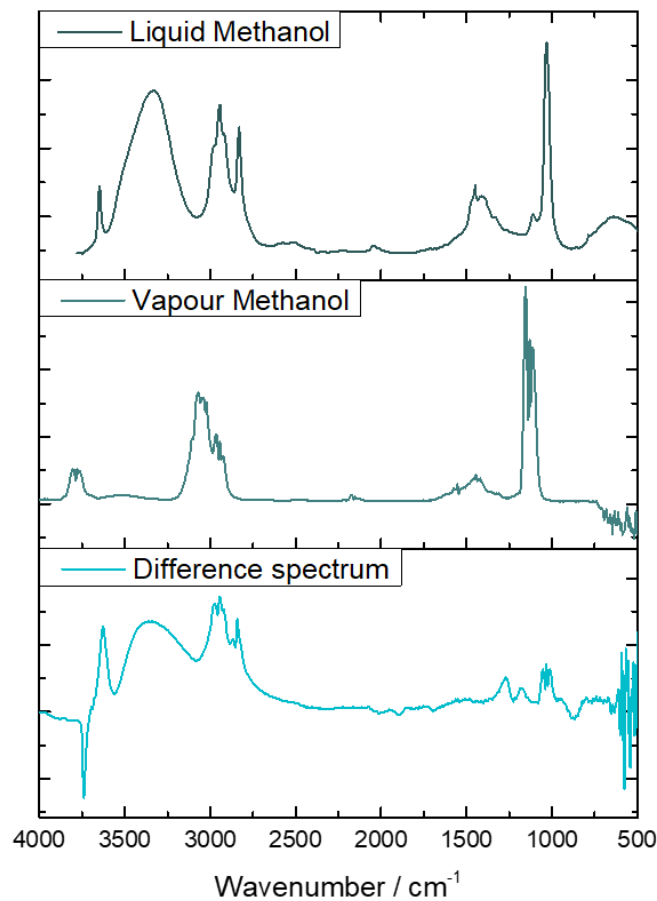


Figure A. 11: Difference spectrum of the methanol injection spectrum minus the flushed spectrum after injection. Liquid methanol spectrum<sup>1</sup> and vapour methanol spectrum are used for comparison purposes

- **Higher Methanol Loading**

A multiple injection experiment of 1  $\mu\text{l}$  injections of methanol per minute under a 20 ml/min  $\text{N}_2$  flow, with the spectra of the multiple injections seen in Figure A.12. The spectra show the rising methanol with the increased injection number, with the hope of oversaturating the zeolite sample. This experiment was designed in order to study the effect of the increased loading on the zeolite. However, it was evident that the spectra were dominated by methanol vapour, which was removed upon flushing the sample over a longer period of time. Figure A. 13 shows the changes on the spectra after flushing. The excess methanol is no longer present. Small differences in the low energy region of the flushed spectra in Figure A. 13 and the 4.6 in Chapter 4, could be due to subtraction errors as manipulating the spectra at those regions is problematic due to the zeolite framework modes. The difference could be due to what Matam et al. suggested as the methoxylation being loading dependent,<sup>2</sup> however, the INS and NMR data presented in Chapter 4 have shown that scenario to be unlikely.

In the C-H stretch region viewed in detail in Figure A. 13.b it shows that there is a shift in the C-H stretch peaks from the oversaturated spectrum to the flushed spectra. It is also seen that most of the methanol is flushed away with one hour of flushing.

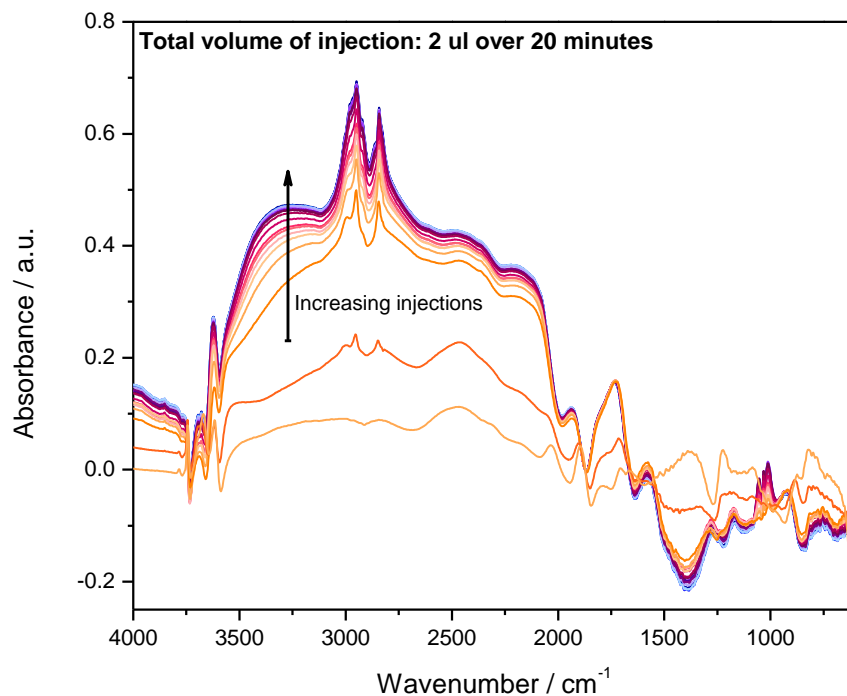


Figure A.12: Injection of  $1\mu\text{l}$  of Methanol every one minute over 20 minutes, with 20 ml/min  $\text{N}_2$  flow.

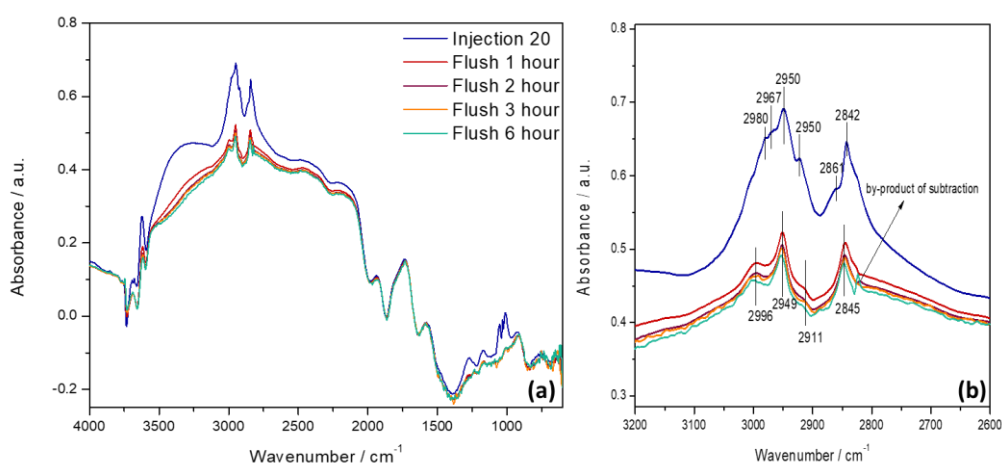


Figure A.13: (a) Injection 20 from Figure A.12 and spectra after flushing for 6 hours (b) detailed view of (a) in the  $3200 - 2600\text{ cm}^{-1}$  region.

### • DRIFTS Spectra: The Exchange Experiment

The INS experiment with the methanol-OD exchanged (Section 4.4.4) with regular methanol was also completed with the DRIFTS set up. The DRIFTS results can be found in the following Figure A.14.

The deuterated methanol injections show a difference in the ABC structure of the hydrogen bonded methanol. This is because of the difference in OH and OD in the two methanol isotopomers. Once the normal OH methanol is reinjected into the zeolite, the ABC structure we are familiar with returns. Due to the zeolite being constantly under flow, we were not able to saturate the zeolite, therefore, this is not a true exchange as was observed with the INS data.

The mass spectrometry profile for Figure A.14 is seen in Figure A.15. The deuterated methanol was monitored with the  $m/z$  33 whereas normal methanol was monitored with the  $m/z$  31. Masses 34 and 35 were also monitored however other than a small increase in  $m/z$  35, it remained close to the baseline.

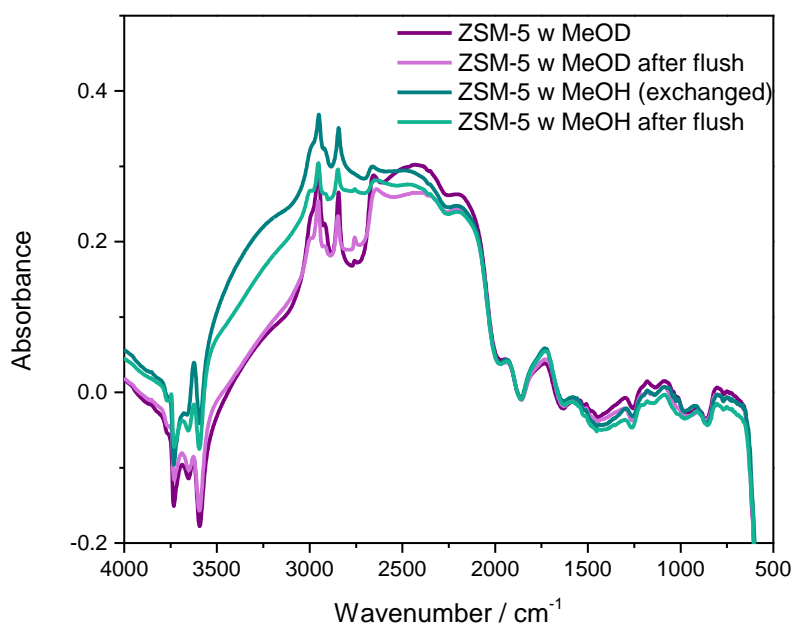


Figure A.14: ZSM-5 with MeOD injections (8 injections of 2 ul MeOD), flush for 1 hour and then second series of injections with MeOH (8 injections of 2 ul MeOH) and then flushed for another hour.

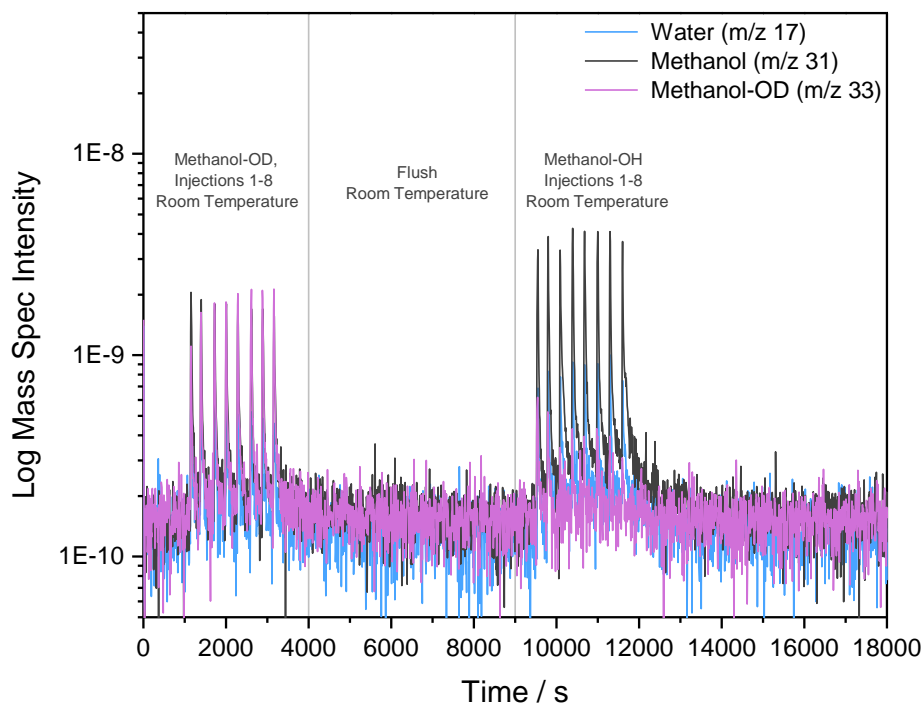


Figure A.15: Mass spectrometry profile for Figure A.10

- **Methanol Interaction in Different Zeolites**

The interaction of methanol and different ZSM-5 samples was also studied. This was done in order to compare any differences that could be observed when the methanol interacted at room temperature with a less acidic version of the zeolite. This was in preparation for an ISIS beam time which would have used INS in order to study the same samples. The hypothesis tested would have been that the ZSM-5 of Si:Al ratio of 27, is very acidic causing strong hydrogen bonding on the zeolite not able to be seen by the INS spectrometer. By using steamed samples of the same zeolite as well as different Si:Al ratio zeolites, the acid site density would be a lot less and thus the hydrogen bonding maybe not as strong. Figure A. 16 shows a comparison of the DRIFTS spectra of the empty dried zeolite samples. The steamed samples are fully characterised in Alex Hawkins thesis, however, the other JM samples were not characterised fully and therefore their actual Si:Al ratio is unknown. The Zeolite Y is the same zeolite used in the O'Malley paper which first noticed the loss of functionality in ZSM-5.<sup>3</sup> It will be used for comparison purposes.

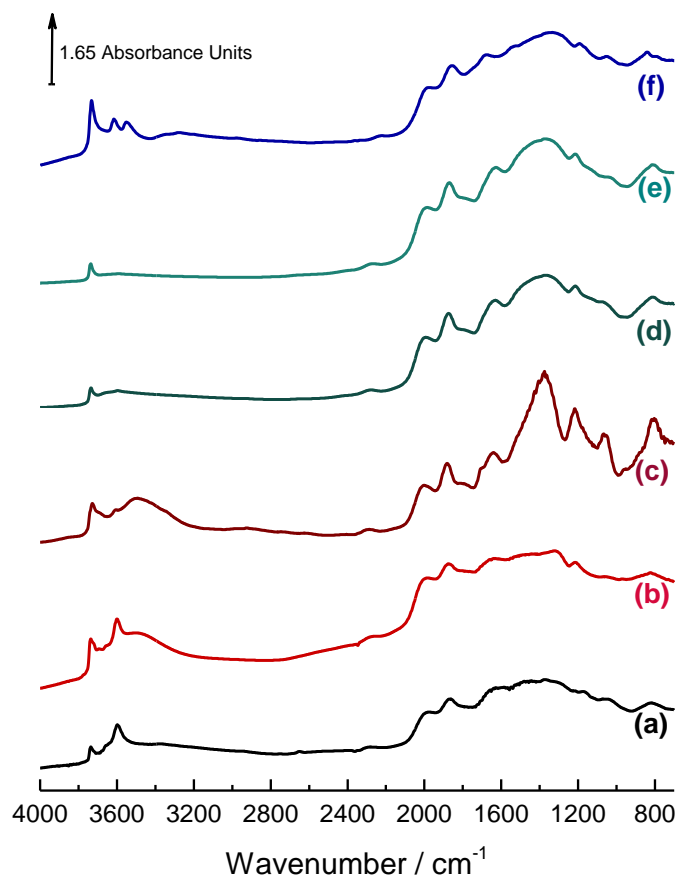


Figure A. 16: DRIFTS spectra of different zeolites compared to the (a) ZSM-5 Si:Al Ratio of 27 as quantified by INS (b) JM provided ZSM-5 with Si:Al 29.5 (c) JM provided ZSM-5 with Si:Al ratio of 100 (d) ISIS Steamed ZSM-5 (a) at 873K for 48 hrs and (e) JM Steamed ZSM-5 (a) at 1073K for 12 hours (f) Zeolite Y (Zeolyst, Si:Al ratio 15, same batch used in O'Malley et. al. paper)<sup>3</sup>

The same experiment was completed in all zeolites shown above, with their methanol injected spectra compared against the zeolite Y and the original ZSM-5 used throughout this project. 6 consecutive injections of 2  $\mu\text{l}$  with a total of 12  $\mu\text{l}$  injections over the different zeolites can be seen in Figure A.17. The difference spectra of the injected samples using their own blank zeolites as the subtracted background can be seen in Figure A.17. The methanol ABC structure is similar in the original ZSM-5 and the JM provided ZSM-5 of Si:Al ratio of 29.5. This is unsurprising due to the similarities in their Si:Al ratio. The JM, Si:Al ratio of 100, as well as the two steamed ZSM-5 samples show that there is a significant change in the ABC structure. There is very little contribution from the B band (the same is observed in Zeolite Y) and the contributions of the A and C bands are unknown and less clear than in the original zeolite. Zeolite Y has some ABC structure observed. The hump

observed in all zeolites but mostly defined in zeolite Y, steamed samples and the high silica ZSM-5 at about  $3400 - 3300 \text{ cm}^{-1}$ , is allocated to methanol clusters hydrogen bonded to each other.<sup>4</sup>

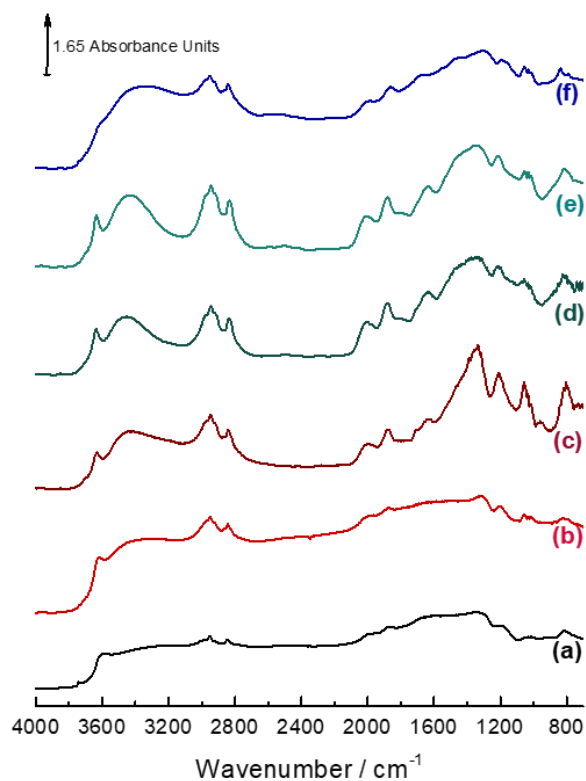


Figure A.17: DRIFTS spectra of  $12 \mu\text{l}$  injection of methanol over different zeolites (a) ZSM-5 Si:Al Ratio of 27 as quantified by INS (b) JM provided ZSM-5 with Si:Al 29.5 (c) JM provided ZSM-5 with Si:Al ratio of 100 (d) ISIS Steamed ZSM-5 (a) at 873K for 48 hrs and (e) JM Steamed ZM-5 (a) at 1073K for 12 hours (f) Zeolite Y

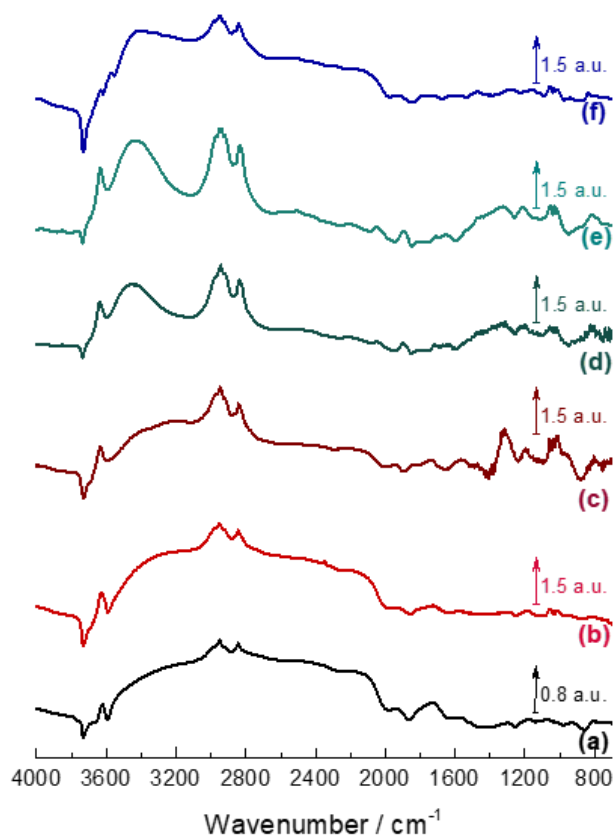


Figure A.18: The difference DRIFTS spectra of 12  $\mu\text{l}$  injection of methanol over different zeolites (a) ZSM-5 Si:Al Ratio of 27 as quantified by INS (b) JM provided ZSM-5 with Si:Al 29.5 (c) JM provided ZSM-5 with Si:Al ratio of 100 (d) ISIS Steamed ZSM-5 (a) at 873K for 48 hrs and (e) JM Steamed ZM-5 (a) at 1073K for 12 hours (f) Zeolite Y (Zeolist, Si:Al ratio 15, same batch used in O'Malley et. al. paper)<sup>3</sup>

From the DRIFTS data seen above, it would have been interesting to study the high silica ZSM-5 and the steamed samples using INS, as the decreased density in acid sites has lowered the contribution of the ABC structure. This could possibly mean that there are weaker hydrogen bonded methanol molecules present within those zeolite and hence the hydrogen bonded species might be visible with the INS technique.

## Appendix: Chapter 6

- **Dead Volume Calculation**

The dead volume of the gas manifold used for the QENS measurements used He at room temperature. The assumption was that He behaved as an ideal gas. The volumes seen in Table A. 1, have been calculated using Equation A.1 (Boyle's law) where  $P_1$  and  $V_1$  is the pressure and volume of the buffer (pre-calibrated by the ISIS team), and  $P_2$  is the final pressure seen in the manifold when opening up a new section, and  $V_2$  is the respective calculated volumes. This equation is only valid when the number of moles and the temperature are not changing. Since this is a closed system, Equation A.1 is safe to use in order to calculate the volume of the manifold.

$$P_1V_1 = P_2V_2 \quad \text{Equation A.1}$$

Table A. 1: Dead Volume Calculation

	Pressure Initial mBar	Pressure Final mBar	Volume cm <sup>3</sup>
<b>Line 1</b>			
<b>Buffer</b>		518.5	475.477
<b>+ Manifold</b>	518.5	478.3	515.46
<b>+ Splitter</b>	478.3	473.7	520.47
<b>+ Line to Stick</b>	473.7	457.9	538.43
<b>+ Stick</b>	457.9	450.2	547.64
<b>Line 2</b>			
<b>Up to Splitter</b>		450.2	520.47
<b>+ Line to Stick</b>	450.2	436.1	537.30
<b>+Stick</b>	436.1	428.1	547.34

- **Calculation of Methane Dosing**

The moles of methane loading seen in Table 6.1 in Chapter 6 are calculated using the Ideal Gas Law seen in Equation A.2 where P is the pressure in Pascals, V is the volume in m<sup>3</sup>, n is the number of moles, R is the ideal gas constant (8.314 J K<sup>-1</sup> mol<sup>-1</sup>) and T is the temperature in Kelvin which in our case is 298 K.

$$PV = nRT \quad \text{Equation A.2}$$

The sample dosing details are found in Table A.2.

Table A.2: Dosing experimental details

	<b>Buffer Pressure mBar</b>	<b>Methane (in Buffer) moles</b>	<b>Manifold Pressure (Removed) mBar</b>	<b>Methane (Removed) moles</b>
<b><i>Blank</i></b>				
<b>Dose 1</b>	919.9	0.017657	701.3	0.014591
<b>Dose 2</b>	983.9	0.018883	877.2	0.019389
<b><i>MTH-2h</i></b>				
<b>Dose 1</b>	920.7	0.017670	722.6	0.015033
<b>Dose 2</b>	959.8	0.018421	864.2	0.019090
<b><i>MTH-110h</i></b>				
<b>Dose 1</b>	918.6	0.017632	946.3	0.018162
<b>Dose 2</b>	781.3	0.018163	865.7	0.019125

## Appendix: Chapter 7

- **INS Spectra of MeOAc with no Stacking**

The INS spectra of the MeOAc reactions with the intensity normalised by the sample weight can be seen in Figure A.19. The spectra are not stacked as have been shown in Chapter 7 in order to show the difference in their intensity.

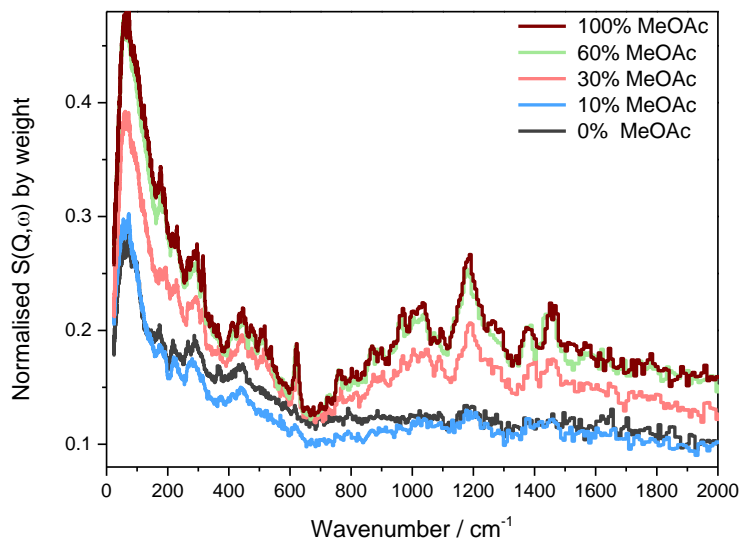


Figure A.19: INS spectra collected with the TOSCA instrument of the MeOAc reactions, 100% MeOAc (dark red), 60% MeOAc (green), 30% MeOAc (pink), 10% MeOAc (light blue) and 0% MeOAc (dark grey). Intensity normalised by the weight of the samples.

## References

- 1 NIST, Liquid Methanol - NIST, <https://webbook.nist.gov/cgi/cbook.cgi?ID=C67561&Type=IR-SPEC&Index=2#IR-SPEC>, (accessed 30 September 2020).
- 2 S. K. Matam, S. A. F. Nastase, A. J. Logsdail and C. R. A. Catlow, *Chem. Sci.*, 2020, **11**, 6805–6814.
- 3 C. R. A. Catlow, A. J. O'Malley, S. F. Parker and I. P. Silverwood, *Chem. Commun.*, 2016, **52**, 2897.
- 4 A. Zecchina, S. Bordiga, G. Spoto, D. Scarano, G. Spanò and F. Geobaldo, *J. Chem. Soc., Faraday Trans.*, 1996, **92**, 4863–4875.